Ultra-Red Galaxies

Thesis by
Alexander John Robert Lewis

Defended on 22 June, 2018

Fulfilment of the Requirements for
the Degree of
Doctor of Philosophy

The University of Edinburgh
Edinburgh, United Kingdom

2018

Butternut squash noodles . . .

Acknowledgements

I'd like to thank my supervisor, Rob Ivison, for taking a gamble with me and Philip Best for more often than not taking the brunt of that gamble.

Finally, I'd like to thank James Geach and Andy Lawrence for their constructive feedback on this thesis.

Abstract

Dusty star-forming galaxies (DSFGs) are highly luminous ($L_{\rm FIR} \gtrsim 10^{12}\,L_{\odot}$), very distant ($z \gtrsim 2.5$) and $\gtrsim 10\times$ rarer then 'normal', NIR-selected (BzK), star-forming galaxies. Capable of producing a $M_{\rm stars} \gtrsim 10^{11}$-$M_{\odot}$ galaxy after a $t_{\rm burst} \sim$ 100-Myr burst of late-stage, merger-induced star formation, DSFGs naturally provide extreme laboratories with which to study the formation and evolution of massive structures within the Universe. Thus far, however, theoretical models have struggled to reconcile the observed abundance and redshift distribution of these massive, dust-enshrouded galaxies that occupy the high-end tail of the galaxy stellar mass function. Therefore, it is of paramount importance, from an observational point of view, to both increase the number of known distant ($z \gtrsim 4$) DSFGs and to thoroughly explore their extreme environments in order to provide further constraints on such models.

Thus, in Chapter 2 of this thesis, I report on efforts to substantially increase the number of distant DSFGs using the uniquely wide *H*-ATLAS imaging survey. I analysed a sample of 109, so-called 'ultra-red galaxies' selected via their red *Herschel*-SPIRE flux densities ($\sigma_{500} > 3.5$ and $S_{500} < 100\,$mJy) and flux-density ratios ($S_{500}/S_{250} > 1.5$ and $S_{500}/S_{350} > 0.85$). Ground-Based continuum imaging at $\sim 850\,\mu$m with the JCMT and APEX telescopes allowed me to locate the dust peaks of these $S_{500} \gtrsim 30$-mJy ultra-red galaxies and derive a median photometric redshift of $z_{\rm phot} = 3.66$ (3.30–4.27, IQR) for them (assuming that they can satisfactorily be represented by a $T_{\rm dust} \sim 30$-K template SED). Using 25 spectroscopically confirmed DSFGs with SPIRE flux densities matching this ultra-red criteria, I determined that these FIR photometric redshift estimates have a minimum intrinsic scatter of $\sigma = 0.14(1 + z_{\rm spec})$ and systematically under-estimate the spectroscopic redshifts below $z_{\rm spec} \lesssim 5$. With over a third of these ultra-red galaxies lying above $z > 4$, I derived a space density of at least $\rho \approx 6 \times 10^{-7}\,{\rm Mpc}^{-3}$ for this sample (assuming a $t_{\rm burst} =$ 100-Myr burst of star formation), which is only a factor of 7$\times$ less numerous than that of the most massive ($M_{\rm stars} \gtrsim 10^{11}\,M_{\odot}$), compact, quiescent galaxies selected in the NIR at $z \sim 3$. Finally, although the space density of $z > 4$ ultra-red galaxies aligns very well with that of massive ($M_{\rm BH} \gtrsim 10^{8}\,M_{\odot}$) AGN at $z > 6$, none have yet to be uncovered within this sample to date.

In the following chapter, I present wide images obtained with LABOCA of a sub-sample of 22, representative ultra-red galaxies to see if these galaxies are signposting over-dense regions in the early Universe, as might be expected if they were to evolve into the most massive, compact, quiescent galaxies at $z \sim 0$. This LABOCA ultra-red galaxy survey

covers an area of $\approx 0.8\,\mathrm{deg}^2$ down to an average r.m.s. of $3.9\,\mathrm{mJy\,beam}^{-1}$, with the five deepest images going $\approx 2\times$ deeper still. I catalogue 86 galaxies detected above $> 3.5\sigma_{870}$ surrounding these 22 ultra-red galaxies, which implies a $\delta \approx 100 \pm 30\%$ over-density of $S_{870} > 8.5$-mJy ($L_{\mathrm{FIR}} \approx (7\text{–}30) \times 10^{12}\,L_{\odot}$) DSFGs when compared against LESS. Thus, I am 99.93% confident that these ultra-red galaxies are pinpointing over-dense regions in the Universe, and $\approx 95\%$ confident that these regions are over-dense by a factor of at least $\geq 1.5\times$. Using the same template SEDs as in the previous chapter, I derived a consistent median photometric redshift of $z = 3.2 \pm 0.2$ with an IQR of $z = 2.8$–3.6 for these ultra-red galaxies. I constrained the surrounding galaxies likely responsible for this over-density to within $|\Delta z| \leq 0.65$ of their respective ultra-red galaxies. However, on average, I was only able to associate one surrounding galaxy to within $|\Delta z| \leq 0.5$ of its respective ultra-red galaxy. These 'associated' galaxies are radially distributed within (physical) distances of $1.6 \pm 0.5\,\mathrm{Mpc}$ from their ultra-red galaxies, have median SFRs of $\psi \approx (1.0 \pm 0.2) \times 10^3\,M_{\odot}\,\mathrm{yr}^{-1}$ (assuming a Salpeter stellar IMF) and median gas reservoirs of $M_{\mathrm{gas}} \sim 1.7 \times 10^{11}\,M_{\odot}$. These candidate proto-clusters have average total SFRs of at least $\Psi \approx (2.3 \pm 0.5) \times 10^3\,M_{\odot}\,\mathrm{yr}^{-1}$ and a space density of $\sim 9 \times 10^{-7}\,\mathrm{Mpc}^{-3}$, consistent with the idea that their constituents may occupy the centres of rich galaxy clusters seen today.

Finally, in Chapter 4 of this thesis, I extracted *Herschel*-SPIRE photometry at the 850-μm positions of DSFGs detected within in the S2CLS and S2COSMOS imaging surveys. I then analysed the multi-wavelength environmental properties around a robust sample of 64 ultra-red galaxies selected via their 'ultra-red probability'. Similar to the findings in Chapter 3, I found that these ultra-red galaxies are preferentially located in over-dense regions extending over scales of $\sim 5'$ (or $\sim 2\,\mathrm{Mpc}$ at $z \sim 3$). Furthermore, I found that these candidate, high-redshift proto-clusters have FIR total dust masses and total SFRs of $M_{\mathrm{dust}} \sim 10^9\,M_{\odot}$ and $\Psi \sim 10^3\,M_{\odot}\,\mathrm{yr}^{-1}$, respectively. Ground-Based, optical/NIR imaging around a subset of 42 ultra-red galaxies shows a factor of $\sim 5\times$ increase in both the stellar mass and the $(M_B - M_I)$-colour of associated LBGs as the radial distance decreases from $\lesssim 500\,\mathrm{kpc}$ – consistent with the emergence of a galaxy red sequence at $z \sim 3$. Furthermore, these data show a 1-σ increase in the fraction of 'green-valley' galaxies within scales of $\sim 5'$ compared to the field – supporting the concept that red-sequence galaxies are appearing at a faster rate around ultra-red galaxies compared to the field. There is a sizeable contribution of $M_{\mathrm{stars}} \sim 10^{12}\,M_{\odot}$ from these high-redshift LBGs within the environments of ultra-red galaxies. On average, I was able to associate ≈ 28 LBGs to a given ultra-red galaxy ($\sim 30\times$ the number of associated DSFGs). Although these systems have average optical/NIR/FIR properties that are consistent with their evolution into present-day galaxy clusters with DM halos of mass $M_{\mathrm{halo}} \sim 10^{14}$–$10^{15}\,M_{\odot}$, I am still likely missing a sizeable contribution from unassociated LBGs and DSFGs due to the large photometric redshift uncertainties for the ultra-red galaxies. Therefore, the results presented in this thesis should be regarded as firm lower limits on these environmental properties around ultra-red galaxies, which can now only be improved upon when spectroscopic data increases the accuracy of the photometric redshift estimates presented here.

Lay Summary

When **two gas-rich galaxies collide** (each containing a billion or so stars intertwined with vast quantities of the most plentiful substance in the Universe, Hydrogen), they eventually merge into a single galaxy after a spectacular display of toing and froing that lasts for around a few hundred million years. During this 'cosmic dance', the gas supplies (or Hydrogen reservoirs) from each galaxy are compressed, which triggers a large burst of star formation that **produces roughly a thousand new stars per year**, many more than compared to that of the Milky Way, namely just one new star per year. The high-end mass tail of these newly born stars (or, equivalently, the stars that are many times greater in size than our Sun) only live for around a hundred million years and explode violently upon their death – **generating vast quantities of dust** (carbon/silicate) grains in the process. Over time these dust grains, which subsequently obscure the remaining stars within a galaxy from conventional optical observations, heat up and **shine brightly in the far-infrared**. These dusty, far-infrared-bright galaxies are the biggest and brightest sources within the Universe and appear to be many times more numerous in the past, when the Universe was *only* three-billion(ish)-years old, or 20 per cent of its current age. Therefore, these galaxies are of great interest for **testing and constraining current models of galaxy formation**. Or, put another way, observations of these distant, dusty galaxies can place valuable constraints on the evolution of massive galaxies that harbour over half of the stars ever made during the lifetime of the Universe.

However, until recently only a handful of these distant, dusty star-forming galaxies (or so-called 'ultra-red galaxies') were known due to a combination of their inherent rareness and difficulties in building instruments sensitive enough to observe them. Thus, in the first part of this thesis, I used freshly taken images with the *Herschel* Space Observatory in order to **generate a large sample of ultra-red galaxies**. Then, using follow-up, ground-based imaging, I was able to determine the distances to these galaxies and thus place valuable constraints on their likely evolutionary path until the present. The work contained within this thesis suggests that **ultra-red galaxies will evolve into the most massive galaxies seen today**, which typically reside in the centres of galaxy clusters – thousands of gravitationally bound galaxies that form the largest known structures in the Universe.

Therefore, in the latter half of this thesis, **I examined the environments around ultra-red galaxies** to test whether or not these galaxies signpost the progenitors of present-day galaxy clusters (or so-called 'proto-clusters'), as might be expected if they truly

do evolve into the most massive galaxies seen today. Our current consensus on massive galaxies within the centres of galaxy clusters is that they formed when the Universe was young, over relatively short time-scales (a few hundred million years or so) and potentially enshrouded in dust. Indeed, I found that the environments around ultra-red galaxies are, on average, consistent with those that are expected for proto-clusters. Thus, I showed that locating **ultra-red galaxies provides an efficient method for signposting proto-clusters in the distant Universe**, for which we do not currently have a complete sample. This is a crucial result as any feasible theory describing galaxy formation, or any coherent cosmological model of the Universe, must satisfactorily explain the observed evolution of galaxy clusters from this early stage.

Declaration

I declare that the thesis has been composed by myself and that the work has not been submitted for any other degree or professional qualification. I confirm that the work submitted is my own, except where work that has formed part of jointly authored publications has been included. My contribution and those of the other authors to this work have been explicitly indicated below. I confirm that appropriate credit has been given within this thesis where reference has been made to the work of others.

The work presented in Chapter 2 was previously published in Ivison et al. (2016) as 'The Space Density of Luminous Dusty Star-Forming Galaxies at $z > 4$: SCUBA-2 and LABOCA Imaging of Ultra-Red Galaxies from *Herschel*-ATLAS' by R. J. Ivison (my supervisor), A. J. R. Lewis (myself), A. Weiss, V. Arumugam, J. M. Simpson, W. S. Holland, S. Maddox, L. Dunne, E. Valiante, P. van der Werf, A. Omont, H. Dannerbauer, Ian Smail, F. Bertoldi, M. Bremer, R. S. Bussmann, Z.-Y. Cai, D. L. Clements, A. Cooray, G. De Zotti, S. A. Eales, C. Fuller, J. Gonzalez-Nuevo, E. Ibar, M. Negrello, I. Oteo, I. Pérez-Fournon, D. Riechers, J. A. Stevens, A. M. Swinbank and J. Wardlow. This study was conceived by all of the authors. I carried out the analysis, discussion and conclusion.

The work presented in Chapter 3 is to be published in Lewis et al. (2017) as 'Ultra-Red Galaxies Signpost Candidate Proto-Clusters at High Redshift' by A. J. R. Lewis (myself), R. J. Ivison (my supervisor), P. N. Best, J. M. Simpson, A. Weiss, I. Oteo, Z-Y. Zhang, V. Arumugam, M. Bremer, S. C. Chapman, D. L. Clements, H. Dannerbauer, L. Dunne, S. Eales, S. Maddox, S. J. Oliver, A. Omont, D. A. Riechers, S. Serjeant, E. Valiante, J. Wardlow, P. van der Werf and G. De Zotti. This study was conceived by all of the authors. I carried out the data reduction, analysis, discussion and conclusion.

.....

Alexander John Robert Lewis, March 2018

Contents

List of Figures

List of Tables

List of Abbreviations

Astronomical and Mathematical Terms

CDF	Cumulative Distribution Function (Φ)
CFIRB	Cosmic Far-Infrared Background
CMB	Cosmic Microwave Background
COB	Cosmic Optical Background
DM	Dark Matter
DSFG	Dusty Star-Forming Galaxy
EGBL	Extragalactic Background Light
ETG	Early-Type Galaxy
FDR	False Detection Rate
FIR	Far-Infrared
FIRRC	Far-Infrared/Radio Correlation
FWHM	Full-Width-at-Half-Maximum (θ)
GDR	Gas-to-Dust ratio (δ_{GDR})
ICM	Intracluster Medium
IGM	Intergalactic Medium
IMF	Initial Mass Function
IQR	Interquartile Range
IR	Infrared
ISM	Interstellar Medium
K-S	Kolmogorov-Smirnov
KDE	Kernel Density Estimate
LBG	Lyman-Break Galaxy
LF	Luminosity Function
LR	Likelihood Ratio

LTG	Late-Type Galaxy
MAD	Median Absolute Deviation
NIR	Near-Infrared
PSF	Point Spread Function
PWV	Precipitable Water Vapour
SED	Spectral Energy Distribution
SFR	Star Formation Rate (ψ)
SMG	Submillimeter Galaxy
SNR	Signal-to-Noise Ratio (S/N)
SNe	Supernovae
ULIRG	Ultraluminous Infrared Galaxy
UV	Ultraviolet
AGN	Active Galactic Nuclei
HzRG	High-Redshift Radio Galaxy

Computer Software and Languages

BOA	BOlometer Array Data Analysis Software
DIMM	Dynamic Iterative Map-Maker
IDL	Interactive Data Language
MADX	Multi-Band Algorithm for Source eXtraction
SMURF	Sub-Millimetre User Reduction Facility ()

Surveys and Fields

ALESS	ALMA-LESS
Akari-NEP	Akari-Northern Ecliptic Pole
CDFS	*Chandra* Deep Field-South Survey
COSMOS	Cosmological Evolution Survey
ECDFS	Extended Chandra Deep Field South
EGS	Extended Groth Strip
ELAIS-S1	European Large-Area Infrared Survey-South 1
GAMA	Galaxy And Mass Assembly
GOODS-N	Great Observatories Origins Deep Survey-North
HeLMS	HerMES Large Mode Survey
LESS	LABOCA ECDFS Submillimetre Survey

NGP	North Galactic Pole
S2COSMOS	SCUBA-2 COSMOS
SGP	South Galactic Pole
SHADES	SCUBA HAlf Degree Extragalactic Survey
SSA22	SuperCosmos Science Archive 22
SXDF	Subaru/XMM-Newton Deep Field
UDS	UKIDSS Ultra-Deep Survey
UKIDSS	UKIRT Infra-Red Deep Sky Survey
VIKING	VISTA Kilo-Degree Infrared Galaxy Survey
VISTA	Visible and Infrared Survey Telescope for Astronomy
ADF-S	*Akari Deep Field*-South
***H*-ATLAS**	*Herschel*-Astrophysical Terahertz Large Area Survey
***Her*MES**	*Herschel* Multi-Tiered Extragalactic Survey
IRAS	*Infrared Astronomical Satellite*
S2CLS	SCUBA-2 Cosmology Legacy Survey
***XMM*-LSS**	X-ray Multi-Mirror Mission-Large Scale Structure

Telescopes, Instruments and Satellites

A-MKID	APEX Microwave Kinetic Inductance Detector
ALMA	Atacama Large Millimeter Array
APEX	Atacama Pathfinder EXperiment
COBE	COsmic Background Explorer
JCMT	James Clerk Maxwell Telescope
LABOCA	Large Apex BOlometer CAmera
NOEMA	Northern Extended Millimeter Array
PACS	Photoconductor Array Camera and Spectrometer
SPIRE	Spectral and Photometric Imaging Receiver
SPT	South Pole Telescope
UKIRT	United Kingdom Infra-Red Telescope
VLA	Very Large Array
SCUBA/-2	Submillimeter Common-User Bolometer Array/-2

1 Introduction

Make sure you get the history of SMGs right, or I will have you shaved from head to toe

R. J. Ivison (1966–present)

1.1 The Far-Infrared Universe

A couple of decades have now passed since low-resolution infrared (IR) detectors on-board the COsmic Background Explorer (COBE) discovered the cosmic far-IR (FIR, $\lambda \sim$ 8–1,000 μm) background (CFIRB — Puget et al., 1996; Fixsen et al., 1998). Apart from the nearly isotropic contribution from the cosmic microwave background (CMB) – shaped shortly after the 'Big Bang' by the decoupling of photons and matter at a redshift of $z \sim 1{,}100$ – the CFIRB and the cosmic optical background (COB — Hauser et al., 1998) are the next equal(ish) contributors to the so-called 'extragalactic background light' (EGBL); a superposition of all of the radiation emitted by all of the galaxies over all of cosmic time (Partridge & Peebles, 1967; Dwek et al., 1998). This discovery by COBE required a drastic change in the existing paradigm of cosmic star formation rates (SFRs, or ψ), which hitherto had been accounted for solely by the detections of ultraviolet (UV, $\lambda \sim 0.01$–$0.5\,\mu$m) and optically selected 'Lyman-break galaxies'[1] (LBGs — Steidel et al., 1996; Giavalisco, 2002). Specifically, these observations now required that the integrated star formation was a factor of at least 2× larger at 'Cosmic High Noon' (or $z \sim 2$) due to equal(ish) contributions from both the CFIRB and COB (Lonsdale et al., 2006). However, in order to conserve the local K-band ($\lambda = 2.2\,\mu$m) luminosity density (which also provides a rough proxy for the stellar mass density as it traces the older stellar population), this increase in the cosmic SFRs had to originate from young, massive, O-/B-type stars within a population

[1] The spectra of distant galaxies ($z < 3$) exhibit a sharp break at the $\lambda = 912$-Å (or $E = 13.6\,$eV, where $1\,\text{eV} \sim 2 \times 10^{-19}\,$J) Lyman limit caused by the absorption of galactic starlight by hydrogen within the interstellar medium. Furthermore, there is an additional, more pronounced break at $\lambda = 1{,}216\,$Å in the spectra of high-redshift ($z \gtrsim 3$) galaxies caused by absorption from the intervening hydrogen within the intergalactic medium, i.e. the so-called 'Lyman-α forest' (Lynds, 1971). These distinct features facilitate the selection of distant galaxies by measuring which passband this break occurs in, or equivalently, from which passband the flux density from a given LBG 'drops out'.

of dust-rich (carbonaceous and amorphous silicate grains) galaxies that had previously escaped detection at UV and optical ($\lambda = 0.4$–$0.7\,\mu$m) wavelengths.

1.2 Ultra-Luminous Infrared Galaxies

Optically dark galaxies were already known to reside within the local ($z \lesssim 0.1$) Universe, albeit only being recorded in small numbers during the first all-sky survey undertaken by the *Infrared Astronomical Satellite* (*IRAS* — Neugebauer et al., 1984). These galaxies were referred to as 'ultra-luminous IR galaxies' (ULIRGs — Lawrence et al., 1986; Sanders et al., 1988; Sanders & Mirabel, 1996) as their vast FIR luminosities[2] ($L_{\rm FIR} \gtrsim 10^{12}\,L_\odot$, where $L_\odot \sim 4 \times 10^{26}\,$W) accounts for a significant fraction of their bolometric (or total) luminosities as compared to 'normal galaxies'[3]. Although in 1985 'the nature of the underlying energy source [responsible for these vast luminosities was yet to be ...] firmly established' (Houck et al., 1985), it is now thought to be driven by an enormous burst of star formation and/or the presence of an active galactic nucleus (AGN) obscured by vast quantities ($M_{\rm dust} = (1$–$10) \times 10^9\,M_\odot$, where $M_\odot \sim 2 \times 10^{30}\,$kg) of dust, originating from asymptotic giant branch stars and supernovae (SNe) explosions (Matsuura et al., 2009).

A sizeable fraction of our knowledge about these types of galaxies has come from our closest[4] (and proto-typical) ULIRG, Arp 220 (Soifer et al., 1984) – one of the 338 entries in the 'Atlas of Peculiar Galaxies' produced by Halton Arp in 1966. The spectral energy distribution (SED) for this galaxy from the near-IR (NIR, $\lambda \sim 1.0$–$2.5\,\mu$m) through to the sub-millimetre (sub-mm, $\lambda \sim 100$–$1{,}000\,\mu$m) is shown in Figure 1.1. This figure illustrates that the bulk of the luminosity is occurring in the FIR, whose shape is well modelled by a modified black-body (i.e. a 'grey-body', which reflects the imperfect balance between absorption and re-emission of a particular dust grain — Hildebrand, 1983) with hot ($T_{\rm hot} \gtrsim 50\,$K) and cold ($T_{\rm cold} \lesssim 30\,$K) dust components, given by:

$$S_\nu \propto \nu^\beta \left[B_\nu \left(T_{\rm hot} \right) + a B_\nu (T_{\rm cold}) \right] , \tag{1.1}$$

where S_ν is the flux density at frequency ν typically measured on the Jansky scale (where $1\,{\rm Jy} = 10^{-26}\,{\rm W\,m^{-2}\,Hz^{-1}}$), $\beta \approx 2$ is the dust emissivity spectral index that enhances/suppresses the black-body radiation above/below some reference frequency at which the emission becomes optically thick, $a \sim 50$ is the ratio of cold-to-hot dust and

[2] The FIR luminosity of a galaxy is derived by integrating the flux density over a rest-frame wavelength of $\lambda_{\rm rest} = 8$–$1{,}000\,\mu$m, i.e. $L_{\rm FIR} = 4\pi D_L^2 \int {\rm d}\nu'\, S_{\nu'}/(1+z)$, where D_L is luminosity distance at a redshift z.

[3] A normal galaxy (such as the Milky Way) has an FIR luminosity of $L_{\rm FIR} \sim 10^{10}\,L_\odot$, a SFR of $\psi \sim 1\,M_\odot\,{\rm yr}^{-1}$ and a size of $a \sim 30\,$kpc, where $1\,{\rm kpc} \sim 3 \times 10^{19}\,$m.

[4] Arp 220 is $\sim 80{,}000\,$kpc away from Earth. To put this in perspective, Alpha Centauri A (our closest star) is $\sim 0.001\,$kpc away, Andromeda (our closest galaxy) is $\sim 800\,$kpc away and the Virgo Cluster (our closest galaxy cluster) is $\sim 20{,}000\,$kpc away.

$B_\nu\,(T)$ is the Planck function at a dust temperature T defined as:

$$B_\nu\,(T) = \frac{2h\nu^3/c^2}{\exp\left(h\nu/(k_BT)\right)-1} \quad \underset{\nu\ll1}{\longrightarrow} \quad \overbrace{\frac{2h\nu^3/c^2}{(1+k_BT/h\nu)-1} = \frac{2k_BT}{c^2}\nu^2}^{\text{Rayleigh-Jeans limit}}, \tag{1.2}$$

where $h \sim 7\times10^{-34}\,\mathrm{m^2\,kg\,s^{-1}}$, $k_B \sim 1\times10^{-23}\,\mathrm{m^2\,kg\,s^{-2}\,K^{-1}}$ and $c \sim 3\times10^{8}\,\mathrm{m\,s^{-1}}$ are the Planck and Boltzmann constants and speed of light, respectively. In the long-wavelength ($\lambda_{\rm rest} \gtrsim 100\,\mu$m) Rayleigh-Jeans side of the SED, Equation 1.1 reduces to $S_\nu \propto \nu^{\beta+2}\,(T_{\rm hot} + aT_{\rm cold})$, or simply $S_\nu \propto \nu^{\beta+2}$.

It is important to note that Equation 1.1 assumes that the dust within these galaxies is optically thick to starlight (i.e. the optical depth is much greater than one, $\tau_\nu \gg 1$) and is optically thin to sub-mm emission ($\tau_\nu \ll 1$). This is the reason that the attenuation due to dust in the optically thin regime can be approximated by:

$$1-\exp\left(-\tau_\nu\right) \rightarrow \tau_\nu = \kappa_\nu\Sigma_{\rm dust} \propto \nu^\beta,$$

where κ_ν is the opacity (or dust mass absorption coefficient — James et al., 2002), which has been represented by a power law in frequency, and $\Sigma_{\rm dust}$ is the surface area of dust mass.

This assumption is justified as the dust grains within the interstellar medium (ISM) have sizes that typically range from $a \sim 0.01$–$0.5\,\mu$m, which are comparable to the wavelength of UV starlight emitted by young, massive stars. Hence, these dust grains in thermal equilibrium essentially absorb all of the UV emission (thus making it optically thick at these wavelengths) and thermally re-radiate it as a grey-body centred on $\lambda \sim 100\,\mu$m (thus making it optically thin at these wavelengths due to the few orders of magnitude difference from the typical dust-grain size — Draine & Li, 2007).

If an assumption is made that *all* of the FIR of a dusty galaxy originates from the reprocessing of starlight emitted by young, massive stars within that galaxy, then this FIR luminosity can be converted into an 'instantaneous SFR'[5]. In his pioneering work, Kennicutt (1998) assumed that when a given star within a given dusty galaxy reaches an age of $t_{\rm star} \gtrsim 100\,$Myr, the dense dust around it has been fully dispersed into the ISM due to years of bombardment by intense solar-radiation pressure. Consequently, the optical depth around 'older' stars (which recall predominantly emit in K-band) reverses, which in turn means that they no longer contribute towards the FIR luminosity of that galaxy. Furthermore, under the assumption that the young, massive stars are in *complete* thermal equilibrium with their surrounding dust clouds, then the FIR luminosity is directly proportional to the SFR, averaged over a 100 Myr of course. Thus, using the radiative

[5]Star formation is not at instantaneous process as it can take up to $\sim 1\,$Myr for a dense, gravitationally bound, $M_{\rm gas} = (10^5$–$10^6)$-$M_\odot$ molecular gas cloud to collapse and thus ignite (Larson, 1981). Thus, the concept of an instantaneous SFR is nonsensical, resulting in the need to time average the stellar mass formed within a galaxy over, say, 100 Myr.

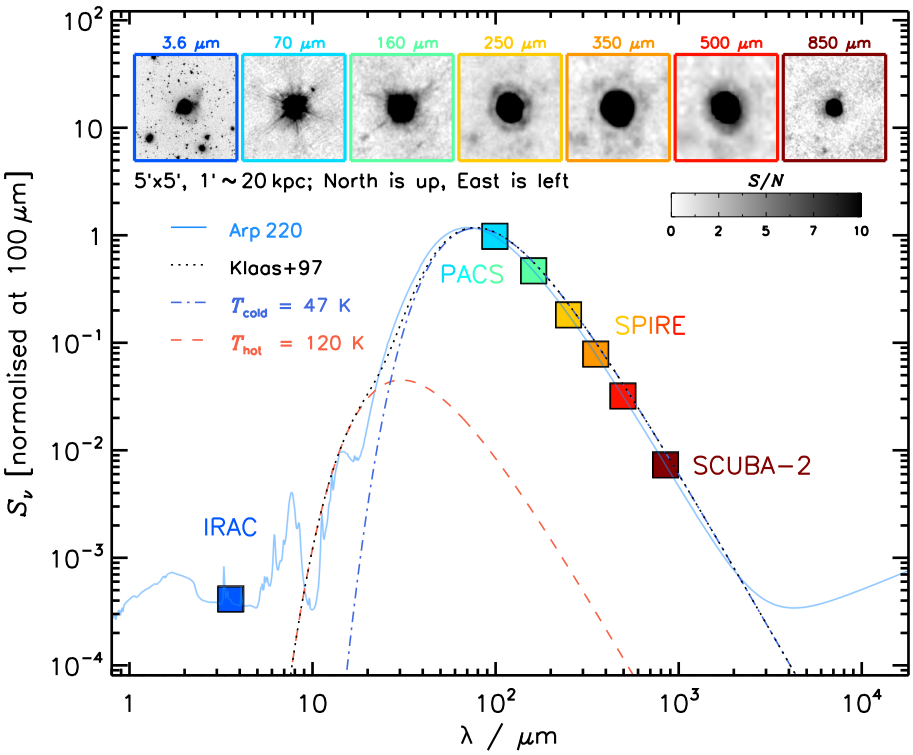

Figure 1.1: Main: SED of Arp 220 (solid light blue). The modified grey-body (black dotted line) – composed of hot ($T_{\rm hot}$ = 120 K, red dashed line) and cold ($T_{\rm cold}$ = 47 K, blue dashed-dotted line) dust components – models the FIR dust emission well (Klaas et al., 1997). As can be seen the cold dust component dominates the FIR luminosity and peaks at a longer wavelength relative to the hot dust component. Thus, as the peak of the SED is also moved to longer wavelengths as the redshift increases, the two effects are indistinguishable, which results in the well-known temperature-redshift degeneracy. **Inset:** colour-coded cut-outs of Arp 220 taken with the JCMT (sub-mm) ground-based telescope and the *Spitzer* (NIR) and *Herschel* (FIR, see Figure 1.4) space-based telescopes. Each cut-out is $5' \times 5'$ (or $\sim 100\,{\rm kpc} \times 100\,{\rm kpc}$ at $z = 0.018$), linearly stretched between a signal-to-noise ratio (SNR or S/N) of $0 < S/N < 10$ (inset scale) and centred on Arp 220. North is up and East is left. These cut-outs highlight the decreasing resolution with increasing wavelength, resulting in sub-mm cosmology being nicknamed 'blobology'. The shortest-wavelength, cut-out shows evidence, via tidal debris, that Arp 220 experienced a galaxy-merger event in its past.

transfer models of Leitherer & Heckman (1995) for continuous starbursts[6] ranging in age from 10–100 Myr and a Salpeter initial mass function (IMF, or $\xi(m) \propto m^{-\alpha}$, with $\alpha = 2.35$ being empirically based on stars within the solar neighborhood — Salpeter, 1955) that describes the distribution of stellar mass at birth, Kennicutt (1998) concluded that there is a linear relationship between the FIR luminosity and the SFR of a galaxy, given by:

$$\frac{\psi}{M_\odot\,\mathrm{yr}^{-1}} = 4.5 \times 10^{44} \left(\frac{L_\mathrm{FIR}}{\mathrm{erg\,s}^{-1}}\right) \approx 1.7 \times 10^{-10} \left(\frac{L_\mathrm{FIR}}{L_\odot}\right). \tag{1.3}$$

Thus, this equation suggests that a $L_\mathrm{FIR} \gtrsim 10^{12}$-$L_\odot$ ULIRG could be producing stars at a rate of $\psi \gtrsim 2 \times 10^2\,M_\odot\,\mathrm{yr}^{-1}$, and thus has the potential to generate a $M_\mathrm{stars} \gtrsim 10^{11}$-$M_\odot$ galaxy within a burst of star formation that lasts $t_\mathrm{burst} = 100\,\mathrm{Myr}$. However, it should be noted that this time-scale is uncertain at the 2× level, at the very least; a starburst episode could be shorter and episodic, perhaps even enduring for up to $\sim 1\,\mathrm{Gyr}$, interspersed with periods of relative inactivity (Lapi et al., 2014; Aversa et al., 2015).

The SFRs computed in this way are very sensitive to the underlying assumption made about the IMF. For instance, if a Chabrier IMF (Chabrier, 2003) is assumed, which exponentially decreases the number of low mass ($m \leq 1\,M_\odot$) stars produced, then the results obtained by Equation 1.3 would be need to be scaled by a factor of $\approx 0.6\times$. Furthermore, there is also growing support that the IMF may actually be 'top heavy' within these dusty galaxies, i.e. for every high-mass star formed there would be many fewer low-mass stars formed (Baugh et al., 2005; Romano et al., 2017; Zhang et al., 2018, but see Hayward et al., 2013; Safarzadeh et al., 2017). This excess of high-mass stars also boosts the production of dust, which is necessary for increasing the FIR luminosity of these dusty galaxies. If the IMF were top heavy, then the SFRs calculated with Equation 1.3 would be over-estimated by a factor of $\approx 3\times$.

There is also an assumption with Equation 1.3 that none of the FIR luminosity is caused by the presence of an AGN heating the surrounding dust. Once again, if this were the case then the SFRs would be over-estimated as AGN are known to contribute by as much as 10–50% to the FIR luminosity. However, even in the worst possible case that all of the above caveats are proved right (i.e. in the event that the SFRs are scaled down by a factor of $\sim 0.1\times$ to $\psi \gtrsim 100\,\mathrm{Myr}$), the SFRs in these systems still remain high.

Finally, as the surface area of dust mass (or Σ_dust) mentioned earlier represents the amount of dust (M_dust) integrated along the line-of-sight of a particular dusty galaxy, Equation 1.2 can be re-arranged to:

$$M_\mathrm{dust} = \frac{S_\nu D_L^2}{(1+z)\kappa_\nu B_\nu(T)}, \tag{1.4}$$

where the factor of $(1 + z)$ accounts for the band-shifting and compression of frequency space with redshift.

Thus, although in principle the integrated SED can provide an estimate of the stellar mass

[6] If the surrounding dust clouds are not dispersed within 100 Myr and over that time the SFR does not remain relatively constant then the FIR luminosity will not be directly proportional to the SFR.

for a normal galaxy (which of course excludes the stellar remnants, such as black holes, that no longer contribute to the SED), the most that can be estimated from the SED of a dusty galaxy is the dust mass, using Equation 1.4. However, if an assumption is made on how the dust mass correlates with the molecular gas mass ($M_{\rm gas}$, which is assumed to be homogeneously mixed together) using a gas-to-dust ratio (GDR or $\delta_{\rm GDR}$ — Santini et al., 2010; Eales et al., 2012; Scoville et al., 2014, 2015), then the number of stars made through the lifetime of a dusty galaxy can be inferred by assuming that all of the molecular gas within it is converted into stars.

Figure 1.1 also shows a range of $5' \times 5'$ (where $1' \approx 20\,{\rm kpc}$ at $z = 0.018$, the redshift of Arp 220) cut-outs, which illustrates the wavelength-dependent, morphological properties of this ULIRG. A long tidal tail and relaxed central body as seen through the high-resolution NIR imaging supports the concept that Arp 220 has undergone a violent interaction event in its past – triggering a late-stage, merger-induced burst of star formation and/or AGN activity that results in its vast FIR luminosity. Arp 220 has a NIR brightness profile that is well described by an $r^{1/4}$ de Vaucouleurs profile – indicating that it closely resembles an early-type galaxy (ETG, i.e. a relatively passive elliptical or lenticular), or at least one in formation. This dense, compact galaxy contains $\sim 2/3$ of its total stellar mass ($M_{\rm stars} \sim 2 \times 10^{10}\,M_{\odot}$) within a central 3-kpc region in which two *distinct* nuclei (or so-called 'East' and 'West' components) have been shown to reside using the Atacama Large Millimeter/submillimeter Array (ALMA — Scoville et al., 2017).

Thus, it is temping to think of ULIRGs as present-day ETGs in the process of forming after a major-merger event between two dust-rich, late-type galaxies (LTGs, i.e. star-forming spirals). Theory has shown that huge quantities of gas can be built up in the central regions as the dynamical friction introduced through such collisions causes the gas to lose angular momentum and funnel towards the centre – providing an ideal breeding ground for new star formation and/or an ideal environment for building an AGN (Barnes & Hernquist, 1992). This merger-induced, dissipative collapse offers a natural gap between dust-rich colliding LTGs and passively evolving ETGs, whose gas-poor properties are reconciled by the presence of 'super-winds' that can easily expel all of the vast reservoirs of cold gas and dust seen in ULIRGs (Martin, 1999; Greve et al., 2005). Caused by the resulting SNe of young, massive stars, these super-winds also help to explain the abundances of iron present in the intracluster medium (ICM) in which ETGs are typically seen to reside. Indeed, a huge H-α bubble enclosing Arp 220 is indicative of up to $M_{\rm gas} \sim 50\,M_{\odot}\,{\rm yr}^{-1}$ of gas being ejected into the intergalactic medium (IGM).

The long-wavelength cut-outs of Arp 220 illustrate the effects from confusion (Condon, 1974), which results from the large fundamental size of the full-width-at-half-maximum (FWHM or θ) of the point-spread function (PSF or 'beam') given by the Airy limit:

$$\frac{\theta}{\rm rad} \approx 1.22 \left(\frac{\lambda/{\rm m}}{D/{\rm m}} \right) \quad \text{or} \quad \frac{\theta}{''} \approx \frac{\lambda/\mu{\rm m}}{4D/{\rm m}}. \tag{1.5}$$

Thus, the above equation suggests that a large FWHM of $\theta \sim 20$–$10''$ (or $\sim 130\,{\rm kpc}$

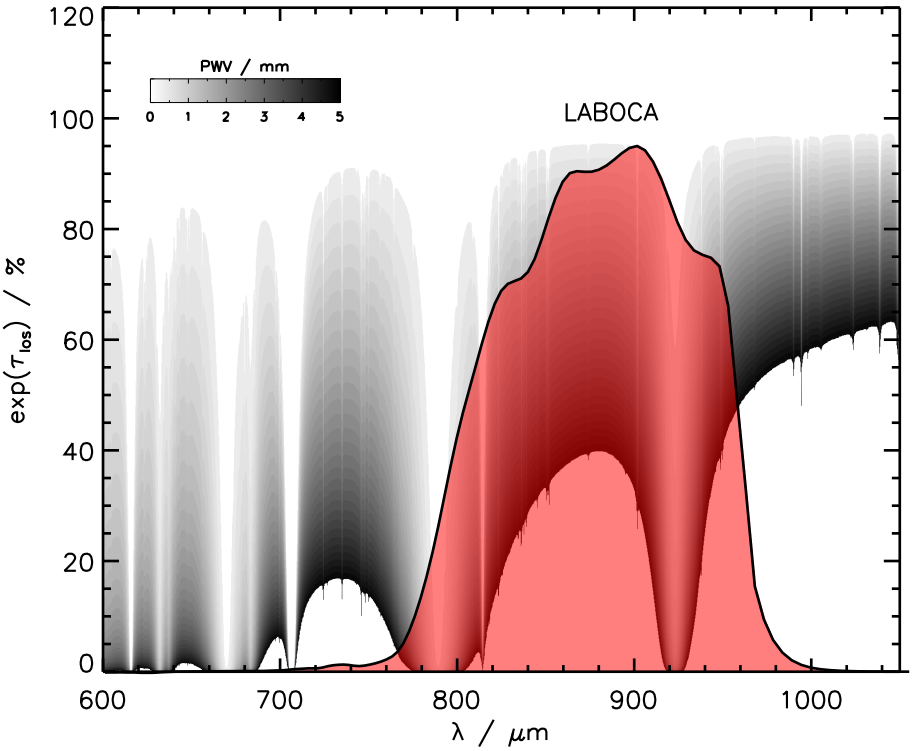

Figure 1.2: The atmospheric spectrum as a function of PWV at the APEX telescope site. This figure illustrates the three broad, naturally occurring atmospheric windows between 700–1,100 μm, with the LABOCA passband straddling the central window. The PWV at APEX is typically PWV = 1 mm (dark blue), which corresponds to an $\sim$ 80% reduction in an astronomical signal.

at $z \sim 2$–3) can be expected for 850-μm observations using ground-based, single-dish telescopes with typical sizes of $D \sim 10$–20 m. Such a broad FWHM results in the detection of brighter, 'blob-like' sources lying above a sea of undetected, fainter galaxies. This increases the flux-density measurement of the brighter sources, an effect known as flux-boosting (Blain et al., 1998), which must be corrected for by extensive simulations involving telescope/instrument specifics and brightness thresholds.

Furthermore, ground-based, sub-mm observations are also affected by an almost opaque atmosphere that exponentially diminishes the intensity of a given source by $\exp(\tau_{\rm los})$, where $\tau_{\rm los}$ is the line-of-sight opacity of the atmosphere. The few semi-transparent, atmospheric windows that are available to sub-mm observations and the effects of this attenuation are shown in Figure 1.2. The amount of atmospheric attenuation as a function of wavelength has been evaluated using the atmospheric transmission model of Pardo et al. (2001) and shown as a function of precipitable water vapour[7] (PWV) at the Atacama Pathfinder EXperiment (APEX) telescope, which is situated on Llano Chajnantor in Chile at an altitude of 5,100 m. Typically two independent methods are used to determine the atmospheric opacity at APEX and they are subsequently combined in order to correct observations for its effect. The first uses PWV measurements made every minute by

[7]The amount of water vapour integrated from the top of the atmosphere down to the observing site, which is typically measured in millimetres.

the APEX radiometer, whilst the second uses elevation-dependent measurements of the atmosphere.

1.3 Dusty Star-Forming Galaxies

Although the FIR luminosity generated by the local ULIRG population is substantial, it still only accounts for $\sim 1/3$ of that measured in the optical. Hence, this suggests that both the luminosity and density of the *IRAS* 60-μm luminosity function (LF) derived for the local ULIRG population must evolve with redshift in order to match the optical output as suggested by the COBE measurements (Blain & Longair, 1996).

The distant analogues to the local ULIRGs were finally discovered when Smail et al. (1997) targeted two rich galaxy cluster fields with the Submillimetre Common-User Bolometer Array (SCUBA — Holland et al., 1999) – a sophisticated instrument sensitive to 850-μm emission mounted on the $D = 15$-m James Clerk Maxwell Telescope (JCMT), which is situated on Mauna Kea in Hawaii at an altitude of 4,210 m. These so-called 'sub-millimetre galaxies' (SMGs — Blain et al., 2002) – an $\sim$ 850-μm-selected sub-sample of 'dusty star-forming galaxies' (DSFGs — Casey et al., 2014) – are many times more luminous ($\sim 10\times$) and numerous ($\sim (10^2$–$10^3)\times$) than the local ULIRG population. The increase in luminosity and density of the *IRAS* 60-μm LF was well described by an evolution of the form $(1+z)^3$ out to $z \sim 2.5$ and these likely (as unconfirmed at the time) high-redshift DSFGs successfully accounted for the majority of the CFIRB at 850 μm – a fact later confirmed by even deeper ($\sim 3\times$) lensed surveys (Knudsen et al., 2003, 2008).

This SCUBA Lens Survey was later extended and combined with high-resolution, space-based optical imaging in order to place valuable constraints on the redshifts and morphologies of these lensed DSFGs (Smail et al., 1998). A significant fraction were shown to lie below $z \leq 5$ – consistent with the time-scales associated with the LBG population lying at $2 < z < 4.5$, albeit possessing much higher ($\sim 5\times$) inferred SFRs (Madau et al., 1996). The majority of these DSFGs were classified as having 'disturbed and interacting' morphologies, which supports the concept that at higher redshift – an epoch when both the merger rates and abundances of gas-rich, rather than star-formation-efficient, galaxies are comparatively higher (Le Floc'h et al., 2009; Tacconi et al., 2010; Rodriguez-Gomez et al., 2015) – the star formation and/or AGN activity is also induced by merger events as seen locally (Engel et al., 2010).

Targeting galaxy clusters in order to exploit the benefits resulting from gravitational lensing (i.e. improved sensitivity) is not without its own problems though. Firstly, the crowded nature of galaxy cluster fields leads to numerous potential optical counterparts for a given DSFG, which, if incorrectly matched, will likely bias the resulting redshift distribution to lower values. However, this problem exists even without targeting galaxy clusters due to the broad FWHM of the PSF for ground-based, sub-mm observations (see Equation 1.5) and the large on-sky density of optical galaxies. Secondly, lensing itself introduces biases that must be addressed; such as the larger fraction of sources with higher flux densities compared

to so-called 'blank-field' surveys (Scott et al., 2002) or the complex corrections necessary to measure the true flux density of a galaxy that has been magnified by some factor μ. Furthermore, the latter can be exacerbated by differential magnification that causes the gravitational lensing to be systematically greater within hotter, spatially offset regions of a background galaxy[8] (Blain, 1999; Serjeant, 2012). Although gravitational lensing – resulting solely from geometrical effects – increases the inferred luminosity of a background galaxy, differential lensing increases the inferred temperature of that background galaxy as well. This effect was used by Blain to explain the excess mid-IR emission in some lensed DSFGs, as the increase in their inferred temperature causes their observed SEDs to flatten at wavelengths shorter than their peak at $\sim (1+z)\times 100\,\mu$m. Thus, in a flux-limited survey, where the number density of galaxies decreases with increasing redshift, differential lensing could further decrease the number distant galaxies expected due to their inferred hotter temperatures that makes them appear less red and thus less distant.

Blank-Field surveys (targeted towards regions free of known galaxies or galaxy clusters) remove many of these problems[9] at the obvious expense of requiring longer integration times in order to reach comparable sensitivities.

Key Point 1.1
Barger et al. (1998), Hughes et al. (1998) and Eales et al. (1999) all targeted blank fields with SCUBA and, by modelling their sources based on the SED of Arp 220 (see Figure 1.1), arrived at the general consensus that DSFGs were highly luminous ($L_{\rm FIR} = 10^{12}$–$10^{14}\,L_{\odot}$), likely very distant ($1.5 \lesssim z \lesssim 3$ — Lilly et al., 1999) and forming stars at a tremendous rate ($\psi \gtrsim 1{,}000\,M_{\odot}\,{\rm yr}^{-1}$).

However, the exact epoch of the star formation and/or AGN activity occurring within these DSFGs was still largely unconstrained due to the inherent difficulties in determining the redshifts of these optically dark, dusty galaxies.

1.3.1 Redshift Distribution of DSFGs

Although spectroscopic redshifts existed for a small sample of (atypical) optically bright ($\sim 20\,{\rm mag_{AB}}$) DSFGs within the SCUBA Lens Survey (ranging from $0.2 \lesssim z_{\rm spec} \lesssim 3$ — Ivison et al., 1998; Barger et al., 1999; Smail et al., 2002), a general consensus on their redshift distribution had yet to be reached. This changed, however, when high-precision, 1.4-GHz radio ($\lambda \gtrsim 1{,}000\,\mu$m) imaging had been taken with the Very Large Array (VLA) for a larger sample of SCUBA-selected DSFGs (Smail et al., 2000; Ivison et al., 2002). As the on-sky density of radio-bright ($S_{1.4} \gtrsim 50\,\mu$Jy) galaxies is much lower than that for optically bright galaxies (Ivison et al., 2007), it is rare to have more than one radio

[8]The effects of differential lensing are more pronounced in galaxy-galaxy (rather than cluster-galaxy-galaxy) lensing scenarios as specific regions exhibiting colour gradients in an extended background galaxy are more likely to be amplified by the former.

[9]A slight irony exists here in that the brightest DSFGs in blank-field surveys often tend to be gravitationally lensed by chance alignments (e.g. HDF850.1, which has a magnification of $\mu \approx 3$ — Zepf et al., 1997; Hughes et al., 1998; Dunlop et al., 2004).

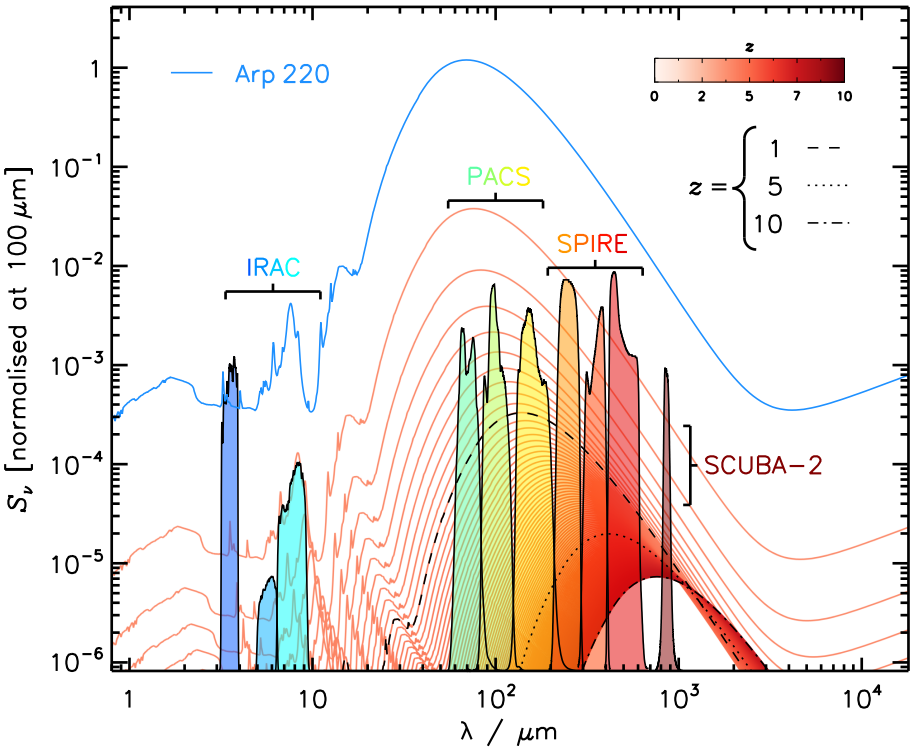

Figure 1.3: Observed flux density as a function of redshift using the SED for Arp 220. As the redshift increases, the location of the peak of the SED increases from $\lambda_{\rm rest} \sim 100\,\mu$m to $\lambda_{\rm obs} = (1+z)\lambda_{\rm rest}$. From $z = 1$–10 the reduction in the measured intensity from cosmological dimming at $850\,\mu$m is counteracted by the rise in the Rayleigh-Jeans side of the SED, which results in a fairly constant observed flux density for a constant luminosity, or the very negative K correction. At shorter (NIR) and longer (radio) wavelengths, however, the effects from cosmological dimming substantially decrease the observed flux density.

source within a single SCUBA PSF and thus eases the process of matching potential radio counterparts to a sample of DSFGs. Furthermore, the empirically discovered FIR/radio correlation[10] (FIRRC — de Jong et al., 1985; Helou et al., 1985) means that DSFGs over a broad range of luminosities ($L_{\rm FIR} = 10^9$–$10^{12}\,L_\odot$) are expected to emit strongly in the radio. *What the FIRRC* additionally provides to high-redshift DSFG samples is an ability to further constrain their redshifts and dust temperatures (through assumed spectral shapes), and to detect the presence of AGN (through characteristic, lobe-like radio morphologies — Carilli & Yun, 1999; Ivison et al., 2002, 2010a). Once a radio source has been matched to a given DSFG, it is then relatively straightforward to locate the optical counterpart to that radio source (with typical astrometric uncertainties of $\mathcal{R} \lesssim 1''$) and thus obtain an accurate spectroscopic redshift, albeit in rather slow (and expensive) method as demonstrated in the first survey based on a sub-mm/radio sample (Chapman et al., 2003, 2005).

Chapman et al. (2005) found a median redshift of $z_{\rm spec} = 2.2$ for $\sim 75\%$ of their sample using this technique, which subsequently facilitated the first molecular gas measurements of DSFGs (namely $M_{\rm gas} \sim 10^{11}\,M_\odot$ — Neri et al., 2003; Greve et al., 2005). However, care must be taken when interpreting these results as despite them being more reliable than those from previous estimates they were not without their own biases. For instance, contrary to the very negative K correction witnessed for ~ 850-μm observations, which allows galaxies at $z \sim 5$–10 to be detected almost as easily as those at $z \sim 1$ with the same luminosity (see Figure 1.3 — Blain & Longair, 1993), the cosmological dimming with redshift significantly attenuates the flux density at radio wavelengths. As a consequence, many high-redshift DSFGs are missed if selection is based solely on the requirement of a radio detection, which in-turn will bias the redshift distribution to lower values. Chapman et al. do however acknowledge and attempt to correct for this effect via dust-temperature variations through SED modelling, which shifts the peak of the redshift distribution closer to $z \sim 2.5$.

1.3.2 The 'Ultra-Red Galaxy' Sub-Sample

The advent of the *Herschel* Space Observatory (see Figure 1.4 — Pilbratt et al., 2010) allowed astronomers to simultaneously image large regions of the Universe at 250-, 350- and 500-μm wavelengths with its Spectral and Photometric Imaging Receiver (SPIRE — Griffin et al., 2010) instrument. These FIR observations provided a quick and relatively inexpensive means with which to generate a large sample of distant and/or colder DSFGs based on the location of the dust peak within their observed SEDs – since $\lambda_{\rm obs} = (1+z)\lambda_{\rm rest} \sim (1+z) \times 100\,\mu$m, see Figures 1.1 and 1.3. Thus, DSFGs with SPIRE flux densities that increase with increasing central wavelength of each SPIRE passband

[10]Despite not having a complete theoretical explanation for its existence, the FIRRC is believed to originate from the young, massive stars within a galaxy. The FIR emission is believed to arise from the reprocessing of starlight by dust (as discussed previously), whilst the radio emission is believed to arise from the resulting SNe remnants once these massive ($M_{\rm stars} \gtrsim 8\,M_\odot$) stars have exhausted all of their fuel (after $\sim 10\,$Myr).

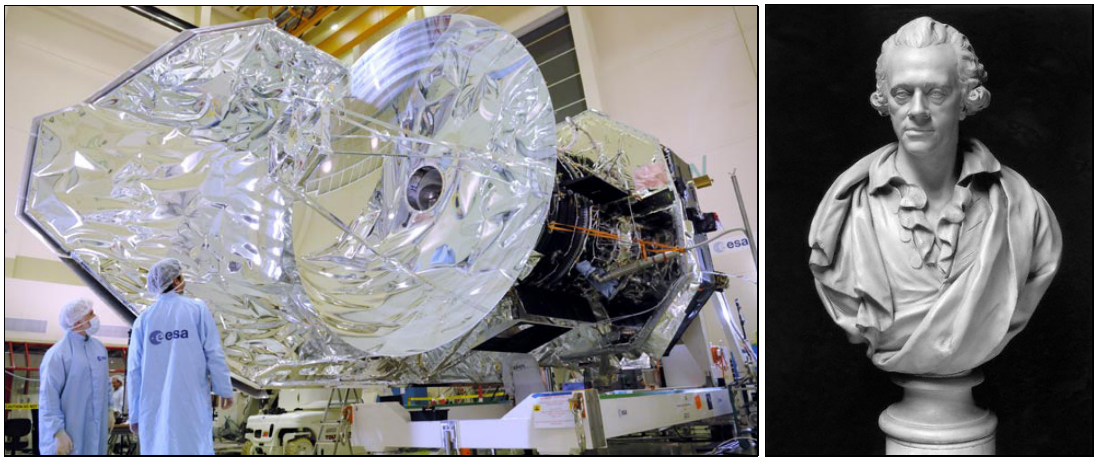

Figure 1.4: Left: the *Herschel* Space Observatory on the 13th of May 2009 taken on the day before its launch. The $D = 3.5$-m diameter of the primary mirror of the Cassegrain reflector results in broad Airy limits that range from $\theta \approx 1.22\lambda/D \approx 5$–$35''$ across the PACS ($\lambda = 100\,\mu$m and $160\,\mu$m) and SPIRE ($\lambda = 250\,\mu$m, $350\,\mu$m and $\lambda = 500\,\mu$m) instruments (see Equation 1.5). **Right:** bust of Sir Frederick William Herschel who discovered 'calorific rays' (or the IR spectrum) in 1800. **Credit**. *Left:* ESA/NASA – SOHO/LASCO. *Right:* ©National Portrait Gallery, London.

(i.e. $S_{250} < S_{350} < S_{500}$, or so-called '500-$\mu$m risers') must therefore lie at $z \gtrsim 3$–4 and/or be colder as their FIR photometry samples the Wein side ($\lambda_{\rm rest} \lesssim 100\,\mu$m) of their thermal dust emission. Such an accurate and reliable tool for selecting distant DSFGs is crucial in order to better characterise the most luminous, star-bursting galaxies in the $z \gtrsim 3$–4 Universe, which collectively place valuable constraints on current galaxy formation models (Tacconi et al., 2010).

For instance, there is a growing consensus that DSFGs are the likely progenitors of present-day massive ($M_{\rm stars} \gtrsim 10^{11}\,M_{\odot}$) ETGs due to their ability to form large numbers of stars over relatively short time-scales (Toft et al., 2014; Simpson et al., 2014, 2015; Ikarashi et al., 2015). Furthermore, distant quiescent ETGs uncovered in NIR surveys are found to be extremely compact (~ 1–$2\,$kpc, compared to $\sim 5\,$kpc for ETGs at $z \sim 0$) and composed of an older stellar population (Newman et al., 2012; Straatman et al., 2014). The latter, which is consistent with the concept of 'cosmic downsizing' (Cowie et al., 1996; and see Figure 9 in Thomas et al., 2010), suggests that the most massive ETGs must have formed the bulk of their stars early ($z \gtrsim 3$) during a short-lived[11], intense burst of star formation – potentially enshrouded in dust (Nelan et al., 2005; Thomas et al., 2005; Snyder et al., 2012). Thus, the evolutionary picture of ETGs from $z \sim 2$ until the present, appears to be that of a relatively passive event, i.e. slowly gaining in size (and thus losing stellar density) through many so-called 'dry mergers', which trigger little-to-no new star formation (van Dokkum, 2005; van Dokkum et al., 2008).

[11] As the first galaxies are thought to have formed around $z \sim 8$–9, or 600 Myr after the Big Bang, there is obviously a limited amount of time available for star formation to have ceased by $z \sim 3$, or when the Universe was only 2-Gyr old.

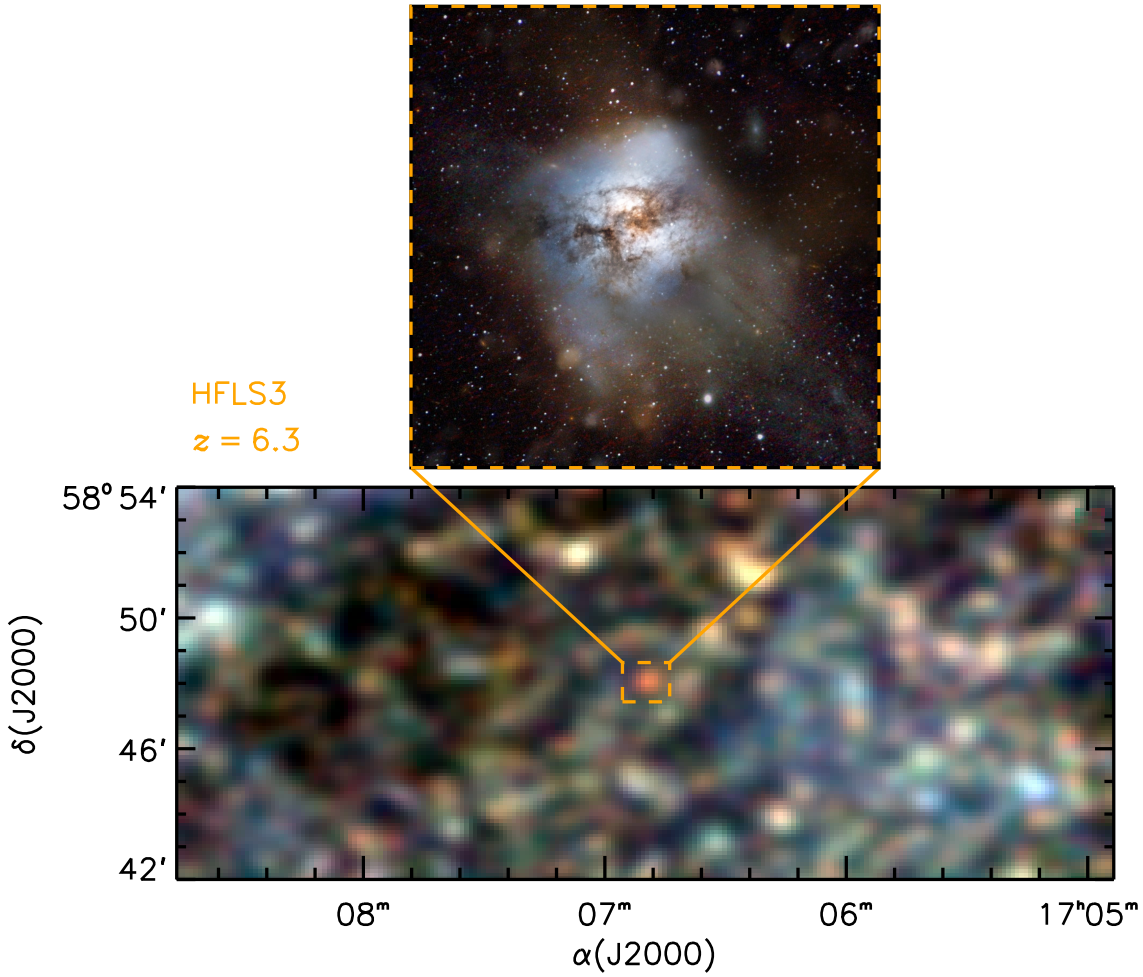

Figure 1.5: Main: SPIRE false-colour cut-out of one of the most distant ultra-red galaxies known, HFLS3. *Inset:* artist's impression of HFLS3. **Credit. Inset:** ESA – C. Carreau.

Key Point 1.2

Although the co-moving space density of DSFGs is broadly consistent with that of present-day ETGs (albeit being heavily dependent on strong assumptions about the largely unconstrained duration of this intense star-bursting phase) the co-moving space density of high-redshift DSFGs has yet to be fully constrained. Due to their rarity, however, large cosmological areas (or volumes) need to be imaged in order to generate robust samples of these so-called 'ultra-red galaxies'.

The largest ($\approx$ 600 deg^2) imaging survey undertaken with *Herschel*, *H*-ATLAS (*Herschel*-Astrophysical Terahertz Large Area Survey — Eales et al., 2010), facilitated the first discovery of ultra-red galaxies; a lensed, dusty star-bursting system at $z = 4.2$ known as HATLAS J142413.9+022304 (or G15.141 — Cox et al., 2011). This technique was further exploited to discover HATLAS 090045.4+004125 (or G09−83808 — Ivison et al., 2016; Zavala et al., 2018; Fudamoto et al., 2017) at $z = 6.0$ and 1HERMES S350 J170647.8+584623 (or HFLS3, see Figure 1.5 — Riechers et al., 2013; Dowell et al., 2014)

at $z = 6.3$. Thus, although conventional wisdom places DSFGs at $z \sim 2.5$, those with ultra-red SPIRE flux-density ratios appear to be at very high redshift.

Finally, it is worth mentioning that lensed DSFGs at similarly high redshifts have also been found by surveys conducted at $\lambda_{\rm obs} > 1{,}000\,\mu$m with the South Pole Telescope (SPT), which have relied on flux-density ratios at even longer wavelengths in order to generate a sample of distant, dusty sources (Vieira et al., 2010; Weiß et al., 2013; Strandet et al., 2016), such as SPT-S J0311320−5823.4 (or SPT0311−58) at $z = 6.9$ (the most distant DSFG discovered to date — Strandet et al., 2017). Due to the well-known correlation between the FIR wavelength at which a survey is conducted at and the resulting median redshift of DSFGs detected within it, these SPT-selected sources are expected to have a broader redshift distribution than that measured for *Herschel*-selected sources (Symeonidis et al., 2011; Béthermin et al., 2012, 2015). The reasons for this correlation are twofold. Firstly, the negative K correction results in the detection limit (in bolometric luminosity) remaining fairly constant at $\sim 1{,}000\,\mu$m, whilst rising steeply at $\sim 250\,\mu$m from $z = 1$–4. Secondly, the redshift evolution in the LF means that there are many more brighter galaxies and fewer fainter galaxies at $z = 4$ than there are at $z = 1$. Taken together, there are more galaxies detected at $z = 4$ at $1{,}000\,\mu$m than there are at $z = 1$, and vice versa at $\sim 250\,\mu$m – resulting in this correlation.

1.4 The Assembly of Large Structure

Galaxy clusters whose cores are rich with ETGs (see Figure 1.6), mark the densest regions in the distribution of dark matter (DM) within the Universe[12]. These regions have grown hierarchically since the decoupling of photons and matter, with initial peak positions supposedly etched into the Universe at some arbitrarily early epoch (Peebles & Yu, 1970; Spergel et al., 2003). In the local Universe, galaxy clusters harbour the majority of ETGs, which in turn harbour over half of the present-day stellar mass. Thus studying their cosmic evolution can place valuable constraints on models of galaxy formation (Springel et al., 2005; Robertson et al., 2007; Overzier et al., 2009a).

ETGs obey a tight scaling relation between their colour and magnitude, where magnitude equates roughly to $M_{\rm stars}$. This is known as the 'red sequence', in which more massive galaxies are typically redder with older stellar populations and less ongoing star formation (Bower et al., 1998; Baldry et al., 2004). Furthermore, ETGs in local galaxy clusters appear redder (and thus more massive, since they follow the scaling relation) as their distance to the cluster centre decreases (Bernardi et al., 2006).

As discussed previously, ETGs have commonly been viewed as transformed LTGs, which have had their star formation quenched via some mechanism, leaving behind an ETG on the red sequence (Dressler et al., 1997; Gerke et al., 2007). In local galaxy clusters this quenching can be brought about rapidly via ram pressure stripping (Gunn & Gott,

[12]Typically, individual galaxies, groups of galaxies and galaxy clusters have DM halo masses of $M_{\rm halo} = 10^{10}$–$10^{11}\,M_\odot\,h^{-1}$, $M_{\rm halo} = 10^{13}$–$10^{14}\,M_\odot\,h^{-1}$ and $M_{\rm halo} \gtrsim 10^{14}\,M_\odot\,h^{-1}$, respectively (Behroozi et al., 2013).

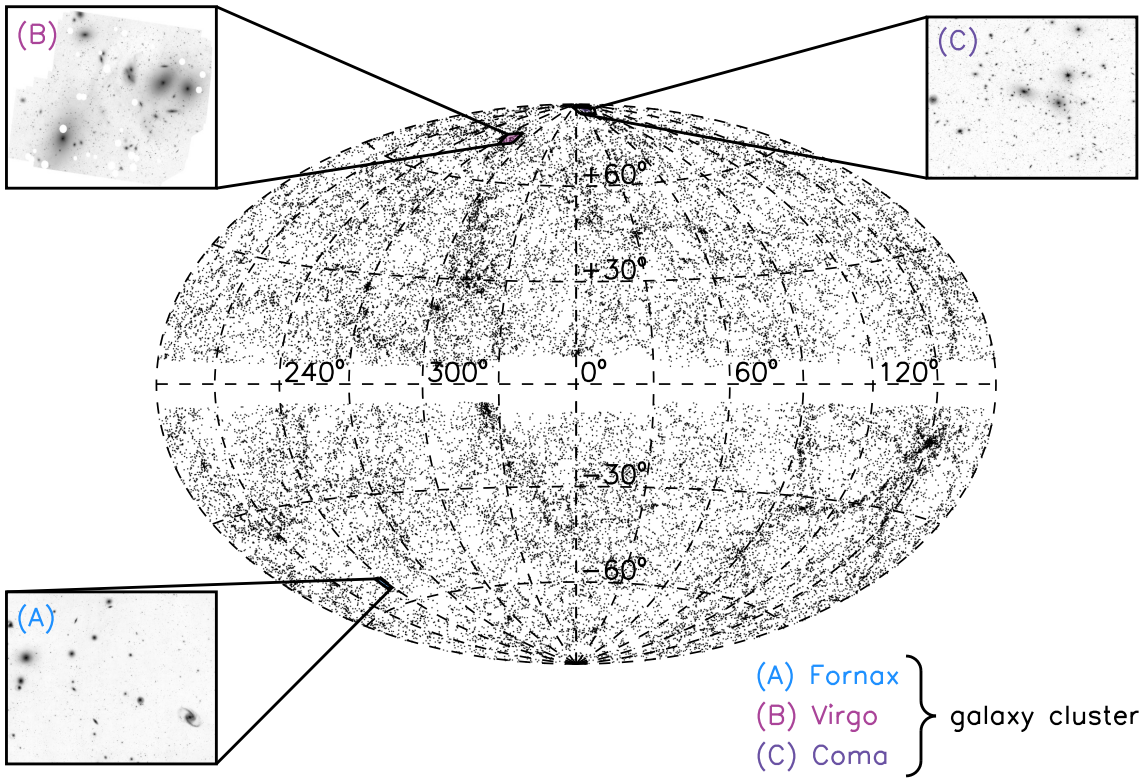

Figure 1.6: Main: Aitoff projection of galaxies within the Two Micron All Sky Survey (Skrutskie et al., 2006) Redshift Survey (Huchra et al., 2012) and the locations of three galaxy clusters. *Inset A*: cut-out of the Fornax (or furnace) galaxy cluster, which is located ~ 18 Mpc away in the southern hemisphere. This is a small galaxy cluster with a halo mass of $M_{\rm halo} \sim (1.5\text{–}3) \times 10^{14}\,M_{\odot}$. *Inset B*: cut-out of the Virgo galaxy cluster, which is located ~ 17 Mpc away in the northern hemisphere. This is a medium-sized galaxy cluster with a halo mass of $M_{\rm halo} \sim (3\text{–}10) \times 10^{14}\,M_{\odot}$. *Inset C*: cut-out of the Coma galaxy cluster, which is located ~ 100 Mpc away also in the northern hemisphere. This is the largest type of galaxy cluster considered in this thesis, with a halo mass of $M_{\rm halo} > 10^{15}\,M_{\odot}$. In the 1930s, Swiss astronomer F. Zwicky derived a mass of $\sim 5 \times 10^{13}\,M_{\odot}$ for this galaxy cluster – less than 2% of its total mass derived from other methods. This measurement was one of the early proofs to the existence of 'missing mass'. **Note**. The large intensities at $\sim (300°, +30°)$, $\sim (330°, -10°)$ and $\sim (150°, -15°)$ represent the Shapley Concentration, Great Attractor and the Perseus-Pisces Super-Cluster, respectively. Each of these are vast collections of galaxy clusters that extend over many tens of degrees across the sky and thus form the largest known structures within the Universe. The white band through the centre indicates the so-called 'Zone of Avoidance'; the area of sky obscured by the Milky Way, except for at the longest wavelengths. **Credit**. *Inset A*: ESO / J. Emerson / VISTA. *Inset B*: Chris Mihos (Case Western Reserve University) / ESO. *Inset C*: NASA/JPL-Caltech.

1972) or by so-called 'starvation' and/or 'strangulation' processes (Larson et al., 1980; Balogh et al., 2000; Elbaz et al., 2007; Tanaka et al., 2013). This is occurs because galaxy clusters reside in deep gravitational potentials, which heat the ICM and in-turn strip the cold gas from in-falling LTGs. This subsequently starves/strangles the LTGs of cold gas, which is necessary for further star formation.

At higher redshifts, however, the progenitors of galaxy clusters have yet to fully virialise and as such the most massive ETGs in their cores are likely the remnants of two (or more) distant, gas-rich, colliding LTGs. These high-redshift, unvirialized systems are known as 'proto-clusters' and are characterised by less-pronounced over-densities of (physically associated, but not gravitationally bound) galaxies that can extend over 10 Mpc (Chiang et al., 2013, 2017; Casey, 2016; Overzier, 2016). As any feasible theory describing galaxy formation, or any coherent cosmological model of the Universe, must satisfactorily explain the evolution of galaxy clusters from this early stage, the study of proto-clusters, for which we currently do not have a complete sample (see Figure 1.7), is crucial.

Systems exhibiting excesses, or over-densities, of DSFGs have already been discovered in the $z > 3$ Universe. However, these discoveries have typically relied on either high-redshift radio galaxies (HzRGs — Ivison et al., 2000; Stevens et al., 2003, 2004; Rigby et al., 2014), *pairs* of quasi-stellar objects (Uchiyama et al., 2017) or even strong over-densities of Lyman-α emitters as signposts (Capak et al., 2011; Tamura et al., 2009). Furthermore, predictions by Negrello et al. (2005) suggested that bright-intensity peaks within low-resolution data taken with the Planck High Frequency Instrument, could represent clumps of DSFGs. Indeed, over-densities of DSFGs at $z \sim 3$ have been found using this technique (Clements et al., 2016). However, the number of spectroscopically confirmed proto-clusters is small (~ 20) and the number of those that are rich in DSFGs is even smaller, despite the apparent effectiveness of over-densities of DSFGs in the distant Universe at signposting these systems. Thus, even though not all proto-clusters contain large numbers of DSFGs, the rarity of this dusty population makes them ideal signposts for candidate proto-clusters as five or more (compared to hundreds of normal galaxies) in close proximity is very unlikely (Casey, 2016), although this rarity also increases the Poisson noise resulting in possible false detections (Miller et al., 2015).

A few ultra-red galaxies discovered at $z \sim 5$ support the concept that they signpost candidate proto-clusters in the early Universe (Miller et al., 2016; Oteo et al., 2017a) – contrary to the findings of simulations that suggest DSFGs are poor tracers of large structure below $z \lesssim 2.5$ (Miller et al., 2015). At odds with this concept, however, is the ultra-red galaxy, HFLS3 (see Figure 1.5), as confusion-limited observations of its environments showed little evidence that it signposted an over-density of DSFGs (Robson et al., 2014). However, in light of new and improved comparison data, it appears that HFLS3 perhaps signposts a region that is over-dense by a factor of at least $\sim 2\times$ compared to that expected within the field.

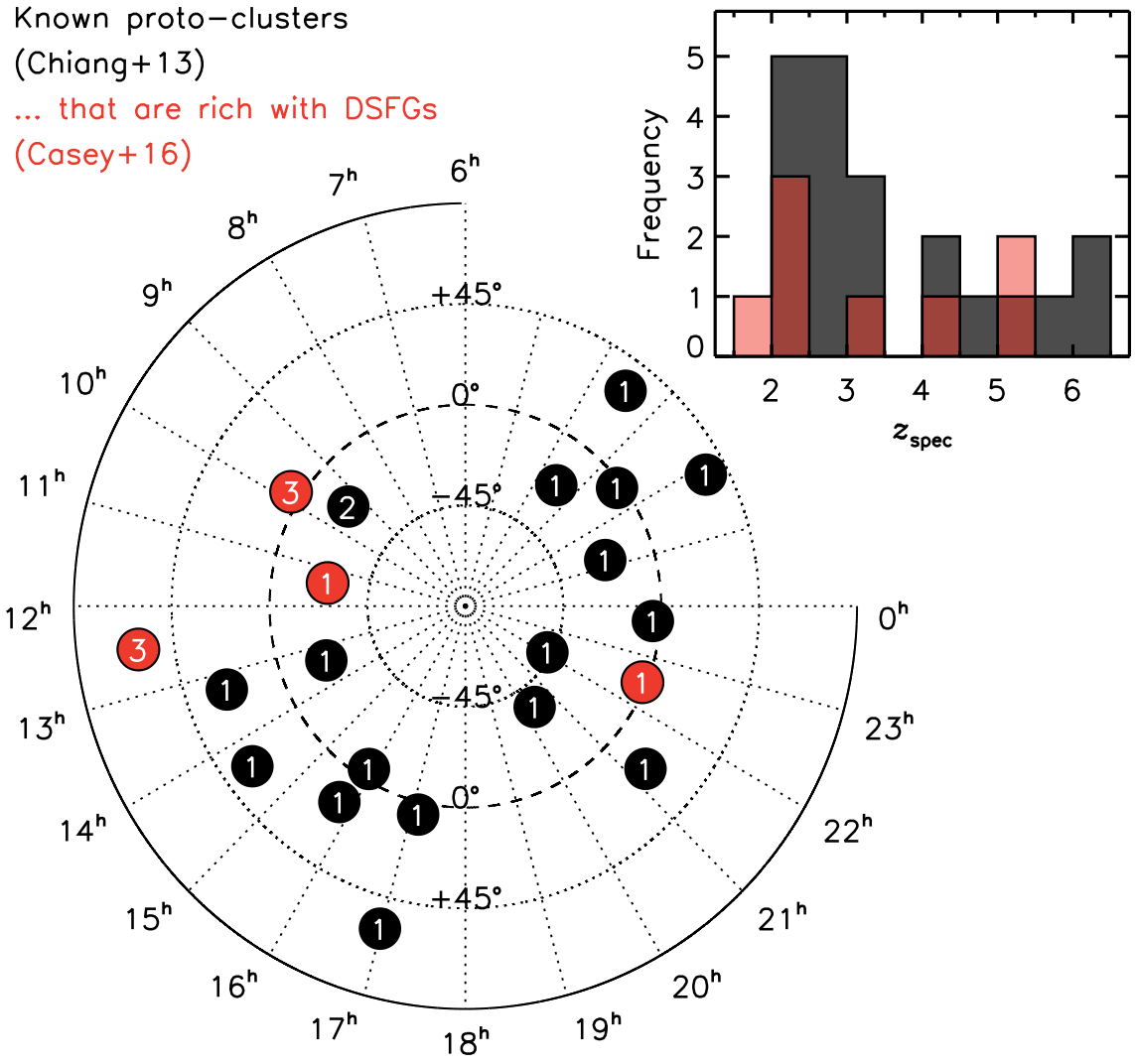

Figure 1.7: Main: spatial distribution of spectroscopically confirmed proto-clusters (black — Chiang et al., 2013) and those that are rich in DSFGs (red — Casey, 2016). The number inside of the circle represents the number of proto-clusters at that location. **Inset:** spectroscopic redshift distribution for both samples. Clearly the current sample size of high-redshift ($z \gtrsim 3$–4) proto-clusters that are rich in DSFGs is very low.

Key Point 1.3

Thus, in order to provide clarity on this, a representative sample of ultra-red galaxies needs to be generated and subsequently imaged. Furthermore, follow-up optical imaging/spectroscopy of their environments are needed in order to place strong constraints on their $M_{\rm stars}$ and DM components. A joint approach – combining models (Springel et al., 2005) and observations – is necessary to fully predict the eventual fate of these proto-clusters at $z \sim 0$ (Casey, 2016; Overzier, 2016).

1.5 Thesis Overview

In the following chapter, I make use of SPIRE data from the *H*-ATLAS imaging survey in order to generate a robust sample of ultra-red galaxies based on their FIR flux-density ratios. To ensure that this sample is comprised of intrinsically luminous and very distant DSFGs – and thus contains the most massive DSFGs in the early Universe – only ultra-red galaxies that have SPIRE 500-μm flux densities below $S_{500} < 100\,\mathrm{mJy}$ are considered. DSFGs detected above this flux-density limit are expected to be gravitationally lensed and/or blends of multiple less luminous DSFGs (Negrello et al., 2010, 2017; Conley et al., 2011). Using ground-based, $\sim$ 850-μm imaging obtained for this sample, I aim to place constraints on their redshift distribution, which in-turn I use to derive their $z > 4$, co-moving space density and thus predict their potential evolutionary path.

In Chapter 3, I examine the 870-μm environments around a representative sub-sample of ultra-red galaxies in order to see if they exhibit evidence of clustering consistent with their eventual membership of massive galaxy clusters at $z \sim 0$. In order to achieve this objective, I search these 870-μm images for less luminous and/or colder DSFGs within the $\sim$ 2-Mpc vicinity of their respective signpost ultra-red galaxies and compare them to those expected from blank-field surveys. Using complementary *Herschel* imaging, I estimate their photometric redshifts in order to place plausible constraints on their eventual, $z \sim 0$ properties.

I go one step further in Chapter 4 by examining the multi-wavelength environments around ultra-red galaxies detected within deep, blank-field surveys at 850 μm in order to test and improve upon the work presented in Chapter 3. As these blank-field surveys contain deep, complimentary imaging in the optical and NIR, I examine the $z \sim 3$ LBG population around these ultra-red galaxies in order to test for the presence (or emergence) of the red sequence, which would be consistent with the idea that ultra-red galaxies signpost candidate proto-clusters at high redshift. Furthermore, LBGs discovered within the vicinity of these ultra-red galaxies will place additional constraints on the $z \sim 0$ properties of these candidate proto-clusters.

Finally, I provide a brief summary of the work within this thesis in Chapter 5 and describe a handful of directions that future work could take.

Throughout this thesis, I adopt a 'concordance cosmology' with $H_0 = 71\,\mathrm{km\,s^{-1}\,Mpc^{-1}}$, $\Omega_M = 0.27$, $\Omega_k = 0$ and $\Omega_\Lambda = 0.73$ (Hinshaw et al., 2009), in which $1'$ corresponds to a (co-moving) distance of 2 Mpc at $z = 3$, the typical redshift of ultra-red galaxies. All magnitudes presented here are in the AB magnitude system (m_{AB} — Oke & Gunn, 1983), where conversion onto the Jansky scale is given by:

$$\frac{S_\nu}{\mathrm{Jy}} = 3{,}631 \times 10^{(-2/5)m_{\mathrm{AB}}}.$$

The $z > 4$ Space Density of Ultra-Red Galaxies

2

'To the scientist there is the joy in pursuing truth which nearly counteracts the depressing revelations of truth' – excerpt from 'The Call of Cthulhu and Other Weird Stories'

H. P. Lovecraft ~~(2013–2018)~~ (1890–1937)

Declaration: the work presented in this chapter was previously published in Ivison et al. (2016) as 'The Space Density of Luminous Dusty Star-Forming Galaxies at $z > 4$: SCUBA-2 and LABOCA Imaging of Ultra-Red Galaxies from Herschel-ATLAS' by R. J. Ivison (my supervisor), A. J. R. Lewis (myself), A. Weiss, V. Arumugam, J. M. Simpson, W. S. Holland, S. Maddox, L. Dunne, E. Valiante, P. van der Werf, A. Omont, H. Dannerbauer, Ian Smail, F. Bertoldi, M. Bremer, R. S. Bussmann, Z.-Y. Cai, D. L. Clements, A. Cooray, G. De Zotti, S. A. Eales, C. Fuller, J. Gonzalez-Nuevo, E. Ibar, M. Negrello, I. Oteo, I. Pérez-Fournon, D. Riechers, J. A. Stevens, A. M. Swinbank and J. Wardlow. This study was conceived by all of the authors. I carried out the analysis, discussion and conclusion.

2.1 Introduction

As discussed in Chapter 1, FIR observations using the SPIRE instrument on-board the *Herschel* Space Observatory have provided complementary data to vast numbers of DSFGs, first discovered by Smail et al. (1997), Barger et al. (1998) and Hughes et al. (1998). These highly luminous galaxies in the FIR are likely undergoing an intense burst of star formation plausibly triggered by merger-induced compressions (Engel et al., 2010). Able to generate a $M_{\rm stars} \gtrsim 10^{11}$-$M_{\odot}$ galaxy within ~ 100 Myr, DSFGs provide an extreme sample with which to study the formation and evolution of massive galaxies within the Universe. However, until recently only a handful of DSFGs in the distant ($z > 4$) Universe were known. A significant fraction of these DSFGs were gravitationally lensed, too, which introduces additional uncertainties such as differential magnification (Blain, 1999; Serjeant, 2012).

Thus, in this chapter, I will report on a collaborative effort to substantially increase the

number of so-called 'ultra-red galaxies' – a distant sub-sample of DSFGs selected via their SPIRE flux-density ratios – within the *H*-ATLAS imaging survey. Throughout this search for colder and/or more distant ($z \gtrsim 3$–4) ultra-red galaxies, I will focus on DSFGs with $S_{500} < 100\,\mathrm{mJy}$, a flux-density limit that mitigates the effects from severe gravitational lensing (Negrello et al., 2010; Conley et al., 2011). Using follow-up, 850-/870-μm ground-based imaging of a sample of ultra-red galaxies, I will hopefully be able to meaningfully constrain their $z > 4$ space density. I will attempt to reconcile this space density with other galaxy populations, in particular, focussing on less distant ($z \sim 2$–3), quiescent galaxies uncovered in the NIR (Straatman et al., 2014).

The format of this chapter is as follows. In the next section I will describe the data acquisition and reduction methods. I subsequently outline the ultra-red-galaxy selection criteria before presenting, analysing, interpreting and discussing the findings in Section 2.4. Finally, I will briefly summarise the conclusions in Section 2.5.

2.2 Sample Selection

The team selected ultra-red galaxies from the SPIRE images created for the *H*-ATLAS Data Release 1 (DR1 — Valiante et al., 2016; Bourne et al., 2016), which cover $\approx 600\,\mathrm{deg}^2$ split across the three equatorial Galaxy And Mass Assembly (GAMA 09, GAMA 12 and GAMA 15, $\approx 54\,\mathrm{deg}^2$), the North Galactic Pole (NGP, $\approx 170\,\mathrm{deg}^2$) and, finally, the South Galactic Pole (SGP, $\approx 285\,\mathrm{deg}^2$) fields. The acquisition and reduction of these data are described fully in Valiante et al. (2016). The raw 250-, 350- and 500-μm SPIRE images used here have 6, 8 and 12″ pixels, point spread functions (PSFs) with azimuthally-averaged full-width-at-half-maxima (FWHM) of $\theta_{\mathrm{beam}} = 17.8$, 24.0 and 35.2″, mean instrumental r.m.s. noise levels of $\sigma_{\mathrm{inst}} = 9.4$-, 9.2- and 10.6-mJy and mean confusion noise levels of $\sigma_{\mathrm{conf}} = 7.0$-, 7.5- and 7.2-mJy, respectively.

2.2.1 Source Extraction

Sources in the *H*-ATLAS images were identified and extracted using a modified version of the Multi-band Algorithm for source eXtraction (MADX — Maddox et al., in preparation, but see Maddox et al., 2010, 2018 for a brief overview). This algorithm subtracts a smooth background from the raw SPIRE images – estimated from the peak of the histogram of pixel values in 2–5′ sub-images – before applying a wavelength-dependent 'matched filter'[1]. The subtraction of the background removes the highly variable foreground caused by dust in our own galaxy (the so-called galactic 'cirrus'). Furthermore, clustered sources, which are undetected at the *Herschel* sensitivities probed here, as well as low-frequency noise

[1]Matched, rather than PSF, filtering can improve the signal-to-noise ratio of point sources in the presence of instrumental and confusion noise by up to 15–20%. For signal (S) and total noise ($N = 1/\sqrt{W}$) images, the corresponding matched-filtered signal (F) and matched-filtered noise (ΔF) images are defined as $F = ((SW) * P)/(W * P^2)$ and $\Delta F = 1/\sqrt{W * P^2}$, respectively, where '$*P$' represents a convolution with a kernel P (Serjeant et al., 2003; Chapin et al., 2011).

in the detectors not completely removed during the image-making process, each provide additional variations that the smooth background subtraction should correct.

The resulting matched-filtered images have a highly non-Gaussian positive tail due to the presence of astronomical sources, which are subsequently searched for as follows.

- First-Pass, flux-density estimates are generated for each SPIRE image at the pixel positions of > 2.2-σ_{250} peaks in the 250-μm images.

- The SPIRE flux densities and positions of these sources are then refined using a bi-cubic interpolation algorithm. These sources are ordered by decreasing SNR, catalogued with their 250-μm astrometric positions and then labelled as BANDFLAG = 1.

- Residual images are then generated by subtracting scaled PSFs of each source (sorted by its brightness) at its given pixel position in each passband[2].

- The non-Gaussian positive tail in the 250-μm image is now heavily truncated in its residual image due to the (nearly) complete removal of astronomical sources. However, the residual 350- and 500-μm images still have sources present and are thus still non-Gaussian in appearance. Therefore, the same sequence of events as above are performed but this time searching for > 2.4-σ_{350} and > 2.0-σ_{500} peaks in the 350- and 500-μm images, respectively. Sources then detected in 350-μm images were labelled as BANDFLAG = 2 and those detected in the in 500-μm images were labelled as BANDFLAG = 3. Interestingly, the final residual 350- and 500-μm images still show significant non-Gaussian positive tails. This is due to the incomplete removal of sources that are not well fit by the PSF, such as multiple sources being misconstrued as a single blend or heavily extended sources – both effects of the poor resolution in each image.

No flux-boosting corrections were made to the extracted flux densities of these sources as they depended heavily on the flux-density and colour distributions, neither of which is known well.

Finally, the need for modifying the original MADX algorithm, which results in somewhat arbitrary parameter values adopted throughout the extraction process described above, arose due to the SPIRE flux densities and errors changing in *H*-ATLAS catalogues over time. Unfortunately, many of the ultra-red galaxies already observed at $\sim 850\,\mu$m had improved SPIRE photometric measurements that were somewhat different to those in the early release catalogues. Only by re-running the MADX algorithm with different parameters were the ultra-red galaxies that were already imaged able to be recovered. Since all simulations were done with this modified version of the MADX algorithm, the completeness of this sample should be accurate. However, undeniably this is not an ideal situation,

[2]Note that in the modified version of the MADX algorithm used here, the PSF subtraction was only applied for sources with 250-μm peaks greater than $> 3.2\sigma_{250}$.

which will result in a residual bias as the $\sim$ 850-μm followed-up ultra-red galaxies do not have the most reliable SPIRE photometry.

Thus, the catalogue generated by MADX across the five fields contained 7×10^5 sources that are above $> 3.5\sigma$ in at least one of the SPIRE passbands.

2.2.2 Parent Sample of Ultra-Red Galaxy Candidates

The MADX catalogue was reduced to 7,961 sources by enforcing the following criteria:

$$\overbrace{\left(S_{500}/S_{250} \geq 1.5\right) \wedge \left(S_{500}/S_{350} \geq 0.85\right)}^{\text{ultra-red}} \wedge \overbrace{\left(S_{500} \geq 3.5\sigma_{500}\right)}^{\text{robust}} \wedge \overbrace{\left(S_{500} < 100\,\text{mJy}\right)}^{\text{unlensed}}, \quad (2.1)$$

where '$\wedge$' is the logical 'and' symbol.

Key Point 2.1
The above criteria select DSFGs that are ultra-red – ergo very distant, $z \gtrsim 3$–4 (see the colour against redshift tracks for the Cosmic Eyelash, SMM J2135−0102 — Swinbank et al., 2010; Ivison et al., 2010b, in Figure 2.2) – robust and unlensed, with the criterion responsible for each of these qualities covered by the brackets in Equation 2.1.

Applying these criteria resulted in the parent sample of ultra-red galaxies, which was comprised of 29, 42 and 29% BANDFLAG = 1, 2 and 3 sources, respectively.

Completeness of the Parent Sample

In order to assess the completeness of the parent sample of candidate ultra-red galaxies, 15,000 artificial sources were injected into the raw *H*-ATLAS images, the modified MADX algorithm was re-run and then the number of recovered galaxies meeting the ultra-red criteria in Equation 2.1 was measured. These artificial sources were represented as PSF-convolved point sources with mean S_{500}/S_{250} and S_{500}/S_{350} colours of 2.25 and 1.16, respectively[3] – typical of a 'generic' DSFG between $z = 0$–10.

The results of this analysis are shown in Figure 2.1 as function of input 500-μm flux density. At the flux-density (i.e. $\approx$ 30 mJy) and colour limits (see Equation 2.1) of the sample presented here, the completeness of the parent sample of candidate ultra-red galaxies is $\mathcal{C}_{\text{parent}} = 77 \pm 3\%$.

Although not shown in Figure 2.1, the completeness is also a function of BANDFLAG – such that by selecting only BANDFLAG = 1, or BANDFLAG = 1 and 2, sources results in $\mathcal{C}_{\text{parent}}$ decreasing significantly.

[3]These values are comparable to the median colours of the ultra-red galaxies that were chosen for ground-based observation, namely $S_{500}/S_{250} = 2.15$ and $S_{500}/S_{350} = 1.26$.

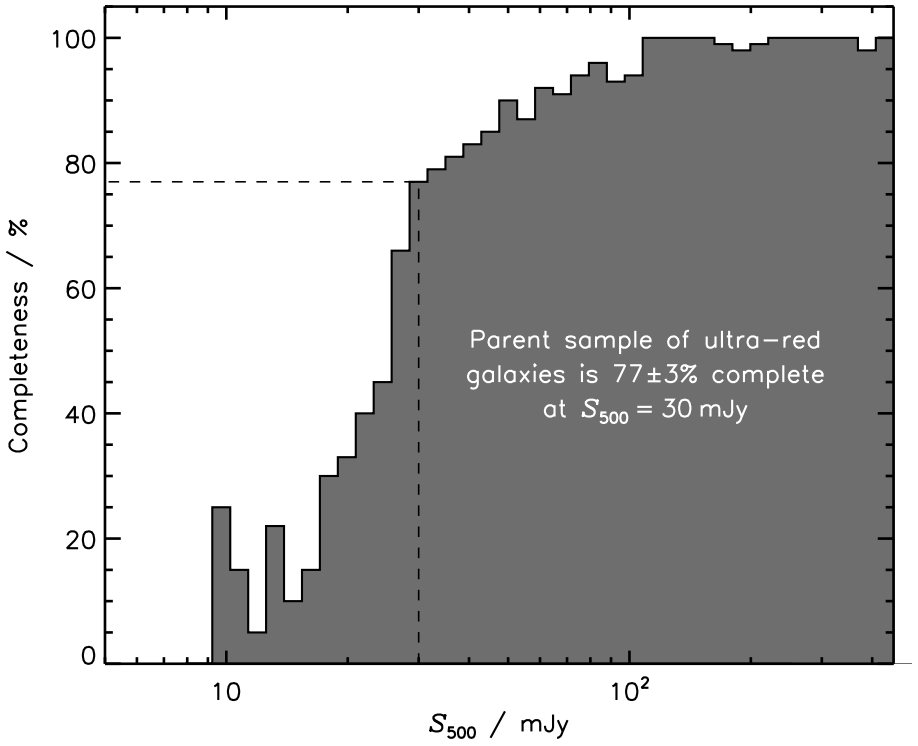

Figure 2.1: Completeness for the parent sample of candidate ultra-red galaxies as a function of 500-μm flux density. The completeness is measured for all recovered sources, i.e. BANDFLAG = 1, 2 and 3. At the 3.5-σ_{500} $\approx$ 30-mJy flux-density limit, the parent sample is $\approx$ 80% complete. **Note**. This sample of ultra-red galaxies never reaches $\approx$ 100% completeness due to the S_{500} < 100-mJy criteria imposed to mitigate the effects from gravitational lensing.

2.2.3 Eyeballed Sub-Sample of Ultra-Red Galaxies

A random sub-sample of 2,725 candidate ultra-red galaxies was 'eyeballed' in order to select reliable DSFGs for follow-up ground-based observations with the Submillimetre Common-User Bolometer Array-2[4] (SCUBA-2 — Holland et al., 2013) and/or the Large APEX BOlometer CAmera[5] (LABOCA — Siringo et al., 2009). This eyeballing stage was undertaken by a team of five and successfully reduced the sub-sample to 708, i.e. by $26 \pm 5\%$, where the uncertainty reflects the 'disagreements' between individual members of the eyeballing team.

Eyeballers were each given the same criteria in order to independently generate a truly reliable subset of ultra-red galaxies from the 2,725 candidates as follows:

1. To visually inspect each SPIRE $3' \times 3'$ cut-out for a given ultra-red galaxy and assess whether the MADX algorithm has failed to account for all of the flux density in either the 250- or 350-μm passband – making sure to be ultra-cautious in their assessment.

2. To judge whether either the 350- or 500-μm cut-outs show significant signs on confusion from faint neighbouring sources that may cast doubts on their ultra-red nature.

3. To check whether there are any image artefacts or bright local local galaxies that could potentially lead to MADX miscalculating the true flux density of the ultra-red galaxies.

4. To assess whether the background level is consistent with zero and relatively unstructured after the smooth background has been removed.

5. And finally, to look for signatures of instrumental glitches, such as striping and point sources that seem to be smaller than the PSF in each SPIRE cut-out.

Although whether or not a given ultra-red galaxy satisfies these criteria is highly subjective to a particular eyeballer, by averaging the verdicts across the team of five this individual subjectivity should be reduced. However, given the large ($\sim 75\%$) removal of candidate sources by the eyeballers, the ultra-cautious selection of ultra-red galaxies may not be fully representative of the general ultra-red galaxy population.

The most common reason (in 49% of cases) for eyeballers rejecting sources was due to their visual interpretation that the MADX algorithm was either missing or underestimating the 250-μm flux density, casting doubts on their ultra-red nature. Heavy confusion was responsible in 22% of cases as the flux densities and thus colours were deemed unreliable. Less common reasons (in $\lesssim 3\%$ of cases) included the proximity of candidate ultra-red

[4]The SCUBA-2 passband is centred at 850 μm with a half power width of 85 μm. The FWHM of the main beam is 13.0″ with around 25% of the total power originating from the broader (49″) secondary component.

[5]The LABOCA passband is centred at 870 μm with a half power width 150 μm – a wider/redder passband that SCUBA-2. Comprised of 295 hexagonally arranged composite bolometers (or channels), LABOCA has a FWHM resolution of 19.2″, well described by a single Gaussian (see Figure 2.5).

galaxies to very bright local galaxies or a morphology suggestive of Galactic cirrus and/or imaging artefacts.

From the reduced sub-sample of 708 candidate ultra-red galaxies, a random subset of 109 were selected for follow-up observations with LABOCA and/or SCUBA-2. The BANDFLAG = 1, 2 and 3 subsets contribute to 48 (44%), 53 (44%) and 8 (8%) of the ultra-red galaxies in this follow-up sample, respectively. This BANDFLAG distribution is somewhat different to the parent candidate ultra-red galaxy sample with the fraction of BANDFLAG = 1 sources increasing whilst the fraction of BANDFLAG = 3 sources decreases. This is likely due to the high level of confusion in the 500-μm images resulting in the eyeballers rejecting a higher proportion of BANDFLAG = 3 sources.

The SPIRE colours of these 109 ultra-red galaxies are shown in Figure 2.2. Finally, Figure 2.3 shows the location of these ultra-red galaxies in the five *H*-ATLAS fields.

Completeness of the Eyeballed Sub-Sample

In order to quantitatively determine the completeness associated with the eyeballing process described in the previous section, I generated a sample of 500 artificial, ultra-red sources with flux-density and colour distributions matching the parent sample. These fake sources were then mixed with 500 real candidate ultra-red galaxies to generate a sample of 1,000 fake/real sources/galaxies. Our team of eyeballers then classified these sources in an identical manner to that described in the previous section. The percentage of fake sources that were accepted by the eyeballers for follow-up observations then yielded the completeness, $\mathcal{C}_{\rm eyeball} = 69 \pm 8\%$.

2.2.4 Summary of Completeness

I now provide a short summary (see Table 2.1) of the considerable number of completeness corrections that have been discussed in the previous sections.

- The parent sample contains 7,961 candidate ultra-red galaxies with a completeness of $\boldsymbol{\mathcal{C}_{\rm parent} = 77 \pm 3\%}$.
- A sub-sample of 2,725 ($\boldsymbol{F_{\rm eyeball} = 34 \pm 1\%}$) of these candidate ultra-red galaxies were eyeballed in order to select robust galaxies for follow-up observations with SCUBA-2 and/or LABOCA. This eyeballing process was deemed to be $\boldsymbol{\mathcal{C}_{\rm eyeball} = 69 \pm 8\%}$ complete, i.e. eyeballers failed to select $\sim 30\%$ of the galaxies that were truly ultra-red for follow-up observations.
- From this eyeballed sub-sample, 708 ($\boldsymbol{F_{\rm suitable} = 26 \pm 1\%}$) of the candidate ultra-red galaxies were deemed suitable for follow-up observations, from which a random selection of 109 ($\boldsymbol{F_{\rm obs} = 15 \pm 1\%}$) were chosen.

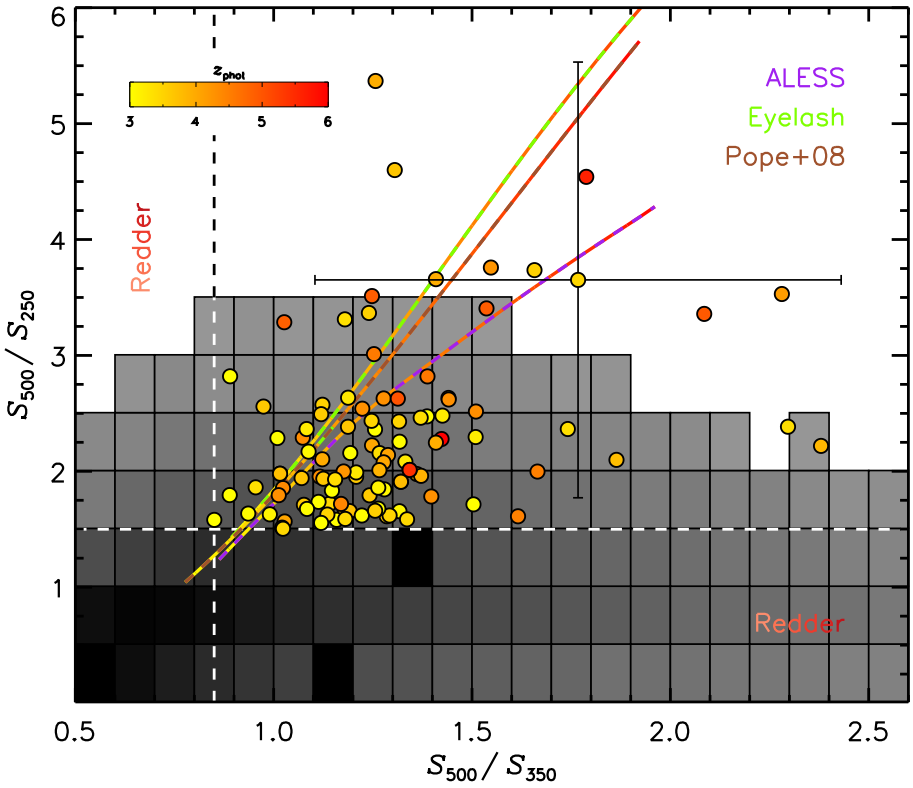

Figure 2.2: S_{350}/S_{500} versus S_{250}/S_{500} for the sample of ultra-red galaxies (circles), overlaid with the redshift tracks (dashed lines) for the ALESS, Cosmic Eyelash and Pope et al. (2008) template SEDs. Both the sample and the redshift tracks are colour-coded according to their photometric redshift (see Section 2.4.2) and a scale from $z = 3$–6 is provided in the lower-right corner. Dashed black lines indicate the $S_{500}/S_{250} \geq 1.5$ and $S_{500}/S_{350} \geq 0.85$ colour-cut boundaries from the ultra-red galaxy criteria (see Equation 2.1), i.e. ultra-red galaxies must lie in the top-right region of the plot. I show a two-dimensional histogram of all sources from the Phase 1 data release of *H*-ATLAS (Valiante et al., 2016) colour-coded such that darker colours represent larger numbers of sources. Clearly there are a large number of DSFGs in the bottom-left corner and thus there are many more blue DSFGs that can be scattered red-ward, than vice versa – a form of Eddington bias (Eddington, 1913). Without prior knowledge of the underlying ultra-red distribution, I am unable to meaningfully quantify this effect. However, the majority of these galaxies should be amongst the fraction shown to lie at $z_{\rm phot} < 4$ in Section 2.4.2 and thus additional corrections to the $z > 4$ space density in Section 2.4.3 are not necessary. Finally, a representative colour 1-σ error bar is shown.

Table 2.1: Candidate ultra-red galaxy selection

Sample	Number (N)	Fraction (F) %	Completeness ($\mathcal{C}$) %	Description
Entire	700,000	—	—	Entire sample of DSFGs detected with MADX
Parent	7,961	< 1	77 ± 3	Parent sample of candidate ultra-red galaxies
Eyeball	2,725	34 ± 1	69 ± 8	Sub-sample that was eyeballed
Suitable	708	—	—	Eyeballed sub-sample suitable for observing
Observed	109	15 ± 1	—	Final subset observed

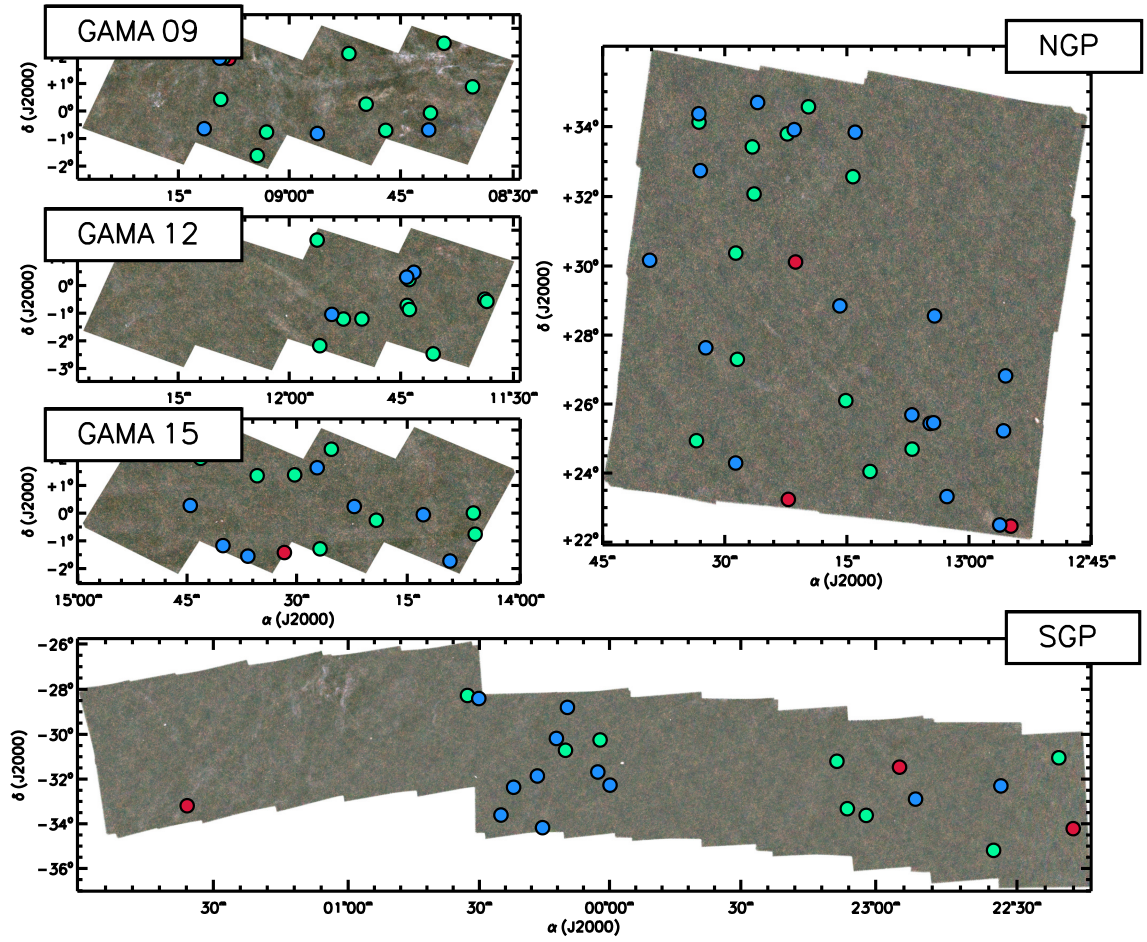

Figure 2.3: *Herschel*-SPIRE false-colour image of the five fields observed as part of the *H*-ATLAS imaging survey. Blue-, green- and red-coloured circles represent BANDFLAG = 1, 2 or 3 ultra-red galaxies observed, respectively.

Figure 2.4: Sunset at the 12-m APEX telescope at the Llano de Chajnantor Observatory taken on the 2nd of April 2016, during the P097.F Swedish observing run that I participated in. The dry skies and high altitude of this site make it one of the best locations in the world for sub-mm observations.

Key Point 2.2

The contributions outlined above are combined to generate an overall completeness value $\mathcal{C} = \mathcal{C}_{\rm parent} \times F_{\rm eyeball} \times \mathcal{C}_{\rm eyeball} \times F_{\rm obs} \approx 2 \pm 1\%$, which is used to scale the number of ultra-red galaxies detected above $z > 4$ during the space density calculation in Section 2.4.3.

2.3 Observations and Data Reduction

I now outline the ground-based observations and data reduction techniques of the 109 ultra-red galaxies using the LABOCA and SCUBA-2 instruments.

2.3.1 870-μm Continuum Imaging and Reduction with LABOCA

The ultra-red galaxies were observed with the LABOCA instrument on the APEX telescope (see Figure 2.4) in a compact-raster scanning mode, whereby the telescope scans in an Archimedean spiral for 35 s at four equally spaced raster positions in a $27'' \times 27''$ grid. Each scan was approximately ≈ 7 min long such that each raster position was visited three times. This led to a fully sampled image over the full 11-arcmin-diameter field of view of LABOCA. Around 2–4 hr was spent integrating on each ultra-red galaxy (see Table 2.2).

During the observations, typical PWV values between 0.4–1.3 mm – corresponding to a zenith atmospheric opacity of $\tau_{\rm los} = 0.2$–0.4 – were measured. Finally, the flux-density scale was determined to an r.m.s. accuracy of $\sigma_{\rm calib} \approx 7\%$ using observations of

primary/secondary calibrators, whilst the pointing – checked every hour using nearby quasars – was found to be stable to within $\sigma_{\rm point} \approx 3''$ (r.m.s.).

The data were reduced by myself using the Python-based BOlometer data Analysis software package (BOA v4.1 — Schuller, 2012), following the prescription outlined in Section 10.2 and Section 3.1 of Siringo et al. (2009) and Schuller et al. (2009), respectively, which I summarise below.

- Time-Streams for each scan are calibrated onto the Jy beam^{-1} scale using a linear interpolation of the calibration factors derived from primary or secondary flux-density calibrators[6]. 'Blind bolos' – dedicated temperature-monitoring channels of the LABOCA heat shield – are averaged and then used to correct any He^3 temperature fluctuations that may have occurred during the observation (i.e. when the telescope tilts).

- Each channel is systematically flagged depending on whether it exhibits strong cross talk with its neighbours; is not connected to any bolometer; is connected to a 1-MΩ resistor or simply shows no signal or very high noise. During the periods that the data were observed, this process typically flagged around 100 channels. The remaining unflagged channels are subsequently flat-fielded.

- Time-Streams are flagged in regions where the speed of the telescope is too low or too high to guarantee reliable positional information at every time-stamp. Speeds $> 30'' \, s^{-1}$ are required to gain sufficient source modulation – thus being able to differentiate the target from the resulting uncorrelated noise - whilst speeds $< 500'' \, s^{-1}$ guarantee that the positional information of the telescope in each time-stamp is reliable (Reichertz et al., 2001). The typical mean speed during these observations was $100'' \, s^{-1}$. Time-Stamps exhibiting large $> 800'' \, s^{-2}$ accelerations are also flagged.

- In an iterative manner, the following sequence is performed:

  1. Noisy channels are σ-clipped relative to all channels, with the degree of clipping decreasing from 5–3 with each iteration.
  2. Sky noise determined across all channels is removed from each channel.
  3. Each channel's time-streams are 'de-spiked' about their mean value.
  4. An $n^{\rm th}$-order polynomial baseline is subtracted from the time-streams to remove any low frequency drifts, where $n = 1$–4 with each iteration.

- Large discontinuities (or so-called 'jumps') in the time-streams seen by all channels and correlated noise between groups of channels (e.g. channels that share the same part of the electronics or are connected to the same cable) are removed.

[6]The primary calibrators for LABOCA include the planets Mars, Uranus and Neptune. To remove any systematics (mainly as a result of elevation differences) a calibration source is chosen to be as close to a target under observation as possible, which often results in having to use a secondary calibrator instead. These secondary calibrators include ultra-compact H II regions, low-luminosity proto-stars with dust-rich envelopes or nearby quasars.

– The Fourier spectrum of the time-streams are high-pass filtered below 0.5 Hz using a noise-whitening algorithm to remove the so-called '$1/f$' noise common in most amplifiers. This process also removes large spatial noise present in the time-streams, extending $\approx 3'$ for the typical scanning speeds of $100'' \, \mathrm{s}^{-1}$ that were measured during the observations.

– At this stage, the mean noise-weighted point-source sensitivity of all channels ($\mathcal{S} = \sum_c \left(\sigma_c \sqrt{\delta t} \sigma_c^2 \right) / \sum_c \left(1/\sigma_c^2 \right)$, where σ_c is the r.m.s. scatter in the time-streams of channel c and $\delta t \sim 0.04\,\mathrm{s}$ is the sample rate) is calculated and scans with $\mathcal{S} > 70\,\mathrm{mJy\,s^{1/2}}$ are inspected and then removed if deemed to be corrupted by electronical interference.

– Scans are opacity corrected using the mean elevation (θ) and opacity values (τ) derived from so-called 'skydips'[7] (τ_{sd}) and the radiometer (τ_{rm}), i.e. they are multiplied by $\exp(\tau / \sin(\theta))$.

– Finally, the time-streams are 'pixelated' onto a two-dimensional intensity image. The r.m.s. scatter between time-streams is used to generate a weight image of equal size. During this process, the pixels are over-sampled by a factor of four in order to preserve the spatial information across the image. This results in a final pixel scale of $p \approx 4.8'' \, \mathrm{pix}^{-1}$.

These pixelated intensity images for each scan are subsequently co-added, with inverse weighting. The final image is then PSF-filtered in order to remove any high-frequency noise on scales smaller than the beam and to ease the detection of point sources. The effect of filtering with a Gaussian with FWHM of $\theta = 19.2''$ (see Figure 2.5) degrades the spatial resolution to $\sqrt{\theta^2 + \theta^2} = \sqrt{2}\theta \approx 27''$. Therefore, I scale the final image by $\sqrt{2}$ in order to preserve its peak intensity (i.e. keeping the $\mathrm{mJy\,beam^{-1}}$ unit). As the r.m.s. ($= 1/\sqrt{\mathrm{weight}}$) images are also filtered to this resolution, an additional scaling to them is required in order to preserve the SNR in regions 'free of sources', i.e. $S/N = 1$. This scaling is taken to be the median absolute deviation (MAD) of the 3.5-σ-clipped SNR pixel distribution, multiplied by ≈ 1.4826 to mimic a Gaussian σ.

These reduction steps are then repeated but this time using the final PSF-filtered image as a model to mask significant sources before flagging any time-streams. Using a model in this fashion helps to increase the final SNR of detections (Schuller et al., 2009; Belloche et al., 2011). I find that one repetition is sufficient to achieve convergence in the SNR of a point source, in agreement with the findings of Weiß et al. (2009) and Gomez et al. (2010).

[7] Skydips provide a measurement of the atmosphere as a function of airmass by continuously tipping from high ($\sim 80°$) to low ($\sim 20°$) elevation in $\approx 30\,\mathrm{s}$. A multi-parameter model is then fit to the data, which is calibrated using an additional scan that determines the absolute measurement of the sky, to deduce the opacity (τ_{sd}).

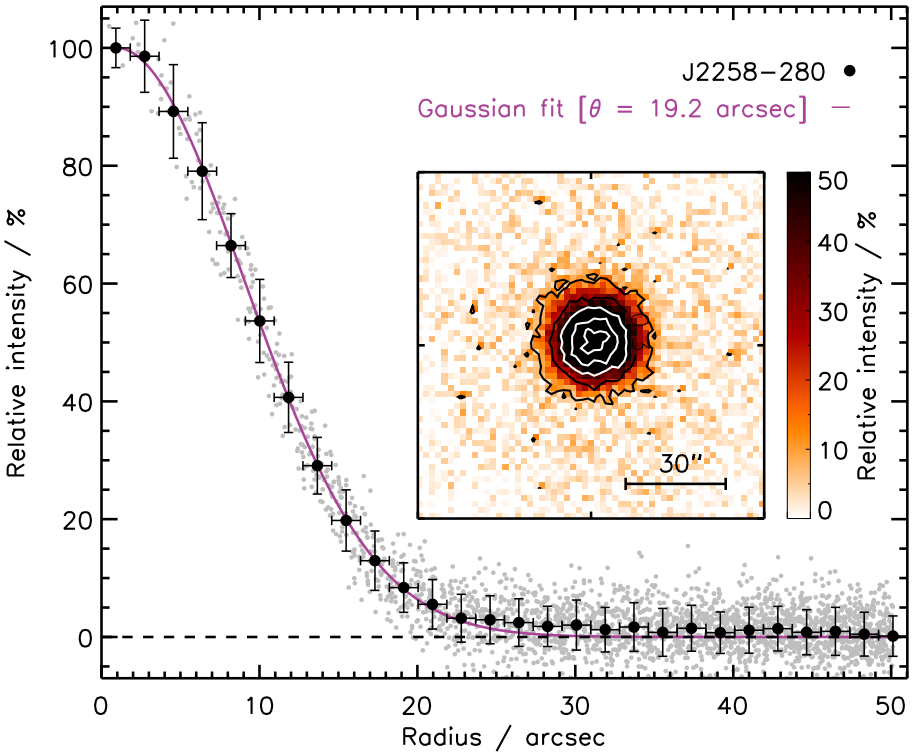

Figure 2.5: Main: LABOCA radially-averaged PSF of J2258−280, the most frequently visited pointing source during observations, which was reduced in the same manner described in Section 2.3.1. Black points indicate bin averages and their respective r.m.s. values, after sky subtraction. The PSF is well described by a Gaussian with FWHM of $\theta = 19.2''$ (purple line), which was used to PSF-filter the final images. **Inset:** normalised flux image of J2258−280 ($S_\nu = 765.4 \pm 26.2\,\mathrm{mJy}$) with contours indicating the 10, 30 (black), 50, 70 and 99 (white)% peak flux levels.

2.3.2 850-μm Continuum Imaging and Reduction with SCUBA-2

The ultra-red galaxies were observed during the period 2012–13 with the SCUBA-2 instrument on the JCMT under good or excellent weather with typical PWV values between 0.6–2.0 mm – corresponding to typical zenith atmospheric opacities of $\tau_{\rm los} = 0.2$–0.4.

Observations were carried out using the so-called 'DAISY' pattern, in which the telescope scans in a continuous 'petal-like' path that provides uniform exposure over the central $\lesssim$ 3-arcmin region of a source. Furthermore, this scanning pattern ensures that a given source is covered at all times by one part of a SCUBA-2 sub-array[8].

Around 10–15 min was spent observing each source, which is a sufficient duration with which to robustly detect $z > 4$ DSFGs with dust temperatures in the range 10–100 K. As each target was only visited once for a single $\sim$ 10-min 'snapshot', the astrometry of the SCUBA-2 images is expected to be accurate to $\sigma_{\rm point} \approx 2$–$3''$ – i.e. the same as the JCMT pointing accuracy.

Conversion to the Janksy scale was accomplished using the planets Uranus and Mars, and the secondary calibrators from the JCMT calibrator list (Dempsey et al., 2013). Both of these calibrator have an estimated 850-μm calibration error of $\sigma_{\rm calib} \approx 5\%$.

The data were reduced by Wayne Holland using the Dynamic Iterative Map-Maker (DIMM, which is similar in its mechanics to the BOA software described previously) within the Sub-Millimetre User Reduction Facility (SMURF, or ) Starlink software package (Chapin et al., 2013) using the 'zero-mask' algorithm that is effective at suppressing large-scale noise. This algorithm masks the central 30-arcsec-diameter region of the data at the likely positions of the ultra-red galaxies, i.e. at the SPIRE coordinates. As the calibrators were reduced in a similar manner, the flux-density conversion of the ultra-red galaxies from pico-Watts onto the Jansky scale was deemed to be reliable.

I summarise below the steps of the reduction process used, which is also illustrated via a flow chart in Figure 2.6:

- The bolometers are sampled at approximately 200 Hz, split into 30 s time-stream bundles for each of the four arrays and written to multiple raw files. These raw files are **concatenated** into a continuous time-stream, multiplied by the appropriate **flat-field** correction determined via the prescription outlined in Section 2.1 of Dempsey et al. (2013). Finally, they are subsequently **down-sampled** to match the selected output image pixel size, which in this case was $p = 1''\text{pix}^{-1}$.

- A variety of imperfections in the concatenated time-streams are now **repaired**. Sudden **steps** in the time-streams – more often than not occurring due to cosmic-ray events – can result in either severe ringing during the filtering stages that occur later, or can introduce other artefacts (such as streaks) in the final image. These steps are therefore removed via a median-smoothing algorithm between the two levels.

[8] SCUBA-2 is comprised of four arrays that contain the $\sim$ 10,000 transition edge sensor bolometers, which operate simultaneously at 850- and 450-μm via 'beam-splitting' mirrors.

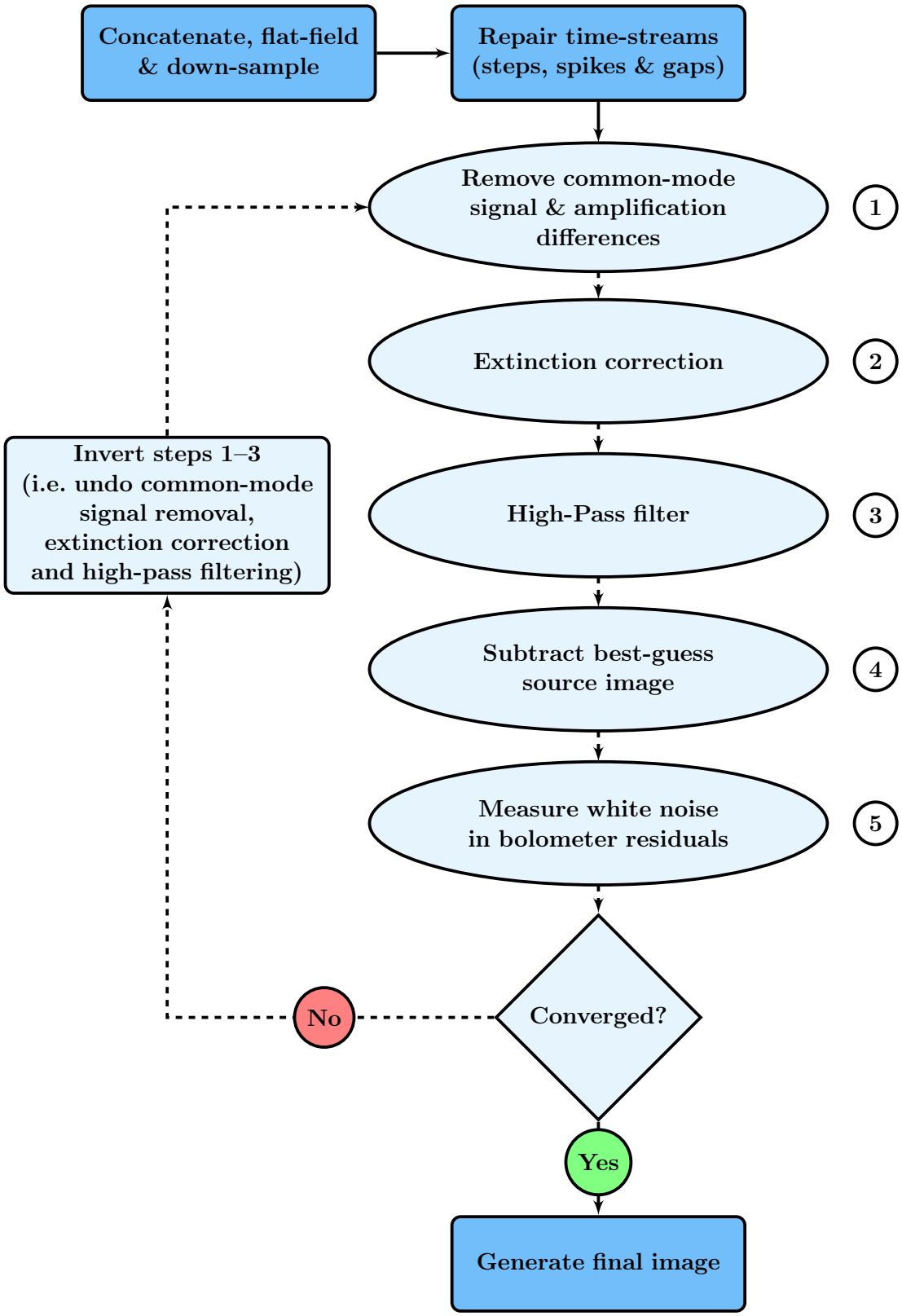

Figure 2.6: Flowchart illustrating the SCUBA-2 data reduction steps used in the DIMM algorithm in the SMURF software package (Chapin et al., 2013), which converts the raw time-streams of a given ultra-red galaxy into a reduced image. The light shaded, numbered steps indicate the sequence of events that are iterated until convergence in the bolometer residual variances is achieved (i.e. the signal appears as white noise).

Additionally, short-duration **spikes** in the time-streams are clipped away based on the median value and dispersion of each time-stream. Finally, the bad data samples (due to, for e.g., the sudden steps or short-duration spikes) result in **gaps** in the time-streams that require filling. This is achieved via a least-squares linear fit to neighbouring regions that contain 'good' data.

– In an iterative manner, the following sequence is performed:

1. The so-called 'common-mode signal' shared by *all* of the bolometers is a reasonable model for the correlated noise in SCUBA-2 and is computed by averaging the time-streams from all of these bolometers. The common-mode signal is then **subtracted** from each bolometer having been corrected for amplification differences (i.e. differing gain values in the bolometers) and offsets, which in some sense provides an additional flat-fielding step to that already described.
2. The time-streams are then corrected (i.e. multiplied) for **atmospheric extinction**, which is derived using both the 183-GHz Water Vapour Monitor on the JCMT and the elevation of the telescope at any given time-stamp.
3. A **high-pass Fourier transform filter** is then applied to the time-streams to remove most of the residual low-frequency, $1/f$ noise over spatial scales of $\approx 3'$, i.e. a filter with a $\approx (0.5 - 0.8)$-Hz cut-off is applied.
4. The time-streams from all bolometers are now averaged and pixelated onto a best-guess source image, which is assumed to only contain the real astronomical source(s). A best-guess variance image is also generated and is used in subsequent iterations to weight the best-guess source image. After the best-guess source image has been made, it is projected back into the time domain and **subtracted** from each bolometer.
5. The **residual variance** in each bolometer is now **measured** and compared to the white-noise levels between 2–10 Hz.
6. Whether or not these iterative steps have **converged** is now assessed. If the ratio of the residual variance to the white noise is on the order of unity, then the iterative steps have converged. Or, if the absolute difference between the best-guess source image pixels is less than $< 5\%$, then the iterative steps have converged. Or, finally, if the number of iterations (in this case four) has been reached, then the iterative steps have converged. However, if none of the convergence criteria are satisfied, then the iterative steps are repeated, with steps 1–3 being inverted. At the end of each iteration, the new best-guess source image (now weighted by the bolometer variances) is added to the existing best-guess source image and the convergence criteria are re-assessed.

– After the iterative steps have converged, the reduced data are pixelated and written to a file.

Finally, as with the LABOCA data, the reduced SCUBA-2 image is filtered with a Gaussian with a FWHM of $\theta = 13''$ such that the final resolution of a $3' \times 3'$ reduced image is $\theta \approx 18''$.

2.4 Results, Analysis and Discussion

I now describe the measurements of 850-/870-μm for SCUBA-2/LABOCA flux densities for the ultra-red galaxies. For the handful of galaxies where data exist from both SCUBA-2 and LABOCA, e.g. SGP−354388, the measured flux densities are consistent to within 1σ.

2.4.1 Measurements of Flux Density

I measured peak and aperture flux densities for the ultra-red galaxies in the SCUBA-2/LABOCA images and list the results in Table 2.2.

The peak flux densities were measured on the PSF-filtered images and located by searching for the brightest pixel within a 45-arcsec-diameter circle centred on the SPIRE coordinates of the ultra-red galaxies. Uncertainties ($\sigma^{\rm peak}$) were derived from the σ-clipped r.m.s. scatter within a $9' \times 9'$ box centred at the pixel position of the peak flux density. Given the small circular area searched over, there is a high probability that a single, real DSFG is detected via this method, and therefore I ignored the small degree of flux boosting that may happen.

The aperture flux densities were measured within 45-arcsec and 60-arcsec-diameter apertures (again centred on the pixel position of the peak flux densities) using the APER routine in Interactive Data Language (IDL — Landsman, 1993), with annuli between 1.5× and 2.0× the aperture radius being used to determine the sky background (Dempsey et al., 2013). Such large apertures ($\gtrsim$ (2–3)× the size of the filtered SCUBA-2 PSF) adequately enclose the majority of the sub-mm emission when a given ultra-red galaxy is clearly extended. Uncertainties for this method were derived from the r.m.s. scatter in the values of 500 aperture/annulus pairs randomly placed across the image – ensuring that no overlap occurred with the central aperture.

Key Point 2.3
The flux density adopted for a given ultra-red galaxy during the photometric redshift algorithm (described in the following section) was governed by the procedure outlined in Karim et al. (2013), i.e. the peak flux density was used *unless* the 45-arcsec-aperture measurement was

$$S^{45} \geq S^{\rm peak} + 3\sigma^{\rm peak},$$

indicating that a given ultra-red galaxy is extended.

Exceptions to this rule were NGP−239358, where the peak flux density was adopted as the extended emission was deemed unreliable, and SGP−354388, where the 45-arcsec-aperture

Table 2.2: Properties of ultra-red galaxies.

IAU name	Nickname	S_{250} mJy	S_{350} mJy	S_{500} mJy	$S_{850}^{\rm peak}$ mJy	S_{850}^{45} mJy	S_{850}^{60} mJy	Date observed† yyyy–mm–dd
HATLAS 085612.1−004922	G09−47693	**27.4 ± 7.3**	34.4 ± 8.1	45.4 ± 8.6	12.5 ± 4.0	6.4 ± 9.1	5.4 ± 10.8	2012–04–28
HATLAS 091642.6+022147	G09−51190	**28.5 ± 7.6**	39.5 ± 8.1	46.6 ± 8.6	15.2 ± 3.8	28.3 ± 7.3	24.2 ± 8.7	2012–12–21
HATLAS 084113.6−004114	G09−59393	**24.1 ± 7.0**	43.8 ± 8.3	46.8 ± 8.6	23.7 ± 3.5	27.7 ± 5.6	12.4 ± 9.8	2012–04–27
HATLAS 090925.0+015542	G09−62610	**18.6 ± 5.4**	37.3 ± 7.4	44.3 ± 7.8	19.5 ± 4.9	23.1 ± 9.0	32.7 ± 14.4	2012–03–06
HATLAS 091130.1−003846	G09−64889	**20.2 ± 5.9**	30.4 ± 7.7	34.7 ± 8.1	15.1 ± 4.3	4.4 ± 8.9	−21.2 ± 10.0	2012–12–16
HATLAS 083909.9+022718	G09−79552	16.6 ± 6.2	**38.1 ± 8.1**	42.8 ± 8.5	17.0 ± 3.6	11.1 ± 7.3	3.2 ± 14.0	2013–03–09
HATLAS 090419.9−013742	G09−79553	14.0 ± 5.9	**36.8 ± 8.0**	35.9 ± 8.4	16.8 ± 3.7	20.1 ± 7.1	14.4 ± 10.1	2013–03–09
HATLAS 084659.0−004219	G09−80620	13.5 ± 5.0	**25.3 ± 7.4**	28.4 ± 7.7	13.2 ± 4.3	6.8 ± 9.8	−9.7 ± 9.3	2012–12–16
HATLAS 085156.0+020533	G09−80658	17.8 ± 6.4	**31.6 ± 8.3**	39.5 ± 8.8	17.6 ± 4.1	13.6 ± 9.4	24.0 ± 9.4	2013–03–09
HATLAS 084937.0+001455	G09−81106	14.0 ± 6.0	**30.9 ± 8.2**	47.5 ± 8.8	30.2 ± 5.2	37.4 ± 11.4	37.0 ± 12.0	2012–12–18
HATLAS 084059.3−000417	G09−81271	15.0 ± 6.1	**30.5 ± 8.2**	42.3 ± 8.6	29.7 ± 3.7	35.8 ± 6.4	44.2 ± 10.6	2013–03–09
HATLAS 090304.2−004614	G09−83017	10.2 ± 5.7	**26.4 ± 8.0**	37.2 ± 8.8	16.1 ± 4.4	17.9 ± 9.4	1.7 ± 9.1	2012–12–16
HATLAS 090045.4+004125	G09−83808	9.7 ± 5.4	**24.6 ± 7.9**	44.0 ± 8.2	36.0 ± 3.1	36.2 ± 9.1	23.5 ± 10.4	2012–12–16
HATLAS 083522.1+005228	G09−84477	20.0 ± 6.6	**27.3 ± 8.3**	31.6 ± 9.0	7.6 ± 3.8	−6.5 ± 7.4	−25.8 ± 8.9	2012–04–27
HATLAS 090916.2+002523	G09−87123	10.4 ± 5.8	**25.3 ± 8.2**	39.2 ± 8.7	20.7 ± 4.6	24.5 ± 9.3	43.7 ± 12.4	2012–12–16
HATLAS 090855.6+015638	G09−100369	15.4 ± 5.5	**17.3 ± 7.6**	32.3 ± 8.0	13.2 ± 3.6	22.1 ± 8.2	14.3 ± 9.8	2013–03–09
HATLAS 090808.9+015459	G09−101355	9.5 ± 5.5	14.6 ± 7.9	**33.4 ± 8.3**	13.5 ± 4.9	−2.5 ± 10.0	−40.2 ± 12.7	2012–12–16
HATLAS 115415.5−010255	G12−34009	**30.2 ± 7.2**	36.3 ± 8.2	60.4 ± 8.7	39.9 ± 4.2	38.9 ± 9.0	38.2 ± 17.5	2013–03–09
HATLAS 114314.6+002846	G12−42911	**21.2 ± 5.8**	44.1 ± 7.4	53.9 ± 7.7	35.4 ± 3.6	32.8 ± 7.0	21.0 ± 8.0	2012–04–27
HATLAS 114412.1+001812	G12−66356	**18.3 ± 5.4**	26.5 ± 7.4	32.9 ± 7.8	11.2 ± 4.6	−7.5 ± 8.8	−2.2 ± 12.5	2012–12–18
HATLAS 114353.5+001252	G12−77450	14.8 ± 5.1	**27.3 ± 7.4**	35.9 ± 7.7	11.9 ± 4.1	−0.3 ± 7.9	−6.3 ± 8.7	2012–04–27
HATLAS 115012.2−011252	G12−78339	17.0 ± 6.2	**30.8 ± 8.1**	31.6 ± 9.0	18.1 ± 4.3	31.3 ± 8.9	33.3 ± 11.2	2012–04–27
HATLAS 115614.2+013905	G12−78868	13.1 ± 5.9	**29.5 ± 8.2**	49.0 ± 8.5	12.2 ± 3.5	13.6 ± 6.4	5.8 ± 9.6	2012–04–27
HATLAS 114038.8−022811	G12−79192	15.8 ± 6.3	**28.6 ± 8.1**	34.1 ± 8.8	5.1 ± 3.5	−4.3 ± 6.4	−17.4 ± 7.8	2012–12–21
HATLAS 113348.0−002930	G12−79248	18.4 ± 6.2	**29.5 ± 8.2**	42.0 ± 8.9	27.6 ± 5.0	62.4 ± 9.8	71.3 ± 12.0	2012–12–18
HATLAS 114408.1−004312	G12−80302	15.9 ± 6.2	**27.2 ± 8.1**	35.9 ± 9.0	6.0 ± 3.8	−15.0 ± 8.9	−28.8 ± 9.5	2012–04–27
HATLAS 115552.7−021111	G12−81658	14.9 ± 6.1	**26.5 ± 8.1**	36.8 ± 8.7	1.0 ± 4.4	−25.5 ± 8.7	−32.0 ± 12.2	2012–12–21
HATLAS 113331.1−003415	G12−85249	13.3 ± 6.1	**25.0 ± 8.3**	31.4 ± 8.8	4.4 ± 2.7	−0.3 ± 5.7	−3.3 ± 6.6	2012–12–18
HATLAS 115241.5−011258	G12−87169	13.5 ± 6.0	**23.5 ± 8.2**	33.5 ± 8.8	6.9 ± 4.0	9.8 ± 9.2	6.1 ± 9.6	2012–12–21
HATLAS 114350.1−005211	G12−87695	19.0 ± 6.4	**23.9 ± 8.3**	30.7 ± 8.7	15.6 ± 3.9	2.2 ± 7.1	−6.2 ± 10.4	2012–12–21
HATLAS 142208.7+001419	G15−21998	**36.0 ± 7.2**	56.2 ± 8.1	62.6 ± 8.8	13.2 ± 3.4	7.2 ± 7.0	7.3 ± 9.0	2012–04–26
HATLAS 144003.9−011019	G15−24822	**33.9 ± 7.1**	38.6 ± 8.2	58.0 ± 8.8	8.0 ± 3.5	5.8 ± 7.5	1.4 ± 9.0	2012–04–27
HATLAS 144433.3+001639	G15−26675	**26.8 ± 6.3**	57.2 ± 7.4	61.4 ± 7.7	45.6 ± 3.6	36.6 ± 10.3	27.9 ± 9.6	2012–04–27
HATLAS 141250.2−000323	G15−47828	**28.0 ± 7.4**	35.1 ± 8.1	45.3 ± 8.8	19.6 ± 4.5	15.1 ± 9.3	10.7 ± 10.8	2012–07–28
HATLAS 142710.6+013806	G15−64467	**20.2 ± 5.8**	28.0 ± 7.5	33.4 ± 7.8	18.7 ± 4.9	30.7 ± 10.8	39.2 ± 16.2	2013–03–09
HATLAS 143639.5−013305	G15−66874	**22.9 ± 6.6**	34.9 ± 8.1	35.8 ± 8.5	27.3 ± 5.3	34.1 ± 12.5	29.2 ± 12.6	2012–07–27
HATLAS 140916.8−014214	G15−82412	**21.2 ± 6.6**	30.8 ± 8.1	41.9 ± 8.8	17.2 ± 4.4	9.4 ± 8.1	6.2 ± 10.9	2012–07–28
HATLAS 145012.7+014813	G15−82684	17.3 ± 6.4	**38.5 ± 8.1**	43.2 ± 8.8	18.5 ± 4.1	15.3 ± 8.2	5.5 ± 9.3	2012–04–27
HATLAS 140555.8−004450	G15−83543	16.5 ± 6.4	**32.3 ± 8.1**	40.2 ± 8.8	13.7 ± 4.7	18.3 ± 10.0	18.4 ± 9.5	2012–07–28
HATLAS 143522.8+012105	G15−83702	14.0 ± 6.1	**30.6 ± 8.0**	33.1 ± 8.7	7.9 ± 4.6	4.7 ± 8.3	−0.4 ± 11.2	2012–07–27

Table 2.2 (continued from previous page)

IAU name	Nickname	S_{250} mJy	S_{350} mJy	S_{500} mJy	$S_{850}^{\rm peak}$ mJy	S_{850}^{45} mJy	S_{850}^{60} mJy	Date observed† yyyy–mm–dd
HATLAS 141909.7−001514	G15−84546	11.5 ± 4.7	$\mathbf{23.7 \pm 7.4}$	30.3 ± 7.7	19.4 ± 5.0	10.2 ± 9.3	7.4 ± 12.2	2012–07–27
HATLAS 142647.8−011702	G15−85113	10.5 ± 5.7	$\mathbf{29.6 \pm 8.2}$	34.9 ± 8.7	8.7 ± 3.4	1.6 ± 6.9	5.2 ± 7.5	2012–04–27
HATLAS 143015.0+012248	G15−85592	12.9 ± 5.0	$\mathbf{23.5 \pm 7.5}$	33.9 ± 7.9	4.7 ± 5.6	6.3 ± 11.7	-4.3 ± 13.7	2012–07–27
HATLAS 142514.7+021758	G15−86652	15.6 ± 6.0	$\mathbf{28.1 \pm 8.2}$	38.5 ± 8.9	11.4 ± 3.8	5.1 ± 5.8	4.3 ± 7.8	2012–04–26
HATLAS 140609.2+000019	G15−93387	15.5 ± 6.1	$\mathbf{23.6 \pm 8.2}$	35.6 ± 8.5	8.8 ± 3.0	14.9 ± 6.8	15.7 ± 8.5	2012–04–27
HATLAS 144308.3+015853	G15−99748	14.0 ± 5.8	$\mathbf{22.4 \pm 8.3}$	31.5 ± 8.8	12.2 ± 3.8	5.0 ± 6.4	17.9 ± 9.7	2012–04–26
HATLAS 143139.7−012511	G15−105504	15.0 ± 6.6	15.6 ± 8.4	$\mathbf{35.9 \pm 9.0}$	8.5 ± 3.8	9.9 ± 8.1	11.8 ± 9.5	2012–07–27
HATLAS 134040.3+323709	NGP−63663	$\mathbf{30.6 \pm 6.8}$	53.5 ± 7.8	50.1 ± 8.1	15.5 ± 4.1	7.9 ± 8.3	-12.5 ± 9.2	2012–04–28
HATLAS 131901.6+285438	NGP−82853	$\mathbf{23.6 \pm 5.8}$	37.6 ± 7.3	40.5 ± 7.5	15.8 ± 3.6	2.1 ± 5.2	-3.8 ± 7.8	2012–06–23
HATLAS 134119.4+341346	NGP−101333	$\mathbf{32.4 \pm 7.5}$	46.5 ± 8.2	52.8 ± 9.0	24.6 ± 3.8	17.6 ± 8.2	13.0 ± 9.2	2012–04–28
HATLAS 125512.4+251358	NGP−101432	$\mathbf{27.7 \pm 6.9}$	44.8 ± 7.8	54.1 ± 8.3	24.3 ± 4.0	32.0 ± 7.2	41.9 ± 10.9	2012–06–23
HATLAS 130823.9+254514	NGP−111912	$\mathbf{25.2 \pm 6.5}$	41.5 ± 7.6	50.2 ± 8.0	14.9 ± 3.9	8.8 ± 6.7	2.3 ± 9.1	2012–04–26
HATLAS 133836.0+273247	NGP−113609	$\mathbf{29.4 \pm 7.3}$	50.1 ± 8.0	63.5 ± 8.6	21.9 ± 3.5	12.5 ± 6.2	9.2 ± 9.5	2012–04–26
HATLAS 133217.4+343945	NGP−126191	$\mathbf{24.5 \pm 6.4}$	31.3 ± 7.7	43.7 ± 8.2	29.7 ± 4.3	37.2 ± 7.5	45.1 ± 11.6	2012–04–28
HATLAS 130329.2+232212	NGP−134174	$\mathbf{27.6 \pm 7.3}$	38.3 ± 8.4	42.9 ± 9.4	11.4 ± 4.0	21.3 ± 7.4	11.7 ± 8.9	2012–04–26
HATLAS 132627.5+335633	NGP−136156	$\mathbf{29.3 \pm 7.4}$	41.9 ± 8.3	57.5 ± 9.2	23.4 ± 3.4	29.7 ± 4.6	27.7 ± 9.8	2012–04–26
HATLAS J130545.8+252953	NGP−136610	$\mathbf{23.1 \pm 6.2}$	39.3 ± 7.7	46.3 ± 8.3	19.4 ± 3.6	34.6 ± 7.5	29.3 ± 9.9	2012–07–12
HATLAS J130456.6+283711	NGP−158576	$\mathbf{23.4 \pm 6.3}$	38.5 ± 7.7	38.2 ± 8.1	13.1 ± 4.0	12.0 ± 7.3	15.8 ± 10.2	2012–04–26
HATLAS J130515.8+253057	NGP−168885	$\mathbf{21.2 \pm 6.0}$	35.2 ± 7.7	45.3 ± 8.0	26.5 ± 3.8	17.8 ± 7.2	4.7 ± 8.9	2013–03–09
HATLAS J131658.1+335457	NGP−172391	$\mathbf{25.1 \pm 7.1}$	39.2 ± 8.1	52.3 ± 9.1	15.4 ± 3.1	7.2 ± 6.0	5.3 ± 8.6	2012–04–26
HATLAS J125607.2+223046	NGP−185990	$\mathbf{24.3 \pm 7.0}$	35.6 ± 8.1	41.7 ± 8.9	33.6 ± 4.1	18.4 ± 9.9	13.4 ± 12.0	2013–03–09
HATLAS J133337.6+241541	NGP−190387	$\mathbf{25.2 \pm 7.2}$	41.9 ± 8.0	63.3 ± 8.8	37.4 ± 3.8	33.4 ± 8.0	29.4 ± 10.0	2012–04–26
HATLAS J125440.7+264925	NGP−206987	$\mathbf{24.1 \pm 7.1}$	39.2 ± 8.2	50.1 ± 8.7	22.7 ± 3.7	17.5 ± 6.5	25.7 ± 9.4	2012–04–26
HATLAS J134729.9+295630	NGP−239358	$\mathbf{21.3 \pm 6.6}$	28.7 ± 8.1	33.9 ± 8.7	15.2 ± 5.1	39.5 ± 13.0	61.5 ± 15.7	2013–03–09
HATLAS J133220.4+320308	NGP−242820	18.1 ± 6.1	$\mathbf{35.4 \pm 7.9}$	33.8 ± 8.6	14.7 ± 3.9	10.5 ± 7.8	-4.6 ± 9.4	2012–04–26
HATLAS J130823.8+244529	NGP−244709	23.1 ± 6.9	$\mathbf{34.2 \pm 8.2}$	34.9 ± 8.7	17.4 ± 4.0	15.6 ± 9.7	24.0 ± 11.5	2013–03–09
HATLAS J134114.2+335934	NGP−246114	17.3 ± 6.5	$\mathbf{30.4 \pm 8.1}$	33.9 ± 8.5	25.9 ± 4.6	32.4 ± 8.2	37.2 ± 8.9	2012–04–26
HATLAS J131715.3+323835	NGP−247012	10.5 ± 4.8	$\mathbf{25.3 \pm 7.5}$	31.7 ± 7.7	18.4 ± 3.9	18.5 ± 8.4	6.4 ± 8.7	2013–03–09
HATLAS J131759.9+260943	NGP−247691	16.5 ± 5.6	$\mathbf{26.2 \pm 7.6}$	33.2 ± 8.2	17.8 ± 4.2	17.5 ± 8.7	21.2 ± 13.1	2013–03–09
HATLAS J133446.1+301933	NGP−248307	10.4 ± 5.4	$\mathbf{28.3 \pm 8.0}$	35.1 ± 8.3	10.7 ± 3.7	2.6 ± 7.1	-8.5 ± 9.1	2012–04–26
HATLAS J133919.3+245056	NGP−252305	15.3 ± 6.1	$\mathbf{27.7 \pm 8.1}$	40.0 ± 9.4	24.0 ± 3.5	23.5 ± 7.6	21.2 ± 8.7	2012–04–26
HATLAS J133356.3+271541	NGP−255731	8.4 ± 5.0	$\mathbf{23.6 \pm 7.7}$	29.5 ± 7.9	24.6 ± 5.2	31.0 ± 12.4	29.5 ± 18.4	2013–03–09
HATLAS J132731.0+334850	NGP−260332	12.2 ± 5.8	$\mathbf{25.1 \pm 8.1}$	44.4 ± 8.6	10.1 ± 3.2	15.9 ± 6.0	12.0 ± 8.8	2012–04–26
HATLAS J133251.5+332339	NGP−284357	12.6 ± 5.3	$\mathbf{20.4 \pm 7.8}$	42.4 ± 8.3	28.9 ± 4.3	27.4 ± 9.9	37.0 ± 14.4	2013–03–09
HATLAS J132419.5+343625	NGP−287896	3.4 ± 5.7	$\mathbf{21.8 \pm 8.1}$	36.4 ± 8.7	18.7 ± 4.3	-8.7 ± 8.9	-10.7 ± 11.7	2013–03–09
HATLAS J131425.9+240634	NGP−297140	15.5 ± 6.2	$\mathbf{21.1 \pm 8.2}$	36.8 ± 8.6	9.0 ± 4.3	18.2 ± 9.8	14.5 ± 10.2	2013–03–09
HATLAS J132600.0+231546	NGP−315918	8.1 ± 5.7	15.4 ± 8.2	$\mathbf{41.8 \pm 8.8}$	16.1 ± 3.9	21.8 ± 8.4	31.7 ± 11.6	2013–03–09
HATLAS J132546.1+300849	NGP−315920	17.8 ± 6.2	16.6 ± 8.1	$\mathbf{39.4 \pm 8.6}$	10.4 ± 4.3	0.0 ± 10.3	-1.5 ± 14.2	2013–03–09
HATLAS J125433.5+222809	NGP−316031	7.0 ± 5.5	11.4 ± 8.2	$\mathbf{33.2 \pm 8.6}$	16.8 ± 4.0	14.1 ± 9.3	9.1 ± 10.9	2013–03–09

Table 2.2 (continued from previous page)

IAU name	Nickname	S_{250} mJy	S_{350} mJy	S_{500} mJy	$S_{850}^{\rm peak}$ mJy	S_{850}^{45} mJy	S_{850}^{60} mJy	Date observed† yyyy–mm–dd
HATLAS J000124.9−354212	SGP−28124	**61.6 ± 7.7**	89.1 ± 8.3	117.7 ± 8.8	37.2 ± 2.6	46.7 ± 6.0	51.6 ± 7.8	2012–12–15
HATLAS J000124.9−354212	SGP−28124‡	**61.6 ± 7.7**	89.1 ± 8.3	117.7 ± 8.8	46.9 ± 1.7	48.4 ± 2.5	55.1 ± 3.8	2013–04
HATLAS J000018.0−333737	SGP−72464	**43.4 ± 7.6**	67.0 ± 8.0	72.6 ± 8.9	20.0 ± 4.2	17.2 ± 8.9	7.5 ± 8.2	2012–12–15
HATLAS J000624.3−323019	SGP−93302	**31.2 ± 6.7**	60.7 ± 7.7	61.7 ± 7.8	37.1 ± 3.7	18.4 ± 9.1	3.6 ± 8.3	2012–12–19
HATLAS J000624.3−323019	SGP−93302‡	**31.2 ± 6.7**	60.7 ± 7.7	61.7 ± 7.8	35.3 ± 1.6	31.3 ± 2.3	30.9 ± 3.7	2013–04
HATLAS J001526.4−353738	SGP−135338	**32.9 ± 7.3**	43.6 ± 8.1	53.3 ± 8.8	14.7 ± 3.8	20.8 ± 8.0	17.9 ± 8.4	2012–12–19
HATLAS J223835.6−312009	SGP−156751	**28.4 ± 6.9**	37.7 ± 7.9	47.6 ± 8.4	12.6 ± 2.0	12.0 ± 2.9	12.5 ± 3.5	2013–04
HATLAS J000306.9−330248	SGP−196076	**28.6 ± 7.3**	28.6 ± 8.2	46.2 ± 8.6	32.5 ± 4.1	32.5 ± 9.8	32.2 ± 11.2	2012–12–15
HATLAS J003533.9−280302	SGP−208073	**28.0 ± 7.4**	33.2 ± 8.1	44.3 ± 8.5	19.4 ± 2.9	19.7 ± 4.3	18.9 ± 6.3	2013–04
HATLAS J001223.5−313242	SGP−213813	**23.9 ± 6.3**	35.1 ± 7.6	35.9 ± 8.2	18.1 ± 3.6	18.6 ± 6.9	12.0 ± 8.9	2012–12–19
HATLAS J001635.8−331553	SGP−219197	**27.6 ± 7.4**	51.3 ± 8.1	43.6 ± 8.4	12.2 ± 3.7	15.0 ± 7.5	6.4 ± 10.1	2012–12–21
HATLAS J002455.5−350141	SGP−240731	**25.1 ± 7.0**	40.2 ± 8.4	46.1 ± 8.9	1.4 ± 4.4	−2.7 ± 12.2	−7.8 ± 10.2	2012–12–21
HATLAS J000607.6−322639	SGP−261206	**22.6 ± 6.3**	45.2 ± 8.0	59.4 ± 8.4	45.8 ± 3.5	56.9 ± 8.9	65.1 ± 12.4	2012–12–18
HATLAS J002156.8−334611	SGP−304822	**23.0 ± 6.7**	40.7 ± 8.0	41.3 ± 8.7	19.8 ± 3.8	38.8 ± 8.3	35.1 ± 9.0	2012–12–21
HATLAS J001003.6−300720	SGP−310026	**23.1 ± 6.8**	33.2 ± 8.2	42.5 ± 8.7	10.9 ± 3.8	17.7 ± 7.2	13.5 ± 8.5	2012–12–15
HATLAS J002907.0−294045	SGP−312316	**20.2 ± 6.0**	29.8 ± 7.7	37.6 ± 8.0	10.3 ± 3.5	19.8 ± 7.2	10.5 ± 8.5	2012–12–19
HATLAS J225432.0−323904	SGP−317726	**20.4 ± 6.0**	35.1 ± 7.7	39.5 ± 8.0	19.4 ± 3.2	7.9 ± 5.9	10.5 ± 7.3	2013–09–01
HATLAS J004223.5−334340	SGP−354388	**26.6 ± 8.0**	39.8 ± 8.9	53.5 ± 9.8	40.4 ± 2.4	46.0 ± 5.7	57.5 ± 7.2	2014–06–30
HATLAS J004223.5−334340	SGP−354388‡	**26.6 ± 8.0**	39.8 ± 8.9	53.5 ± 9.8	38.7 ± 3.2	39.9 ± 4.7	64.1 ± 10.9	2013–10
HATLAS J010740.7−282711	SGP−32338	16.0 ± 7.1	**33.2 ± 8.0**	63.7 ± 8.7	23.1 ± 2.9	27.9 ± 9.4	14.3 ± 10.0	2012–12–17
HATLAS J004614.1−321826	SGP−380990	14.4 ± 5.9	**45.6 ± 8.2**	40.6 ± 8.5	7.7 ± 1.8	6.8 ± 2.7	7.8 ± 3.1	2013–01
HATLAS J000248.8−313444	SGP−381615	19.4 ± 6.6	**39.1 ± 8.1**	34.7 ± 8.5	8.5 ± 3.6	4.4 ± 6.5	2.5 ± 7.3	2012–12–15
HATLAS J223702.2−340551	SGP−381637	18.7 ± 6.8	**41.5 ± 8.4**	49.3 ± 8.6	12.6 ± 3.7	5.9 ± 6.8	−3.1 ± 8.3	2013–09–01
HATLAS J001022.4−320456	SGP−382394	15.7 ± 5.9	**35.6 ± 8.1**	35.9 ± 8.6	8.0 ± 2.4	3.5 ± 2.9	9.1 ± 3.9	2012–09
HATLAS J230805.9−333600	SGP−383428	16.4 ± 5.6	**32.7 ± 7.9**	35.6 ± 8.4	8.2 ± 2.9	4.3 ± 4.8	7.0 ± 6.8	2013–08–19
HATLAS J222919.2−293731	SGP−385891	13.0 ± 8.2	**45.6 ± 9.8**	59.6 ± 11.5	20.5 ± 3.6	21.6 ± 7.1	11.7 ± 10.4	2013–09–01
HATLAS J231146.6−313518	SGP−386447	10.5 ± 6.0	**33.6 ± 8.4**	34.5 ± 8.6	22.4 ± 3.6	34.3 ± 8.4	29.0 ± 11.3	2013–08–19
HATLAS J003131.1−293122	SGP−392029	18.3 ± 6.5	**30.5 ± 8.3**	35.3 ± 8.4	13.8 ± 3.5	17.4 ± 6.2	20.0 ± 8.1	2012–12–19
HATLAS J230357.0−334506	SGP−424346	0.7 ± 5.9	**25.1 ± 8.3**	31.6 ± 8.8	10.5 ± 3.6	−14.2 ± 5.7	−19.1 ± 7.6	2013–08–19
HATLAS J222737.1−333835	SGP−433089	23.8 ± 9.4	**31.5 ± 9.7**	39.5 ± 10.6	14.8 ± 1.7	15.6 ± 2.9	14.7 ± 4.1	2012–09
HATLAS J225855.7−312405	SGP−499646	5.8 ± 5.9	10.8 ± 8.1	**41.4 ± 8.6**	18.7 ± 3.0	15.2 ± 5.6	11.9 ± 6.5	2013–08–19
HATLAS J222318.1−322204	SGP−499698	−7.8 ± 8.5	14.9 ± 10.3	**57.0 ± 11.6**	11.1 ± 3.7	8.5 ± 7.7	6.4 ± 10.0	2013–09–01
HATLAS J013301.9−330421	SGP−499828	5.6 ± 5.8	13.5 ± 8.3	**36.6 ± 8.9**	9.8 ± 2.6	6.4 ± 4.2	4.2 ± 5.0	2013–10

†Ultra-Red galaxies observed with LABOCA have dates in the format yyyy-mm, since data were taken over a number of nights.
‡Ultra-Red galaxies observed with both LABOCA and SCUBA-2 (previous row).
Note. SPIRE flux densities highlighted in **bold** indicate the BANDFLAG of a detection, i.e. bold $\boldsymbol{S_{250}}$ values indicate BANDFLAG = 1 sources.

measurement was used as the sub-mm emission was clearly distributed on that scale – a fact later confirmed by ALMA 3-mm high-resolution imaging presented in Oteo et al. (2017a).

It is important to note that the peak flux densities on the PSF-filtered images are in agreement to within 1σ of the aperture flux-density measurements made on the raw images, when the sub-mm emission on the ultra-red galaxies is not extended, i.e. when the ultra-red galaxies have either a bright or faint point-source nature.

I now present a summary of the 850-/870-μm statistics of the candidate ultra-red galaxies considered in this chapter:

- 86% of the ultra-red galaxies are detected above $> 2.5\sigma$.
- 94, 81 and 75% of the BANDFLAG = 1, 2 and 3 galaxies are detected above $> 2.5\sigma$. This likely reflects the higher reliability of BANDFLAG = 1 sources, although the small sample (8) of BANDFLAG = 3 sources makes this hard to accurately determine.
- The > 2.5-σ sub-sample have slightly lower S_{500}/S_{250} colours (2.08) compared to the entire sample (2.15) but similar S_{500}/S_{350} colours, which reflects the increase in BANDFLAG = 1 sources. There is no appreciable change in colour as the SNR increases.

2.4.2 Photometric Redshifts

The Algorithm

Photometric redshifts were generated for the ultra-red galaxies using a custom-written χ^2-minimisation routine in IDL. The routine uses seven template SEDs, each one being representative of a typical DSFG, which I show normalised at a rest-frame wavelength of $\lambda_{\rm rest} = 100\,\mu$m in Figure 2.7. Four template SEDs are for the DSFGs Arp 220, HFLS3, the Cosmic Eyelash and G15.141. I model G15.141 as a modified greybody with hot and cold dust temperatures of 60 K and 32 K, respectively, cold-to-hot dust mass ratio of 50 : 1 and a dust emissivity of $\beta = +2$ (Lapi et al., 2011). The remaining three template SEDs are synthesized from Pope et al. (2008), Pearson et al. (2013)[9] and Swinbank et al. (2014, ALESS).

During the fitting process, I convolved the FIR (SPIRE through to SCUBA-2/LABOCA) photometry with their respective passband transmission profiles and searched for the lowest χ^2 value within $0 < z_{\rm phot} < 10$ down to a resolution of $\delta z_{\rm phot} = 0.01$. The χ^2 value for a

[9]The Pearson et al. template was modelled from 40 bright *H*-ATLAS sources (with known spectroscopic redshifts) assuming hot and cold dust components of 46.9 K and 23.9 K, respectively, cold-to-hot dust mass ratio of 30.1 : 1 and a dust emissivity of $\beta = +2$. There is a slight circularity here in that over half of this sample were spectroscopically observed based on their photometric redshifts.

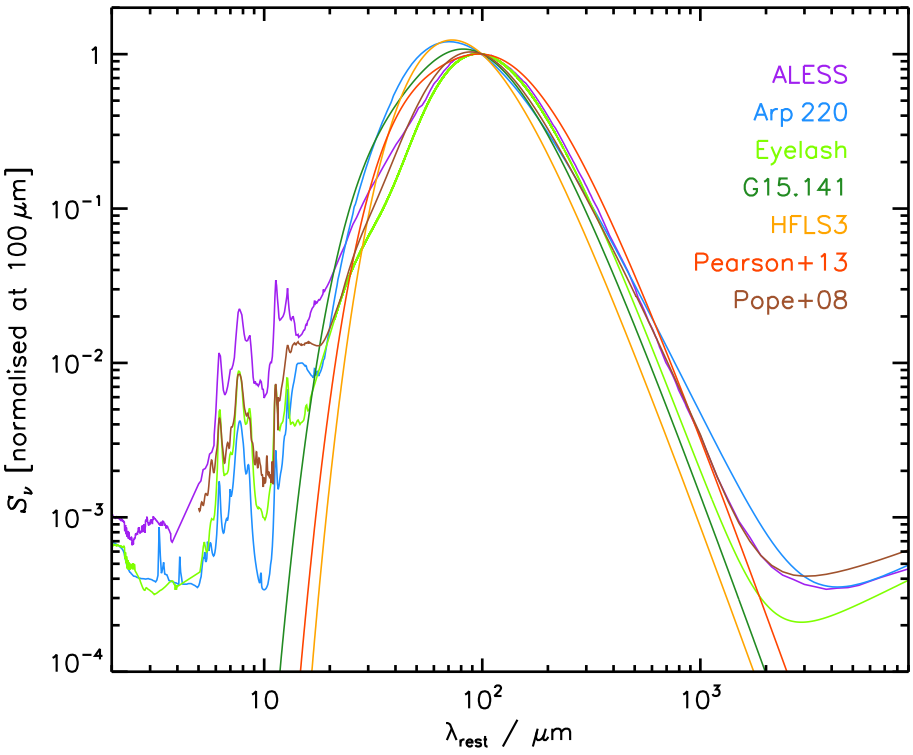

Figure 2.7: Seven representative template SEDs used to derive photometric redshifts – all normalised in flux density at a rest-frame wavelength of $\lambda_{\rm rest} = 100\,\mu$m. Both HFLS3 and Arp 220 are relatively blue compared to the other template SEDs (i.e. they peak at shorter wavelengths), which results in a diverse range of plausible representative template SEDs.

given redshift (z) is computed using the following equation:

$$\chi^2_z = \sum_{p=1}^{N} \left(\frac{S_p - a_z S'_{z,p}}{\sigma_p} \right)^2 , \tag{2.2}$$

where the sum is over all N passbands (i.e. $N = 4$), S_p and σ_p are the observed flux density and 1-σ uncertainty for the ultra-red galaxies through passband p and $S'_{z,p}$ is the template flux density through passband p at a redshift z. The template normalisation a_z is the value that minimises χ^2, calculated from:

$$\begin{aligned}
\frac{{\rm d}\chi^2_z}{{\rm d}a} &= 0, \\
2\sum_p^N \left(\frac{S_p - a_z S'_{z,p}}{\sigma_p} \right) \left(\frac{-S'_{z,p}}{\sigma_p} \right) &= 0, \\
-\sum_p^N \left(\frac{S_p S'_{z,p}}{\sigma_p^2} \right) + a_z \sum_p^N \left(\frac{S'_{p,z} S'_{p,z}}{\sigma_p^2} \right) &= 0, \\
\Rightarrow a_z = \frac{\sum_p^N S_{z,p} S'_p / \sigma_p^2}{\sum_p^N (S'_{z,p})^2 / \sigma_p^2}&.
\end{aligned} \tag{2.3}$$

I derived 1-σ uncertainties by repeating this fitting process on 1,000 Monte Carlo

realisations of the FIR flux densities drawn from a Gaussian distribution and then determining the 16–84 values from the resulting photometric redshifts. I computed photometric redshifts in this way for all of the ultra-red galaxies using each template. Finally, the adopted photometric redshift comes from the template that yields the lowest χ^2 value.

Photometric Redshift Accuracy and Scatter

In order to quantify the accuracy ($\mu_{\Delta z}$) and scatter ($\sigma_{\Delta z}$) of these seven template SEDs – and to discover if there are any underlying systematics that might question their effectiveness – I tested the fitting process on a training sample of 69 bright DSFGs. I used the available FIR photometry (Bussmann et al., 2013) – taking care to match the sampled passbands 'like-for-like' with the ultra-red galaxies in order to mitigate any wavelength-dependent biases – to derive photometric redshifts for these DSFGs. Then, in conjunction with their spectroscopic redshifts (Weiß et al., 2013; Riechers et al., 2013; Asboth et al., 2016; Strandet et al., 2016), I evaluated the familiar equation:

$$\frac{\Delta z}{1 + z_{\rm spec}} \equiv \frac{z_{\rm phot} - z_{\rm spec}}{1 + z_{\rm spec}}, \tag{2.4}$$

which I used to obtain a measure of the accuracy and dispersion.

The left-hand column of Figure 2.8 shows the results of Equation 2.4 using the seven template SEDs for these 69 bright DSFGs. Despite being comprised of many of the *H*-ATLAS sources in the training sample, the Pearson et al. template SED appears not to as be as accurate as many of the others, somewhat against intuition. This could in part be due to the inclusion of galaxies with optically confirmed spectroscopic redshifts, resulting in a redder SED perhaps due to blending/lensing effects contributing to the FIR flux density.

These results also show that the template SEDs from Arp 220, G15.141 and HFLS3 also have comparably high and positive offsets, $|\mu_{\Delta z}| \sim 0.2(1 + z_{\rm spec})$, and scatter, $|\sigma_{\Delta z}| \sim 0.2(1 + z_{\rm spec})$. These three template SEDs are the hottest adopted in this thesis – peaking at relatively shorter wavelengths compared to the rest. Neither of these templates successfully predict the true spectroscopic redshift until around $z_{\rm spec} \approx 5$–6. As the majority of training sample analysed here is below this redshift, the average systematic offset from zero is both large and positive for these three template SEDs.

Therefore, in order to derive the most accurate and reliable photometric redshifts as possible for this sample, I only kept the three template SEDs which have an accuracy of $|\mu_{\Delta z}| < 0.1(1 + z_{\rm spec})$ and an outlier fraction that is fewer than 10%, i.e. the ALESS, Pope et al. and Cosmic Eyelash template SEDs.

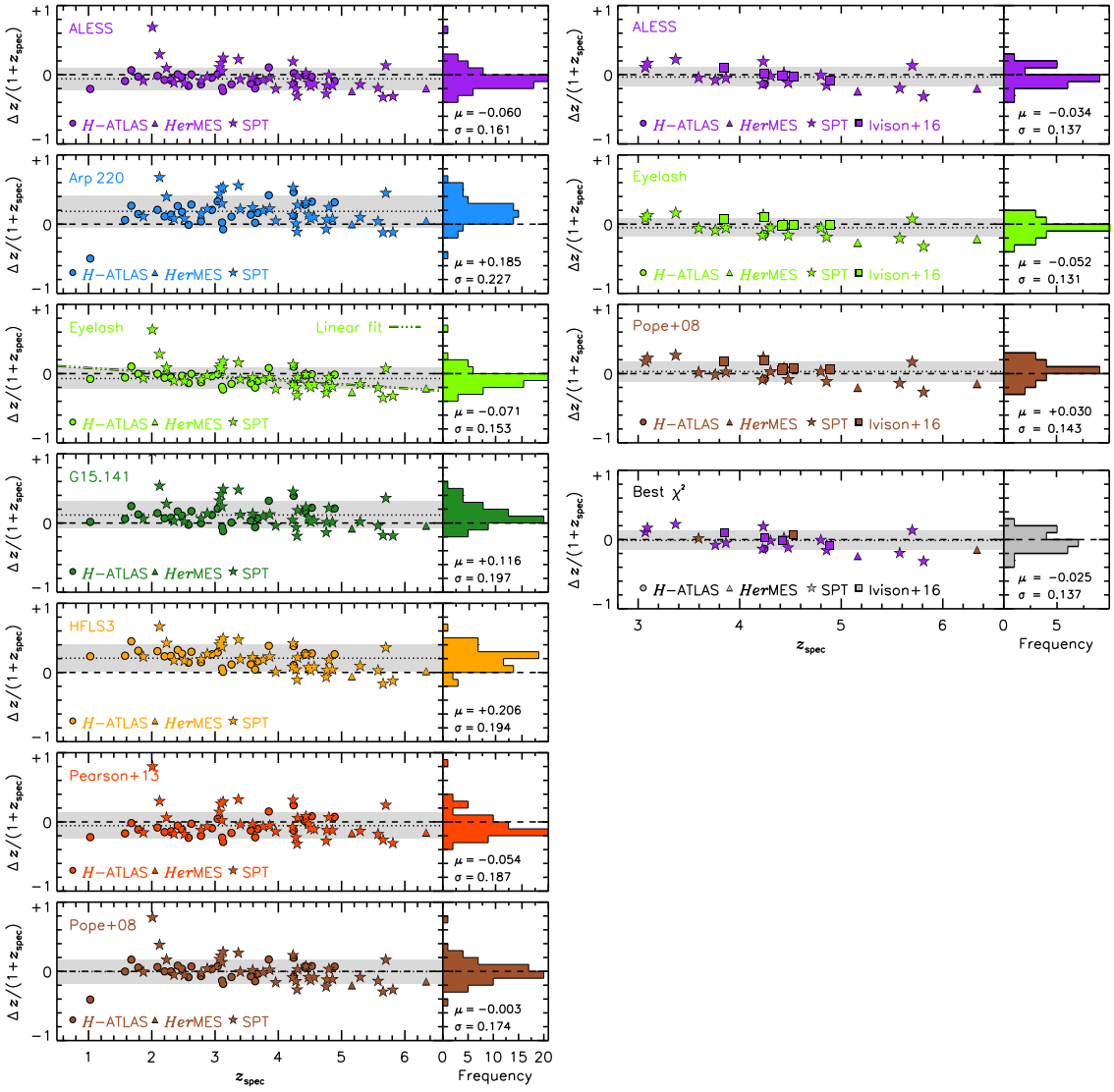

Figure 2.8: Left: normalised difference between photometric and spectroscopic redshift (see Equation 2.4) as a function of spectroscopic redshift for the seven template SEDs shown in Figure 2.7 using a training sample of 69 bright DSFGs. The photometric redshifts systematically under-/over-estimate the spectroscopic redshifts as the spectroscopic redshift increases/decreases. This linear trend – seen across all templates and indicated by the $\Delta z/(1+z_{\rm spec}) \propto -0.06\times z_{\rm spec}$ line in the Eyelash panel – is due to an increase in the dust temperature of the training DSFGs with redshift (see text). Correcting for this trend reduces the scatter from $\sigma_{\Delta z} \sim 0.15(1+z_{\rm spec})$ to $\sigma_{\Delta z} \sim 0.10(1+z_{\rm spec})$, a non-negligible effect. The black dotted line and shaded grey region show the mean and r.m.s. of $\Delta z/(1+z_{\rm spec})$, respectively, which I list in the bottom-right corner. **Right:** a sub-sample (25) of ultra-red galaxies using the three best templates that I decided to keep based on their statistics shown in the left-hand column. The squares indicate 6 ultra-red galaxies taken from this chapter that have spectroscopic redshifts (Fudamoto et al., 2017). I also show the template that yields the best χ^2 value – typically the ALESS template. The r.m.s. of $\Delta z/(1+z_{\rm spec})$ in the best χ^2 values, $\sigma_{\Delta z} \approx 0.14(1+z_{\rm spec})$, represents the minimum systematic uncertainty in photometric redshift using these three template SEDs. Clearly the predictive force is strong with this one.

Sanity Test of the Reliable Template SEDs on Ultra-Red Galaxies

I performed a final sanity test of the photometric redshifts derived using the three best template SEDs described above.

The right-hand column of Figure 2.8 shows the results of Equation 2.4 as a function of $z_{\rm spec}$ applied to a suitably chosen ultra-red training sample (25) of DSFGs (a sub-sample of 19 from the bright training sample and 6 from the ultra-red galaxies presented here — Fudamoto et al., 2017) using these template SEDs. The three template SEDs have excellent predictive capabilities, with $|\mu_{\Delta z}| \lesssim 0.05(1+z_{\rm spec})$ and $\sigma_{\Delta z} \sim 0.14(1+z_{\rm spec})$. However, the linear trend with spectroscopic redshift, which is discussed in more detail in the following section, is still present.

Furthermore, in the lower panel of the right-hand column of Figure 2.8, I show $\Delta z/(1+z_{\rm spec})$ versus $z_{\rm spec}$ for the template SED that yields the lowest χ^2 value for each ultra-red galaxy.

Key Point 2.4
Despite having a scatter, $\sigma_{\Delta z} \sim 0.14(1+z_{\rm spec})$, equal to that of the ALESS template SED (as this template SED is responsible for many of the photometric redshifts with the lowest χ^2 value) the accuracy amongst this panel is slightly improved, $|\mu_{\Delta z}| = 0.025(1+z_{\rm spec})$ – supporting the earlier decision to adopt the template SED with the lowest χ^2 value.

It is important to note that the scatter in $\Delta z/(1+z_{\rm spec})$ represents the minimum systematic uncertainty in determining photometric redshifts for the ultra-red galaxies presented here as this sub-sample of brighter DSFGs tend to be of a relatively higher quality, or equally, higher SNR.

In Figure 2.9, I show the best-fitting photometric redshift for an ultra-red galaxy (NGP−190387) within the sample presented here that has a secure spectroscopic redshift determined with ALMA and the NOrthern Extended Millimeter Array (NOEMA — Fudamoto et al., 2017).

The Effect of the Linear-Trend on Photometric Redshifts

As already mentioned, there appears to be a linear trend for the majority of the template SEDs such that at lower/higher spectroscopic redshifts the photometric redshifts over-/under-predict the true value (see Figure 2.8). This linear trend takes the form:

$$\frac{\Delta z}{1+z_{\rm spec}} = A + B z_{\rm spec}, \tag{2.5}$$

where A and B are arbitrary constants. I attribute this linear trend to changing dust temperatures, such that at a higher/lower spectroscopic redshift a typical $\sim 30\,{\rm K}$ template SED needs to be hotter/colder. How much hotter or colder depends on A, B, $z_{\rm spec}$ and

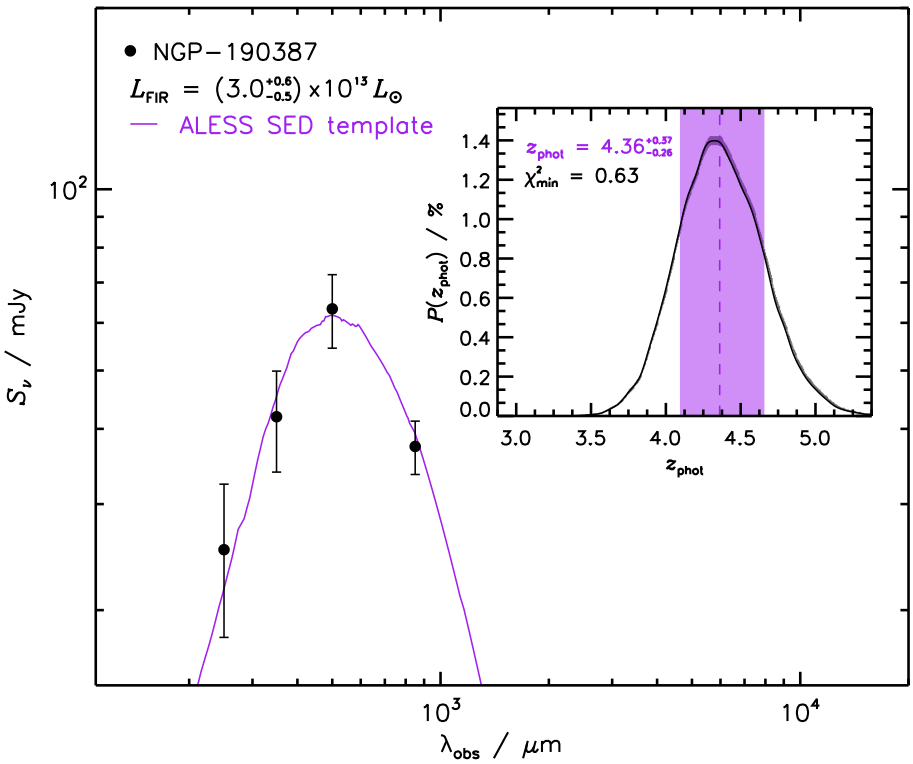

Figure 2.9: Main: SPIRE and SCUBA-2 photometry (black circles) for one of the ultra-red galaxies presented here with a spectroscopic redshift of $z_{\rm spec} = 4.42$ (Fudamoto et al., 2017). The best fit to the data (purple line) yields a photometric redshift of $z_{\rm phot} = 4.36^{+0.37}_{-0.26}$ using the ALESS template SED (Swinbank et al., 2014). **Inset:** photometric redshift probability distribution (black) used to derive the 1-σ errors on the best fit to the data (shaded purple region).

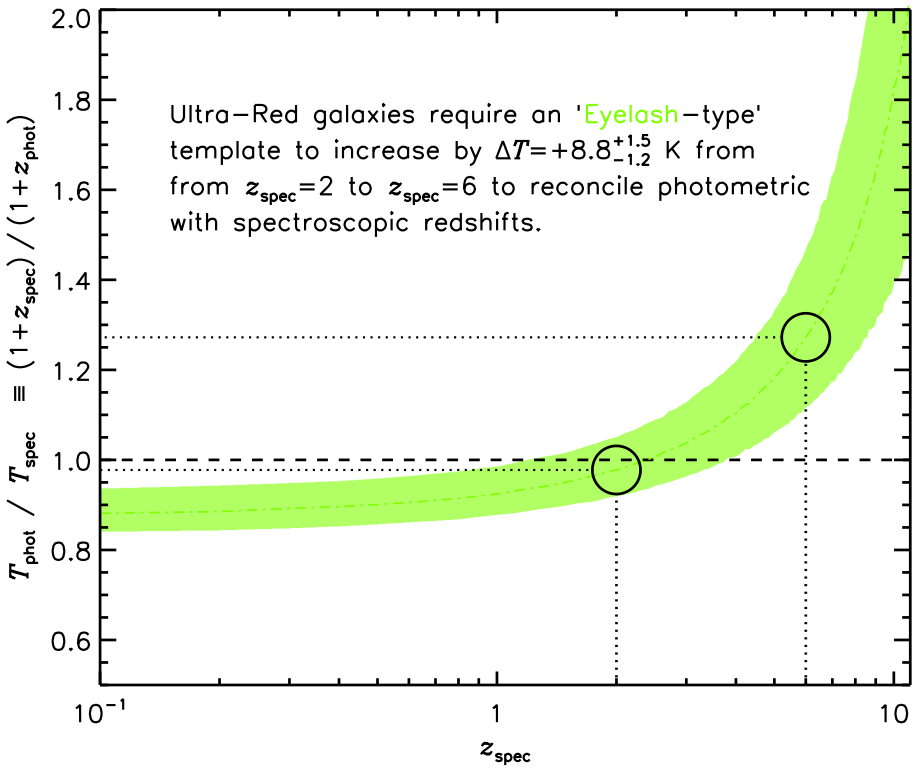

Figure 2.10: The ratio of photometric to spectroscopic template SED dust temperatures versus spectroscopic redshift, whose shape is inversely proportional to $z_{\rm spec}$ (see Equation 2.6). Over $z_{\rm spec} \approx$ 2–6, a 30-K template SED must in temperature by $\Delta T_{\rm dust} \approx 8\,$K in order for photometric redshifts to successfully image onto spectroscopic redshifts.

$T_{\rm dust}$. As the dust temperature ($T_{\rm dust}$) of a black body at redshift (z) is simply $T_{\rm dust}/(1+z)$, it follows that the ratio of two temperatures at two different redshifts, $z_{\rm phot}$ and $z_{\rm spec}$, is simply:

$$\frac{T_{\rm phot}}{T_{\rm spec}} \equiv \frac{1+z_{\rm spec}}{1+z_{\rm phot}} = \frac{1+z_{\rm spec}}{(1+z_{\rm spec})+(A+Bz_{\rm spec})(1+z_{\rm spec})} = \frac{1}{1+A+Bz_{\rm spec}}, \qquad (2.6)$$

where I have substituted $z_{\rm phot} = z_{\rm spec} + (A + Bz_{\rm spec})(1 + z_{\rm spec})$ using Equation 2.5.

The above expression yields the dust temperature scaling necessary for a template in order to map a photometric redshift onto its respective spectroscopic redshift. I show the form of Equation 2.6 in Figure 2.10.

Key Point 2.5
This figure illustrates that at $z_{\rm spec} \approx 2$, $T_{\rm phot}/T_{\rm spec} \approx 1$ and thus $\Delta z \approx 0$. However, by $z_{\rm spec} \approx 6$, $T_{\rm phot}/T_{\rm spec} \approx 1.3$ and therefore the dust temperature of the template SED must rise by $\approx 1.3\times$, or equally $\Delta T_{\rm dust} \approx 8\,$K.

I list the best-fitting parameters to Equation 2.5 (with their correlation coefficients) and the expected temperature change (assuming a 30 K dust temperature) in Table 2.3.

This link between dust temperature and redshift could very well be related to that

Table 2.3: Best-fitting linear parameters to Equation 2.5.

Template SED	A	B	$r^{\dagger}$	$\Delta T^{\ddagger}$ K
ALESS	$0.098^{+0.070}_{-0.080}$	$-0.045^{+0.018}_{-0.018}$	$-0.331^{+0.123}_{-0.098}$	$6.6^{+1.4}_{-1.0}$
Eyelash	$0.140^{+0.057}_{-0.067}$	$-0.059^{+0.016}_{-0.014}$	$-0.459^{+0.087}_{-0.078}$	$8.8^{+1.5}_{-1.2}$
Pope et al.	$0.167^{+0.095}_{-0.088}$	$-0.048^{+0.022}_{-0.024}$	$-0.328^{+0.164}_{-0.116}$	$5.9^{+1.5}_{-1.0}$

†Pearson correlation coefficient.
‡Change in dust temperature assumes an initial temperature of 30 K.

between temperature and FIR luminosity witnessed by Symeonidis et al. (2013), namely a 10 K rise from $\sim$ 10^{10}–$10^{12} L_{\odot}$. However, disentangling the complex relationship between dust temperature, dust mass and FIR luminosity would be remarkably challenging. Interestingly, the redshift-temperature trend is opposite to that reported in Symeonidis et al. (2013) – namely a 10 K rise from high to low redshift – which may be related to a higher fraction of gravitationally lensed, and therefore intrinsically less luminous, DSFGs that comprise the training sample.

Finally, this evolution in temperature with redshift will bias the photometric redshifts to lower values, and thus lower the space density of ultra-red galaxies at $z > 4$.

The Effect of the CMB on Photometric Redshifts

The increase in the temperature of the CMB with redshift is given by:

$$T_{\rm CMB}\left(z\right) = T_{\rm CMB}^{z=0}\left(1+z\right), \tag{2.7}$$

where $T_{\rm CMB}^{z=0} = 2.73$ K is the present-day temperature of the CMB. As a result of this increase, the thermodynamic interaction between the cold ($\sim$ 30 K) dust component of DSFGs and the surrounding CMB must be taken into account at high redshift (da Cunha et al., 2013; Zhang et al., 2016). The resulting equilibrium dust temperature as a function of redshift is given by:

$$T_{\rm dust}\left(z\right) = \left(\left(T_{\rm dust}^{z=0}\right)^{4+\beta} + \left(T_{\rm CMB}^{z=0}\right)^{4+\beta}\left[\left(1+z\right)^{4+\beta} - 1\right]\right)^{\frac{1}{4+\beta}}, \tag{2.8}$$

where $T_{\rm dust}^{z=0}$ is the dust temperature of the DSFG at $z = 0$ and $\beta = 2$ is the dust emissivity.

To quantify this CMB effect, the Cosmic Eyelash template SED (represented as a modified greybody with hot and cold dust components of 60 K and 30 K, respectively — Ivison et al., 2010b) was 'CMB-modified' from $z = 4$–10 using Equation 2.8. Flux densities at 250-, 350-, 500- and 870-μm were then drawn from these CMB-modified SEDs and the photometric redshift algorithm was rerun using the unmodified Cosmic Eyelash template SED.

Key Point 2.6
The effects on $(1 + z)$ were slight, namely that the CMB causes the algorithm to

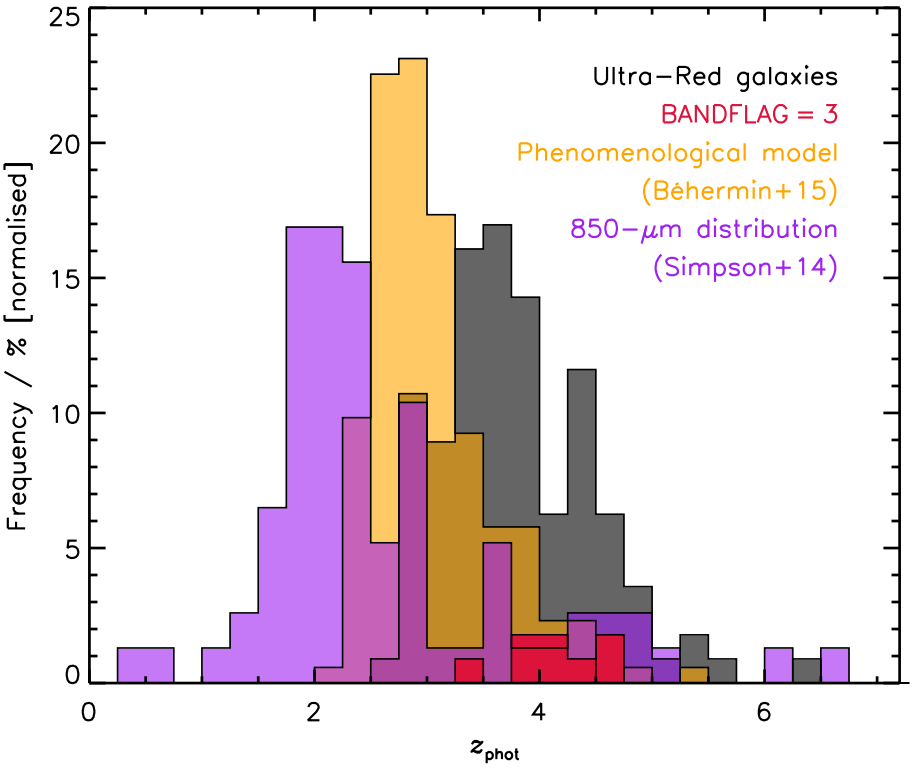

Figure 2.11: Photometric redshift distribution of the ultra-red galaxies (black) and the BANDFLAG = 3 subset (red). Although only a small sample, the redshift distribution of DSFGs selected at 500 μm appears to be shifted by $\Delta z \approx +0.25$–0.5 compared to the entire sample. In purple, I show the 870-μm-selected photometric redshift distribution from Simpson et al. (2014), which is significantly offset ($\Delta z \approx -1.5$) from that of the ultra-red galaxies. Finally, the redshift distribution from Béthermin et al. (2015) (orange), representing a phenomenological model of galaxy evolution (Béthermin et al., 2012) chosen to match the ultra-red galaxy criteria in Equation 2.1, shows a larger offset from the observations presented here.

underestimate this parameter by 0.03, 0.05, 0.10 and 0.18 at $z = 4$, 6, 8 and 10, respectively.

Thus, this effect will also bias the photometric redshifts to lower values, which in-turn will further bias the estimate of the $z > 4$ space density presented in Section 2.4.3 to lower values. However, this effect will be less than the redshift-temperature trend explained above.

Summary of z_{phot} and L_{FIR} Statistics

The photometric redshifts and FIR luminosities for the ultra-red galaxies are listed in Table 2.4. I computed the FIR luminosities using the following equation:

$$L_{\rm FIR} = 4\pi D_L^2 \int {\rm d}\nu' \left(\frac{a_z S'}{1+z} \right), \tag{2.9}$$

where D_L is the luminosity distance, the integral limits are across $\lambda = 8$–$1{,}000\,\mu$m (e.g. Kennicutt, 1998) and $a_z S'/(1+z)$ is the normalised template SED flux density at the redshift z of an ultra-red galaxy.

I show the photometric redshift distribution of the ultra-red galaxies in Figure 2.11. These ultra-red galaxies span $2.7 < z_{\rm phot} < 6.4$, with a median value of 3.66, a mean value of 3.79 and an IQR of 3.30–4.27. I find that $33 \pm 6\%$ (1-σ errors — Gehrels, 1986) and $63^{+20}_{-24}\%$ of the BANDFLAG = 3 subset are above $z_{\rm phot} > 4$. These findings support the relationship between the peak of observed SED and redshift, such that SEDs peaking at longer wavelengths select DSFGs at higher redshifts (Swinbank et al., 2014).

Figure 2.11 also shows the redshift distribution from Simpson et al. (2014) and Béthermin et al. (2015). The former portrays that of 870-μm-selected DSFGs, which are significantly offset ($\Delta z \approx -1.5$) from the ultra-red galaxies – illustrating the effectiveness of this method to locate distant DSFGs. The latter – also showing a relatively large offset ($\Delta z \approx -1$) – represents a phenomenological model of galaxy evolution (Béthermin et al., 2012), chosen to match the ultra-red criteria given in Equation 2.1. Such a significant mismatch between theory and observation suggests that our current understanding of galaxy evolution involving distant DSFGs is incomplete.

The median and IQR of the 8–1,000-μm luminosities evaluated using Equation 2.9 are $1.3 \times 10^{13}\,L_\odot$ and 9.7×10^{12}–$2.0 \times 10^{13}\,L_\odot$, respectively. I show these values in Figure 2.12 for the ultra-red galaxy sample, separated by BANDFLAG. Ultra-Red galaxies occupy three distinct regions governed by their BANDFLAG. This reflects the fact that at any given redshift, BANDFLAG = 1 sources are – by definition – the most luminous ultra-red galaxies within the sample as they are detected in all three SPIRE passbands. The ultra-red galaxies that fall below the $S_{500} > 30$-mJy detection limit for the three template SEDs reflects the redshift-temperature trend discussed at length in Section 2.4.2

Although, I have not made any correction for lensing in this work, this effect cannot be entirely ignored as at $z \sim 4$ it becomes more common ($\approx$ 10–30%) for $S_{500} > 30$-mJy DSFGs (Fudamoto et al., 2017). The effects from lensing will bias the luminosities higher, but have very little impact on the $z > 4$ space density calculation in the following section.

2.4.3 The Co-Moving Space Density of Ultra-Red Galaxies

I now set a lower limit on the co-moving space density of $S_{500} > 30$-mJy ultra-red galaxies, whose photometric redshift estimates are consistent with lying at $z > 4$, using the following equation:

$$\rho = \left(\frac{N/\mathcal{C}}{V_{\rm survey}}\right)\left(\frac{t_{\rm survey}}{t_{\rm burst}}\right), \tag{2.10}$$

where $N/\mathcal{C}$ represents the completeness-corrected number of sources within $4 < z < 6$ and $t_{\rm survey}/t_{\rm burst}$ is a duty-cycle correction to account for the finite duration of ongoing, obscured star formation in DSFGs, $t_{\rm burst} \approx 100\,$Myr – a time-scale that is in agreement, but uncertain at the $\approx 2\times$ level, with the expected gas depletion times (Swinbank et al.,

Table 2.4: Photometric redshift properties of ultra-red galaxies.

Nickname	$z_{\rm phot}$	$\log_{10}(L_{\rm FIR})$	Nickname	$z_{\rm phot}$	$\log_{10}(L_{\rm FIR})$
G09−47693	$3.12^{+0.39}_{-0.33}$	$13.01^{+0.14}_{-0.07}$	NGP−136610	$4.27^{+0.51}_{-0.51}$	$13.40^{+0.09}_{-0.12}$
G09−51190	$3.83^{+0.58}_{-0.48}$	$13.31^{+0.11}_{-0.12}$	NGP−158576	$3.15^{+0.36}_{-0.29}$	$13.00^{+0.12}_{-0.07}$
G09−59393	$3.70^{+0.35}_{-0.26}$	$13.28^{+0.05}_{-0.09}$	NGP−168885	$4.09^{+0.42}_{-0.30}$	$13.32^{+0.06}_{-0.08}$
G09−62610	$3.70^{+0.44}_{-0.26}$	$13.15^{+0.13}_{-0.06}$	NGP−172391	$3.27^{+0.34}_{-0.26}$	$13.08^{+0.09}_{-0.06}$
G09−64889	$3.48^{+0.48}_{-0.40}$	$13.10^{+0.09}_{-0.14}$	NGP−185990	$4.47^{+0.49}_{-0.37}$	$13.42^{+0.06}_{-0.06}$
G09−79552	$3.59^{+0.34}_{-0.26}$	$13.11^{+0.09}_{-0.06}$	NGP−190387	$4.36^{+0.37}_{-0.26}$	$13.49^{+0.05}_{-0.06}$
G09−79553	$3.66^{+0.39}_{-0.30}$	$13.08^{+0.11}_{-0.07}$	NGP−206987	$4.07^{+0.06}_{-0.60}$	$13.31^{+0.02}_{-0.13}$
G09−80620	$4.01^{+0.22}_{-0.78}$	$13.07^{+0.06}_{-0.19}$	NGP−239358	$3.47^{+0.52}_{-0.49}$	$13.09^{+0.10}_{-0.15}$
G09−80658	$4.07^{+0.09}_{-0.72}$	$13.20^{+0.03}_{-0.17}$	NGP−242820	$3.41^{+0.44}_{-0.30}$	$13.02^{+0.13}_{-0.06}$
G09−81106	$4.95^{+0.13}_{-0.73}$	$13.43^{+0.04}_{-0.13}$	NGP−244709	$3.48^{+0.42}_{-0.40}$	$13.14^{+0.07}_{-0.12}$
G09−81271	$4.62^{+0.46}_{-0.38}$	$13.39^{+0.05}_{-0.09}$	NGP−246114	$4.35^{+0.51}_{-0.46}$	$13.30^{+0.08}_{-0.10}$
G09−83017	$3.99^{+0.53}_{-0.34}$	$13.09^{+0.12}_{-0.08}$	NGP−247012	$4.59^{+0.16}_{-0.71}$	$13.21^{+0.04}_{-0.16}$
G09−83808	$5.66^{+0.06}_{-0.76}$	$13.51^{+0.02}_{-0.11}$	NGP−247691	$3.90^{+0.51}_{-0.45}$	$13.15^{+0.08}_{-0.13}$
G09−84477	$2.94^{+0.44}_{-0.39}$	$12.83^{+0.15}_{-0.09}$	NGP−248307	$3.59^{+0.36}_{-0.36}$	$12.96^{+0.10}_{-0.10}$
G09−87123	$4.28^{+0.52}_{-0.34}$	$13.17^{+0.12}_{-0.06}$	NGP−252305	$4.34^{+0.43}_{-0.38}$	$13.29^{+0.06}_{-0.09}$
G09−100369	$3.79^{+0.61}_{-0.46}$	$13.05^{+0.09}_{-0.13}$	NGP−255731	$4.94^{+0.73}_{-0.66}$	$13.30^{+0.09}_{-0.15}$
G09−101355	$4.20^{+0.70}_{-0.39}$	$13.03^{+0.16}_{-0.08}$	NGP−260332	$3.50^{+0.38}_{-0.29}$	$12.96^{+0.10}_{-0.08}$
G12−34009	$4.53^{+0.37}_{-0.31}$	$13.51^{+0.05}_{-0.06}$	NGP−284357	$4.99^{+0.44}_{-0.45}$	$13.40^{+0.05}_{-0.10}$
G12−42911	$4.33^{+0.31}_{-0.26}$	$13.45^{+0.05}_{-0.07}$	NGP−287896	$4.54^{+0.53}_{-0.37}$	$13.15^{+0.10}_{-0.09}$
G12−66356	$3.66^{+0.19}_{-0.72}$	$13.04^{+0.06}_{-0.19}$	NGP−297140	$3.41^{+0.57}_{-0.44}$	$12.91^{+0.15}_{-0.11}$
G12−77450	$3.53^{+0.46}_{-0.31}$	$12.99^{+0.14}_{-0.07}$	NGP−315918	$4.32^{+0.54}_{-0.33}$	$13.10^{+0.11}_{-0.07}$
G12−78339	$4.41^{+0.98}_{-0.70}$	$13.31^{+0.17}_{-0.18}$	NGP−315920	$3.88^{+0.33}_{-0.89}$	$13.05^{+0.07}_{-0.21}$
G12−78868	$3.58^{+0.34}_{-0.26}$	$13.04^{+0.08}_{-0.08}$	NGP−316031	$4.65^{+0.68}_{-0.47}$	$13.10^{+0.13}_{-0.07}$
G12−79192	$2.95^{+0.38}_{-0.36}$	$12.80^{+0.12}_{-0.12}$	SGP−28124	$3.93^{+0.08}_{-0.45}$	$13.65^{+0.02}_{-0.09}$
G12−79248	$6.43^{+0.81}_{-0.89}$	$13.76^{+0.11}_{-0.14}$	SGP−28124‡	$3.80^{+0.02}_{-0.42}$	$13.61^{+0.00}_{-0.11}$
G12−80302	$3.06^{+0.39}_{-0.35}$	$12.83^{+0.12}_{-0.10}$	SGP−72464	$3.06^{+0.21}_{-0.19}$	$13.23^{+0.07}_{-0.05}$
G12−81658	$2.93^{+0.38}_{-0.42}$	$12.77^{+0.12}_{-0.14}$	SGP−93302	$3.91^{+0.27}_{-0.22}$	$13.46^{+0.04}_{-0.07}$
G12−85249	$2.87^{+0.37}_{-0.36}$	$12.70^{+0.11}_{-0.12}$	SGP−93302‡	$3.79^{+0.24}_{-0.21}$	$13.43^{+0.04}_{-0.07}$
G12−87169	$3.26^{+0.51}_{-0.39}$	$12.85^{+0.13}_{-0.12}$	SGP−135338	$3.06^{+0.33}_{-0.26}$	$13.08^{+0.11}_{-0.04}$
G12−87695	$3.68^{+0.58}_{-0.53}$	$13.09^{+0.09}_{-0.14}$	SGP−156751	$2.93^{+0.24}_{-0.22}$	$12.97^{+0.08}_{-0.04}$
G15−21998	$2.91^{+0.20}_{-0.19}$	$13.10^{+0.06}_{-0.05}$	SGP−196076	$4.51^{+0.47}_{-0.39}$	$13.42^{+0.07}_{-0.06}$
G15−24822	$2.77^{+0.27}_{-0.27}$	$12.97^{+0.09}_{-0.08}$	SGP−208073	$3.48^{+0.40}_{-0.28}$	$13.18^{+0.06}_{-0.08}$
G15−26675	$4.36^{+0.25}_{-0.21}$	$13.55^{+0.04}_{-0.05}$	SGP−213813	$3.49^{+0.40}_{-0.32}$	$13.15^{+0.07}_{-0.10}$
G15−47828	$3.52^{+0.50}_{-0.39}$	$13.20^{+0.09}_{-0.11}$	SGP−219197	$2.94^{+0.25}_{-0.24}$	$13.03^{+0.08}_{-0.07}$
G15−64467	$3.75^{+0.55}_{-0.49}$	$13.15^{+0.09}_{-0.14}$	SGP−240731	$2.70^{+0.27}_{-0.25}$	$12.88^{+0.10}_{-0.09}$
G15−66874	$4.07^{+0.57}_{-0.49}$	$13.30^{+0.10}_{-0.11}$	SGP−261206	$5.03^{+0.58}_{-0.47}$	$13.64^{+0.09}_{-0.10}$
G15−82412	$3.96^{+0.15}_{-0.70}$	$13.20^{+0.04}_{-0.16}$	SGP−304822	$4.33^{+0.63}_{-0.51}$	$13.41^{+0.12}_{-0.12}$
G15−82684	$3.65^{+0.38}_{-0.25}$	$13.13^{+0.11}_{-0.06}$	SGP−310026	$3.12^{+0.38}_{-0.31}$	$12.97^{+0.12}_{-0.07}$
G15−83543	$3.53^{+0.42}_{-0.34}$	$13.05^{+0.12}_{-0.09}$	SGP−312316	$3.17^{+0.41}_{-0.32}$	$12.94^{+0.12}_{-0.08}$
G15−83702	$3.27^{+0.39}_{-0.36}$	$12.90^{+0.12}_{-0.12}$	SGP−317726	$3.69^{+0.39}_{-0.30}$	$13.20^{+0.06}_{-0.10}$
G15−84546	$4.34^{+0.56}_{-0.53}$	$13.19^{+0.10}_{-0.14}$	SGP−354388	$5.35^{+0.56}_{-0.52}$	$13.68^{+0.08}_{-0.08}$
G15−85113	$3.40^{+0.37}_{-0.34}$	$12.90^{+0.09}_{-0.11}$	SGP−354388‡	$5.43^{+0.84}_{-0.72}$	$13.69^{+0.12}_{-0.13}$
G15−85592	$3.39^{+0.49}_{-0.39}$	$12.89^{+0.15}_{-0.13}$	SGP−32338	$3.93^{+0.26}_{-0.24}$	$13.24^{+0.03}_{-0.04}$
G15−86652	$3.43^{+0.44}_{-0.35}$	$12.97^{+0.11}_{-0.09}$	SGP−380990	$2.84^{+0.22}_{-0.21}$	$12.84^{+0.06}_{-0.07}$
G15−93387	$3.24^{+0.50}_{-0.33}$	$12.87^{+0.12}_{-0.08}$	SGP−381615	$2.98^{+0.29}_{-0.29}$	$12.91^{+0.09}_{-0.09}$
G15−99748	$3.98^{+0.25}_{-0.79}$	$13.06^{+0.05}_{-0.20}$	SGP−381637	$3.30^{+0.28}_{-0.25}$	$13.06^{+0.08}_{-0.07}$
G15−105504	$3.43^{+0.64}_{-0.53}$	$12.87^{+0.16}_{-0.13}$	SGP−382394	$2.96^{+0.29}_{-0.26}$	$12.84^{+0.08}_{-0.08}$
NGP−63663	$3.08^{+0.23}_{-0.22}$	$13.11^{+0.08}_{-0.06}$	SGP−383428	$3.08^{+0.33}_{-0.30}$	$12.88^{+0.10}_{-0.09}$
NGP−82853	$3.66^{+0.06}_{-0.61}$	$13.17^{+0.02}_{-0.15}$	SGP−385891	$3.70^{+0.29}_{-0.24}$	$13.20^{+0.07}_{-0.06}$
NGP−101333	$3.53^{+0.34}_{-0.27}$	$13.30^{+0.06}_{-0.09}$	SGP−386447	$4.89^{+0.78}_{-0.73}$	$13.41^{+0.13}_{-0.17}$
NGP−101432	$3.65^{+0.36}_{-0.28}$	$13.31^{+0.05}_{-0.10}$	SGP−392029	$3.42^{+0.47}_{-0.32}$	$13.00^{+0.13}_{-0.06}$
NGP−111912	$3.27^{+0.36}_{-0.26}$	$13.09^{+0.10}_{-0.06}$	SGP−424346	$3.99^{+0.45}_{-0.39}$	$12.95^{+0.10}_{-0.10}$
NGP−113609	$3.43^{+0.34}_{-0.20}$	$13.22^{+0.09}_{-0.04}$	SGP−433089	$3.60^{+0.08}_{-0.62}$	$13.11^{+0.01}_{-0.13}$
NGP−126191	$4.33^{+0.45}_{-0.46}$	$13.37^{+0.07}_{-0.08}$	SGP−499646	$4.68^{+0.49}_{-0.34}$	$13.14^{+0.10}_{-0.05}$
NGP−134174	$2.98^{+0.34}_{-0.31}$	$12.98^{+0.12}_{-0.07}$	SGP−499698	$4.22^{+0.39}_{-0.38}$	$13.00^{+0.09}_{-0.11}$
NGP−136156	$3.95^{+0.06}_{-0.57}$	$13.33^{+0.01}_{-0.12}$	SGP−499828	$3.88^{+0.49}_{-0.41}$	$12.88^{+0.10}_{-0.09}$

‡Ultra-Red galaxies observed with both LABOCA and SCUBA-2 (previous row).

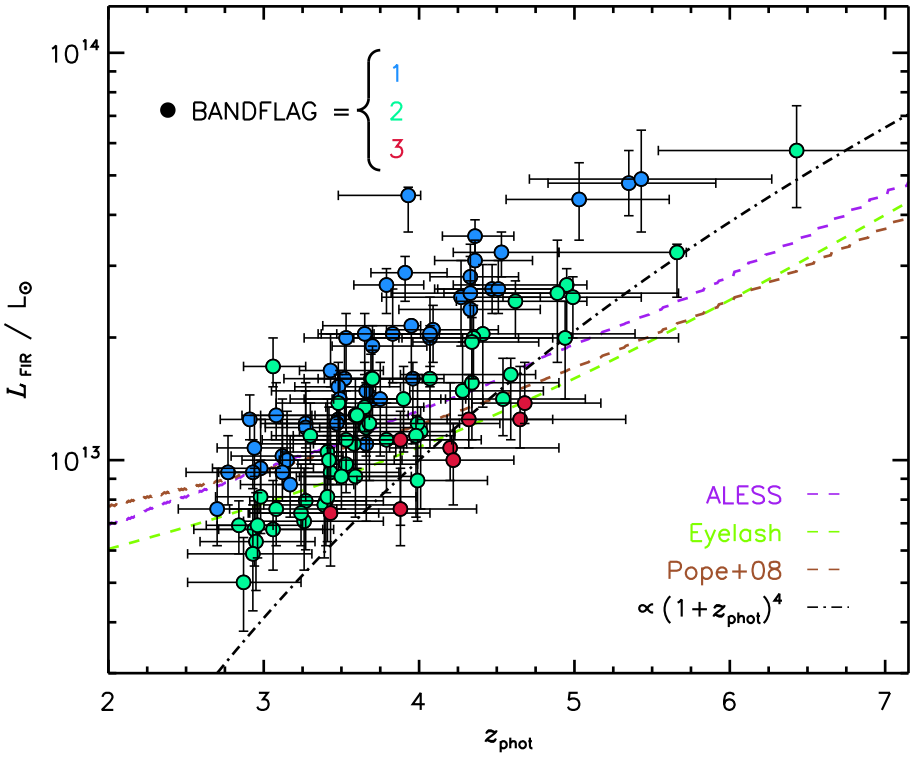

Figure 2.12: Rest-frame FIR luminosity of ultra-red galaxies as a function of redshift. I colour-code galaxies by their BANDFLAG, as per Figure 2.3, which clearly shows that each separate BANDFLAG occupies its own distinct region at any given redshift. Ultra-Red galaxies that are detected in all three SPIRE passbands are intrinsically more luminous compared to those detected only in 500-μm. These are thus the most luminous galaxies typically seen at any given redshift. I show the $S_{500} > 30$-mJy detection limit for the three best template SEDs and a luminosity evolution proportional to $(1+z)^4$.

2006; Ivison et al., 2011; Hickox et al., 2012; Bothwell et al., 2013), but could equally be as high as $t_{\rm burst} = 0.5$–$1\,{\rm Gyr}$ (Lapi et al., 2014; Aversa et al., 2015). Note, that under the redshift interval of interest ($4 < z < 6$), $t_{\rm survey} \approx 600\,{\rm Myr}$.

Finally, the co-moving volume ($V_{\rm survey}$) contained within the redshift range considered is given by:

$$V_{\rm survey} = \frac{4\pi}{3}\left[D_c(z)^3\right]_{z=4}^{z=6}\left(\frac{\mathcal{A}_{\rm survey}}{\mathcal{A}_{\rm sky}}\right), \tag{2.11}$$

where $\mathcal{A}_{\rm survey}/\mathcal{A}_{\rm sky}$ accounts for the fractional area of sky that was surveyed ($\approx 600\,{\rm deg}^2/41{,}000\,{\rm deg}^2$, or $\approx 1.5\%$) and the line-of-sight co-moving distance ($D_c(z)$, i.e. the proper distance multiplied by $(1+z)$ — Hogg, 1999), which is given in terms of the Hubble distance (D_H) and 'Peebles (1993) function' ($E(z)$) by:

$$D_c(z) \equiv D_H \int_0^z {\rm d}z' \frac{1}{E(z')} = c/H_0 \int_0^z {\rm d}z' \frac{1}{\sqrt{\Omega_M(1+z')^3 + \Omega_k(1+z')^2 + \Omega_\Lambda}}. \tag{2.12}$$

Note that the co-moving distance is also related to the luminosity distance by $D_L(z) = (1+z)D_c(z)$.

Key Point 2.7
Bringing this all together, in Section 2.2.4 I showed that the completeness of the candidate ultra-red galaxy sample was $\mathcal{C} \sim 2 \pm 1\%$ and in Section 2.4.2 I showed that $33 \pm 6\%$ the 109 followed-up galaxies lie in the redshift range $4 < z < 6$, which results in the first direct measurement of the $z > 4$ space density of

$$\rho \approx 6 \times 10^{-7}\,{\rm Mpc}^{-3}.$$

As this is the first direct measurement of the $z > 4$ space density, meaningful comparison with the literature is limited. Recently, Asboth et al. (2016) have presented a sample of 477, 500-μm-selected DSFGs identified within the $274\,{\rm deg}^2$ of the *Herschel* Multi-tiered Extragalactic Survey (*Her*MES) Large Mode Survey (HeLMS). Although $\approx 15\%$ of these DSFGs match the ultra-red criteria, they are considerably brighter ($\Delta S_{500} = +20\,{\rm mJy}$) and lack photometric redshift estimates. However, assuming that they follow a similar redshift distribution to the ultra-red galaxies presented here, I derived a 'back-of-the-envelope' calculation that suggests that they have a comparable $z > 4$ space density of $\rho \approx 10^{-7}\,{\rm Mpc}^{-3}$.

2.4.4 Relationship to Other Populations

Given the $4 < z < 6$ space density of ultra-red galaxies derived in the previous section, $\approx 6 \times 10^{-7}\,{\rm Mpc}^{-3}$, I checked the possibility that these galaxies are the high-redshift progenitors of the most massive ($\sim 10^{11}\,M_\odot$) quiescent galaxies at $z \gtrsim 2$, which has been suggested across the literature (Newman et al., 2012; Simpson et al., 2014; Toft et al., 2014; Ikarashi et al., 2015). Given the typical redshift and stellar population of these

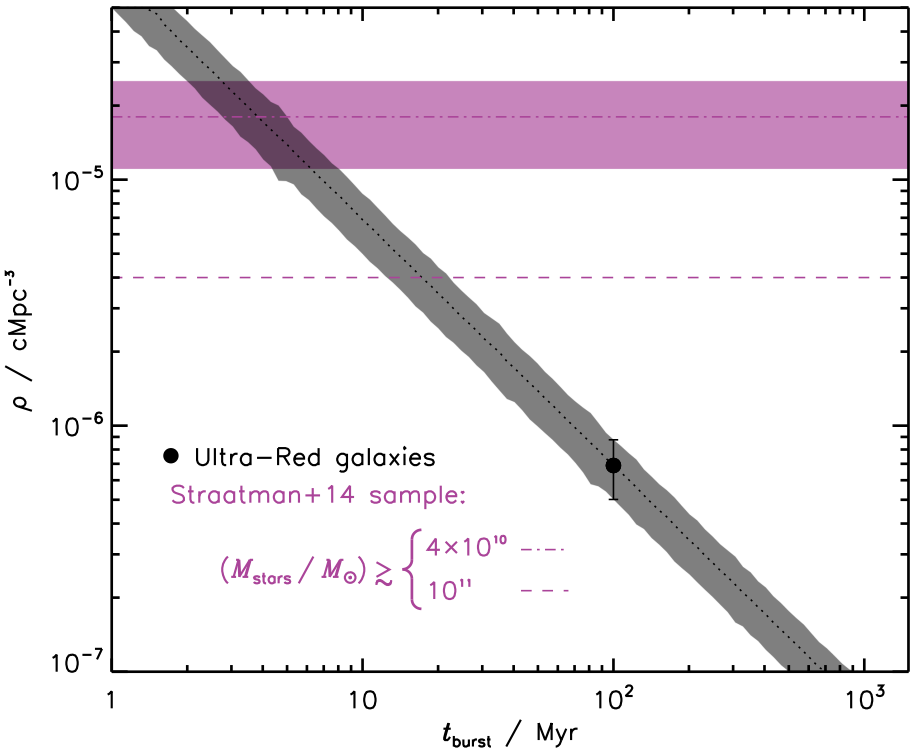

Figure 2.13: The variation in the $z > 4$ space density when a different duty-cycle correction is assumed for Equation 2.10 (black dotted line). The 1-σ errors in the space density are derived from the scatter of Monte Carlo realisations of the ultra-red-galaxy completeness and photometric redshifts. The space densities determined by Straatman et al. (2014) for $M_{\rm stars} > 4 \times 10^{10}$-$M_{\odot}$ and $M_{\rm stars} \gtrsim 10^{11}$-$M_{\odot}$ galaxies are shown as dotted-dashed and dashed purple lines, respectively. Clearly reducing the time-scale for star formation brings the two populations into agreement. **Note**. No error is provided for the $M_{\rm stars} \gtrsim 10^{11}$-$M_{\odot}$ galaxy sample. However, as it is based a only a handful of sources it is likely to be large.

NIR-selected galaxies, it would appear that they formed the bulk of their stars in an intense burst of star formation possibly hidden behind a cloud of dust.

To make this comparison, I utilised the work presented by Straatman et al. (2014). This mass-limited sample ($M_{\rm stars} > 4 \times 10^{10}\,M_{\odot}$) lies between $3.4 < z < 4.2$ and is comprised of stellar populations with typical ages of ≈ 0.8 Gyr. The stellar ages suggest that they likely formed between $5.0 < z < 6.5$, which makes Straatman et al. a suitable sample with which to compare against.

However, the Straatman et al. (2014) sample is a factor of $\approx 30\times$ more numerous than that presented here, with a reported space density of $\rho \approx 2 \times 10^{-5}\,{\rm Mpc}^{-3}$. This suggests that $z > 4$ ultra-red galaxies cannot fully account for the population of NIR-selected, quiescent galaxies at $z = 3$–4, at least at the $S_{500} > 30$-mJy thresholds probed here. Increasing the mass limit of the Straatman et al. (2014) sample to $M_{\rm stars} \gtrsim 10^{11}\,M_{\odot}$ only yields a space density of $\rho \approx 4 \times 10^{-6}\,{\rm Mpc}^{-3}$, which is still a factor of $\approx 7\times$ more numerous than here, albeit the measurement is highly uncertain. Altering the duration of star formation in Equation 2.10 to an infeasibly short time of $t_{\rm burst} \lesssim 10$ Myr brings the Straatman et al. (2014) space density to within a factor of $\approx 1.5\times$ of that for ultra-red

galaxies (see Figure 2.13) – suggesting that these ultra-red galaxies are enduring a very rapid ($\ll 100\,\mathrm{Myr}$) phase of extreme star formation.

Key Point 2.8
Thus, it would appear that this sample of ultra-red galaxies is just within the grasp of evolving into either the most massive ($M_{\mathrm{stars}} \gtrsim 10^{11}\,M_{\odot}$) galaxies and/or an even more massive/rarer sub-sample, modulo chance gravitational lensing.

2.5 Conclusion

In this chapter, I have presented work from Ivison et al. (2016) that analyses a sample of 109 so-called 'ultra-red galaxies' – as they are selected via their red *Herschel*-SPIRE flux-density ratios – within the *H*-ATLAS imaging survey.

Using ground-based 'snapshots' taken with SCUBA-2/LABOCA, I have constrained the photometric redshift estimates of these ultra-red galaxies. Thus, they appear to have a median redshift of $z_{\mathrm{phot}} = 3.66$, an IQR of $z_{\mathrm{phot}} = 3.30$–4.27 and $33 \pm 6\%$ of them lie above $z_{\mathrm{phot}} > 4$. Therefore, the ultra-red galaxy criteria presented in this chapter effectively samples distant DSFGs, especially compared to the general 870-μm-selected population. A comparison with a phenomenological model of galaxy evolution designed to mimic this selection technique has revealed a significant mismatch, with the model under-predicting the redshift distribution derived from these observations by $\Delta z \approx -1$.

In order to compare ultra-red galaxies to other existing galaxy populations, I determined the first direct measurement of the $z > 4$ space density, namely $\rho \approx 6 \times 10^{-7}\,\mathrm{Mpc}^{-3}$. Comparisons with NIR-selected galaxies at $z = 3$–4 with stellar masses of $M_{\mathrm{stars}} \gtrsim 10^{10}\,M_{\odot}$ suggests that the $z > 4$ space density of ultra-red galaxies is $\approx 30\times$ too low to achieve reconciliation. Therefore, it seems unlikely that ultra-red galaxies are the progenitors of the general NIR population at $z = 3$–4, at least ultra-red galaxies that have been selected above $S_{500} > 30$-mJy (like those presented here).

However, it appears that the most massive ($M_{\mathrm{stars}} > 10^{11}\,M_{\odot}$) NIR galaxies are only a factor of $\approx 7\times$ more numerous than ultra-red galaxies. Such massive galaxies play a very dominant role in the evolution and formation of large structure, i.e. galaxy clusters. Thus, in the next chapter I will explore whether ultra-red galaxies exhibit evidence of clustering consistent with their eventual membership of galaxy clusters.

Finally, in Appendix A I present SPIRE and SCUBA-2/LABOCA cut-outs of the 109 ultra-red galaxies presented here.

Ultra-Red Galaxies Signpost Candidate Proto-Clusters at High Redshift

3

The secret is comprised in three words
– Work. Finish. Publish.

M. Faraday (1791–1867)

Declaration: the work presented in Chapter 3 is to be published in Lewis et al. (2017) as 'Ultra-Red Galaxies Signpost Candidate Proto-Clusters at High Redshift' by A. J. R. Lewis (myself), R. J. Ivison (my supervisor), P. N. Best, J. M. Simpson, A. Weiss, I. Oteo, Z-Y. Zhang, V. Arumugam, M. Bremer, S. C. Chapman, D. L. Clements, H. Dannerbauer, L. Dunne, S. Eales, S. Maddox, S. J. Oliver, A. Omont, D. A. Riechers, S. Serjeant, E. Valiante, J. Wardlow, P. van der Werf and G. De Zotti. This study was conceived by all of the authors. I carried out the data reductions, analysis, discussion and conclusion.

3.1 Introduction

In the previous chapter, I showed that the $z > 4$ space density of ultra-red galaxies is just consistent with their evolution into the most massive ($M_{\rm stars} > 10^{11}\,M_{\odot}$), NIR-selected, quiescent galaxies presented in Straatman et al. (2014). In the hierarchical paradigm of galaxy formation, these massive galaxies reside within the densest regions of the DM distribution – themselves having evolved from once tiny fluctuations into the largest structures (indirectly) seen today. These large structures, or nodes in the DM distribution, are populated with galaxy clusters — amalgamations of hundreds to thousands of galactic sub-units, whose stellar portfolios hint at a formation epoch of $z \gtrsim 3$. Thus, at some earlier time, these young galaxy clusters, or so-called 'proto-clusters', would have been much smaller, with their constituents orbiting around a central massive, perhaps even dusty and star forming, galaxy.

In this chapter, I will therefore examine whether the $\sim$ 2-Mpc, FIR environments around ultra-red galaxies at $z \gtrsim 3$ are consistent with those expected for distant proto-clusters. If this is the case, then I will have presented a novel technique for signposting high-redshift candidate proto-clusters based on the *Herschel*-SPIRE flux-density ratios of distant DSFGs. If, however, this is not the case, then serious revisions on our understanding of the role that massive galaxies play in the distant Universe will need to be considered.

The format of this chapter is as follows. In the next section, I will describe the ultra-red galaxies selected for follow-up observations. In Section 3.3, I will then outline the method used to detect and extract DSFGs around these ultra-red galaxies, before analysing whether their on-sky density is consistent with that expected for distant proto-clusters. Finally, I will discuss the results and summarise my conclusion in Section 3.4 and Section 3.5, respectively.

3.2 Sample, Observations and Data Reduction

3.2.1 Ultra-Red Galaxy Sample

Based on their initial shallow imaging reported in the previous chapter, a representative sample of 12 ultra-red galaxies within the *H*-ATLAS DR1 images (1 from each of the GAMA 09 and GAMA 15 fields and 10 from the SGP field) were chosen for deeper/wider, follow-up observations with LABOCA. The selection criteria for ultra-red galaxies is discussed fully in Section 2.2.2 of Chapter 2.

An extra 10 ultra-red galaxies from five fields within the *Her*MES imaging survey were added to this *H*-ATLAS sample. Ultra-Red galaxies within the *Akari Deep Field*-South (ADF-S, 2), the *Chandra* Deep Field-South Survey (CDFS, 1), the European Large-Area Infrared Survey-South 1 (ELAIS-S1, 3) and the X-ray Multi-Mirror Mission-Large Scale Survey (*XMM*-LSS, 2) fields are contained within the DR4.0 xID250 catalogues by Roseboom et al. (2010, 2012). The remaining (2) ultra-red galaxies were selected from the HeLMS are amongst the sample presented by Asboth et al. (2016). All *Her*MES images and catalogues were accessed through the *Herschel* Database in Marseille[1] (Roehlly et al., 2011).

Key Point 3.1
The final sample selected for follow-up observations with LABOCA contains 22 ultra-red galaxies across 8 independent fields and is listed in Table 3.1.

3.2.2 Observing Strategy

The observing strategy for the sample of 22 ultra-red galaxies closely follows that described in Section 2.3.1 of Chapter 2.

Observations were carried out with LABOCA from September 2012 to March 2014 during the European Southern Observatory programme E-191.A-0748 and Max Planck Institute programmes M-090.F-0025-2012, M-091.F-0021-2013 and M-092.F-0015-2013. An average time of $t_{\rm int} \approx 4.6\,{\rm hr}$ was spent integrating around the environments of each ultra-red galaxy. Images with longer integration times ($t_{\rm int} \gtrsim 10\,{\rm hr}$) provide deeper data sensitive to less

[1] http://hedam.oamp.fr/hermes/.

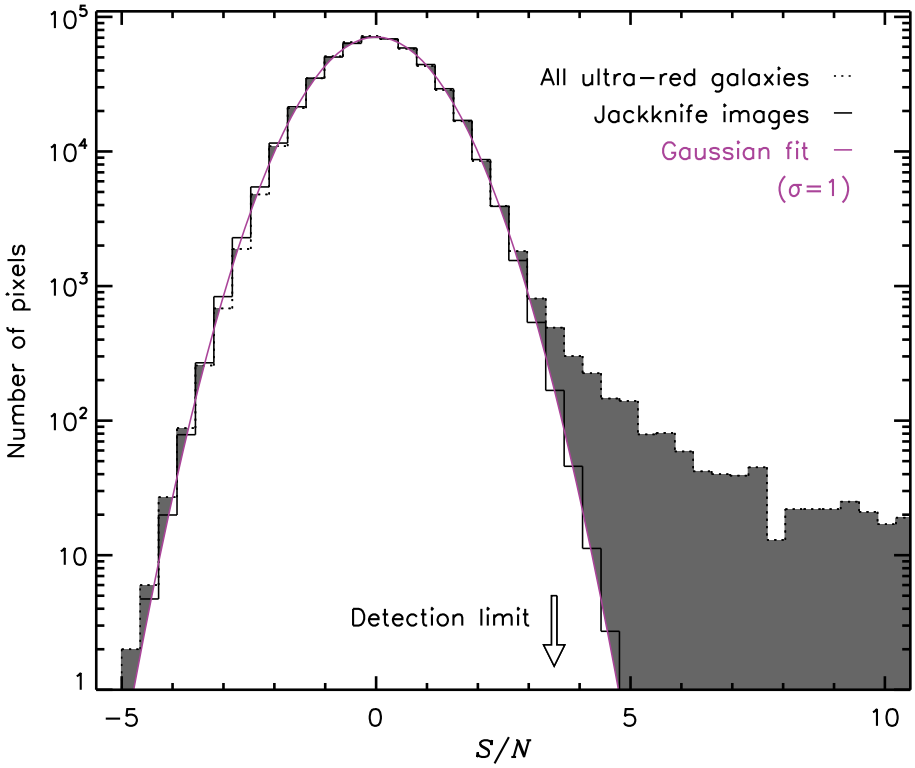

Figure 3.1: PSF-Filtered SNR pixel distribution of the LABOCA images (dotted black histogram). A non-Gaussian tail emerges above $S/N \gtrsim 3$ due to the presence of astronomical sources (shaded black region). I also plot the PSF-filtered SNR pixel distribution of the jackknife images (black solid histogram), whose mean is well modelled by a Gaussian (purple solid line) with a mean of $\mu = 0$ and a standard deviation of $\sigma = 1$, as expected for an image free of sources.

luminous and/or colder DSFGs within the vicinity of these ultra-red galaxies, whilst the shallower images ($t_{\rm int} \lesssim 1\,{\rm hr}$) help to constrain the abundance of bright DSFGs. These deep/shallow data at 870 μm allow photometric redshift estimates to be made for all DSFGs detected around these ultra-red galaxies – providing a means with which to associate them to the same structure signposted by these ultra-red galaxies.

Key Point 3.2

During the observations, typical PWV values between 0.4–1.3 mm, corresponding to a zenith atmospheric opacity of $\tau = 0.2$–0.4, were recorded. The flux-density scale was determined to an r.m.s. accuracy of $\sigma_{\rm calib} \approx 7\%$ using observations of primary/secondary calibrators. Pointing was checked every hour using nearby quasars and found to be stable to $\sigma_{\rm point} \approx 3''$ (r.m.s.). The observing properties of these ultra-red galaxies are also listed in Table 3.1.

Table 3.1: Properties of ultra-red galaxy signposts.

Nickname	α (J2000) h m s	δ ° ′ ″	$t_{\rm int}$ hr	$\overline{\tau}^{\Cross}$	$\overline{\sigma}^{\dagger}$ mJy beam^{-1}	$\Omega^{\ddagger}$ arcmin^2	Date observed yyyy–mm	Programme
SGP-28124	00:01:24.73	−35:42:13.7	13.4	0.3	1.9	133	2013–04	E-191.A-0748
HeLMS-42	00:03:04.39	+02:40:49.8	0.8	0.3	6.3	121	2013–10	M-092.F
SGP-93302	00:06:24.26	−32:30:21.4	16.6	0.3	1.7	129	2013–04	E-191.A-0748
ELAIS-S1-18	00:28:51.23	−43:13:51.5	0.9	0.2	5.3	117	2013–04	M-091.F
ELAIS-S1-26	00:33:52.52	−45:20:11.9	4.4	0.4	4.0	118	2014–04	M-093.F
SGP-208073	00:35:33.82	−28:03:03.2	4.9	0.3	3.2	130	2013–04	M-091.F, E-191.A-0748, M-092.F
ELAIS-S1-29	00:37:56.76	−42:15:20.5	2.9	0.3	4.2	137	2013–10	M-092.F, M-093.F
SGP-354388	00:42:23.23	−33:43:41.8	11.4	0.3	1.8	124	2013–10	M-092.F, E-191.A-0748
SGP-380990	00:46:14.80	−32:18:26.5	4.0	0.3	2.9	115	2012–11	M-090.F
HeLMS-10	00:52:58.61	+06:13:19.7	0.5	0.3	8.0	114	2013–10	M-092.F
SGP-221606	01:19:18.98	−29:45:14.4	1.3	0.4	6.0	112	2014–05	M-093.F
SGP-146631	01:32:04.35	−31:12:34.6	2.4	0.3	5.0	119	2014–04	M-093.F
SGP-278539	01:42:09.08	−32:34:23.0	3.2	0.4	4.4	121	2014–04	M-093.F
SGP-142679	01:44:56.46	−28:41:38.3	3.0	0.4	4.3	116	2014–04	M-093.F
XMM-LSS-15	02:17:43.86	−03:09:11.2	2.0	0.3	4.4	118	2013–10	M-092.F
XMM-LSS-30	02:26:56.52	−03:27:05.0	4.1	0.3	3.4	132	2013–09	E-191.A-0748, M-090.F, M-092.F
CDFS-13	03:37:00.91	−29:21:43.6	1.0	0.2	5.3	118	2013–10	M-092.F
ADF-S-27	04:36:56.47	−54:38:14.6	3.4	0.3	3.7	135	2012–09	M-090.F
ADF-S-32	04:44:10.30	−53:49:31.4	2.0	0.3	5.0	129	2013–04	M-091.F, M-092.F
G09-83808	09:00:45.41	+00:41:26.0	9.2	0.3	1.8	125	2013–10	E-191.A-0748
G15-82684	14:50:12.91	+01:48:15.0	6.7	0.3	2.3	116	2014–03	M-093.F
SGP-433089	22:27:36.98	−33:38:33.9	13.2	0.3	1.8	117	2012–09	M-090.F, M-091.F, M-093.F

$^{\Cross}$Average opacity value during observations.
†Average depth computed across each PSF-filtered LABOCA image, where the resulting FWHM is $\theta \approx 27''$.
‡Areal extent of each LABOCA image.
Note. Ultra-Red galaxies are listed in order of increasing right ascension.

3.2.3 Data Reduction

The LABOCA data were reduced exactly following the procedure outlined in Section 2.3.1 of Chapter 2.

After reducing these LABOCA data, however, I modelled the instrumental noise by generating so-called 'jackknife' images. These are constructed by randomly inverting (i.e. multiplying by -1) half of the reduced scans before the co-addition stage – effectively resulting in a image 'free of astronomical sources' and confusion, estimated to be $\sigma_{\rm conf} \approx 0.9\,{\rm mJy}$ in the deepest LABOCA images. I created 100 jackknife images for each ultra-red galaxy, which were used throughout my analysis in the following sections. Note that there are

$$N = \frac{1}{2}\binom{n}{n/2}$$

independent jackknife images that can be made from n reduced scans. Thus, even for the shallowest image comprised of 12 reduced scans used in this chapter (HeLMS-10), there are $N = 1/2\binom{12}{6} = 924/2 = 462$ unique, possible jackknife images that can be made for this image.

In Figure 3.1, I show the PSF-filtered SNR pixel distributions of the LABOCA images and their respective jackknife images. There is clearly a positive excess above $S/N \gtrsim 3$ in the LABOCA images due to the presence of astronomical sources that is not seen in the jackknife images.

3.3 Analysis

3.3.1 Choosing a SNR Detection Threshold

In order to detect the astronomical sources responsible for the excess above $S/N \gtrsim 3$, I needed to choose a suitable SNR detection threshold based on a fidelity (or 'trustworthiness') parameter ($\mathcal{F}$ — Aravena et al., 2016) of the detected sources. This parameter was calculated by comparing the number of sources detected in the LABOCA images ($\mathcal{N}$) to those detected in the jackknife images ($\mathcal{N}_{\rm jk}$) as a function of detected SNR, given by:

$$\mathcal{F} = 1 - \frac{\mathcal{N}_{\rm jk}}{\mathcal{N}} \equiv 1 - {\rm FDR}, \tag{3.1}$$

where FDR is the false detection rate.

I show the average fidelity in Figure 3.2, which illustrates that as the detection threshold is increased, the confidence in the recovered sources also increases. A fidelity of $\mathcal{F} \approx 100\%$ is reached at $\gtrsim 5\sigma$ and a fidelity of $\mathcal{F} = 50\%$ is reached at $\approx 3\sigma$, with the latter indicating that around a half of the sources detected at this threshold may be spurious. Therefore, I chose (as a compromise between reliability and the number of catalogued sources) a detection threshold of $S/N > 3.5$, where the fidelity is $\mathcal{F} \approx 65 \pm 8\%$.

The scatter seen in the fidelity parameter is caused by the varying abundance of sources

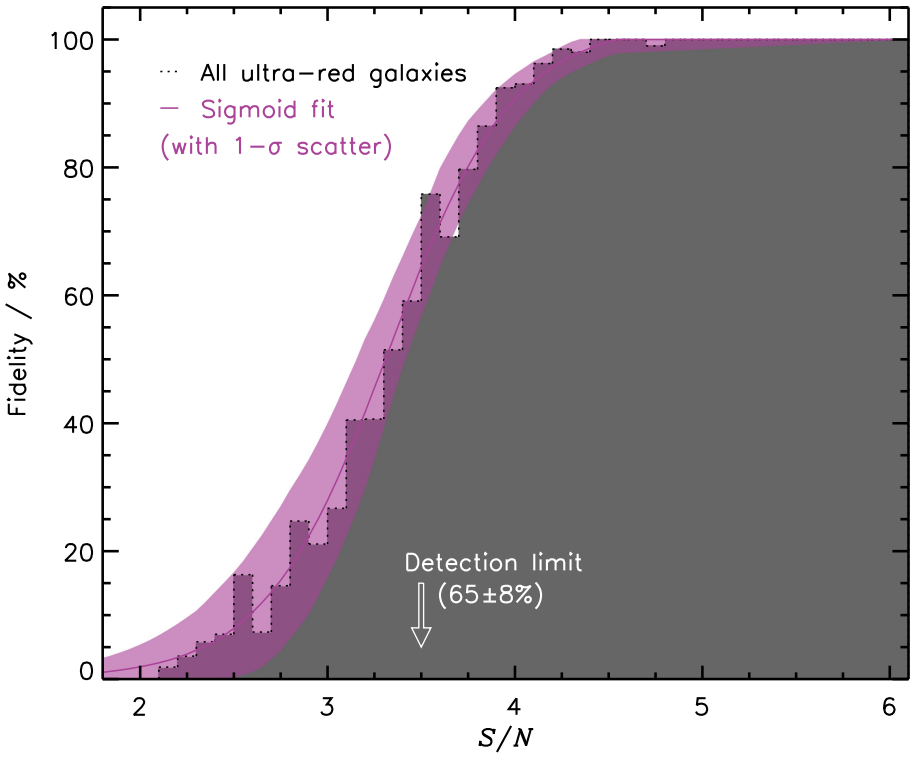

Figure 3.2: Mean fidelity parameter (black dotted histogram) across all LABOCA images as a function of detected SNR. I parametrise the histogram by a sigmoid function ($\propto 1/\left(1+\exp\left(\mathcal{F}\right)\right)$, purple solid line), which I use to deduce the fidelity for a given source. **Note**. On average $65 \pm 8\%$ of sources detected at 3.5σ will be trustworthy, i.e. roughly a third of these sources may be spurious.

in each image, due to the effects of cosmic variance and different image-to-image average r.m.s. values. This scatter decreases with increasing detection threshold and is $\sigma_{\mathcal{F}} \approx \pm 3\%$ at 5σ.

3.3.2 Source Extraction

I used a custom-written IDL source extraction algorithm to identify and extract sources in the PSF-filtered SNR images – noting that filtering an image with a PSF optimises the detection of point sources within that image.

In a top-down fashion, I searched for pixels above the SNR detection threshold, i.e. $S/N > 3.5$. In order to accommodate those sources whose true peak falls between pixels, I temporarily lowered the S/N (by $\approx 95\%$) and kept sources that had bi-cubically interpolated sub-pixel values, which met the original SNR detection threshold. In Table B.1, I catalogue the peak flux density, noise and position determined from a three-parameter Gaussian fit made inside a $\approx 27'' \times 27''$ sub-image centred on a source. After removing the best fit from the image, I searched for and catalogued subsequent peaks until no more were found.

During the extraction process I performed some additional steps; sources deemed too close ($\lesssim 15''$) to each other had their parameters re-evaluated by simultaneously fitting multiple three-parameter gaussians, whilst sources deemed too close ($\lesssim 15''$) to the image boundaries were rejected.

Completeness, Flux Boosting and Positional Offsets

In order to derive the completeness ($\mathcal{C}$, the fraction of recovered sources to modelled sources), flux boosting ($\mathcal{B}$, the ratio of recovered to modelled flux densities) and positional offsets ($\mathcal{R}$, the radial distance between recovered and modelled positions) associated with each extracted source, I simulated and injected artificial point sources into the jackknife images at random, unclustered positions. Model flux densities for these sources were drawn down to $S_{\rm mod} = 1\,{\rm mJy}$ using a Schechter parametrisation of the differential number counts, given by:

$$\frac{{\rm d}N}{{\rm d}S_{\rm mod}} \propto \left(\frac{S_{\rm mod}}{S_0}\right)^{-\alpha} \exp\left(-S_{\rm mod}/S_0\right), \tag{3.2}$$

where $S_0 = 3.7\,{\rm mJy}$ and $\alpha = 1.4$ (Casey et al., 2013). I scaled these 850-μm flux densities to 870 μm using a spectral index of ν^2, i.e. the model flux densities were divided by $(\nu_{870}/\nu_{850})^2 \approx 1.05$.

For each simulated source, I ran the source-extraction algorithm and, if a peak was detected within a threshold radius of $r_{\rm thresh} \leq 1.5\theta \approx 40''$ from the injection site, I recorded its best-fitting Gaussian parameters. If, however, multiple peaks were detected within the threshold radius due to the Gaussian nature of the jackknife images, I took the most significant. Finally, if I failed to recover anything, I simply recorded the model flux density and instrumental noise at the injection site.

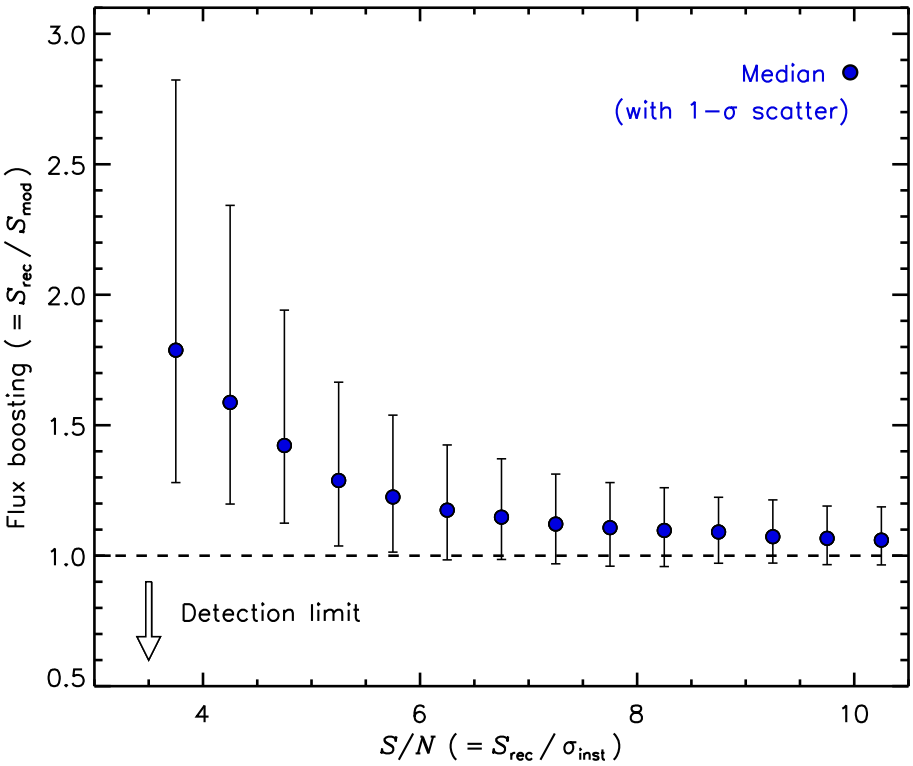

Figure 3.3: Flux boosting as a function of recovered SNR for the ultra-red galaxy, SGP−93302. I record a negligible flux-boosting value of $\mathcal{B} < 1.1$ at $S/N \gtrsim 6.0$, which increases to $\mathcal{B} \approx 1.7$ at the detection threshold. These results are comparable to those presented in Geach et al. (2017), i.e. $\mathcal{B} \approx 1.5$ at $S/N \gtrsim 3.5$.

This procedure was repeated 10,000 times for each ultra-red galaxy – resulting in a large, realistic catalogue of detected/undetected simulated sources. From this simulated catalogue, I computed the median flux boosting as a function of recovered SNR, the two-dimensional[2] average completeness as a function of modelled flux density and instrumental noise and the median radial offset as a function of modelled SNR.

The de-boosting factors were spline interpolated using the flux densities and instrumental noises for detections within the catalogue produced in Section 3.3.2 (see Figure 3.3). I then used these de-boosted flux densities and instrumental noises to spline interpolate the noise-dependent completeness (see Figure 3.4) and modelled-SNR-dependent radial offset (see Figure 3.5).

At the adopted detection threshold here, the flux density of a source in the deepest image (SGP−93302) is typically boosted by $\mathcal{B} = 1.7$ (in agreement with the literature — Geach et al., 2017). At higher SNRs (i.e. $S/N \gtrsim 6$) the flux boosting becomes negligible. However, the noisiest images (with $\sigma \gtrsim 5\,\mathrm{mJy}$) suffer severe de-boosting factors due to the steep bright-end slope of the Schechter number counts adopted here (see Equation 3.2).

For SGP−93302, the two-dimensional completeness function indicates that detections around this ultra-red galaxy have a completeness of $\mathcal{C} \approx 100\%$ at a de-boosted flux density

[2]The two-dimensional treatment of the completeness is necessary in order to account for the varying r.m.s. across a given LABOCA image (Geach et al., 2013).

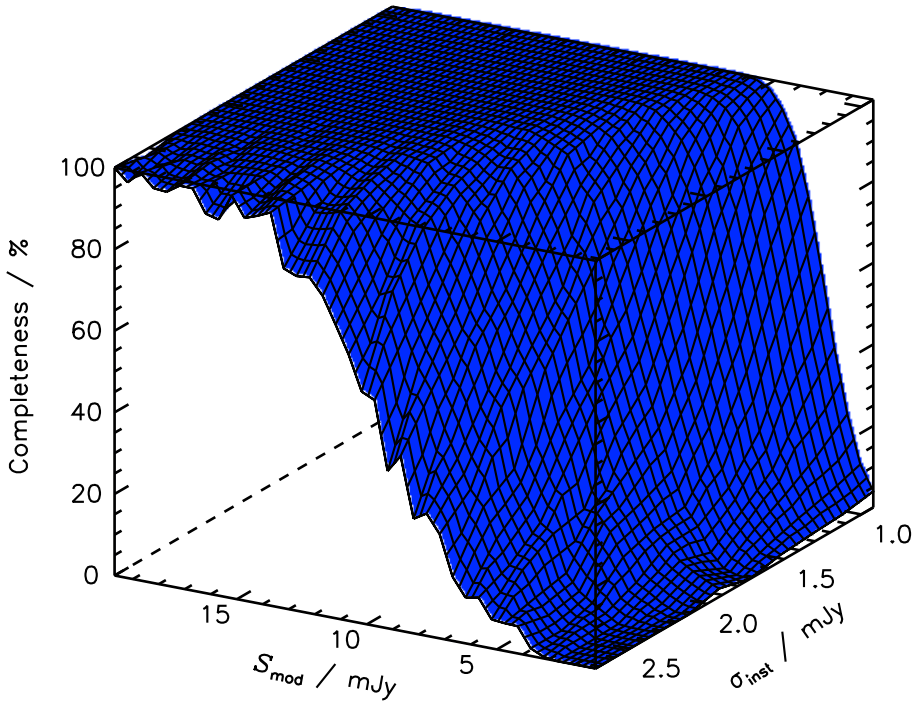

Figure 3.4: Two-Dimensional completeness for the ultra-red galaxy, SGP−93302, as a function of modelled flux density and instrumental noise. The two-dimensional treatment of the completeness is vital due to the radially varying sensitivity across a given image. As the instrumental noise decreases and the model flux density increases, the completeness increases too. For SGP−93302, at an instrumental noise and model flux density of $\sigma_{\rm inst} \approx 1.2\,{\rm mJy}$ and $S_{\rm mod} \approx 1\,{\rm mJy}$, respectively, I recover hardly any sources, i.e. $\mathcal{C} \approx 0\%$. However, increasing the model flux density to $\gtrsim 5\,{\rm mJy}$, whilst keeping the noise constant, results in most sources being recovered successfully, i.e. $\mathcal{C} \approx 100\%$.

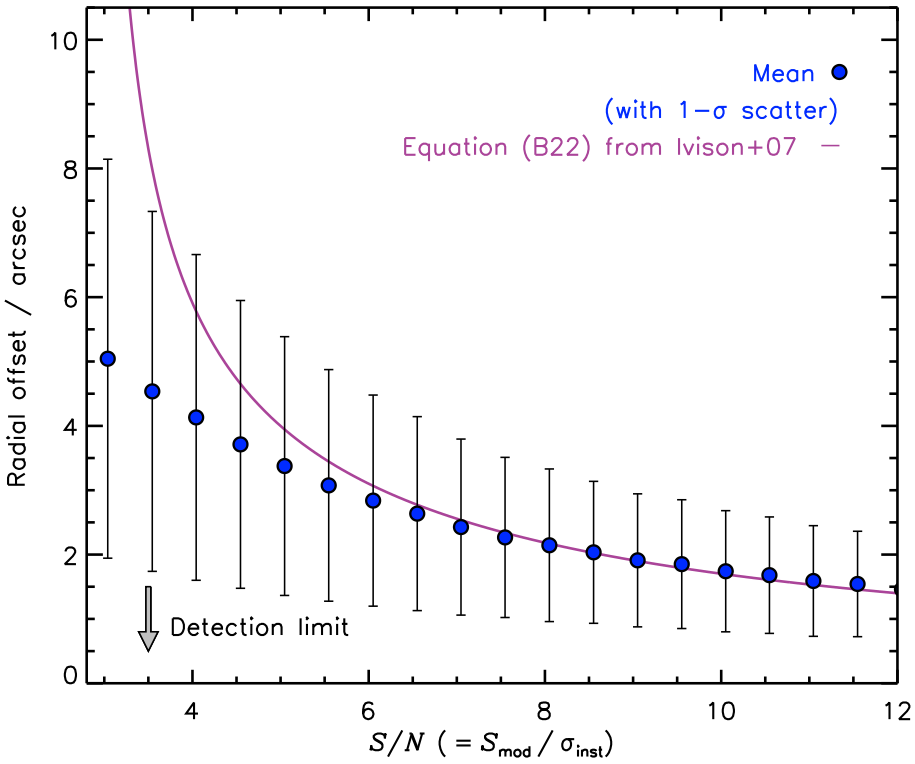

Figure 3.5: Radial offset as a function of modelled SNR for the ultra-red galaxy, SGP−93302. The 1-σ errors for a given bin are taken from the r.m.s. scatter within that bin. I also plot the predicted form given by Equation B22 in Ivison et al. (2007), which is in good agreement.

and instrumental noise of $S_{\rm mod} \approx 5\,{\rm mJy}$ and $\sigma_{\rm inst} \approx 1.2\,{\rm mJy}$, respectively. However, in this same flux-density plane, the completeness falls to $\mathcal{C} \approx 0\%$ as the instrumental noise increases to $\sigma_{\rm inst} \approx 2.5\,{\rm mJy}$.

The mean radial offset (see Figure 3.5) appears to be in good agreement with that expected from Equation B22 in Ivison et al. (2007), which gives the expected radial offset for a source with a given SNR (that has been corrected for the effects from flux boosting assuming an underlying power-law distribution in the number counts) and a given FWHM (θ) of the PSF:

$$\frac{\mathcal{R}}{\sqrt{2}} \approx 0.6 \frac{\theta}{S/N}.$$

There exists a large scatter in the low $S/N \lesssim 5$ bins, which indicates that the radial offsets can vary by as much as $\Delta\mathcal{R} \approx \pm 2.5''$. The brightest detections with $S/N \approx 30$ have radial offsets as low as $\mathcal{R} \approx 0.5''$, which indicates that their positions can be accurately constrained.

Finally, the simulated sources that were successfully recovered match the input differential number counts parametrised by Equation 3.2 to within 1σ, i.e. there appears to be no underlying systematics within the method described in this section.

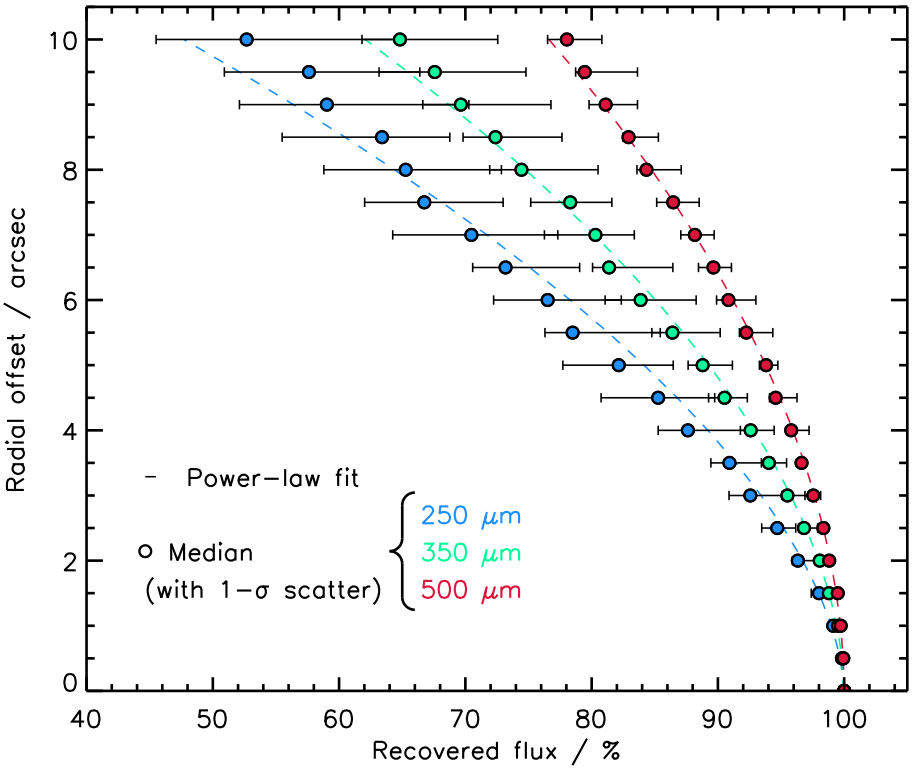

Figure 3.6: SPIRE flux correction to accommodate the drop in the measured flux density due to the LABOCA radial offset (see Figure 3.5). The SPIRE 250-, 350- and 500-μm passbands are represented by green-, blue- and red-coloured circles, respectively. The uncertainties represent the 1-σ scatter in the recovered flux density. At $\mathcal{R} = 4''$, roughly equating to a modelled $S/N \approx 5$, I recover 85, 92 and 97% of the flux density across the 250-, 350- and 500-μm passbands, respectively. This decreasing loss of flux density represents the increasing optimal pixel size due to the changes in the FWHM of the PSF in each SPIRE image.

3.3.3 *Herschel*-SPIRE Photometry

In order to derive the FIR photometric redshifts for the DSFGs detected within the LABOCA images, I needed to firstly measure their SPIRE photometry. I achieved this by bi-cubically interpolating the SPIRE images at their catalogued LABOCA source positions (see Section 3.3.2). Their photometric errors and local sky values were derived from a $\approx 10\theta \times 10\theta$ sub-image centred on each catalogued source, where $\theta \approx 18$, 24 and $35''$ for the SPIRE 250-, 350- and 500-μm images, respectively.

The effect that the LABOCA radial offset (see Figure 3.5) has on determining the SPIRE flux densities was quantified by analysing how the 'true' flux density of a source varied as I 'tweaked' the position that it was measured at. Thus, for each survey field *and* passband, I selected a bright ($S_{250} \approx S_{350} \approx S_{500} \gtrsim 1\,\mathrm{Jy}$) point source and measured the (true) flux density at its catalogued position. I then performed 500 Monte Carlo simulations, drawing radial offsets from a Gaussian distribution centred on its catalogued position with a standard deviation[3] of $\sigma = \mathcal{R}$. I allowed the radial offset – and thus the standard deviation – to increase from $0'' \leq \mathcal{R} \leq 10''$ in order to simulate the typical radial offsets for sources detected within this chapter. For each simulation, I measured the flux density at the tweaked position and compared it to the true flux density. I used this ratio to correct a SPIRE photometric measurement, depending on the LABOCA radial offset that it exhibited.

Key Point 3.3
In Figure 3.5, I show that the average radial offset is passband related, reflecting the different pixel sizes of 6, 8.3 and $12''\,\mathrm{pix}^{-1}$ for the 250-, 350- and 500-μm passbands in *H*-ATLAS, respectively (similar values are recorded in *Her*MES).

For detections with low radial offsets ($\mathcal{R} < 2''$) and thus high SNRs ($S/N \gtrsim 8$), I recover $\approx 95\%$ of their true flux density. Due to the large SPIRE 500-μm pixel size, even at the highest radial offsets ($\mathcal{R} \approx 10''$) considered in this chapter, I still recover $\gtrsim 80\%$ of the true flux density. On the other hand, however, I only recover $\gtrsim 55\%$ and $\gtrsim 65\%$ of the true flux densities for the highest offsets reported in this chapter at 250- and 350-μm, respectively.

I draw attention to 16 (i.e. $\approx 15\%$) LABOCA detections that are undetected (above $> 1\sigma$) in all of the SPIRE images. The majority (12) of these have SNRs of $S/N \lesssim 4.5$, which is approximately the number of spurious sources expected at this threshold from the fidelity analysis given in Section 3.3.1. The number of undetected sources with higher SNR values is also expected from the fidelity analysis once the scatter has been taken into account. These sources do not affect the number counts derived in this chapter because, on average, this effect is corrected for. However, I chose not to include any of these sources in the photometric redshift analysis as their FIR photometry is unable to be accurately constrained.

[3] As the radial offset is defined as the radial distance from the modelled to the recovered position of a simulated source, I varied each coordinate of each spatial dimension (α and δ) by $\mathcal{R}_\alpha = \mathcal{R}_\delta = \mathcal{R}/\sqrt{2}$.

The SPIRE flux densities derived in this manner for the ultra-red galaxies (i.e. using a LABOCA position prior and correcting them for the LABOCA radial offset) are broadly consistent with those from which they were originally selected – varying on the $\approx \pm 1$-σ level.

3.3.4 Photometric Redshifts

I used the custom-written, χ^2-minimisation routine in IDL described in Section 2.4.2 of the previous chapter to determine the FIR-based photometric redshifts for catalogued sources with at least one SPIRE detection above $> 1\sigma$. To recap, this photometric redshift algorithm adopts three template SEDs (that of the Cosmic Eyelash and the synthesised templates from Pope et al. (2008) and ALESS), which were shown to have an intrinsic uncertainty of $\sigma_{\Delta z} \approx 0.14(1 + z_{\rm spec})$ when used together.

The de-boosted 870-μm and corrected-SPIRE flux densities were used during the template fitting and, again, I adopted the photometric redshift associated with the template that yielded the lowest χ^2 value overall. However, contrary to previous chapter, I derived 1-σ errors based on the $\chi^2_{\rm min}+1$ locations, which were consistent with those derived from Monte Carlo simulations.

The results of these fits, as well as the rest-frame, 8–1,000-μm luminosities are presented in Table B.2 in Appendix B.

3.4 Discussion

Key Point 3.4
I catalogue 108 DSFGs above $S/N > 3.5$ around the 22 ultra-red galaxies.

I list their de-boosted-LABOCA and corrected-SPIRE flux densities, along with their mean flux-boosting and fidelity parameters in Table B.1 in Appendix B. The ultra-red galaxies span a wide de-boosted flux-density range of $S_{870} = 2.9$–$42.8\,$mJy and have an average de-boosted flux density of $\overline{S_{870}} = 17.0\,$mJy. The surrounding DSFGs span a less wide de-boosted flux-density range of $S_{870} = 1.9$–$31.3\,$mJy and have an average de-boosted flux density of $\overline{S_{870}} = 6.8\,$mJy. Although there are two (new) bright DSFGs with $S_{870} \gtrsim 25\,$mJy, the surrounding DSFGs are typically fainter than the signpost ultra-red galaxies.

I was unable to detect four of the ultra-red galaxies above the $S/N > 3.5$ threshold; all of these are located in the shallower images. In such cases, I report the peak flux density and r.m.s. pixel value within a 45-arcsec aperture centred on the telescope pointing position, i.e. adopting the method used in the previous chapter. I do not provide completeness, flux-boosting or fidelity values for these sources.

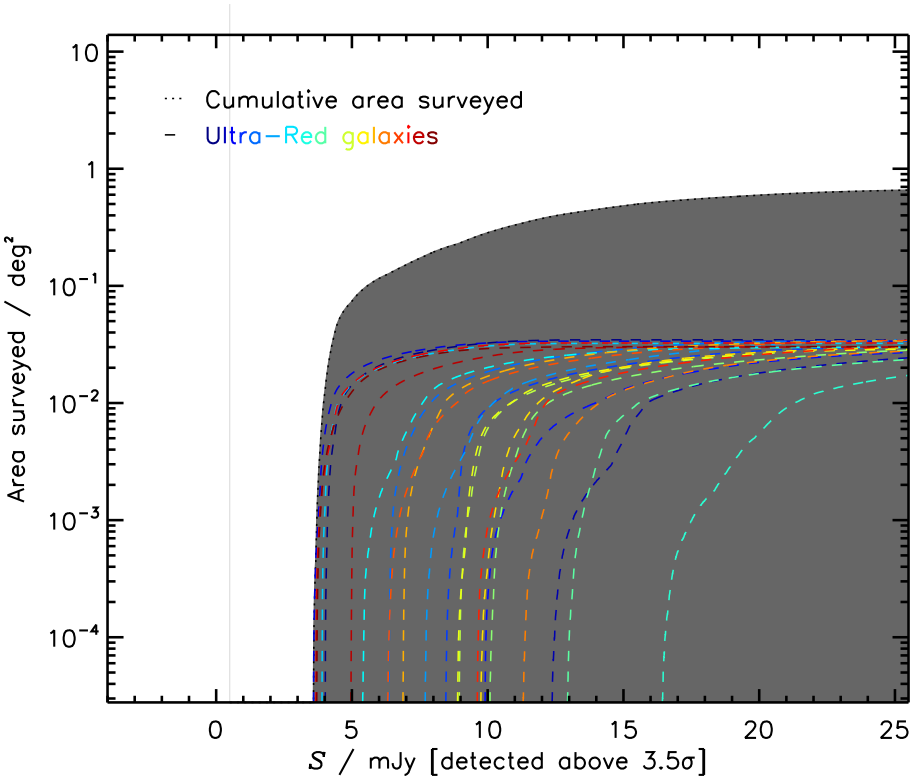

Figure 3.7: The area surveyed around ultra-red galaxies as a function of 'detectable' 870-μm flux density. As the flux density increases, each image converges to a surveyed area of $\mathcal{A} \approx 0.03\,\mathrm{deg}^{-2}$, or $\approx 10' \times 10'$. The deepest images, with typical central r.m.s. values of $\approx 1.5\,\mathrm{mJy}$, converge to this surveyed area at $\approx 5\,\mathrm{mJy}$. On the contrary, the shallowest images do not converge until $\gtrsim 10\,\mathrm{mJy}$. At $S = 8.5\,\mathrm{mJy}$, the cumulative surveyed area is $\mathcal{A} \approx 0.2\,\mathrm{deg}^2$.

3.4.1 870-μm Number Counts Around Ultra-Red Galaxies

I determined the 870-μm number counts around ultra-red galaxies (which are shown and listed in the top-panel of Figure 3.8 and Table 3.2, respectively) using the following equation:

$$N(>S') = \sum_{\forall S_i > S'} \frac{\mathcal{F}}{\mathcal{C}\mathcal{A}}, \tag{3.3}$$

where the sum is over all de-boosted flux densities S_i (excluding the central ultra-red galaxies) greater than some threshold flux S' and $\mathcal{A}$ is the area surveyed at a given flux density. The latter was obtained by cumulating the area across all images where a given flux density is detectable (i.e. above the $S/N > 3.5$ detection threshold), which I show in Figure 3.7. Together the fidelity, area surveyed and completeness corrections account for the varying image-to-image r.m.s. values across the sample.

The error on Equation 3.3 was deduced using:

$$\sigma_{N(>S')} = N(>S') \frac{\sigma_{\mathcal{N}}}{\mathcal{N}(>S')}, \tag{3.4}$$

where $\sigma_{\mathcal{N}}$ are the double-sided 1-σ Poisson errors (Gehrels, 1986) on the raw number

Table 3.2: Number counts and over-densities of ultra-red galaxies environments.

$S'^{\dagger}$ mJy	$N(>S')$ deg^{-2}	$\mathcal{N}(>S')^{\ddagger}$	$\delta(>S')$	$\overline{\mathcal{C}}$	$\overline{\mathcal{B}}$	$\overline{\mathcal{F}}$
5.5	$273.9^{+53.7}_{-45.4}$	36^{+7}_{-5}	$+0.4^{+0.1}_{-0.1}$	0.68	1.54	0.98
7.0	$186.4^{+39.9}_{-33.3}$	31^{+6}_{-5}	$+0.7^{+0.2}_{-0.2}$	0.70	1.49	0.98
8.5	$109.5^{+27.2}_{-22.2}$	24^{+5}_{-4}	$+1.0^{+0.3}_{-0.3}$	0.74	1.45	0.99
10.0	$59.6^{+18.9}_{-14.8}$	16^{+5}_{-3}	$+1.3^{+0.6}_{-0.5}$	0.81	1.42	1.00
11.5	$28.2^{+10.7}_{-8.0}$	12^{+4}_{-3}	$+1.5^{+0.9}_{-0.8}$	0.88	1.25	1.00
13.0	$23.1^{+9.9}_{-7.2}$	10^{+4}_{-3}	$+4.0^{+3.6}_{-2.4}$	0.88	1.26	1.00
14.5	$18.8^{+9.3}_{-6.5}$	8^{+3}_{-2}	$+11.4^{+16.5}_{-16.0}$	0.87	1.26	1.00
16.0	$8.4^{+5.7}_{-3.6}$	5^{+3}_{-2}	$+39.2^{+146.3}_{-144.8}$	0.98	1.13	1.00

‡ Flux-Density thresholds are taken from Weiß et al. (2009) to simplify the comparisons we made with LESS.
‡ Represents the raw number of DSFGs detected above a given flux density threshold.

of sources above some flux-density threshold $\mathcal{N}(>S')$. To judge whether using Poisson noises was suitable, I generated a random catalogue of detected flux densities for all DSFGs assuming that they follow a Gaussian distribution. I then re-evaluated Equation 3.3 for this random sample and found no significant variation in the results – suggesting that the (sometimes) high flux-density uncertainties are not severely affecting the number counts presented in this chapter.

Key Point 3.5
In the top-panel of Figure 3.8, I show that the number counts around ultra-red galaxies are always $\gtrsim$ 1-σ above those presented in the LABOCA Extended Chandra Deep Field South (ECDFS) Submillimetre Survey (LESS — Weiß et al., 2009) and the SCUBA-2 Cosmology Legacy Survey (S2CLS — Geach et al., 2017). It is also clear that there is a slight break in the shape of number counts around ultra-red galaxies at $S' > 7$ mJy, similar to that seen in LESS.

Furthermore, the number counts are similar to those around J2142−4423 (a Ly-α proto-cluster — Beelen et al., 2008) at $S' \leq 7$ mJy and $S' \geq 14$ mJy. However, it is unclear whether Beelen et al. (2008) removed the central source from their number counts, which will bias their results higher than those presented here. Furthermore, Beelen et al. (2008) claim that the environments around J2142−4423 are only moderately over-dense compared to the SCUBA HAlf Degree Extragalactic Survey (SHADES — Coppin et al., 2006) – however, I show in Section 3.4.3 that caution should be taken when making comparisons with SHADES.

Finally, the top-panel of Figure 3.8 shows the number counts around MRC 1138262 (the so-called 'Spiderweb galaxy' — Miley et al., 2006; Dannerbauer et al., 2014), a HzRG with an $S' > 7$-mJy over-density of DSFGs compared to LESS. This proto-cluster is a factor of $\approx 2\times$ over-dense compared to the environments around ultra-red galaxies. However, it should be noted that Dannerbauer et al. (2014) neither account for flux boosting, nor survey completeness nor do the authors remove the central galaxy (DKB07) during their

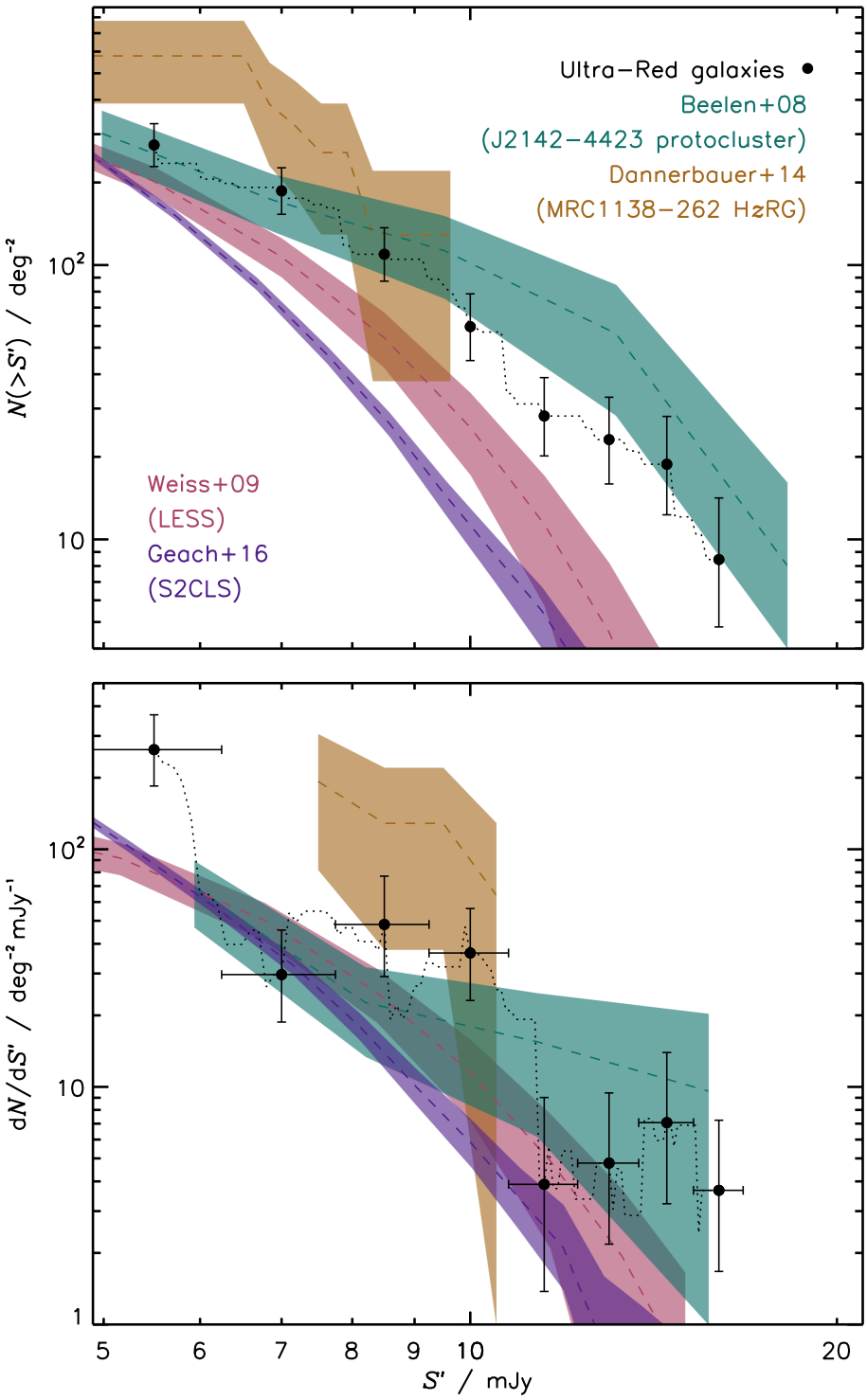

Figure 3.8: Top: number counts (excluding the signpost ultra-red galaxies) as a function of 870-μm flux density (black squares) with 1-σ double-sided Poisson errors (Gehrels, 1986). The blank-field number counts from LESS (pink region) and S2CLS (purple region — scaled with a spectral index of ν^2) surveys are shown. Furthermore, the number counts of two well-known proto-clusters, J2142−4423 (green region — Beelen et al., 2008) and MRC 1138262 (brown region — Dannerbauer et al., 2014) are displayed for reference. It is clearly evident that the number counts presented in this chapter are high at all flux-density thresholds and exhibit a slight break at $S' > 7$ mJy. I believe that the increasing excess at higher flux densities is the result of these ultra-red galaxies signposting similarly extreme DSFGs. The catalogue contains five bright ($S_{870} > 16$ mJy) sources, however, I concede that without ...

Figure 3.8 (continued from previous page): ... high-resolution imaging I am unable to decipher whether these high flux densities are occurring due to chance gravitational lensing. *Bottom:* differential number counts (also excluding the signpost ultra-red galaxies) as a function of 870-μm flux density (black squares). Above $S' > 8.5\,\mathrm{mJy}$, the differential number counts are typically 1-σ greater than those presented in LESS – the comparison field of choice for these ultra-red galaxies.

calculation. I crudely correct for the first two of these differences using the results obtained for SGP−93302, which was observed under similar conditions as MRC 1138262. Adjusting for these corrections, I record less extreme number counts of $N(> 6\,\mathrm{mJy}) \approx 395 \pm 175\,\mathrm{deg}^{-2}$ (1-σ Poisson errors) that exhibit a sharp break at $S' \approx 6.5\,\mathrm{mJy}$ – bringing the number counts of MRC 1138−262 in-line with those presented here.

In the bottom-panel of Figure 3.8, I show the differential number counts of the environments around ultra-red galaxies within 2-mJy wide bins. This figure shows that the bulk of the excess is coming from the ≈ 5-, ≈ 8.5- and ≈ 10-mJy bins.

In Figure 3.9, I show how the contribution to the number counts at the flux densities provided in Table 3.2 varies in two signpost-centric annuli of equal area ($16\pi\,\mathrm{arcmin}^2$). At $S' > 8.5\,\mathrm{mJy}$, ≈ 80% of the contribution to the number counts comes from DSFGs distributed within $r_{\mathrm{UR}} < 4'$ of these ultra-red galaxies. However, due to the low number of DSFGs above these de-boosted flux-density thresholds, this excess contribution is not significant ($\approx 1.5\sigma$). Thus, the increasing instrumental noise with distance from these ultra-red galaxies makes comparisons of the number counts at all but the highest flux densities heavily biased. At the higher flux-density thresholds this perceived excess diminishes rapidly and above $S' > 11.5\,\mathrm{mJy}$ the contribution appears to be equally split between the two annuli. Thus, without uniformly wide imaging of these environments, the number counts as a function of radial distance remains largely unconstrained for ultra-red galaxies.

3.4.2 Over-Density Parameter

In order to make a statistical analysis of the significance of the excess in the number counts, I employed the use of an over-density parameter (Morselli et al., 2014) defined as:

$$\delta(> S') = \frac{N(> S')}{N'(> S')} - 1, \tag{3.5}$$

where $N'(> S')$ are the number counts expected in a blank-field survey above some flux-density threshold S'.

When choosing a suitable blank-field survey, it is important to compare 'like-for-like' (Condon, 2007). For instance, FIR ground-based surveys can hide the multiplicity of DSFGs, which was first identified in early interferometric observations (Ivison et al., 2007), later confirmed with larger samples (Simpson et al., 2015; Bussmann et al., 2015) and found to be consistent with galaxy-formation models (Cowley et al., 2015;

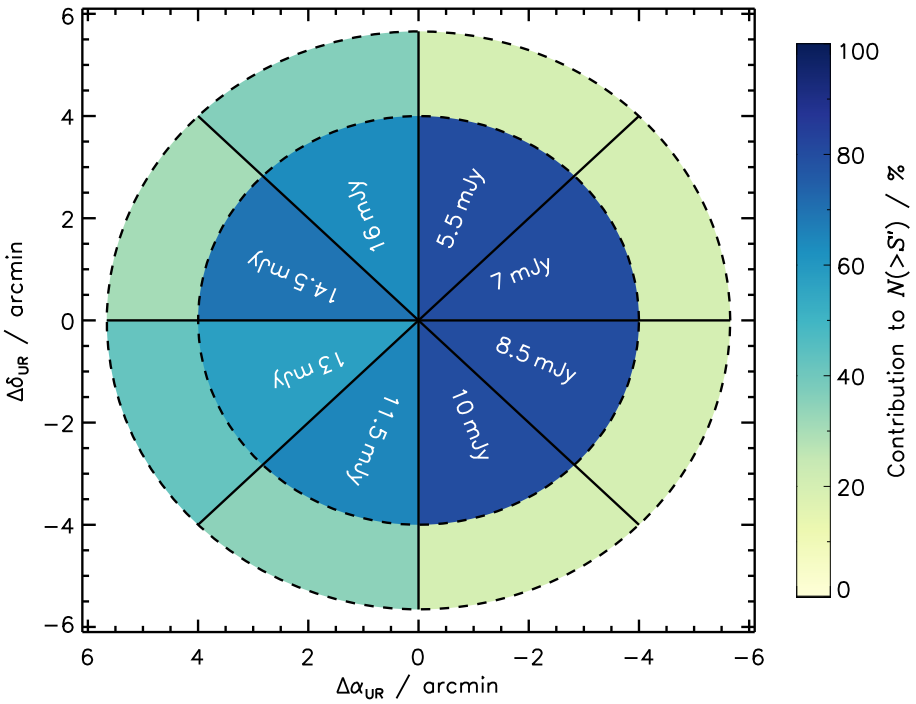

Figure 3.9: Contribution to the cumulative number counts from two signpost-centric annuli with equal area (i.e. 16π arcmin^2) separated by black dashed lines. Each annuli is divided into eight equally sized segments representing the 870-μm, flux-density thresholds listed in Table 3.2. The contribution to the number counts from each annuli in each segment is colour-coded (see scale on the right-hand side). At $S' > 8.5$ mJy, the inner annuli contributes $\approx 80\%$ of the sources responsible to the total number counts. However, by $S' > 11.5$ mJy the contribution is equally split between the two annuli, within the large Poisson errors ($\sigma \approx 30\%$). This highlights the difficulty in claiming any radial dependence on the number counts due to variations in the instrumental noise (i.e. the noise increases as the distance from the ultra-red galaxies increases).

Narayanan et al., 2015). Furthermore, similar (if not identical) data-reduction techniques ensure consistency in the flux-density measurements, which may otherwise lead to a lower or higher estimate of the number counts (see Section 3.4.3).

Hence, I chose the LESS number counts (calculated directly from the source catalogue) in order to make comparisons against. Both datasets were obtained from the same instrument and were reduced in a similar manner using the same software. However, there are slight differences in the results when I run my source extraction algorithm on the LESS DR1.0 SNR image[4]. Using a detection threshold of $S/N > 3.7$, I am only able to recover 95% of their catalogued sources. The 870-μm flux-density measurements of these recovered sources have a mean absolute offset of $\overline{|\Delta S_\nu|} = 0.4\,\mathrm{mJy}$ compared to those presented in Weiß et al. (2009). Thus, these slight differences should have a relatively minor effect on the comparisons made between the two number counts. However, the computation of the completeness and flux-boosting corrections do differ; I recorded $\lesssim 15\%$ differences in the latter at a detection $S/N \approx 3.7$ for sources around SGP−433089, which has a similar (albeit slightly higher) average depth to LESS. Finally, Weiß et al. (2009) claim that LESS is under-dense and also shows a deficit of bright sources relative to other blank fields. Figure 3.8 shows that this is clearly not case when compared against the much deeper and wider (and thus more robust against cosmic variance) results from S2CLS.

Over-Density comparisons were made at a flux-density threshold of $S' > 8.5\,\mathrm{mJy}$, which roughly equates to a surveyed area of $\mathcal{A} \approx 0.2\,\mathrm{deg}^2$ (see Figure 3.7). I chose this flux-density threshold so as to be directly comparable to LESS. Furthermore, this threshold is high enough to minimise the correction effects needed for detections with low SNRs, and at the same time low enough such that the results should not drastically change if the bright sources are magnified by $\mu \lesssim 2$.

Key Point 3.6

I added the number-count error bars in quadrature to those given in Weiß et al. (2009) and determined an over-density of $\delta = 1.0^{+0.3}_{-0.3}$ at $S' > 8.5\,\mathrm{mJy}$. Or, put another way, I am 99.93% confident that the ultra-red galaxies signpost over-dense regions in the Universe, and $\approx 95\%$ confident that these regions are over-dense by a factor of at least $\geq 1.5\times$ compared to LESS.

There exists a strong correlation in flux density with the over-density parameter visible in Figure 4.4. In this figure, I show the over-density parameter for each ultra-red galaxy – logarithmically scaled to reflect its individual contribution to the overall number counts – as a function of de-boosted 870-μm flux density. The large scatter across the 22 images is indicative of both varying levels of image noise and cosmic variance. The effect of the latter is estimated in the following section. Although the over-density increases by a factor of $\sim 50\times$ from $S' = 7$–$16\,\mathrm{mJy}$, the Poisson error from the blank-field number counts rises steeply at the highest flux-densities thresholds, which makes this evolution highly uncertain. However, I believe that this evolution is likely caused by ultra-red galaxies

[4] http://archive.eso.org/cms/eso-data/data-packages/less-data-release-v1-0.html.

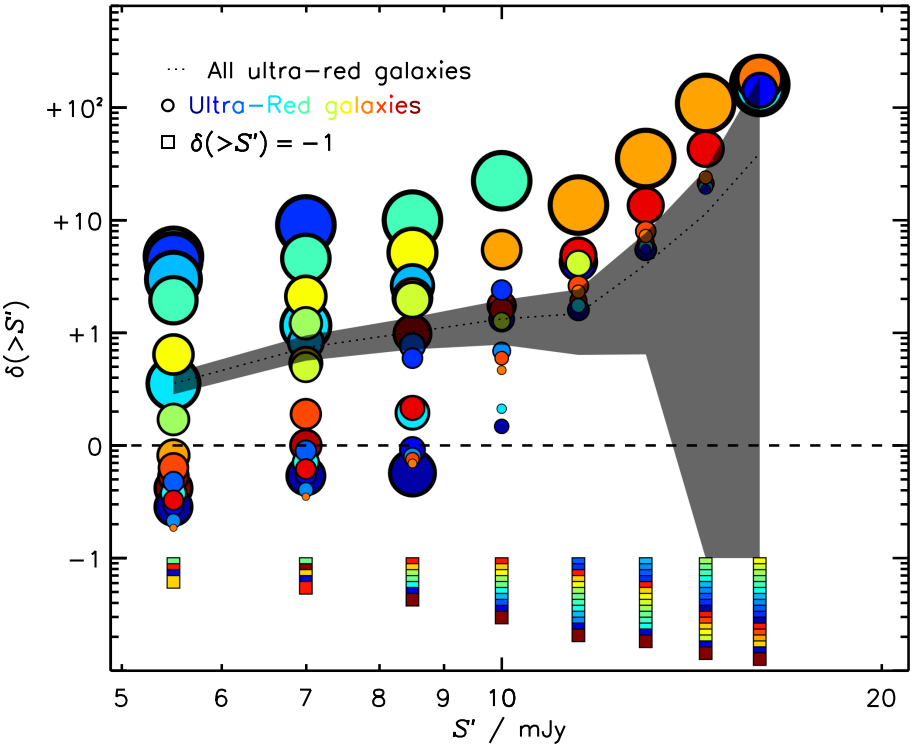

Figure 3.10: Number counts relative to LESS (i.e. the over-density parameter, $\delta(> S')$) versus 870-μm flux density for DSFGs in the vicinity of ultra-red galaxies. I show the results for the entire sample (black dotted line) and each ultra-red galaxy (multi-coloured circles). The size of each circle has been logarithmically scaled to show the influence that each image has in deducing the number counts for the entire sample. Images where no sources are present above a given flux-density threshold are indicated by squares, which I stagger starting from $\delta = -1$ for clarity. These squares highlight the deficit of sources due to intrinsic properties (i.e. cosmic variance) and varying image r.m.s. values. Hence, some ultra-red galaxies probe considerably more over-dense regions than others, with variations being sometimes a factor of $\approx \times 5$ higher. **Note**. Each ultra-red galaxy is colour-coded from blue to red in order of increasing right ascension, i.e. in the order that they appear in Table 3.1 and with the colour that they have in Figure B.1.

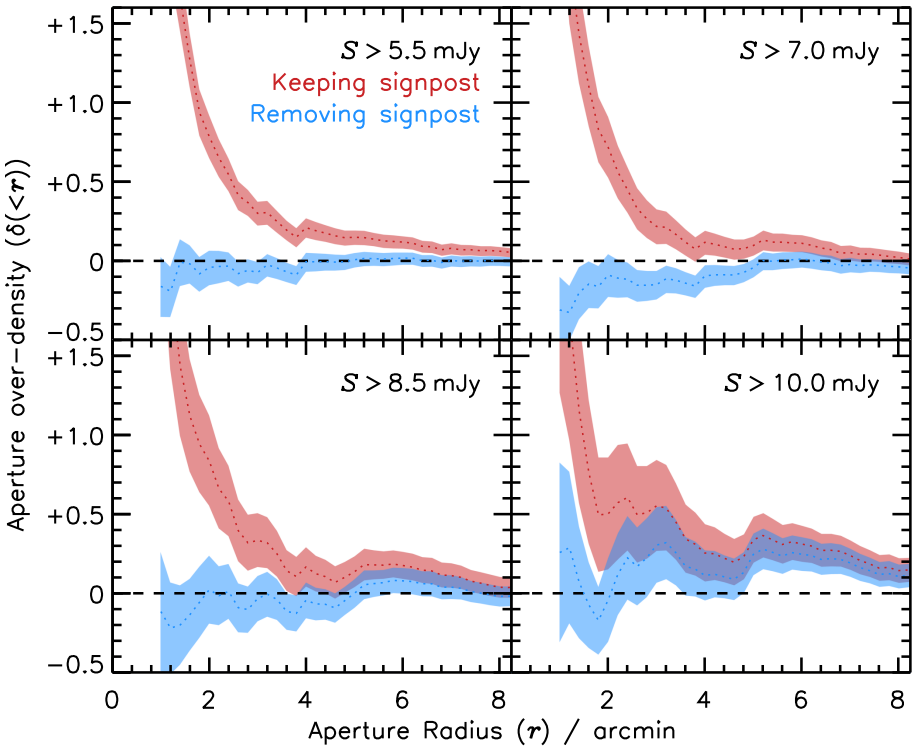

Figure 3.11: The galaxy-centric over-density parameter as a function of radius for DSFGs presented in Weiß et al. (2009). I show how the over-density parameter varies when keeping (red) and removing (blue) the signpost DSFGs at four different flux-density thresholds. The over-density parameter is biased to higher values at all flux-density thresholds when the signpost DSFGs are kept. However, removing these signposts clearly removes most of the over-density associated with imaging a region known to contain a DSFG. At the $S_{870} > 8.5$-mJy threshold, the residual over-density is $\delta \approx +0.1 \pm 0.1$ at the typical image dimensions used in this chapter. As this residual bias is small and comparable to its own uncertainty, I chose not to corrected the reported over-density parameter.

signposting regions that contain brighter DSFGs, but without high-resolution imaging of the environments around these ultra-red galaxies, I cannot completely rule out gravitational lensing by chance alignment.

3.4.3 Biases Affecting the Over-Density Parameter

I now consider a few biases that will be affecting the reported over-density parameter in the previous section.

Firstly, although removing the central ultra-red galaxies from the number counts considerably reduces the bias associated with imaging a region where a galaxy is known to reside (Greve et al., 2004; Weiß et al., 2009), a slight 'residual bias' still remains. To estimate this residual bias, I calculated the galaxy-centric over-density parameter as a function of radius for each of the 126 DSFGs catalogued in Weiß et al. (2009). I then repeated this calculation but this time removing the signpost DSFGs.

These results are shown in Figure 3.11, which confirms that keeping the signpost DSFGs

within the number-count calculation significantly increases the over-density parameter, at least out to $\approx 7'$. This effect appears to decrease with increasing de-boosted flux density, but the low number of sources drastically increases the uncertainty in this measurement. Furthermore, this figure shows that removing the signpost DSFGs significantly reduces this bias but stills leaves behind a slight excess of $\approx +0.1 \pm 0.1$ at $S > 8.5\,\mathrm{mJy}$. As this residual bias is small, and comparable in size to its own 1-σ uncertainty, I chose not to make any corrections to the over-density parameter reported here, but rather simply note its existence.

Secondly, I crudely tested what effect removing sources with $S/N \leq 4$ and $S/N \leq 4.5$ has on this over-density calculation as some of these LABOCA sources were undetected in all of the SPIRE images (see Section 4.2.1). As this SNR regime is close enough to the detection threshold adopted here, the completeness corrections and surveyed area should be fairly similar. Removing these $S/N > 4$ and $S/N > 4.5$ sources, I derived over-density parameters of $\delta = 1.0 \pm 0.3$ and $\delta = 0.7 \pm 0.2$, respectively. Thus, these changes suggest that the over-density above $> 8.5\,\mathrm{mJy}$ is comprised of relatively secure LABOCA detections and that the inclusion of possibly spurious sources is not affecting the measurement.

Thirdly, I tested the effects that cosmic variance might have on the ultra-red galaxy and LESS images. To achieve this, I generated 100, $2^\circ \times 2^\circ$ images populated with $\sim$ 1,500 clustered simulated sources, i.e. the expected number of sources within the image area above $> 3.5\,\mathrm{mJy}$ (Weiß et al., 2009). The clustering of these simulated sources was governed by the two-point correlation function defined as:

$$\omega = A_\omega \left(\theta^{1-\gamma} - C \right), \tag{3.6}$$

where θ is the radial distance from a given source and $A_\omega = 0.011 \pm 0.0046$, $C = 12.4 \pm 2.5$ and $\gamma = 1.8$ are the best-fitting power-law parameters to the observed clustering given in Weiß et al. (2009). For each of the 100 simulated images, I randomly drew a different realisation of ω based on the uncertainties of these best-fitting parameters. To encode this clustering on a simulated image, I adopted the following procedure:

1. The first random source position (obtained from a pseudo-random number generator) is inserted as a delta function into the two-dimensional simulated image.

2. I then derive a two-dimensional probability distribution for this first source,

$$P\left(\omega_1\right) = 1.0 + \omega_1(\theta),$$

   where ω_1 is given by Equation 3.6 and θ is the radial distance to this first source. Upon collapsing this into a 1-dimensional array, I calculate its inverse cumulative distribution function (CDF or Φ), which is used to sample the second random position.

3. This second source is then inserted into the simulated image and its two-dimensional

probability distribution, $P(\omega_2)$, is calculated and combined with the first one thus

$$P(\omega) = \max\{P(\omega_1), P(\omega_2)\}.$$

The 'max' operator is utilised here in order to ensure that a 'sphere of influence' around $P(\omega_1)$ is kept upon the addition of another clustered source.

4. The third random source is then sampled from the collapsed CDF of $P(\omega)$ and this procedure is repeated until all of the simulated sources have been added.

A 'χ-by-eye' analysis of Figures 23–24 in Scott et al. (2006) suggests that A_ω increases by $\approx 60\%$ as the flux density increases by $\approx 40\%$ (i.e. over $S = 5$–$7\,\mathrm{mJy}$). Although this measurement was highly uncertain due to the small number of bright DSFGs that contributed to it, this amplitude rise is caused by brighter and thus – modulo chance gravitational lensing – more massive DSFGs lying in denser (or *more* clustered) regions. Therefore, to err on the side of caution, I increased the clustering strength (A_ω) by a factor of $3\times$ to conservatively accommodate the increase in flux density from $S = 3.5$–$8.5\,\mathrm{mJy}$, the threshold at which number-count comparisons are made in this chapter.

As a sanity check that the clustering procedure had worked properly, I examined whether the best-fitting parameters to Equation 3.6 were successfully recovered in these simulated images by using the Landy & Szalay (1993) estimator defined as:

$$\hat{\omega} = \frac{DD}{RR} - 1, \tag{3.7}$$

where DD is the number of pairs of sources within $\theta + \Delta\theta$ from each source and RR is the number of pairs of sources within $\theta + \Delta\theta$ from a random position. Figure 3.12 shows that the simulated images do indeed encode the clustering governed by Equation 3.6.

To measure the cosmic variance, I then extracted a randomly placed, LESS-sized sub-image from each of these larger simulated images. The standard deviation of the number of sources measured in each of these 100 sub-images incorporates (in quadrature) the Poisson noise and the noise from cosmic variance, which I estimate to be 19.0% – far smaller than contribution from Poisson noise (49.5%). This value is consistent with the field-to-field variation deduced by Cowley et al. (2015) using light-cones calculated from GALFORM (Cole et al., 1994, 2000; Lacey et al., 2016) over a slightly larger area of $\mathcal{A} = 0.5\,\mathrm{deg}^2$, compared to $\mathcal{A} \approx 0.35\,\mathrm{deg}^2$ for LESS.

To derive the cosmic variance term for the 22 ultra-red galaxies, I adopt a slightly different approach to LESS as these are 22, essentially independent observations, albeit smaller in size. For each ultra-red galaxy, I extracted a randomly placed sub-image from a randomly chosen simulated image, ensuring that the area of a given sub-image matched that shown in Figure 3.7. By measuring the total number sources contained within these 22 sub-images and repeating this process 1,000 times, I was able to determine a cosmic variance contribution for these ultra-red galaxies of 12.8%, again significantly smaller than that from the Poisson noise (36.6%).

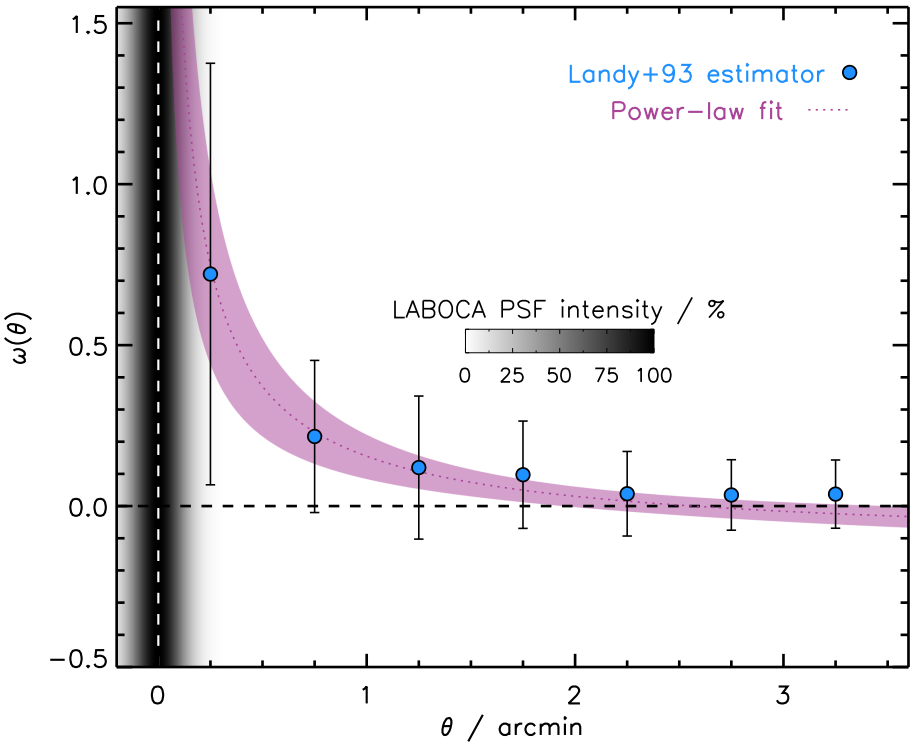

Figure 3.12: The Landy & Szalay (1993) estimator, given by Equation 3.7, on the $2° \times 2°$ simulated images (blue circles). The uncertainty bars represent the 1-σ scatter between the 100 simulated images. The model two-point correlation function (pink dotted line) agrees well with the estimator, especially at $\theta \lesssim 2'$. The slight excess of the estimator compared to the model at $\theta \gtrsim 3'$ is due to the area differences between these simulated images and LESS, i.e. a factor of $\sim 4\times$. The LABOCA PSF ($\theta \approx 19''$) is shown for reference (black).

Key Point 3.7

Thus, as neither of the cosmic variance terms contribute significantly to the overall error budget, their effect on the reported over-density parameter is small. Adding these terms in quadrature, the errors on the over-density parameter change from $\delta = 1.0^{+0.3}_{-0.3}$ to $\delta = 1.0^{+0.4}_{-0.4}$.

Mundane, not Cosmic, Under-Density in LESS

It is often claimed that LESS exhibits an under-density of DSFGs – resulting in the introduction, and use of (Swinbank et al., 2014; Dannerbauer et al., 2014), a multiplicative 'fudge-factor' (of $\sim 2\times$) to the number counts presented in Weiß et al. (2009). An 'adjustment' of this magnitude would require me to significantly lower the value of the over-density parameter, if necessary.

This perceived under-density is concluded against the number counts presented in SHADES as it was the largest, like-for-like survey at the time. Recently, the Subaru/XMM-Newton Deep Field (SXDF) – one of the two extra-galactic fields in SHADES – has been re-imaged during the S2CLS, which has improved the sensitivity of this field by a factor of $\gtrsim 2\times$.

Using these new data, however, I was only able to match 27/60 (45%) of the SXDF detections[5] to a counterpart[6] in the S2CLS. These 'matched' sources have typical offsets of $4.7 \pm 3.0''$ and de-boosted flux densities that are on average $(1.6 \pm 0.1)\times$ greater than those reported in the S2CLS. The 33/60 (55%) 'unmatched' detections have a broad range of *de-boosted* flux densities of $S = 3.1$–$22.0\,\mathrm{mJy}$. These values from SHADES are typically a factor of $\approx 4\times$ higher than measurements that I made at their respective positions in the S2CLS image.

Thus, if these results were to be replicated for the Lockman Hole East – the second extra-galactic field in SHADES – then it would appear that the spurious fraction of sources and/or flux-boosting corrections have been miscalculated. Taken together, these findings suggest that the claimed under-density in LESS, and apparent deficit of bright DSFGs, is unlikely to be true and unlikely to be biasing the over-density parameter of ultra-red galaxies. Furthermore, these findings are very reminiscent of those discussed by Condon (2007), who resolved the inconsistencies amid differing reports of the radio number counts at the time. Thus, in homage, the variance in the number counts between SHADES and LESS appears to be 'mundane' (likely due to instrumental and analysis effects) rather than 'cosmic'.

[5] http://www.roe.ac.uk/ifa/shades/dataproducts.html.
[6] https://zenodo.org/record/57792#.WOtnkRiZNE5.

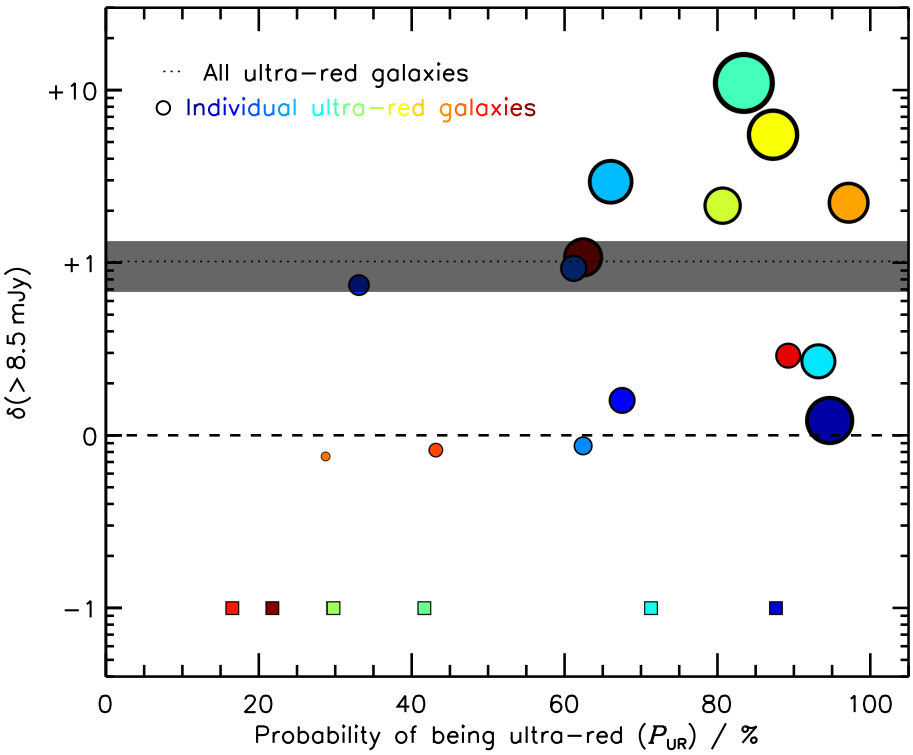

Figure 3.13: Over-Density parameter above $S' > 8.5\,\mathrm{mJy}$ versus ultra-red probability for all 22 ultra-red galaxies. The mean over-density and its uncertainty at this flux-density threshold is shown as a black dotted line and black shaded region, respectively. This figure shows that approximately half of these ultra-red galaxies have $P_{\mathrm{UR}} \lesssim 68\%$ once their SPIRE flux densities have been re-measured at their respective LABOCA positions. Furthermore, ultra-red galaxies that have a higher ultra-red probability contribute more to the mean over-density at this flux-density threshold. **Note.** The size and colour that each ultra-red galaxy has is described in the caption of Figure 4.4.

3.4.4 Ultra-Red Probability

As can be seen in Table B.1, half of the ultra-red galaxies have SPIRE photometry that is *just* consistent with them being ultra-red. This motivated me to derive, for the first time, a probability that a DSFG is actually ultra-red (P_{UR}) based on its SPIRE photometry. To achieve this, for each DSFG I drew 10,000 realisations of the SPIRE photometry from a Gaussian distribution and determined the number of times that these realisations met the ultra-red criteria outlined in the previous chapter[7]. This probability incorporates the photometric errors from all SPIRE bands and can thus be used to generate a subset of robust ultra-red galaxies.

In Figure 3.13, I show how the over-density parameter above $S' > 8.5\,\mathrm{mJy}$ varies as a function of ultra-red probability.

[7]These probabilities were calculated by assuming symmetric colour uncertainties, and do not take account of the bias discussed in the previous chapter that more bluer galaxies will have had their colours scattered red-ward, into the ultra-red category, than vice-versa. However, these are only being used as a guide to the likelihood of a galaxy being ultra-red.

Key Point 3.8
Thus, ultra-red galaxies that have a higher ultra-red probability typically have a much higher over-density parameter. Furthermore, ultra-red galaxies that are over-dense (i.e. those with $\delta > 0$) all have an ultra-red probability greater than $P_{\rm UR} \gtrsim 30\%$, with this lower limit reflecting sources that lie close to the S_{500}/S_{250} and S_{500}/S_{350} flux-density ratio boundaries.

Above a probability of $P_{\rm UR} \gtrsim 60\%$, only three ($\approx 20\%$) of these ultra-red galaxies have environments that are consistent with being under-dense (i.e. $\delta < 0$). Such a low fraction of under-dense environments suggests that using this novel ultra-red-probability technique, in conjunction with 870-μm imaging, provides a robust method with which to signpost over-densities in the distant Universe.

3.4.5 SPIRE Flux-Density Ratios

I analysed the S_{500}/S_{250} and S_{500}/S_{350} flux-density ratios of the ultra-red galaxies and their surrounding DSFGs, which I show in Figure 3.14. Recall that in all further analysis I exclude 16 LABOCA detections as I am unable to meaningfully constrain their photometric redshifts. This leaves me with $86 - 16 = 70$ surrounding DSFGs with $S/N > 3.5$ around the 22 ultra-red galaxies.

Figure 3.14 illustrates that only 7% (or 5) of these surrounding DSFGs meet the ultra-red galaxy criteria outlined in the previous chapter. If I relax the > 3.5-σ_{500} criterion to $> 1\sigma_{500}$, the fraction that meet the ultra-red criteria increases to 17% (or 12), obviously at the expense of being less reliable.

Surrounding field DSFGs have median colours of $(S_{500}/S_{250})_{1/2} = 1.1$ and $(S_{500}/S_{350})_{1/2} = 0.9$, with IQRs of $S_{500}/S_{250} = 0.7$–1.4 and $S_{500}/S_{350} = 0.7$–1.2. If I isolate the surrounding field DSFGs that are assumed to be physically 'associated' to their signpost ultra-red galaxies (see Section 3.4.6), I notice a redder change as the S_{500}/S_{250} colour increases to a median $(S_{500}/S_{250})_{1/2} = 1.4$ with IQR $S_{500}/S_{250} = 1.2$–1.5. However, I see no appreciable change in the S_{500}/S_{350} colour. As can be seen in Figure 3.14, this can be explained by five of the signpost ultra-red galaxies narrowly missing the ultra-red criteria once their SPIRE photometry has been re-measured at their refined LABOCA position.

If I go one step further and isolate the associated galaxies that contribute to the over-density at $S' > 8.5\,{\rm mJy}$, I find that they have even redder median colours of $(S_{500}/S_{250})_{1/2} = 1.0$ and $(S_{500}/S_{350})_{1/2} = 1.4$. This is in part due to the exclusion of SGP−433089 and its associated galaxies, which – having had its SPIRE photometry re-measured at the position of its LABOCA emission – has a low ultra-red probability. I remind the reader that this is shown Figure 3.13, where galaxies with a higher ultra-red probability, and are thus more likely to be distant (or satisfy the ultra-red criteria), are contributing more to the over-density parameter at $S' > 8.5\,{\rm mJy}$.

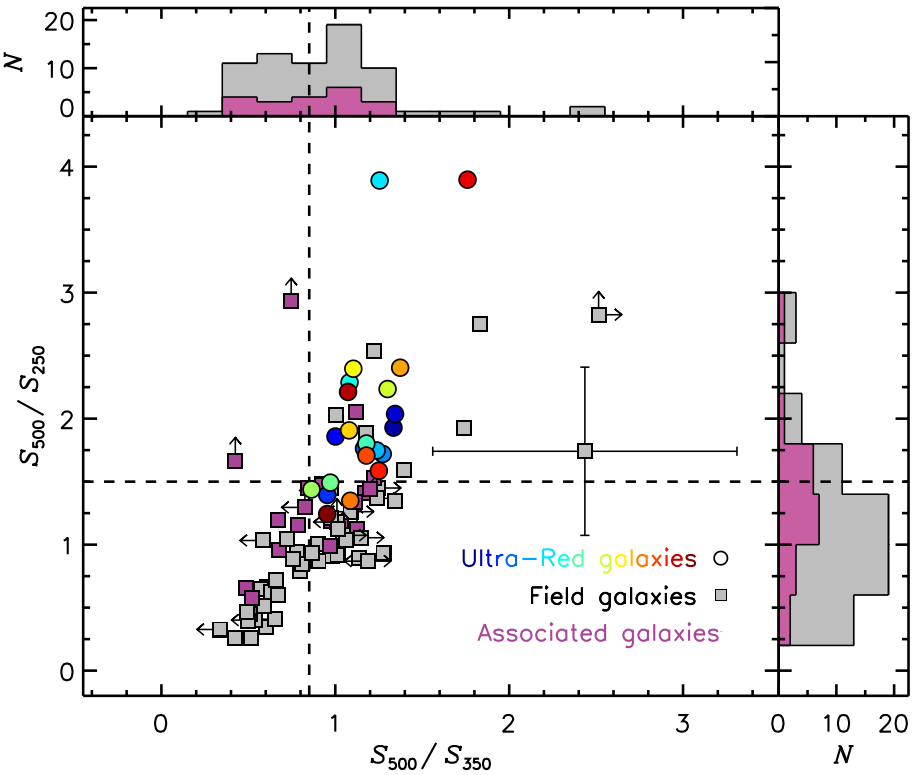

Figure 3.14: S_{500}/S_{350} versus S_{500}/S_{250} for sources that have at least one > 1-σ detection in any SPIRE passband. I show the ultra-red galaxies and surrounding DSFGs as circles and squares, respectively. Surrounding DSFGs that are physically 'associated' (i.e. lie within $|\Delta z| \leq 0.5$) of their signpost ultra-red galaxies are highlight in pink. The colour-cut limits ($S_{500}/S_{250} \geq 1.5$ and $S_{500}/S_{350} \geq 0.85$) that an ultra-red galaxy is required to have are shown as black dashed lines (i.e. the top-right region of the plot). Five ultra-red galaxies narrowly miss the S_{500}/S_{250} colour-cut threshold, three by 0.1 and two by 0.2. This shift towards bluer colours is due to the larger 250-μm correction due to the refined positions at which I made the SPIRE photometric measurements. **Note**. A representative colour uncertainty is shown and I use arrows to highlight 1-σ limits where applicable.

3.4.6 Physical Associations to Signpost Ultra-Red Galaxies

To quantify whether the surrounding DSFGs responsible for the over-density are 'associated' with their signpost ultra-red galaxy – thus comprising a candidate proto-cluster – I analysed their photometric redshifts.

The simplest analysis I could perform is to calculate the absolute difference between the photometric redshifts of the surrounding galaxies ($z_{\rm s}$) relative to their respective ultra-red galaxies ($z_{\rm UR}$). Therefore, I defined a parameter given by:

$$|\Delta z_{\rm UR}| = |z_{\rm UR} - z_{\rm s}|\,, \tag{3.8}$$

in order to determine the fraction of galaxies that lie at, or below, some association threshold of $|\Delta z|_{\rm thresh}$. However, determining an association threshold is complicated by the difficult task of actually determining photometric redshifts using FIR photometry alone.

For instance, to account for the fraction $\phi = \delta/(1+\delta) = 0.5^{+0.6}_{-0.4}$ of galaxies responsible for the over-density of $\delta = 1.0^{+0.6}_{-0.5}$ at $S' > 8.5\,{\rm mJy}$, I would require an association threshold of $|\Delta z|_{\rm thresh} \leq 0.65$. Put another way, I have an over-density of $\delta = 1.0$, comprised of 24 DSFGs with de-boosted flux densities $S > 8.5\,{\rm mJy}$. Therefore, I expect $\phi = 0.5$ (or 12) of these DSFGs to be responsible for this over-density, which I can only achieve if the association threshold is (arbitrarily) set to $|\Delta z|_{\rm thresh} \leq 0.65$.

If, however, I choose an association threshold dependent on the median fitting errors for the ultra-red galaxies and surrounding galaxies, i.e.

$$|\Delta z|_{\rm thresh} \leq \sqrt{\left(\sigma^2_{z_{\rm UR}}\right)_{1/2} + \left(\sigma^2_{z_{\rm s}}\right)_{1/2}} \approx 0.52,$$

I am unable to account for $\approx 20\%$ of the galaxies responsible for the over-density at $S > 8.5\,{\rm mJy}$.

If I go one step further and add in quadrature the intrinsic scatter of the three template SEDs to these median fitting errors, then the association threshold would increase to $|\Delta z|_{\rm thresh} \leq 0.93$.

As can be seen in Figure 3.15, where I show the the fraction of galaxies responsible for the over-density against the association threshold, $|\Delta z|_{\rm thresh} \leq 0.93$ includes all of the galaxies responsible for the over-density but is highly likely to be contaminated by unassociated (or 'field') galaxies (15%).

Both the former and latter association thresholds are too large to make any reliable claim of association. Therefore, as a compromise between reliability and knowingly missing some of the galaxies responsible for the over-density at $S' > 8.5\,{\rm mJy}$, I chose an association threshold of $|\Delta z|_{\rm thresh} \leq 0.52$. Enforcing this association on the entire catalogue, I found that half of the ultra-red galaxies have at least one associated DSFG.

I illustrate the results of this analysis in the top-panel of Figure 3.16, where I have chosen to plot $\Delta z_{\rm UR}$ against the radial distance between surrounding galaxies and their signpost

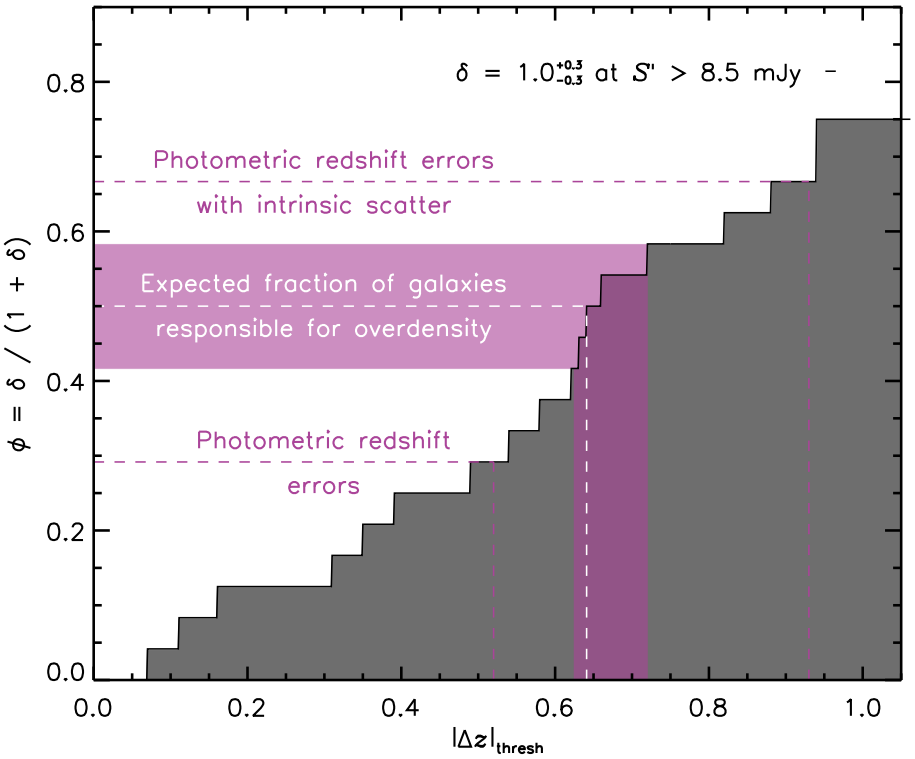

Figure 3.15: The fraction of galaxies responsible for a given over-density as a function of photometric redshift association threshold. The over-density parameter at $S' > 8.5\,\mathrm{mJy}$ suggests that $\phi = 0.5^{+0.2}_{-0.2}$ of the surrounding galaxies must be associated to their respective ultra-red galaxies, which is achieved if the association threshold is set to $|\Delta z|_{\mathrm{thresh}} \leq 0.65$. I under-predict the number of associated galaxies for this over-density parameter if the association threshold is based on the median photometric redshift errors of the ultra-red galaxies and surrounding galaxies. This is then over-predicted if I include the intrinsic template SED scatter in quadrature. This motivated me to choose, as a compromise, an association threshold of $|\Delta z|_{\mathrm{thresh}} \approx 0.5$. This increases the reliability of 'associated' galaxies at the expense of knowingly missing some of the contribution to the over-density at $S' > 8.5\,\mathrm{mJy}$.

ultra-red galaxies ($\Delta r_{\rm UR}$). The majority of the field galaxies (i.e. those not within the association threshold) are at a lower redshift compared to their respective signpost ultra-red galaxies. This is to be expected as the ultra-red galaxies have a high median photometric redshift of $z_{1/2} = 3.2 \pm 0.2$ with an IQR of $z = 2.8$–3.6, whereas the field galaxies lie at a median redshift of $z_{1/2} = 2.3 \pm 0.1$ with an IQR of $z = 1.8$–2.8 – in good agreement with the general ~ 850-μm population (Chapman et al., 2005; Simpson et al., 2014).

Key Point 3.9
The top-panel of Figure 3.16 also shows that half of the associated galaxies are within $\Delta r_{\rm UR} \lesssim 3'$ – suggesting that there is a slight dependence on association with proximity, in agreement with the annuli analysis of their number counts in Section 3.4.1.

In terms of proper radial distances (derived at the redshift of the signpost ultra-red galaxies), these galaxies are distributed within scales of $\Delta r_{\rm UR} \sim 2\,$Mpc. On average, they are separated by $\overline{\Delta r_{\rm UR}} = 1.6 \pm 0.5\,$Mpc with an IQR of $\Delta r_{\rm UR} = 1.0$–$2.2\,$Mpc. There appears to be no dependence on the redshift of the ultra-red galaxies and the average radial separation from $z = 2$–4.

Furthermore, between annuli shells of proper radial distance $\Delta r_{\rm UR} = 0.3$–$1.3\,$Mpc and 2.3–$3.3\,$Mpc, I see a slight average difference in luminosity of $\Delta L_{\rm FIR} = (3 \pm 2) \times 10^{12}\,L_\odot$ for the associated galaxies.

Key Point 3.10
This small increase in luminosity perhaps hints at the existence of a large-scale mechanism capable of simultaneously enhancing the star formation – modulo chance gravitational lensing – across multiple galaxies within a dense environment (e.g. Oteo et al., 2017a).

Photometric Redshift Association Sanity Check

In order to test the validity of the simplistic method for photometric redshift association presented above, I calculated the same association threshold using Equation 3.8 but replacing $z_{\rm UR}$ and $z_{\rm s}$ with galaxy pairs i and j in a LABOCA image k as follows:

$$|\Delta z_{i,j}|_k = |z_i - z_j|_k \quad \forall j > i. \tag{3.9}$$

I then compared the distribution of Equation 3.9 to a control sample, which was made by replacing all galaxies except for the signpost ultra-red galaxies with a random DSFG drawn from the general 870-μm photometric redshift distribution given in Simpson et al. (2014).

This alternative analysis is illustrated in the bottom-panel of Figure 3.16, which shows that a similar excess of $\phi \approx 0.3$ is found to that of the previous analysis. Furthermore, this

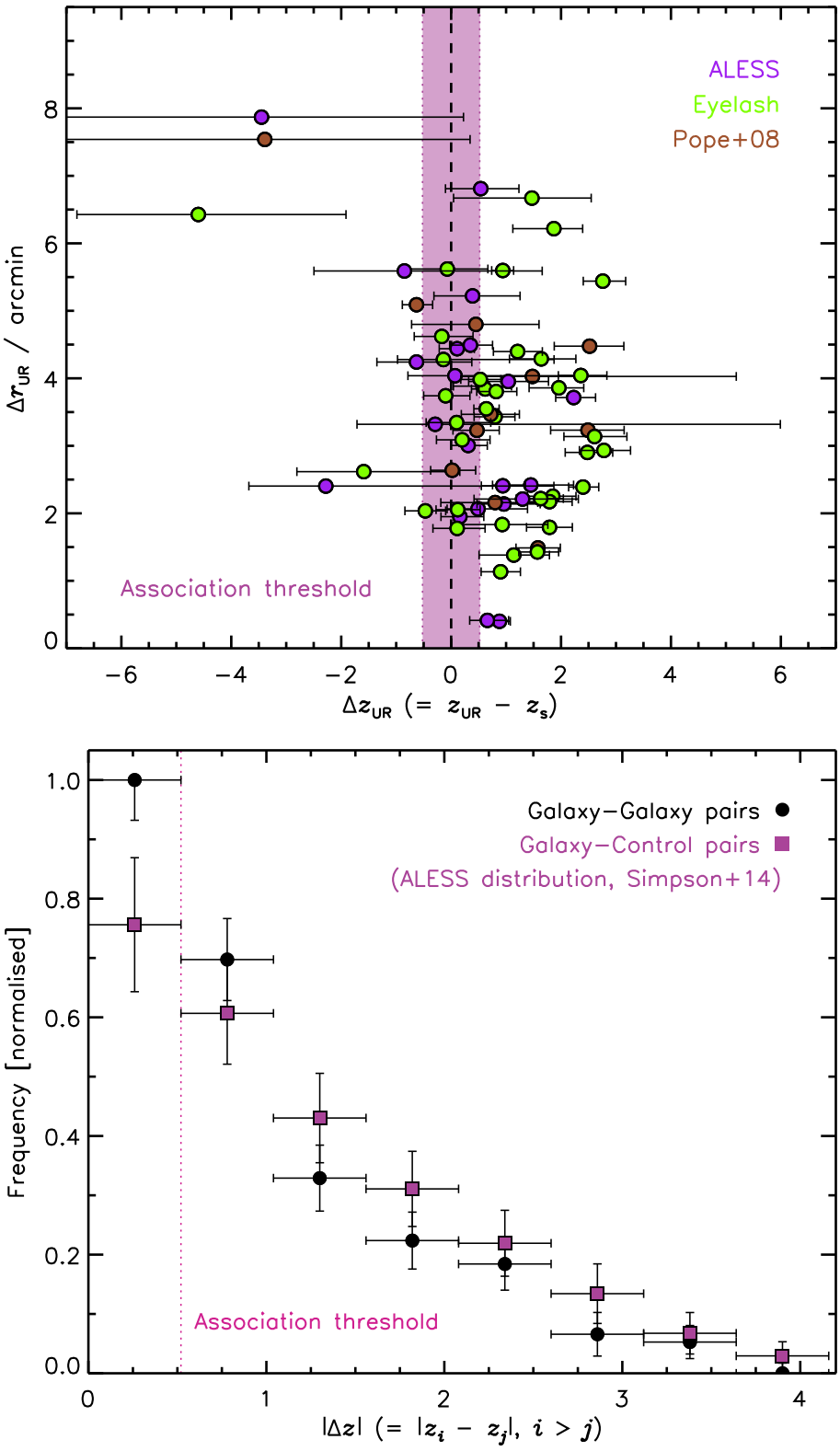

Figure 3.16: Top: radial distance of field galaxies to their respective ultra-red galaxies as a function of photometric redshift difference ($\Delta z_{\rm UR}$). Photometric redshift errors are deduced from the $\chi^2_{\rm min} + 1$ values and are not added in quadrature with the intrinsic template SED scatter. The tail of sources with $\Delta z \geq 0$ reflects the fact that most galaxies are foreground to these signposts, which sit at a median redshift of $z_{1/2} = 3.2$. The pink region indicates the threshold boundaries for association, in which a fraction $\phi \approx 0.3$ of these field DSFGs lie. The large photometric redshift uncertainties highlight the difficulty in ...

Figure 3.16 (continued from previous page): ... accurately constraining the redshifts of these DSFGs. Finally, I colour-code each DSFG to indicate the best-fitting template SED adopted. **Bottom:** alternative analysis of the absolute photometric redshift differences $|\Delta z_{i,j}|$ for all of the images. There is a similar association excess to that of the top panel.

alternative analysis highlights that there is a deficit of $|\Delta z| \geq 1$ pairs – indicating that the surrounding galaxies are preferentially associated to their ultra-red galaxies. However, this sanity check does not indicate which of the surrounding galaxies are associated to their respective ultra-red galaxies.

To conclude, the similarities between the findings of both methods suggest that I can trust the previous analysis.

3.4.7 Consequent Fate at $z \sim 0$

I now briefly discuss the eventual fate of the environments around ultra-red galaxies, which have at least one associated galaxy within them, i.e. approximately half of the sample.

The associated galaxies have a median rest-frame luminosity of $(L_{\rm FIR})_{1/2} = 10^{12.7}\,L_\odot$ with an IQR of $L_{\rm FIR} = 10^{12.6}$–$10^{12.9}\,L_\odot$. These rest-frame luminosities were converted into SFRs using

$$\psi \approx 1.7 \times 10^{10} L_{\rm FIR}/L_\odot\,M_\odot\,{\rm yr}^{-1},$$

which assumes a Salpeter IMF (Kennicutt, 1998) – noting, however, that a top-heavy IMF in distant DSFGs has previously been suggested (Baugh et al., 2005; Romano et al., 2017). This results in a high median SFR of $\psi_{1/2} = 1{,}000 \pm 200\,M_\odot\,{\rm yr}^{-1}$ for the associated DSFGs and an average total SFR of $\Psi = \sum\psi = 2{,}200 \pm 500\,M_\odot\,{\rm yr}^{-1}$ within the environments around these ultra-red galaxies.

I derived a median molecular gas mass of $(M_{\rm gas})_{1/2} = 1.7 \times 10^{11}\,M_\odot$ with an IQR of $M_{\rm gas} = 9.5 \times 10^{10}$–$2.1 \times 10^{11}\,M_\odot$ for these associated and signpost ultra-red galaxies using their FIR photometry and an appropriate scaling factor given by:

$$\alpha_{850} \equiv \frac{L_{850}}{M_{\rm gas}} = (1.0 \pm 0.5) \times 10^{20}\,{\rm erg\,s^{-1}\,Hz^{-1}}\,{M_\odot}^{-1} \tag{3.10}$$

where L_{850} is the rest-frame luminosity at 850 μm (obtained from the best-fitting template SEDs) and α_{850} (the appropriate scaling constant) is determined from a sample of 28 DSFGs with CO(1–0) measurements at $z \lesssim 3$ (Scoville, 2013; Scoville et al., 2014).

Similar to the slight increase in the luminosity of associated galaxies that are closer to their respective signpost ultra-red galaxies (see Section 3.4.6), the signpost ultra-red galaxies themselves have slightly elevated luminosities, modulo chance gravitational lensing, compared to their associated galaxies. The signpost ultra-red galaxies also have slightly elevated average gas masses of $\overline{M_{\rm stars}} = (2.5 \pm 1.2) \times 10^{11}\,M_\odot$, which is reminiscent

of present-day massive ETGs that dominate the centres of present-day galaxy clusters (Kelvin et al., 2014).

Key Point 3.11
Taken together, these total SFRs ($\Psi \sim 2{,}000 M_{\odot}\,\mathrm{yr}^{-1}$) and total gas masses ($\sum M_{\mathrm{gas}} \sim 5 \times 10^{11}\,M_{\odot}$) are consistent with those expected for high-redshift candidate proto-clusters. They support a scenario wherein these galaxies form the bulk of their stellar mass ($\sim 10^{11}\,M_{\odot}$) quickly ($\lesssim 1\,\mathrm{Gyr}$) and at high redshift ($z \sim 3$) – evolving passively to eventually populate the centres of massive, present-day galaxy clusters (Thomas et al., 2005, 2010; Fassbender et al., 2011; Snyder et al., 2012).

However, without optical/NIR imaging of these environments, I am potentially missing many hundreds to thousands of NIR galaxies, each of which could contribute $M_{\mathrm{stars}} \approx (10^9$–$10^{11})$-$M_{\odot}$ worth of stars to these final system (Overzier et al., 2009b; Casey et al., 2015). Thus, the eventual stellar masses of these systems remain largely unconstrained and all results presented here should be regarded as firm lower limits.

Finally, I performed a crude space density calculation of these candidate proto-clusters by adjusting the redshift limits used by Equation 2.10 in the previous chapter to $2 \lesssim z \lesssim 6$. These new limits were motivated by the last epoch of virialized galaxy clusters (Casey, 2016) and the highest ultra-red galaxy redshift measured (Fudamoto et al., 2017; Zavala et al., 2018), respectively.

Key Point 3.12
A space density of $\rho \sim 3{\times}10^{-6}\,\mathrm{Mpc}^{-3}$ was derived for these ultra-red galaxies within $2 \lesssim z \lesssim 6$ assuming a star-formation lifetime of $t_{\mathrm{burst}} = 100\,\mathrm{Myr}$. This roughly equates to the space density of $z < 0.5$ galaxy clusters with DM halo masses of $M_{\mathrm{halo}} \sim 4 \times 10^{14}\,M_{\odot}$, i.e. 'Fornax-/Virgo-type' galaxy clusters (Chiang et al., 2013; Bahcall & Cen, 1993).

Although, it should be noted that perhaps only 20–40% of all proto-clusters within $2 \lesssim z \lesssim 6$ are actually rich in DSFGs (Casey, 2016).

However, as can be seen in Figure 4.4 and Figure 3.13, not all of these ultra-red galaxies reside in over-dense environments. In fact, I estimate that only $33 \pm 8\%$ of this sample have over-density parameters above $\delta > 1$ at 8.5 mJy. Therefore, I scale the space density of ultra-red galaxies accordingly to derive a proto-cluster space density of $\rho \sim 9{\times}10^{-7}\,\mathrm{Mpc}^{-3}$, consistent with $z < 0.5$ galaxy clusters with DM halo masses of $M_{\mathrm{halo}} \sim 8 \times 10^{14}\,M_{\odot}$, or 'Virgo-/Coma-type' galaxy clusters.

3.4.8 Remarks on a Handful of Ultra-Red Galaxies

I now discuss some of the most exciting and/or over-dense environments around these ultra-red galaxies, each of which clearly warrants further exploration. Recall that the small

areas and varying r.m.s. levels of each image makes all further analysis heavily subject to the effects of cosmic variance.

- *SGP−93302*: is the deepest image presented within this chapter, reaching an average PSF-filtered r.m.s. of $\overline{\sigma_{870}} = 1.7\,\mathrm{mJy}$. This 500-$\mu$m riser has a de-boosted flux density of $S_{870} = 30.9 \pm 1.3\,\mathrm{mJy}$ and an estimated photometric redshift of $z = 3.6^{+0.2}_{-0.1}$. One (15%) of its surrounding DSFGs is an equally bright DSFG at $z = 3.4^{+0.4}_{-0.3}$ with a de-boosted flux density of $S_{870} = 31.0 \pm 1.9\,\mathrm{mJy}$. This associated DSFG also meets the strict criteria of being an ultra-red galaxy and is catalogued in the previous chapter as SGP−261206 and is reported to lie at $z = 4.2$ by Fudamoto et al. (2017). Such an environment of robust ultra-red galaxies warrants spectroscopic follow up and high-resolution imaging to explore the morphologies of its constituents. This image shows no particular over-/under-density compared to LESS in the low flux-density regime, but it does show a 1-σ excess at flux-density thresholds of $S' > 10\,\mathrm{mJy}$.

- *SGP−354388*: is discussed in-depth by Oteo et al. (2017a), but here I revised the 870-μm flux density of this extraordinary DSFG to $S_{870} = 33.0 \pm 1.2\,\mathrm{mJy}$ – assuming that it can be de-blended into two, LABOCA point sources, separated by $\approx 25''$. The multiplicitous nature of this source is also seen at higher resolutions, where ALMA 3-mm continuum images resolve the central fragments further, into three or more components. Like SGP−93302, this ultra-red galaxy only shows an over-density of sources at high flux-density thresholds, $S' > 10\,\mathrm{mJy}$. I am only able to associate two of its nine surrounding DSFGs, although a further two DSFGs have unconstrained photometric redshifts. Its photometric redshift is refined to $z = 4.2 \pm 0.2$ using improved SPIRE measurements made at the 870-μm position, which is consistent with its spectroscopic redshift, $z_{\mathrm{spec}} = 4.002$.

- *SGP−433089*: marks the most over-dense field in this sample, which I place at a distance of $z = 2.5 \pm 0.2$. I associate six of its ten surrounding DSFGs, noting that one of its surrounding DSFGs has an unconstrained photometric redshift. This image shows a deficit of bright DSFGs, compared to the other images explored here and as such does not contribute to the over-density parameter at $S > 8.5\,\mathrm{mJy}$. SGP−433089 is the brightest source within the image and has a de-boosted flux density of $S_{870} = 7.2 \pm 1.1\,\mathrm{mJy}$. The mean de-boosted flux density of the surrounding DSFGs is $\overline{S_{870}} = 4.7\,\mathrm{mJy}$. The detection of these relatively faint DSFGs is due to the low average r.m.s., $\overline{\sigma_{870}} = 1.1\,\mathrm{mJy}$, which allows me to confidently report an over-density factor of $\delta = 0.7^{+0.9}_{-0.6}$ at a flux-density threshold of $S' > 4\,\mathrm{mJy}$.

- *ADFS-27*: was shown to lie at $z \approx 5.7$ using ALMA 3-mm scans (Riechers et al., 2017) – drastically different to the photometric redshift estimate that I have provided in this chapter ($z_{\mathrm{phot}} = 4.4^{+0.4}_{-0.3}$). Riechers et al. (2017) derive a dust temperature of $T_{\mathrm{dust}} \approx 55\,\mathrm{K}$ for this source, which highlights the strong degeneracy between temperature and redshift. For instance, if I were to use a hotter, but, on average, less accurate template SED for ultra-red galaxies (such as the HFLS3 template SED),

I would revise the photometric redshift for this ultra-red galaxy to $z_{\rm phot} = 5.9^{+0.5}_{-0.4}$, i.e. to within 1σ of its reported spectroscopic redshift. This source has two associated DSFGs that lie within $\Delta z \approx 0.5$ - making it an ideal high-redshift, candidate proto-cluster to further follow up. Finally, the SPIRE flux densities for this ultra-red galaxy reported here are higher by $\approx$ 2–5 mJy than those presented in Riechers et al. (2017), i.e. from the *Her*MES xID250 catalogue from which this source was originally selected. This is due to re-measuring these flux densities at the position of the LABOCA peak, resulting in photometry that makes ADFS−27 appear less red.

- *G09-83808*: is a gravitationally lensed ($\mu \approx 9$) ultra-red galaxy with a photometric redshift estimate that is also catastrophically lower that its spectroscopic redshift. Recent work by Zavala et al. (2018) shows that this galaxy actually resides at $z \sim 6$, rather than $z_{\rm phot} = 4.45^{+0.4}_{-0.3}$ as presented here. Again, this DSFG highlights the temperature-redshift degeneracy as by adopting HFLS3 again yields a photometric redshift that is more consistent with its spectroscopic redshift, namely $z_{\rm phot} = 6.2^{+0.5}_{-0.4}$.

3.4.9 Caveats

- A larger sample of ultra-red galaxies imaged to a uniform depth of $\approx$ 1.2 mJy could improve the fidelity and thus reduce the number of potentially spurious sources existing in this current sample. A uniformly wide imaging survey of these ultra-red galaxies would also allow the detection of less luminous DSFGs in the vicinity of the ultra-red galaxies that currently have shallow data. Although the fidelity, area surveyed, flux-boosting and completeness corrections as well as the high flux-density threshold adopted here attempt to reduce the influence of the the varying image-to-image r.m.s. values on the over-density parameter quoted here, these differences may still affect the conclusions of this chapter. For instance, if all of these parameters are systematically lower (such as the fidelity) or higher (such as the area surveyed, flux boosting and completeness) by, say, 10%, then the over-density parameter at $S > 8.5$ mJy drops significantly to $\delta = 0.2 \pm 0.1$. Furthermore, the small number of sources above the high flux-density threshold adopted here as a result of the varying r.m.s. values drives the Poisson noise up on the over-density parameter quoted here. Hence, a uniformly wide imaging survey for these ultra-red galaxies would alleviate these uncertainties.

- The intrinsic luminosity of the associated DSFGs will depend on the gravitational lensing that each may have suffered. Although every effort has been made to avoid lensing in the selection of the ultra-red galaxies, as outlined in the previous chapter, a fraction ($\sim$ 25%) of these ultra-red galaxies *are* gravitationally magnified by chance alignments (Oteo et al., 2017b). Thus the SFRs and average total SFRs are upper limits, although the effect of an invariant IMF in these galaxies likely has a greater impact.

- Using the 850-μm number counts from S2CLS increases the $S' > 8.5$-mJy

over-density parameter to $\delta_{\rm S2CLS} = 2.1^{+0.6}_{-0.5}$. Although the errors remain similar (as they are dominated by the Poisson noise), the over-density is $\gtrsim$ 2-σ higher than that determined using LESS as a comparison blank-field survey.

- The over-density parameter reported here does not include the small ($\approx$ 20%) contribution from cosmic variance. Including this effect changes the uncertainty on the over-density from $\delta = 1.0^{+0.3}_{-0.3}$ to $\delta = 1.0^{+0.4}_{-0.4}$.

- The photometric redshift algorithm is only reliable to $\sigma_{\Delta z} = 0.14(1 + z_{\rm spec})$, which is typically much larger than the errors determined from the $\chi^2_{\rm min} + 1$ values at high redshift. Thus, the fixed association threshold likely underestimates the number of true physical associations. Some DSFGs not associated with an ultra-red galaxies will be falsely assigned until ALMA spectroscopy can improve upon the accuracy of their photometric redshifts.

- Finally, optical/NIR identification of the surrounding LBGs is necessary if I am to accurately constrain the total stellar masses – and thus DM components – of these candidate proto-clusters at high redshift.

3.5 Conclusion

In this chapter, I have presented 870-μm imaging obtained with the LABOCA instrument for a sample of 22 ultra-red galaxies – 12 and 10 from the *H*-ATLAS and *Her*MES imaging surveys, respectively.

Surveying $\approx 0.8\,{\rm deg}^2$ down to an average r.m.s. depth of $3.9\,{\rm mJy\,beam}^{-1}$, I have detected and extracted 86 DSFGs above $S/N > 3.5$ around these 22 ultra-red galaxies. By comparing their number counts to those in LESS, I have reported an over-density parameter of $\delta = 1.0^{+0.3}_{-0.3}$ at $S' > 8.5\,{\rm mJy}$ – suggesting that ultra-red galaxies signpost over-dense regions that are rich in bright DSFGs.

Photometric redshift measurements suggest that over half of these ultra-red galaxies have a surrounding galaxy that is associated to within $|\Delta z| \lesssim 0.5$ and distributed within $\lesssim$ 2-Mpc scales. These 'associated' and ultra-red galaxies have average total SFRs and total gas masses of $\Psi = 2{,}200 \pm 500\,M_\odot\,{\rm yr}^{-1}$ and $\sum M_{\rm gas} \sim 10^{11}\,M_\odot$, respectively, and a space density consistent with that of the most massive ($\sim 10^{15}\,M_\odot$) galaxy clusters at $z < 0.5$. Thus, taken together, it seems very plausible that the associated galaxies around ultra-red galaxies and the ultra-red galaxies themselves will evolve into massive ETGs that populate the centres of rich galaxy clusters at $z \sim 0$.

However, due to the varying image r.m.s. values these results are likely missing a significant contribution from undetected DSFGs. Thus, further $\sim$ 870-μm imaging down to a uniform depth (of $\lesssim 1.2\,{\rm mJy}$) is crucial in order to accurately constrain the FIR contribution to these candidate proto-clusters from less luminous and/or colder DSFGs in their vicinity.

Furthermore, there will be a significant contribution from LBGs that deep optical/NIR

imaging could uncover. Currently, the only NIR coverage of these fields comes from the Visible and Infrared Survey Telescope for Astronomy (VISTA — Sutherland et al., 2015) Kilo-Degree Infrared Galaxy Survey (VIKING — Edge et al., 2013). However, this survey only reaches a 5-σ_K < 21.2-$\mathrm{mag_{AB}}$ depth (in 2-arcsec apertures), which is insufficient for accurately measuring the properties of $z \gtrsim 3$ ($K \gtrsim 23\,\mathrm{mag_{AB}}$) galaxies in the vicinity of ultra-red galaxies.

To combat these issues in the meantime, I will exploit the S2CLS imaging survey in the following chapter to search for a sample of robust ultra-red galaxies with uniformly deep and wide 850-μm data, which I will use to better constrain the FIR contribution from DSFGs in their vicinity. Additionally, there is adequate ($5\sigma_K < 23$–$24\,\mathrm{mag_{AB}}$) optical/NIR coverage with which to study the properties of $z \gtrsim 3$ LBGs within the vicinity of any ultra-red galaxies uncovered in these surveys.

Finally, the 870-μm catalogues and SPIRE/LABOCA cut-outs for this chapter are presented in Appendix B.

Ultra-Red Galaxies within the S2CLS and S2COSMOS

4

'The stars are a free show . . . ' – excerpt from 'Down and Out in Paris and London'

G. Orwell (1903–1950)

4.1 Introduction

In the previous chapter, I showed that the environments around ultra-red galaxies are rich in bright ($S_{870} > 8.5\,\mathrm{mJy}$) DSFGs. Furthermore, the galaxies within these environments each have FIR properties consistent with their eventual membership of a massive ($M_{\mathrm{halo}} \gtrsim 10^{14}\,M_{\odot}$) galaxy cluster at $z \sim 0$. However, substantial variations in the r.m.s. across an individual LABOCA image – exacerbated by up to a factor of 5× on an image-to-image basis – resulted in the measurement of the over-density parameter being based on only 22 DSFGs. Hence, this result was highly subjected to Poisson noise and the 'ensemble' FIR properties of these structures were deemed to be firm lower limits, modulo chance gravitational lensing.

Therefore in this chapter, I will search the S2CLS and S2COSMOS imaging surveys in order to compile a large sample of candidate ultra-red galaxies with *uniform* 850-μm imaging around their environments. Furthermore, as these 850-μm data are deeper and wider, I will also attempt to improve upon the FIR properties previously reported and examine the wider environments around ultra-red galaxies.

Complementary ground-based optical/NIR catalogues will allow me to go one step further than the previous chapter and isolate any NIR galaxies within the environments around ultra-red galaxies. By locating these so-called 'U-/B-band drop-outs', I will examine whether they show traits consistent with residing in an over-dense environment at $z \gtrsim 3$. Such traits include being able to determine whether the formation of the red sequence is happening at a faster rate around ultra-red galaxies than in the field, or whether there is any dependence on stellar mass with proximity to an ultra-red galaxy. If successful in this endeavour, I will have shown that it is possible to answer these questions using optical-through-to-FIR photometry alone. On the contrary, if unsuccessful, then either

there is something incorrect with our understanding in the formation and evolution of massive galaxies as traced by distant DSFGs, or I will have pushed these photometric techniques to their limit.

In the following section, I will describe the SCUBA-2 datasets used and the method that I adopted for selecting ultra-red galaxies. In Sections 4.3–4.4, I will provide a detailed analysis of the optical-through-to-FIR environments around ultra-red galaxies, concluding with a brief summary in Section 4.6.

4.2 FIR Data Acquisition and Manipulation

I used the publicly available catalogues for the S2CLS[1] (Geach et al., 2017) and the SCUBA-2 Cosmic Evolution Survey (S2COSMOS — Simpson et al., in preparation) imaging surveys to search for ultra-red galaxies.

The former is comprised of seven extragalactic fields: the Akari-Northern Ecliptic Pole (Akari-NEP — Takagi et al., 2009), the Cosmological Evolution Survey (COSMOS — Scoville et al., 2007, which was further imaged during S2COSMOS), the Extended Groth Strip (EGS — Groth et al., 1994), the Great Observatory Origins Deep Survey-North (GOODS-N — Wang et al., 2004), the Lockman Hole North (Dickey & Lockman, 1990), the Small Selected Area 22 (SSA22 — Lilly et al., 1991) and the United Kingdom Infra-Red Telescope (UKIRT — Casali et al., 2007) Infra-Red Deep Sky Survey-Ultra Deep Survey (UKIDSS-UDS, or simply UDS — Lawrence et al., 2007). The FIR analysis that I performed in this chapter required complementary *Herschel* data and I therefore discarded the Akari-NEP and SSA22 fields as, to the best to my knowledge, the data for these fields are either too shallow or non-existent. Thus, the five extragalactic fields analysed here cover a surveyed area of $\mathcal{A} \approx 3.7\,\mathrm{deg}^2$ down to an instrumental r.m.s. of $\sigma_{\mathrm{inst}} < 1.6\,\mathrm{mJy}$, or a factor of $\sim 4\times$ and $\sim 2\times$ improvement on the area and sensitivity considered in the previous chapter, respectively. The S2CLS and S2COSMOS catalogues contain 1,603 and 1,207 sources above an 850-μm SNR of $S/N > 3.5$ and $S/N > 4.0$, respectively.

4.2.1 PACS and SPIRE Photometry

FIR flux densities were measured on the *Herschel* PACS (100 and 160 μm) and SPIRE (250, 350 and 500 μm) images with PSF FWHM of $\theta = 7$ and $11.6''$ (Ibar et al., 2010) and 18, 24.8 and $35.1''$ (Nguyen et al., 2010), respectively. These images were accessed through the PACS Evolutionary Probe website[2] (Lutz et al., 2011) and the *Herschel* Database in Marseille, respectively.

I adopted a slightly different approach for measuring the *Herschel* flux densities than in the previous chapter. This time, I extracted $2' \times 2'$ sub-images at the SCUBA-2 positions (which were catalogued in decreasing order of 850-μm SNR) and subsequently performed

[1] https://zenodo.org/record/57792#.WOtnkRiZNE5.
[2] www.mpe.mpg.de/ir/Research/PEP/DR1.

a six-dimensional Gaussian fit using the IDL MPFIT package (Markwardt, 2009). During the fitting, I kept the *Herschel* FWHM fixed but allowed the Gaussian centroid (α, δ) to vary according to the 1-σ SCUBA-2 radial offset for a given SCUBA-2 source with a SNR given by:

$$\mathcal{R}_{\alpha} = \mathcal{R}_{\delta} = \frac{\mathcal{R}}{\sqrt{2}} \approx 11.2''(S/N)^{-1.6}, \tag{4.1}$$

where $\mathcal{R}$ has been parameterised using Equation 6 in Geach et al. (2017) to yield a similar expression to that derived in Equation B22 of Ivison et al. (2007). For each fit, I recorded the Gaussian peak flux density and corresponding 1-σ fitting error (both in units of mJy beam^{-1}). To these fitting errors, I added in quadrature the σ-clipped standard deviation of the extracted $2' \times 2'$ sub-image for the PACS measurements and confusion noises[3] for the SPIRE measurements.

The resulting two-dimensional fits were then subtracted from their respective *Herschel* images – effectively de-blending the *Herschel* images using a SCUBA-2 prior. Finally, I made no attempt to fit multiple gaussians to the *Herschel* images in cases where the SCUBA-2 detections are within a SCUBA-2 PSF of each other.

4.2.2 Ultra-Red Probability

In the previous chapter, I showed that not all of the central LABOCA sources were ultra-red after having their SPIRE photometry re-measured at their catalogued 870-μm position. This led me to introduce a probability term that a DSFG is ultra-red ($P_{\rm UR}$), which I then used to isolate a robust sub-sample of ultra-red galaxies.

Key Point 4.1
To recap, this 'ultra-red probability' was derived by drawing 10,000 Gaussian realisations of the SPIRE photometry for a given DSFG and determining the fraction of these realisations that satisfied Equation 2.1 in Chapter 2. This method allows me to generate a robust subset of ultra-red galaxies, which incorporates the photometric errors from *all* SPIRE passbands.

In Figure 4.1, I show the ultra-red probability for $\sim$ 2,000 DSFGs in the S2CLS and S2COSMOS imaging surveys. Motivated by the dark-grey shaded region in this figure, which represents those DSFGs whose mean SPIRE values suggest that they are ultra-red, I considered all galaxies with $P_{\rm UR} > 35\%$ as being ultra-red. At this probability threshold, Figure 4.1 indicates that there is a significant fraction (25) of DSFGs that are not directly classified as being ultra-red based on their mean SPIRE flux densities. These DSFGs are either just under the colour-cut limits and/or have larger SPIRE flux-density uncertainties.

In total, I provide a sample of 64 ultra-red galaxies, primarily from the COSMOS ($\approx 60\%$) and UDS ($\approx 30\%$) fields, as might be expected[4]. In Table 4.1, I show how the number of

[3] The SPIRE 250-, 350- and 500-μm confusion noises are $\sigma_{\rm conf}$ = 5.8, 6.3 and 6.8 mJy, respectively (Nguyen et al., 2010).

[4] In Chapter 2, I analysed ultra-red galaxies from a parent sample of 7,961 detections, which was 77%

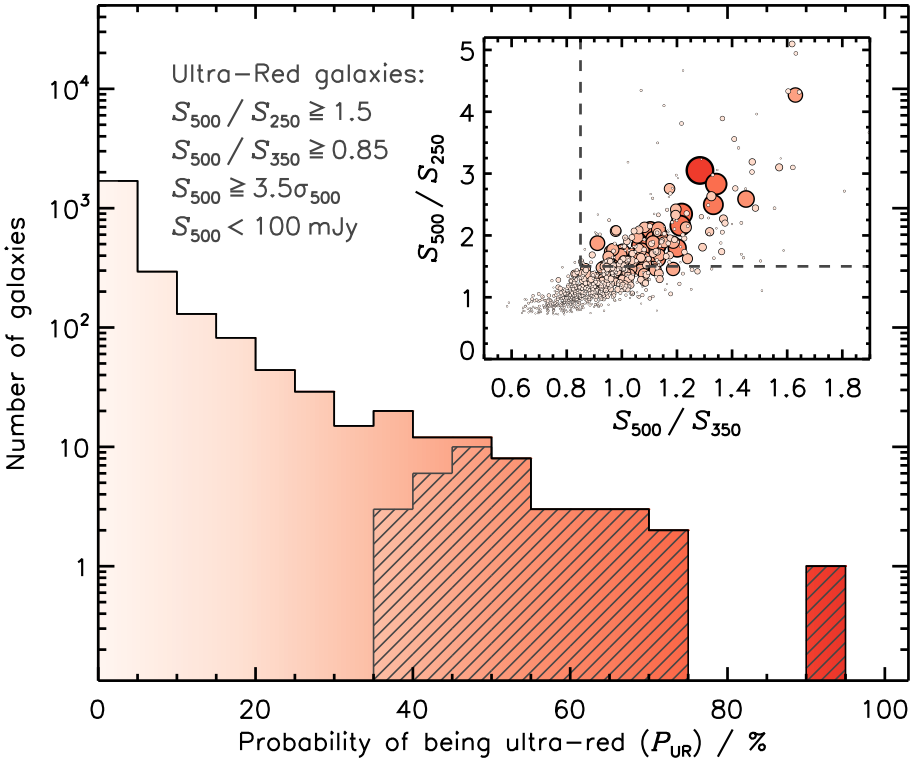

Figure 4.1: Main: histogram of the ultra-red probabilities for ∼ 2,000 DSFGs in the S2CLS and S2COSMOS imaging surveys. I colour-code this histogram from light-to-dark red as the ultra-red probability increases. The ultra-red criteria clearly selects the rarest DSFGs within these two surveys – only a handful (3) have an ultra-red probability above > 68.27%. The dark-grey shaded histogram represents the 39 DSFGs with SPIRE flux densities that directly satisfy Equation 2.1 in Chapter 2. This motivated me to define an 'ultra-red galaxy' as a galaxy that has an ultra-red probability above $P_{\rm UR} > 35\%$, which 64 galaxies satisfy. **Inset:** S_{500}/S_{350} versus S_{500}/S_{250}, colour-coded and scaled such that redder/larger circles have a higher ultra-red probability. The DSFG with the highest ultra-red probability, S2COSMOSJ100249+023255, has SPIRE flux-density ratios of $S_{500}/S_{250} \approx 3$ and $S_{500}/S_{350} \approx 1.3$ and a photometric redshift consistent with it being at $z \sim 4$. **Note**. Black dashed lines represent the ultra-red colour-cut boundaries.

Table 4.1: The number of DSFGs versus ultra-red-probability threshold.

Field	.... $N(> P_{\rm UR}\,/\,\%)$		
	> 0	> 35	> 68.27
COSMOS	1,043	38	2
EGS	186	3	0
GOODS-N	57	1	0
Lockman Hole North	189	1	0
UDS	876	21	1
	2,351	**64**	**3**

ultra-red galaxies varies as I change the ultra-red-probability threshold. Despite having set a fairly lenient threshold, the sample of ultra-red galaxies with $P_{\rm UR} > 35\%$ that I present only accounts for $\approx 3\%$ of the total number of sources catalogued across both of the imaging surveys. If I were to enforce a stricter, more robust threshold of $P_{\rm UR} \gtrsim 68\%$, I would only be left with a sample of three ultra-red galaxies – reflecting the fact that ultra-red galaxies become exponentially rarer with increasing ultra-red probability. However, such a small sample of robust ultra-red galaxies prohibits any meaningful statistical analysis, which justifies the adoption of a less conservative ultra-red-probability threshold in this chapter. Finally, it is worth mentioning that I only used the ultra-red probability to select a sample and not as a weighting for the properties analysed.

4.2.3 FIR Photometric Redshifts

I combined the PACS, SPIRE and SCUBA-2 flux-density measurements in order to determine FIR photometric redshifts for all $\sim$ 2,000 DSFGs. I added in quadrature the confusion noise ($\sigma_{\rm conf} = 0.8\,{\rm mJy}$ – Geach et al., 2017) *and* calibration error ($\sigma_{\rm cal} = 0.048 S_{\rm inst}$, where $S_{\rm inst}$ is the instrumental flux density) to the de-boosted instrumental 850-μm uncertainties. The calibration uncertainty – derived from the 1-σ scatter in the peak flux conversion factors of > 500 calibrator sources (Dempsey et al., 2013) – increases the unrealistically small measurement errors for bright (likely lensed) DSFGs.

FIR photometric redshifts were derived in a similar fashion to that described in the previous chapters. To recap, I used three template SEDs (ALESS, the Cosmic Eyelash, and Pope et al. (2008)) and adopted the template that produces the lowest χ^2 over a redshift interval of $0 < z_{\rm phot} < 10$ (down to a resolution of $\delta z_{\rm phot} = 0.01$). In all further analysis, I used the resulting photometric redshift distribution ($P(z)$) for this best template[5], which was derived from the best-fitting redshift values to 1,000 realisations of the FIR photometry. Adopting the entire photometric redshift distribution accounts for the (sometimes) complex shapes that they may possess better than simply adopting a Gaussian representation for them.

Finally, I draw attention to 459 DSFGs ($\approx 16\%$ of the sample) that were excluded from further analysis as their best-fitting photometric redshift values are within $\pm 1\sigma$ of a grid boundary, i.e. $\sigma^- < z_{\rm phot} < 10 - \sigma^+$. These sources have a median 850-μm SNR and stacked de-boosted flux density of $S/N \approx 4$ and $S_{850} = 3.4 \pm 0.1$, respectively. However, they are undetected in both PACS and SPIRE, with stacked flux densities of $S_{100} = 0.0 \pm 0.1\,{\rm mJy}$, $S_{160} = -0.5 \pm 0.3\,{\rm mJy}$, $S_{250} = -0.5 \pm 0.2\,{\rm mJy}$, $S_{350} = -0.5 \pm 0.2\,{\rm mJy}$ and $S_{500} = -0.7 \pm 0.2\,{\rm mJy}$. Therefore, it seems plausible that these *Herschel*-undetected sources are perhaps spurious (or very faint), which justifies the decision not to include them in any further analysis. The final sample is now based on a reduced sub-sample of $2{,}810 - 459 = 2{,}351$ DSFGs across the two imaging surveys.

complete. Given that the *H*-ATLAS imaging survey covers a factor of $\approx 160\times$ more area, I would expect to uncover $7{,}961/0.77/160 \approx 65$ ultra-red galaxies within the area analysed here, which I do.

[5]These distributions were 'dilated' to take into account the template-to-template scatter in the best-fitting redshift estimates for each DSFG.

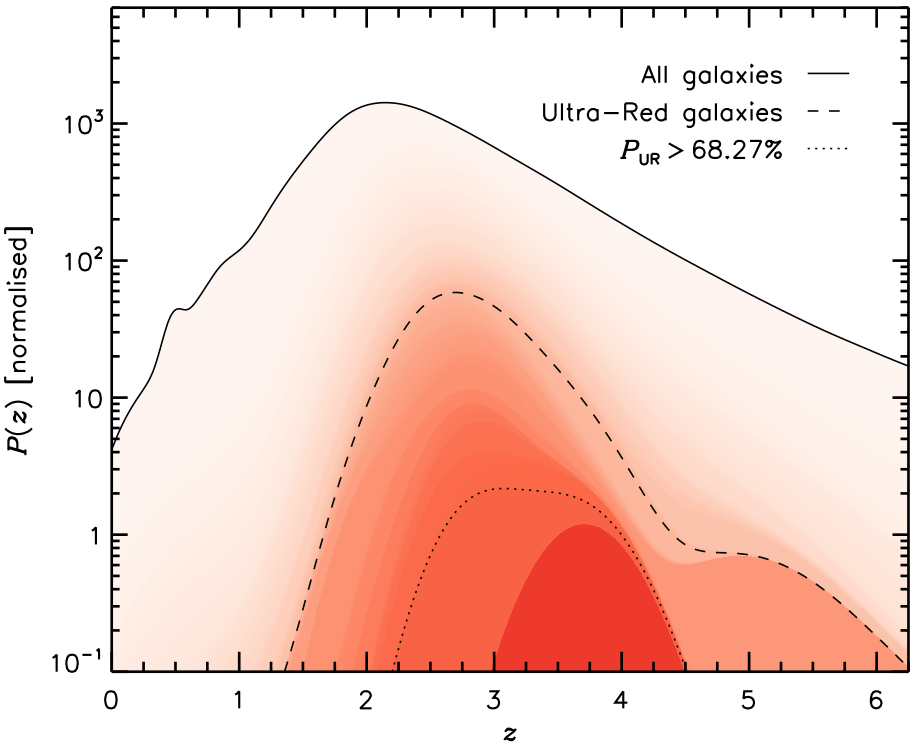

Figure 4.2: Sum of the photometric redshift distributions for all DSFGs (black solid line), ultra-red ($P_{\rm UR} > 35\%$, black dashed line) and the robust ultra-red ($P_{\rm UR} > 68.27\%$, black dotted line) galaxies. I have coloured-coded this figure such that redder colours represent the sum of the photometric redshift distributions for galaxies above a given ultra-red probability, as in Figure 4.1. The general population is peaked at $z \sim 2$, whilst the ultra-red galaxy sample is shifted to $z \sim 3$. Not every DSFG above $z \gtrsim 3$ is contained within the ultra-red galaxy sample, as many of these are likely lensed ($S_{500} \geq 100\,{\rm mJy}$, e.g. Ikarashi et al., 2011) or have poorly constrained SPIRE photometry. Although a very small sub-sample, the robust ultra-red galaxies are peaked closer to $z \approx 3.5$ – in strong agreement with the rigorously 'eyeballed' ultra-red galaxies in Chapter 2. The reddest photometric redshift belongs to the most robust ultra-red galaxy in the sample presented here, S2COSMOSJ100249+023255.

In Figure 4.2, I show how the sum of the photometric redshift distributions varies as the ultra-red probability is changed – highlighting where the ultra-red sub-sample and the three robust ultra-red galaxies lie. The general 850-μm-selected population peaks at $z \sim 2$, whilst the ultra-red galaxy sample presented here is shifted to $z \sim 3$ – reinforcing the effectiveness of this colour-selection technique. Interestingly, the more robust ($P_{\rm UR} > 68.27\%$) ultra-red galaxies peak even further at $z \approx 3.5$ – in good agreement with the results presented in Chapter 2. This reflects the smaller fraction of galaxies with (relatively) low ultra-red probabilities contained within the rigorously 'eyeballed', *H*-ATLAS sub-sample in Chapter 2 than compared to here. Furthermore, this eyeballing stage, in conjunction with shallow $\sim$ 850-μm imaging, seems to have provided a higher fraction ($\approx 40\%$) of robust ($P_{\rm UR} > 68.27\%$) ultra-red galaxies than presented here ($\approx 5\%$).

Finally, I derived a FIR luminosity for each DSFG, which I converted into a SFR and a dust mass (following the methods described in Chapters 1–3). I used these FIR properties in the following section during my analysis of the environments around ultra-red galaxies.

4.3 FIR Results, Analysis and Discussion

I now provide an analysis on the FIR environmental properties around these 64 ultra-red galaxies within the S2CLS and S2COSMOS imaging surveys. It is worth briefly mentioning that by analysing the environments around all ultra-red galaxies, the results presented here should be free from publication bias.

4.3.1 Galaxy-Centric Over-Density

The first property that I considered was the galaxy-centric aperture over-density in order to examine the effectiveness of using ultra-red galaxies to signposts distant, candidate proto-clusters down to a uniform flux limit.

Defining the Convolution Aperture

To help decide on the size of the aperture with which to measure these over-densities, I turned to the work of Chiang et al. (2013). These authors analysed the redshift-dependent properties of $\sim$ 3,000 proto-clusters within the Millennium Simulation (Springel et al., 2005), which they divided into three resulting $z = 0$ halo mass ($M_{\rm halo}^{z=0}$) bins representing Fornax- ($M_{\rm halo}^{z=0} = (1.37\text{–}3) \times 10^{14}\,M_{\odot}$), Virgo- ($M_{\rm halo}^{z=0} = (3\text{–}10) \times 10^{14}\,M_{\odot}$) and Coma-type ($M_{\rm halo}^{z=0} > 10^{15}\,M_{\odot}$) galaxy clusters (see Figure 1.6 in Chapter 1). To quantify the spatial distribution that the smaller member halos occupied along the merger trees for a given proto-cluster at any given redshift, Chiang et al. introduced an effective radius ($R_{\rm e}$) defined as:

$$R_{\rm e}(z) = \sqrt{\frac{1}{M_{\rm halo}(z)} \sum_{i} \Delta r_i}, \tag{4.2}$$

where $M_{\rm halo}(z)$ is the total halo mass at redshift z, the sum is over all smaller member halos and Δr_i is the distance of each smaller member halo to the centre of mass of its respective proto-clusters.

In Figure 4.3, I show the effective radius versus redshift for the three different $z = 0$ halo masses. Over the typical redshift range that ultra-red galaxies subtend ($2 \lesssim z \lesssim 4$), the effective radius for the most massive present-day galaxy clusters varies from $4.9' \lesssim R_{\rm e} \lesssim 3.8'$.

Key Point 4.2
Thus, in order to be sensitive to all proto-clusters with eventual halo masses that range from $M_{\rm halo}^{z=0} \approx 10^{14}$–$10^{15}\,M_{\odot}$, I chose an aperture with size of $R_{\rm e} = 4.9'$.

I represented this aperture as a peak-normalised, two-dimensional Gaussian with a FWHM of $\theta = 2R_{\rm e} \approx 10'$ ($\mathcal{G}_{R_{\rm e}}$).

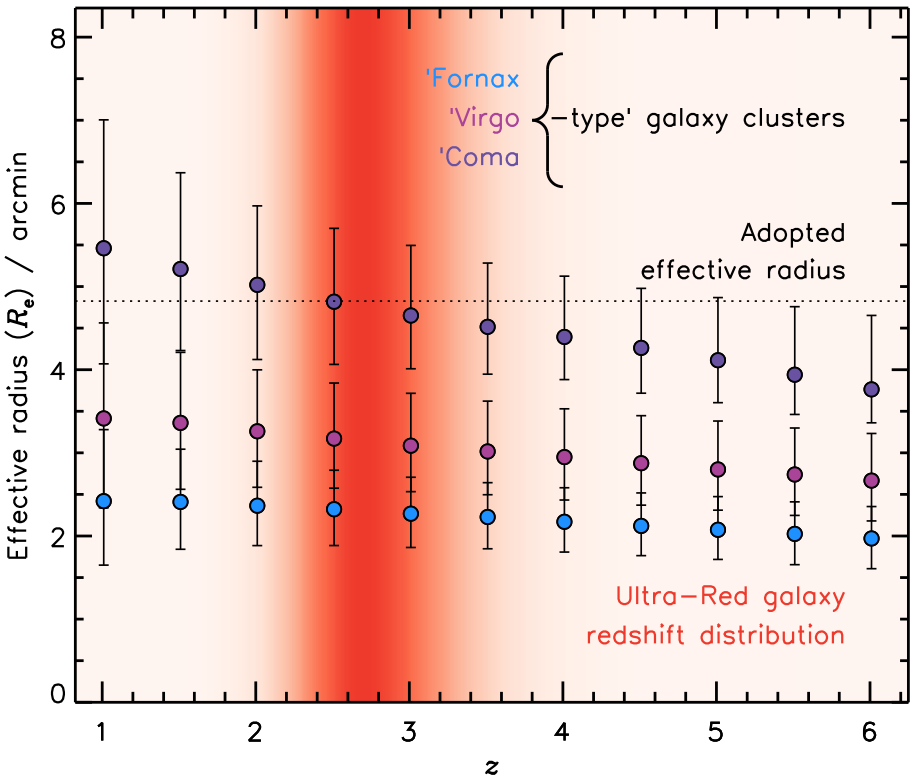

Figure 4.3: The effective radius as a function of redshift for proto-clusters that will eventually evolve into Fornax- (blue), Virgo- (pink) and Coma-type (purple) galaxy clusters. The most massive present-day galaxy clusters have an effective radius that typically varies from $4.9' \lesssim R_{\rm e} \lesssim 3.8'$ over the redshift interval that ultra-red galaxies occupy (shown in red). Therefore, in order to be sensitive to the Coma-type galaxy clusters, I measured the over-density parameters over $R_{\rm e} \approx 5$-arcmin scales (black dotted line).

Measuring the Number of DSFGs within the Aperture

The number of surrounding galaxies around each catalogued DSFG ($\mathcal{N}_{R_e}$) was computed through a convolution between the aperture (centred on the position of a source) and a two-dimensional representation of these surrounding galaxies (N). In this idealised representation, each surrounding galaxies was simulated as a two-dimensional Gaussian with a centroid equal to its catalogued position and a FWHM of

$$\theta = \sqrt{8\ln(2)}\mathcal{R},$$

i.e. each DSFG was slightly 'smeared' around its probable position, with the amount of smearing inversely proportional to its SNR (see Equation 4.1). These Gaussian representations were then normalised to their respective fidelity parameters using the catalogued FDR (see Equation 3.1 in Chapter 3). Again, the signpost galaxy was removed during the measurement of $\mathcal{N}_{R_e}$ in order to mitigate the bias associated with imaging a region where a galaxy is known to reside.

The Expected Number of DSFGs

In order to measure the 'expected' number of sources around each DSFG ($\mathcal{N}'_{R_e}$), I first generated a two-dimensional image for each field representing the expected number of sources at any given position. This was achieved as follows:

1. Using the best-fitting Schechter parameters to the differential number counts suitable for a given field, I derive the number of sources expected per unit area *at* at a given flux density $N(S)$, allowing the flux-density to range from $S = 0.2$–$20.0\,\mathrm{mJy}$.

2. Then, at a given value σ in the instrumental noise image of a given field, I measure how the completeness ($\mathcal{C}(S/\sigma)$) varies over this flux-density range. As this completeness was derived from simulations that used the SNR detection thresholds, it naturally accounts for the number of sources expected with low flux-density values.

3. The sum across all flux densities of the completeness multiplied by the number counts yields the expected number of sources per unit area, at a given value σ. Extending this to all values in the instrumental noise image, and multiplying by the area that each value subtends (i.e. the area of a pixel, $\mathcal{A}_{\mathrm{pix}}$), yields a two-dimensional representation of the number of sources expected at all positions within a given field, given by
$$N'_{\mathrm{field}} = \sum_{\sigma}\sum_{S}\mathcal{C}(S/\sigma)\mathcal{A}_{\mathrm{pix}}N(S).$$

The number of sources expected around each DSFG ($\mathcal{N}'_{R_e}$) is then simply the convolution of the aperture (centred on the position of that DSFG) with the applicable N'_{field}, or

$$\mathcal{N}'_{R_e} = G_{R_e} * N'_{\mathrm{field}}.$$

Finally, I scaled $\mathcal{N}'_{\rm field}$ by $\sim$ 84% in order to account for the slight deficit caused by removing $\approx$ 16% of the sample with poorly constrained photometric redshifts. To re-iterate, generating the expected numbers of sources in this way accounts for the varying instrumental noise across a given image and thus appropriately weights regions with high-/low-instrumental noise.

Over-Density Parameter

In a similar method to the previous chapter, I computed the galaxy-centric over-density parameter for each DSFG using:

$$\delta_{R_{\rm e}} \equiv \frac{(G_{R_{\rm e}} * N) - (G_{R_{\rm e}} * N'_{\rm field})}{(G_{R_{\rm e}} * N'_{\rm field})} = \frac{\mathcal{N}_{R_{\rm e}}}{\mathcal{N}'_{R_{\rm e}}} - 1, \tag{4.3}$$

where $G_{R_{\rm e}}$ is the peak-normalised Gaussian aperture with a FWHM of $\theta = 2R_{\rm e}$, N is the measured spatial distribution of all DSFGs excluding the central one, and $N'_{\rm field}$ is the expected spatial distribution of galaxies, accounting for the varying instrumental noise values across a given field.

In Figure 4.4, I show a histogram and kernel density estimate (KDE) of the over-density parameter for ultra-red and not ultra-red galaxy samples. The KDE was computed by averaging many realisations of the over-density parameter for each DSFG and thus takes into account the uncertainties associated with each measurement.

I also show the normalised CDFs for the the ultra-red ($\Phi_{\rm UR}$) and not ultra-red ($\Phi_{\rm NUR}$) galaxy samples, which I used to perform a two-sample Kolmogorov-Smirnov (K-S) test, defined as:

$$D_{\rm K\text{-}S} = \sup_{\delta_{R_{\rm e}}} |\Phi_{\rm UR}\left(\delta_{R_{\rm e}}\right) - \Phi_{\rm NUR}\left(\delta_{R_{\rm e}}\right)|, \tag{4.4}$$

where $D_{\rm K\text{-}S}$ is the maximum distance between the two CDFs. This distance quantifies the probability that two CDFs are randomly drawn from the same population.

Key Point 4.3
I derived a value of $D_{\rm K\text{-}S} = 0.12$, which equates to a probability of $P_{\rm K\text{-}S} \sim 15\%$ that ultra-red and not ultra-red galaxies are drawn from the same over-density parameter distribution. Therefore, the differences are slight ($\gtrsim 1\sigma$) between the two samples.

However, it appears that not all ultra-red galaxies signpost over-dense regions and $\approx 40\%$ of them lie in under-dense regions ($\delta_{R_{\rm e}} \leq 0$) compared to $\approx 50\%$ of the galaxies that are not ultra-red. These result are similar to that found in the previous chapter for bright ($S > 8\,{\rm mJy}$) DSFGs.

Finally, Figure 4.5, which is continued in Appendix C, shows the over-density and SPIRE false-colour cut-outs for ultra-red galaxies with $P_{\rm UR} > 60\%$. The former indicate where the ultra-red galaxies lie in relation to their closest over-density peaks.

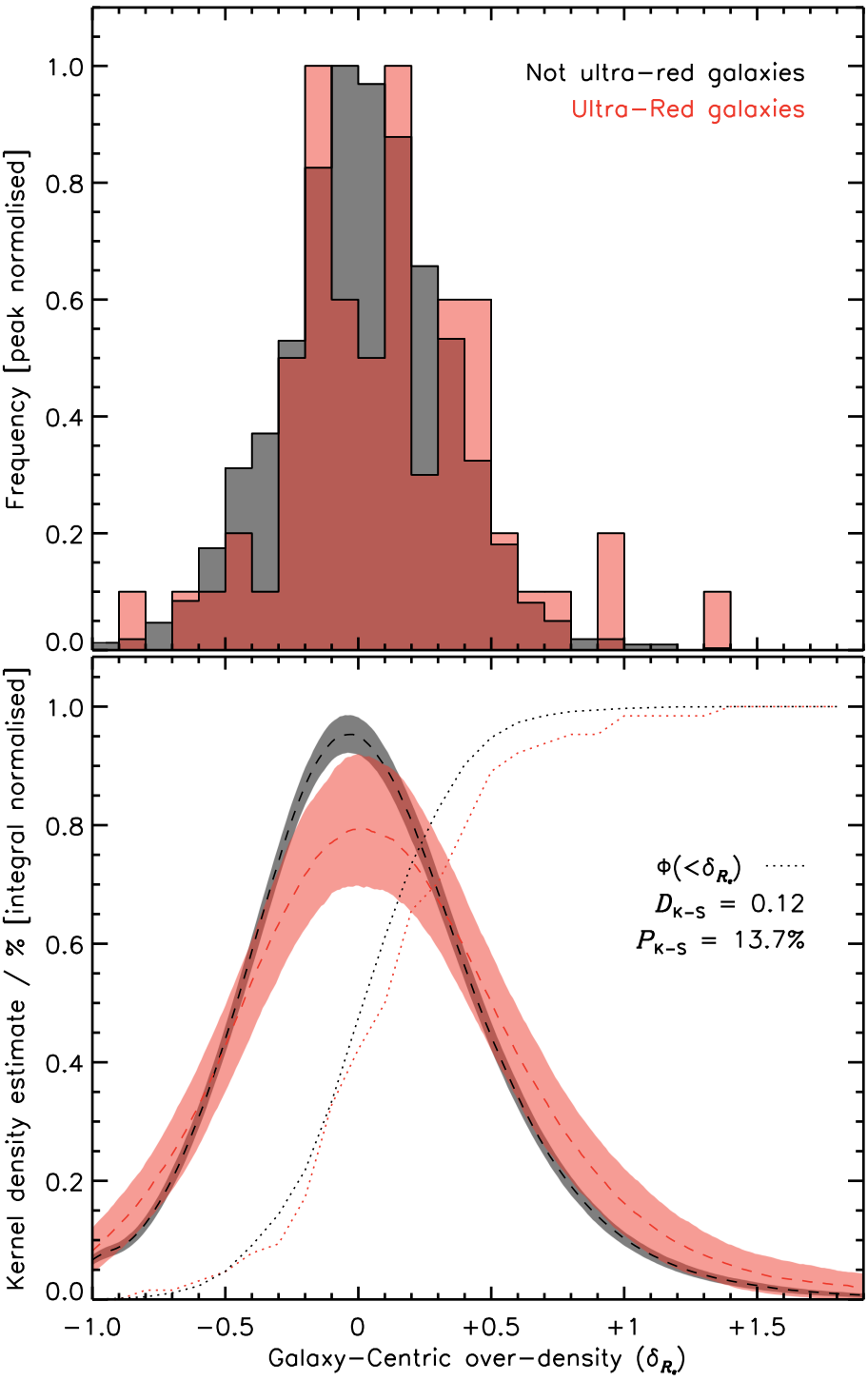

Figure 4.4: Top: peak-normalised histograms of the over-density parameter for ultra-red (red) and not ultra-red (black) galaxies. Each over-density parameter is calculated within an effective radius of $R_{\rm e} \approx 5'$ centred on each galaxy. I ensured that the central galaxy is removed from this calculation in order to reduce the galaxy-centric bias. The distribution for ultra-red galaxies appears to be slightly shifted towards higher over-density parameter values. **Bottom:** KDE of the over-density parameter for both samples derived by averaging 1,000 realisations of the over-density parameter for each DSFG. The shaded regions represent the r.m.s. scatter across these realisations. A slight ($\gtrsim 1\sigma$) excess is present in regions with higher ($\delta_{R_{\rm e}} \gtrsim 1$) over-density parameter values. Clearly not all ultra-red galaxies signpost over-dense regions, but there exists a growing separation between the two samples that ...

Figure 4.4 (continued from previous page): ... becomes more pronounced around $\delta_{R_e} \approx 0.5$–1.5. This indicates that ultra-red galaxies preferentially signpost regions with greater over-density parameter values than galaxies that are not ultra-red, as found in the previous chapter. I over-plot the normalised CDFs (dashed lines) for these two samples, which highlights this divergence more clearly. A K-S test using the CDFs indicates that there is a $\approx 15\%$ chance that the two distributions are the same.

Proximity to their Closest Over-Density Peak

As discussed, $\approx 60\%$ of ultra-red galaxies reside in over-dense regions, which motivated me to examine the exact locations in these environments that they occupy. For example, are these 'over-dense' ultra-red galaxies situated near to the centres of 'high-value' over-density peaks, which would be consistent with them signposting the most extreme nodes in the DM distribution? Or, is the situation closer to them signposting less extreme over-densities forming within the filamentary structure?

To answer this question, I used *all* of the catalogued DSFGs in a given field to generate a 'global' over-density image, which I used to search for 'global peaks' that are above $\delta_{R_e} > 0$. These global peaks were detected and extracted using the same source extraction algorithm described in the previous chapter, i.e. searching for peaks in a top-down fashion that are separated by a distance of $2R_e$ from each other and the image edges. The resulting global peaks were then normalised to the maximum value of the extracted peaks. All extracted peaks were subsequently categorised as having either a low, medium or high value, corresponding to $0 < \delta_{R_e}/\max(\delta_{R_e}) < 1/3$, $1/3 < \delta_{R_e}/\max(\delta_{R_e}) < 2/3$ and $2/3 < \delta_{R_e}/\max(\delta_{R_e}) < 1$, respectively. I then analysed the radial distribution of ultra-red galaxies to their closest global peak, under the assumption that medium-to-high-value global over-density peaks may represent extreme nodes in the DM distribution, whilst low-value global over-density peaks represent the less extreme over-densities with the filamentary structure.

In Figure 4.6, I show this radial distribution for $\approx 60\%$ of the ultra-red galaxies that show a positive ($\delta_{R_e} > 0$) over-density.

Key Point 4.4
The closest global peaks to around $\sim 2/3$ of these galaxies are of medium or high value. All ultra-red galaxies closest to a medium-value peak are distributed over $1.5R_e \approx 7'$ (or ~ 3 Mpc at $z = 3$) scales, suggesting that they play a central role in these over-densities.

The situation is different for the high-value peaks as only $\approx 65\%$ of the ultra-red galaxies are distributed within $1.5R_e$ scales – with some being as far out as $4R_e \approx 15'$.

In the low-value peaks, which $\sim 1/3$ of the $\approx 60\%$ of ultra-red galaxies occupy, they primarily tend to be within $0.5R_e$ (or ~ 1 Mpc at $z = 3$) of the peak position. Thus, ultra-red galaxies are mainly situated in the centres of low-valued over-density regions.

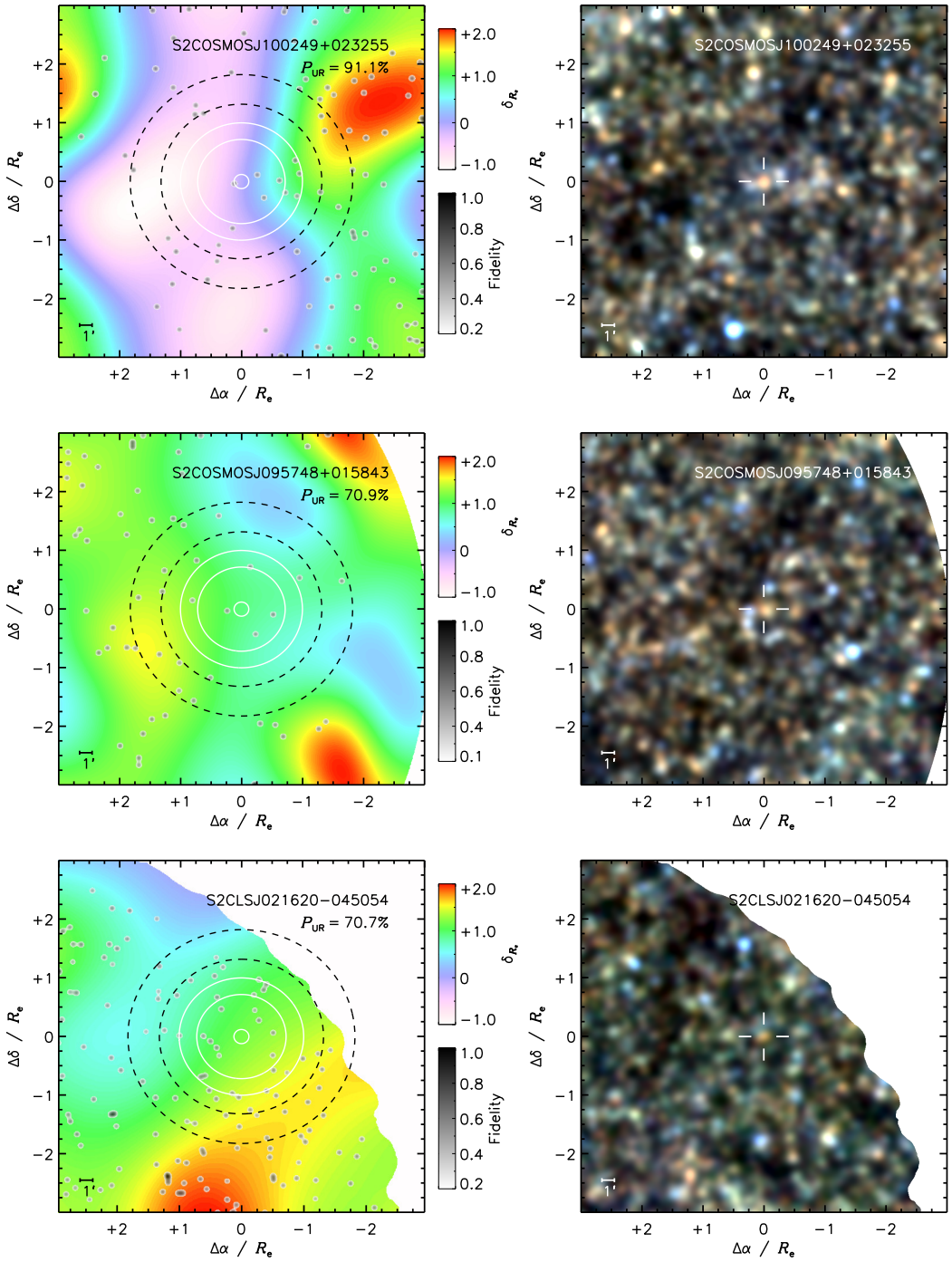

Figure 4.5: Left: $6R_e \times 6R_e$ cut-outs ($R_e \approx 5'$) of the over-density parameter for galaxies with an ultra-red probability above $P_{UR} > 60\%$. These cut-outs are colour-coded such that bluer/redder regions represent lower/higher over-density values. Surrounding DSFGs are shown in black as Gaussian PSFs with FWHM of $\theta = 14''$ that are integral normalised to their respective fidelity parameters. I show contours representing the 10, 30 (dashed black), 50, 70 and 99% (white) values of the Gaussian aperture adopted, i.e. the aperture FWHM of $\theta = 2R_e$ is indicated by the furthermost white contour. **Right:** SPIRE false-colour cut-outs of the same regions. The 250- and 350-μm images have been filtered to the 500-μm resolution. A white cursor indicates the central ultra-red galaxy within each cut-out. **Note**. Ultra-Red galaxies are presented in order of decreasing ultra-red probability. A distance scale is shown in the bottom left corner of each cut-out. This figure is continued in Appendix C for the six extra ultra-red galaxies with $P_{UR} > 60\%$.

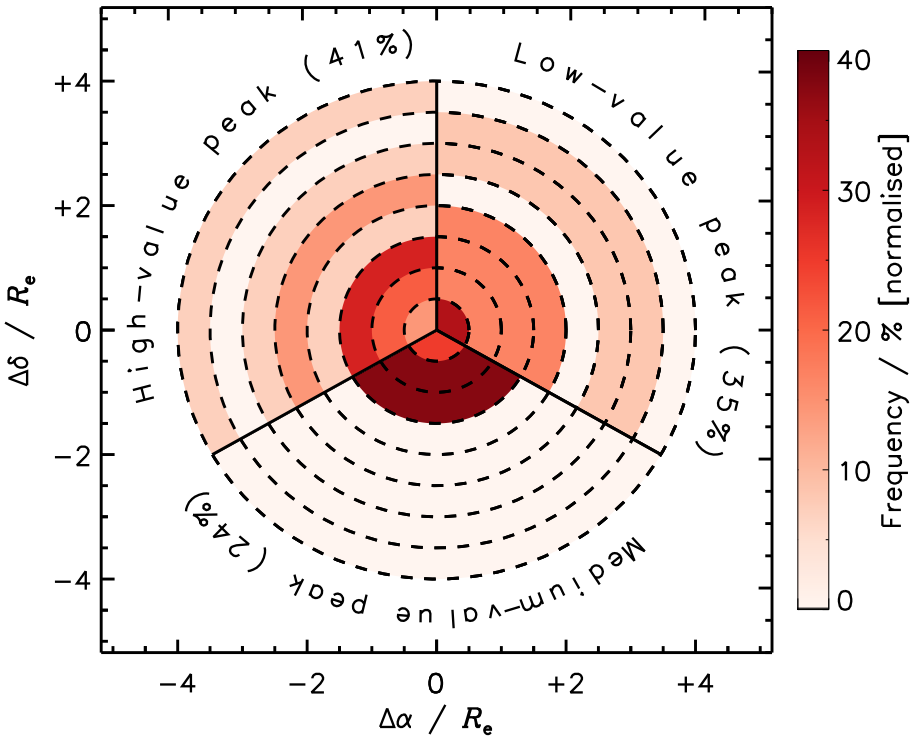

Figure 4.6: Radial distance of the $\sim 60\%$ of ultra-red galaxies that show a positive over-density parameter to their closest global over-density peak. These peaks are divided into low, medium and high values (solid black lines) that are represented by three segments with radial offsets that increment by $0.5R_e \approx 2'$ (dashed black lines). The majority ($\approx 60\%$) of over-dense ultra-red galaxies are located next to a medium- or high-value peak. Those nearest to a medium-value peak are all distributed within $< 1.5R_e \approx 7'$ (or 3 Mpc at $z \sim 3$) of the peak position – suggesting that these ultra-red galaxies may play a dominant role in such environments. On the other hand, only $\sim 2/3$ of ultra-red galaxies that are nearest to a high-value peak are distributed within a similar scale and the remaining $\sim 1/3$ are distributed as far out as $\approx 4R_e \approx 20'$. A similar picture is seen for the $\approx 33\%$ of over-dense ultra-red galaxies that are closest to a low-value peak, although a slight enhancement is seen within the inner-most radial bin.

These findings may suggest that around $\approx 20\%$ of ultra-red galaxies are signposting less extreme over-densities within filamentary structures, rather than the extreme nodes.

Previously Identified Proto-Clusters within the S2CLS and S2COSMOS

A comprehensive review of previously identified/confirmed proto-clusters is given in Casey (2016), but I now briefly outline those found within some of the fields that I have analysed in this chapter.

- A proto-cluster containing seven DSFGs at $z \sim 2.5$ within the COSMOS field was serendipitously unveiled by Casey et al. (2015). Situated in the centre and $\approx 10'$ north of this over-density are the ultra-red galaxies S2COSMOSJ100025+022605 and S2COSMOSJ100013+023429, respectively. Although not officially catalogued as part of this proto-cluster, these ultra-red galaxies have photometric redshifts of

$z_{\rm phot} = 2.95^{+0.36}_{-0.30}$ and $z_{\rm phot} = 2.77^{+0.33}_{-0.29}$, respectively. Thus, it is not inconceivable that these two ultra-red galaxies are members of this $z \sim 2.5$ structure (rather than residing behind it). Interestingly, none of the catalogued members of this structure meet the strict ultra-red criteria. Furthermore, the environment around S2COSMOSJ100025+022605 (at the heart this structure) shows no particular over-/under-density of DSFGs compared to the field over the $\sim$ 5-arcmin scales that I have examined.

- Hung et al. (2016) report a proto-cluster containing nine DSFGs at $z \approx 2.1$ within the COSMOS field, $\approx 10'$ south of the Casey et al. structure.

- There is another confirmed proto-cluster within the COSMOS field containing four galaxies at $z \approx 5.3$ (the AzTEC-3 over-density — Capak et al., 2011; Riechers et al., 2010). However, these galaxies are all contained within a single SCUBA-2 PSF, known as 'COSMOS AzTEC-3'.

- There are five DSFGs comprising a proto-cluster in the GOODS-N field at $z = 1.99$ (Blain et al., 2004; Chapman et al., 2009).

- The gravitationally lensed ultra-red galaxy HDF850.1 (or catalogued here as S2CLSJ123652+621226 in the GOODS-N field) at $z \approx 5.2$ was shown to reside in a galaxy over-density by Walter et al. (2012) using narrow-band Lyman-α imaging around its environment. The photometric redshift estimate obtained for this galaxy using the Pope et al. SED template is very consistent with its spectroscopic one, namely $z_{\rm phot} \approx 5.3$.

- Finally, there is also an over-density at $z = 4.05$ around 'GN20' in this field (Daddi et al., 2009; Hodge et al., 2013) – however, its coordinates are just outside the boundaries of the S2CLS image.

These previously identified proto-clusters provide a sample of 16 spectroscopically confirmed DSFGs within $z \sim$ 2–2.5, which I used to measure the accuracy of the photometric redshift technique using the familiar expression

$$\Delta z/(1+z_{\rm spec}) \equiv (z_{\rm phot} - z_{\rm spec})/(1+z_{\rm spec}).$$

Key Point 4.5
I found an accuracy and dispersion of $\mu_{|\Delta z|} \sim 0.1 \times (1+z_{\rm spec})$ and $\sigma_{\Delta z} \sim 0.1 \times (1+z_{\rm spec})$, respectively, re-iterating the predictive power of this photometric redshift algorithm, especially in this redshift interval. These results are broadly consistent with those found in Chapter 2.

Although this is only a small spectroscopic sample, these results are slightly more accurate,

and reliable, than those achieved by Michałowski et al. (2017) for these same DSFGs, namely $\mu_{|\Delta z|} \sim 0.2 \times (1 + z_{\rm spec})$ and $\sigma_{\Delta z} \sim 0.3 \times (1 + z_{\rm spec})$, respectively.

4.3.2 Associations Based on Photometric Redshifts

The observed redshift $(1 + z_{\rm obs})$ of a given galaxy (typically determined by frequency shifts in its observed spectrum, $\nu_{\rm rest}/\nu_{\rm obs}$) is composed of a (dominant) cosmological factor due to the expansion of space $(1 + z_{\rm cos})$, a peculiar factor due to the velocity of that galaxy with respect to an observer (i.e. the Doppler effect, $1 + z_{\rm pec}$) and a gravitational factor due to the influence of strong gravitational fields in its vicinity $(1 + z_{\rm grav})$ as follows:

$$\frac{\nu_{\rm rest}}{\nu_{\rm obs}} = (1 + z_{\rm obs}) = (1 + z_{\rm cos})(1 + z_{\rm pec})(1 + z_{\rm grav}). \tag{4.5}$$

Thus, testing whether a particular DSFG at a redshift z is 'associated' to another galaxy relies on being able to constrain their observed redshifts to within:

$$|\Delta z|_{\rm assoc} \lesssim \frac{2\sigma_{\rm los}}{c}(1 + z), \tag{4.6}$$

where $\sigma_{\rm los}$ is line-of-sight velocity dispersion. The typical velocity dispersion for (unvirialised) members of a distant ($z \gtrsim 3$) proto-cluster is around $\sigma_{\rm los} \approx 500\,{\rm km\,s^{-1}}$, but values as high as $\sigma_{\rm los} \approx 2{,}000\,{\rm km\,s^{-1}}$ have been recorded (Venemans et al., 2007; Dey et al., 2016). Finally, it is important to note that Equation 4.6 assumes that the two galaxies are at the same cosmological redshift (z) and neglects the effects from strong gravitational fields. Furthermore, the factor of 2 accounts for the fact that these two galaxies may be placed at opposing ends of a given structure when imaged.

In the previous chapter, I associated galaxies within the same structure using an association threshold of $|\Delta z|_{\rm assoc} \lesssim 0.5$, which was based on the median photometric-redshift fitting errors for $z \sim 3$ DSFGs using shallow FIR photometry. However, not only is this threshold an order of magnitude greater than that expected from Equation 4.6 using the maximum velocity dispersion recorded in proto-clusters, this method also treated two DSFGs that were 'associated' to a particular structure signposted by an ultra-red galaxy the same, regardless of their individual redshift errors.

Thus, I have taken a different approach in this chapter and used the photometric redshift probability distributions and Equation 4.6 to assign each surrounding galaxy an 'associated probability' ($\mathcal{P}_{\rm assoc}$).

Key Point 4.6
This probability was calculated by drawing 10,000 redshift realisations from each photometric redshift distribution and determining the number of times that Equation 4.6 was satisfied. Furthermore, I subsequently assigned each surrounding galaxy an 'association weight' ($\mathcal{W}_{\rm assoc}$), which was simply the association probability scaled by the fidelity of that particular galaxy.

For instance, the probability that one ultra-red galaxy is associated to another ultra-red galaxy (assuming that each have a photometric redshift of $z_{\rm phot} = 2.80 \pm 0.19$ and neglecting the $\sigma_z = 0.14(1+z) \sim 0.5$ intrinsic template SED scatter) to within $|\Delta z|_{\rm assoc} \lesssim 0.05$ is $\mathcal{P}_{\rm assoc} \sim 15\%$. Furthermore, assuming that this ultra-red galaxy has a fidelity parameter of $\mathcal{F} = 0.8$, I would assign this particular surrounding galaxy an association weight of $\mathcal{W}_{\rm assoc} \sim 10\%$.

Key Point 4.7
Finally, I was only able to associate (on average) ≈ 1 surrounding DSFG to an ultra-red galaxy, which was determined by summing the association weights from all of its surrounding galaxies within $R_{\rm e} \sim 5'$. Interestingly, this is the same average number of associations achieved in the previous chapter, which is perhaps indicative of the limitations with using FIR-based photometric redshifts.

4.3.3 FIR Total Dust Masses and SFRs

With a method for weighting the contributions from any surrounding DSFGs using Equation 4.6, I derived the total dust masses and total SFRs within the 5-arcmin environments around the ultra-red galaxies catalogued in the S2CLS and S2COSMOS imaging surveys. I show the results of these two properties in the top and bottom panels of Figure 4.7, respectively, noting that these values exclude the contributions from the central ultra-red galaxies.

Key Point 4.8
The total dust masses peak at $M_{\rm dust} \approx 1.8 \times 10^9\,M_\odot$, whilst the total SFRs peak at $\Psi \approx 1{,}400\,M_\odot\,{\rm yr}^{-1}$. These values are broadly consistent with those reported in the previous chapter, namely $M_{\rm dust} \sim 1.7 \times 10^9\,M_\odot$ and $\Psi \approx 1{,}100\,M_\odot\,{\rm yr}^{-1}$, respectively, somewhat expected due to the same number of associated DSFGs.

As the expected number of galaxies within an aperture around any given DSFG varies – reflective of the differing image r.m.s. values and/or edge effects – I also computed the 'missing' number of galaxies necessary to reconcile the shallowest regions with the deepest regions in an image. I represented these missing DSFGs with the global photometric redshift distribution (see Figure 4.2), average dust masses of $1.2 \times 10^9\,M_\odot$ and average SFRs of $575\,M_\odot\,{\rm yr}^{-1}$, with the latter two being computed using the method outlined in Barlow (2004). However, the effect of including these missing galaxies was small, namely it increased the total dust masses and total SFRs by a factor of $\sim 1.25\times$ to $M_{\rm dust} \approx 2.2 \times 10^9\,M_\odot$ and $\Psi \approx 1{,}600\,M_\odot\,{\rm yr}^{-1}$, respectively.

Finally, it is worth mentioning that total dust masses and total SFRs computed via this method converged as the association weight of surrounding galaxies tended to zero

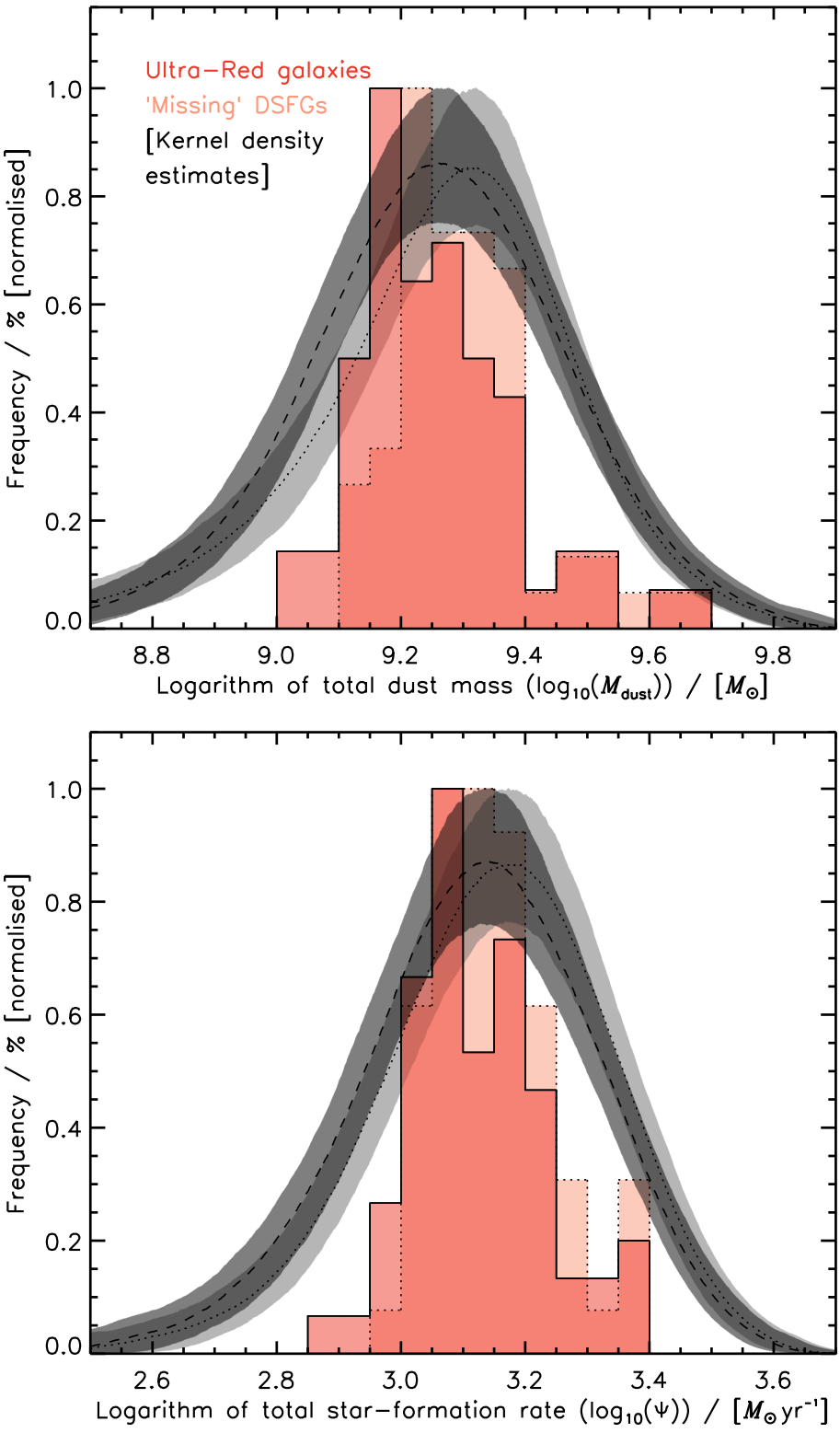

Figure 4.7: Top: histogram of the total dust masses around ultra-red galaxies (red) and an arbitrarily normalised KDE (black), which was derived by averaging 1,000 realisations of the total dust masses for the surrounding galaxies. Each surrounding DSFG within $R_{\rm e} \approx 5'$ has been weighted according to Equation 4.6. The total dust mass peaks at $\approx 2 \times 10^9\,M_\odot$ – equating to a molecular-gas reservoir of $\sim 10^{11}\,M_\odot$, assuming a GDR of $\delta_{\rm GDR} = 100$. The dotted black lines show the effect of accounting for the 'missing' DSFGs due to varying r.m.s. values around each ultra-red galaxy. These missing DSFGs increase the total dust mass in the environments of ultra-red galaxies by a factor of $\sim 1.25\times$. **Bottom:** histogram (red) ...

Figure 4.7 (continued from previous page): ... and normalised KDE (black) of the total SFR for DSFGs in the $R_{\rm e} \approx 5$-arcmin vicinity of ultra-red galaxies. Again, each SFR has been weighted accordingly and a contribution from the missing DSFGs has also been shown (dark grey). The peak of this distribution occurs at a total SFR of $\Psi \sim 1{,}100\,M_{\odot}\,{\rm yr}^{-1}$, which – assuming a 100-Myr burst of star formation – could easily result in a present-day structure with total stellar mass of $M_{\rm stars} \sim 10^{11}\,M_{\odot}$.

($\mathcal{W}_{\rm assoc} \rightarrow 0$), suggesting that including all of the surrounding galaxies in this calculation was reasonable.

4.4 Optical/NIR Data Acquisition and Manipulation

As discussed in Section 4.3.1, ultra-red galaxies appear to preferentially signpost over-densities of DSFGs and furthermore they appear to be situated near to the centres of medium-to-high-value over-density peaks. Thus, this motivated me to examine the optical/NIR environments around these ultra-red galaxies, with the aim to uncover any relationships that may, or may not, be present within such extreme environments at $z \gtrsim 3$. For instance, has the emergence of the red sequence taken place around ultra-red galaxies at these redshifts yet? Or, is their any dependence on the colour and/or stellar mass of galaxies as the radial distance from an ultra-red galaxy varies? If these relationships are not uncovered, it may suggest that something is wrong with our understanding of the formation of massive galaxies at high redshift and the role that they play in the assembly of large structure.

4.4.1 Obtaining the Optical/NIR Data

To answer these questions, I made use of publicly available, multi-wavelength catalogues covering the COSMOS[6] (McCracken et al., 2012; Laigle et al., 2016) and UDS[7] fields (Almaini et al., still in preparation). Although such catalogues do exist for the EGS and GOODS-N fields, their coverage does not include the regions occupied by the ultra-red galaxies presented within this chapter. As for the remaining fields, to the best of my knowledge, there are no available optical/NIR data.

The catalogue for the COSMOS field contains 606,887 sources within an area of $\mathcal{A} \approx 1.70\,{\rm deg}^2$ that comprises the UltraVISTA-DR2 region. The catalogue for the UDS field contains 184,439 sources detected over an area of $\mathcal{A} \approx 0.77\,{\rm deg}^2$ that comprises the 8$^{\rm th}$ release (Hartley et al., 2013) of the United Kingdom IR Telescope (UKIRT) IR Deep Sky Survey (UKIDSS — Lawrence et al., 2007). Therefore, the surveyed area for both of these fields is slightly smaller than that surveyed by SCUBA-2. Hence, although there are 59 ultra-red galaxies within the COSMOS and UDS fields, there is only suitable optical/NIR coverage for 42 ultra-red galaxies; 30 from the COSMOS field and 12 from the UDS field.

[6] ftp://ftp.iap.fr/pub/from_users/hjmcc/COSMOS2015/COSMOS2015_Laigle+_v1.1.fits.gz.
[7] http://www.nottingham.ac.uk/~ppzoa/cls/UDS_DR8_forS2CLS_v4.dat.fits.

Table 4.2: COSMOS and UDS catalogue flags.

FITS field name	Value	FITS field name	Value	Description
..... **COSMOS**		..... **UDS**		
`TYPE`	0	`Basic galaxy catalogue`	T	Galaxy SED shape
`ZPDF`	> 0	`chisq_at_maxL`	≤ 15	Satisfactory $z_{\rm phot}$
`Ksw_MAG_APER2`	< 24.5	`MAG_APER_K_2.0`	< 24.6	K-Band cut
`MASS_BEST`	> 9	`Bestfit_Mass`	> 9	Stellar-Mass cut
`FLAG_HJMCC`	0	—		UltraVISTA-DR2

For both of the fields, the photometric redshifts contained within the catalogues were computed using a χ^2-minimisation code (Arnouts et al., 1999) over a redshift grid of $0 < z_{\rm phot} < 6$ down to a resolution of $\delta z_{\rm phot} = 0.01$. The implementation of this code used a combination of template SEDs (representing spiral, elliptical and young, blue star-forming galaxies), appropriately handled galactic dust extinction and was found to produce an intrinsic scatter of $\sigma_{\Delta z} = 0.021(1+z)$ at $z > 3$ – far better than that achieved with the FIR template SEDs adopted here. However, over $z \sim 0$–3 the median upper and lower fitting uncertainties for these galaxies increases by a factor of $\sim 5\times$ to $\sigma^{+}_{z_{\rm NIR}} = 0.11$ and $\sigma^{-}_{z_{\rm NIR}} = 0.23$, respectively, which dwarfs this intrinsic scatter. I modelled each photometric redshift in the catalogue using a split-normal distribution defined as:

$$P\left(z_{\rm phot}, z_{\rm NIR}, \sigma^{+}_{z_{\rm NIR}}, \sigma^{-}_{z_{\rm NIR}}\right) = A \exp \begin{cases} -(z_{\rm phot} - z_{\rm NIR})^2/2(\sigma^{+}_{z_{\rm NIR}})^2 & \text{if } z_{\rm phot} > z_{\rm NIR} \\ -(z_{\rm phot} - z_{\rm NIR})^2/2(\sigma^{-}_{z_{\rm NIR}})^2 & \text{otherwise,} \end{cases} \quad (4.7)$$

where $A = \sqrt{2/\pi}/(\sigma^{+}_{z_{\rm NIR}} + \sigma^{-}_{z_{\rm NIR}})$ integral normalises this distribution and $z_{\rm phot}$ is the redshift grid covering $0 < z_{\rm phot} < 10$ down to a resolution of $\delta z_{\rm phot} = 0.01$, i.e. mimicking that used for DSFGs throughout this thesis.

These catalogues also provide absolute magnitudes (M) and stellar masses ($M_{\rm stars}$). The former were either taken directly from the best-fitting, rest-frame template SED, or K-corrected from the apparent magnitude (m) measured through the passband closest to $\lambda_M(1+z)$[8]. Stellar masses were typically derived by scaling (in the observed frame) large samples of synthetic spectra to the K-band apparent magnitude and taking the resulting modal (or best-fit) stellar mass of these spectra (e.g. Mortlock et al., 2013, 2015).

4.4.2 Cuts on the Catalogues

NIR galaxies around ultra-red galaxies at $z \sim 3$ should have limited-to-no data at wavelengths shorter than the central wavelength of the U/B bands due to the Lyman-α break at 1,216 Å, which causes them to 'drop-out' of these passbands. Thus, in order to ensure that the NIR galaxies used in this analysis had *robust* stellar mass and/or absolute magnitude estimates, I required that their detected K-band photometry was below the

[8]For instance, the B-band (at $\lambda_M = 4{,}458.3$ Å) absolute magnitude would be calculated from the H-band (at $\lambda_m = 16{,}453.4$ Å) apparent magnitude at $z = 3$.

(3–5)-σ_K limiting magnitude. To further increase the completeness of this sample, I also required that their photometric redshifts were 'satisfactory' (i.e. consistent with having a galaxy-shaped SED and a suitable χ^2 value) and that their stellar masses were above $M_{\rm stars} > 10^9\,M_{\odot}$.

In Table 4.2, I list the FITS binary field names and respective values necessary to implement these constraints on the catalogues, which reduce the number of sources in the COSMOS and UDS fields to 201,376 and 61,750, respectively.

4.5 Optical/NIR Results, Analysis and Discussion

4.5.1 Robust Counterparts to DSFGs

In order to determine which NIR galaxies were associated to the environments around the ultra-red galaxies presented here, I needed to first examine whether there were any underlying systematics between the FIR photometric redshifts ($z_{\rm FIR}$) and those provided in the catalogues discussed above ($z_{\rm NIR}$). To test for such systematics, I first matched all of the available DSFGs to their true (or 'real') counterparts.

A commonly used method to match a galaxy to its real counterpart amongst many potential counterparts is to use the corrected-Poissonian probability, defined as:

$$p = 1 - \exp\Big(-\pi r^2 N(>S)\Big), \tag{4.8}$$

where r is the radial offset between the galaxy and a potential counterpart, and $N(>S)$ is the sky density of sources brighter than the flux density S of this potential counterpart. Hence, for two potential counterparts offset by the same amount, the shape of $N(>S)$ results in a lower value of p being assigned to the brighter potential counterpart. When this method is adopted, a canonical value of $p \leq 0.05$ is used to indicate that a counterpart is secure (Downes et al., 1986; Ivison et al., 2007).

However, Equation 4.8 is typically used to match DSFGs to their radio, rather than optical/NIR, counterparts as their source density is comparatively lower. Furthermore, the closest, brightest optical/NIR galaxy is unlikely to be the real counterpart to a DSFG since DSFGs are known to be optically dark. Therefore, in this chapter I have adopted the likelihood ratio (LR — Chapin et al., 2011; Fleuren et al., 2012; McAlpine et al., 2013) method in order to locate potential counterparts to DSFGs, which is defined as:

$$\mathrm{LR} = \frac{\text{Probability of being related}}{\text{Probability of being unrelated}} = \frac{f(r,\mathcal{R})q(K,z)}{n(K,z)}, \tag{4.9}$$

where $q(K,z)$ and $n(K,z)$ are the K-band magnitude and redshift prior distributions of the real counterparts to DSFGs and background galaxies, respectively, and

$$f(r,\mathcal{R}) = \frac{1}{2\pi\mathcal{R}^2}\exp\left(-r^2/\mathcal{R}^2\right)$$

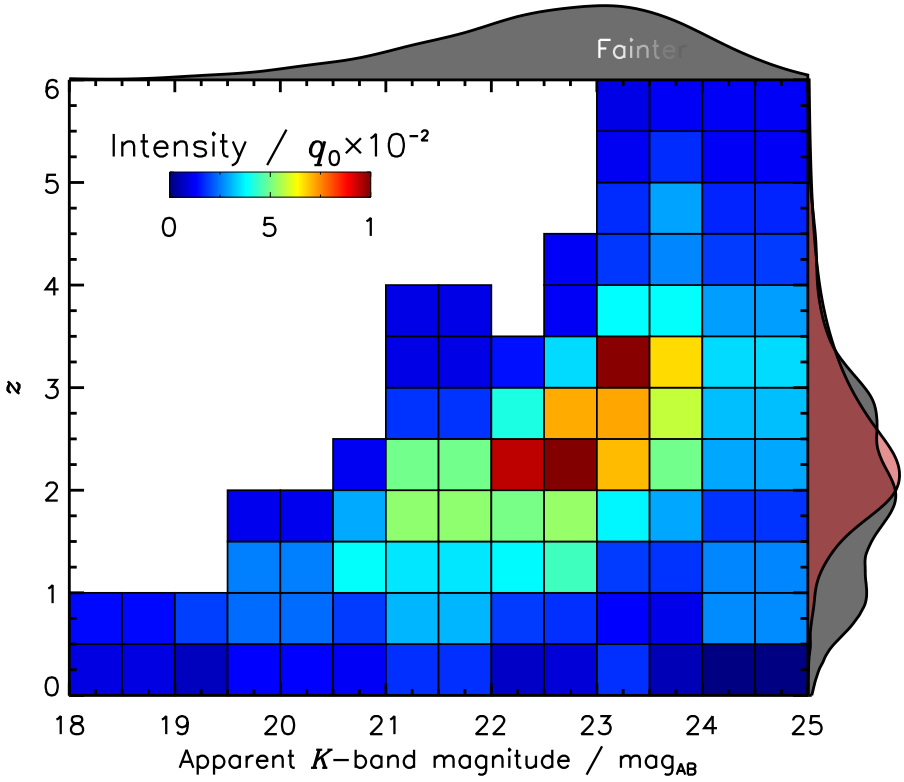

Figure 4.8: The two-dimensional prior distribution for potential optical/NIR counterparts to 829 DSFGs in the COSMOS field as a function of apparent K-band magnitude and redshift. This prior distribution was used to determine the LR that a given galaxy is the real counterpart to a given DSFG (see Equation 4.9). I show the K-band magnitude distribution towards the top of the plot, which clearly shows that counterparts to DSFGs are faint, with K-band magnitudes peaking at $K \sim 23\,\mathrm{mag_{AB}}$ (or $S_K \sim 2 \times 10^{-3}\,\mathrm{mJy}$). To the right, I show the photometric redshift distributions for the potential NIR counterparts (dark grey) and DSFGs (red, see Figure 4.2) The two distributions appear to be well matched around $z \approx 2$–3, but seriously mismatched at $z \sim 1$, which results in an extended tail of K-band magnitudes below $K \lesssim 20\,\mathrm{mag_{AB}}$. This mismatch is likely caused by the incorrect assignation of foreground galaxies to distant DSFGs. **Note**. Fainter apparent K-band magnitudes correspond to brighter galaxies.

is a Gaussian weighting that takes into account the positional accuracy of a given DSFG. The positional accuracy is capped above $\mathcal{R} \geq 2''$ (i.e. the SCUBA-2 pixel scale) to avoid $\mathcal{R} \to 0$ for those DSFGs detected at a high SNR. Furthermore, as it is typically much greater than that deduced for optical/NIR galaxies (i.e. $\mathcal{R} < 0.2''$), I do not add it (in quadrature) to the radial offset for DSFGs.

I estimated the prior distributions of the counterparts and background galaxies as follows.

- Firstly, I search for all galaxies within an $r_{\mathrm{aper}} = 8$-arcsec radius of a given DSFG. Such a conservatively sized search radius accounts for the fact that some of the brightest DSFGs originally catalogued in the S2CLS UDS field were found to be offset by up to half of a SCUBA-2 PSF FWHM from their high-resolution counterparts detected with ALMA (i.e. by as much as $\theta/2 \approx 8''$ — Simpson et al., 2015).

- For any detected galaxies around a given DSFG, I select those that have apparent K-band magnitudes between K' and $K' + \Delta K'$ (with K' ranging from $K' = 18$–$25\,\mathrm{mag_{AB}}$ and $\Delta K' = 0.5\,\mathrm{mag_{AB}}$) and sum their respective photometric redshift distributions represented by Equation 4.7. Performing this process for all DSFGs generates a two-dimensional '$total(K, z)$' image, which contains a contribution from the 'background' galaxies and from the 'real' counterparts, i.e.

$$total(K, z) = background(K, z) + real(K, z).$$

- To determine the contribution from the background galaxies, the above steps are repeated but this time replacing the positions of the DSFGs with 10,000 randomly generated positions. Normalising this background contribution by the area of the search radius, yields the prior distribution for the background galaxies, i.e.

$$n(K, z) = \frac{background(K, z)}{\pi r^2_{\mathrm{aper}}}.$$

- Finally, the prior distribution for the real counterparts to the DSFGs can be determined by:

$$q(K, z) = q_0 \left(\frac{real(K, z)}{\sum_i real(K_i, z_i)} \right),$$

where $q_0 = 69 \pm 4\%$ is a normalisation factor that estimates the probability of finding a real counterpart down to the 5-σ $\lesssim 24\,\mathrm{mag_{AB}}$ survey limit, i.e. $\sim 70\%$ of DSFGs have a real counterpart in the catalogues used here[9].

In Figure 4.8, I show $q(K, z)$ for the potential counterparts to 829 DSFGs in the COSMOS field, noting that a similar prior distribution is derived for the UDS field. Clearly the counterparts to DSFGs are faint, with typical K-band magnitudes of $K \sim 23\,\mathrm{mag_{AB}}$ (or equivalently $S_K \sim 2 \times 10^{-3}\,\mathrm{mJy}$, i.e. a factor of $\gtrsim 3{,}000\times$ fainter than at 850 μm for these DSFGs) – similar to that seen in Simpson et al. (2014). Although the optical/NIR and FIR photometric redshift distribution appear to be well matched around $z \sim 2$–3, there is a serious mismatch towards $z \sim 1$, which results in an extended tail below $K \lesssim 20\,\mathrm{mag_{AB}}$. This is likely caused by foreground (brighter) galaxies that have been incorrectly assigned as a real counterpart to a given DSFG. These incorrect assignations occur because either the real counterpart is too faint to be detected or (in extremely rare cases) outside of the 8-arcsec search radius. As these incorrect matches will heavily skew any future analysis, they needed to be removed before comparing the FIR with the optical/NIR photometric redshift estimates.

To decide which counterparts to remove, I compared the LRs for the DSFGs already computed to those of a large control sample. This large control sample was generated by

[9] q_0 was indirectly determined from a model fit of the form $(1 - q_0 f(r_{\mathrm{aper}}))$ to the ratio of blank apertures (i.e. apertures containing no containing no galaxies) around DSFGs to those around random positions as a function of aperture radius from $r_{\mathrm{aper}} = 0$–$10''$. However, as I later normalise the LR by a factor dependent on the false-positive rate of 'real' counterparts, determining q_0 is this way is not strictly necessary.

calculating the LR for each DSFG after the centre of its search radius had be randomly tweaked. The top-panel of Figure 4.9 shows the distribution of LRs for DSFGs and this large control sample. I highlight the LR that gives a false-positive rate of 10%, which was determined by integrating the tail of the control sample. This false-positive rate corresponds to a LR of LR = 1.3, above which only $\sim$ 50% of DSFGs have a real counterpart.

I then evaluated the normalised difference,

$$\Delta z/(1+z_{\rm FIR}) \equiv (z_{\rm NIR}-z_{\rm FIR})/(1+z_{\rm FIR}),$$

for each of these DSFG with a counterpart, which is shown in the bottom-panel of Figure 4.9.

Key Point 4.9
I obtained a LR-weighted mean and LR-weighted standard deviation of $\mu_{\Delta z} = +0.04(1+z_{\rm FIR})$ and $\sigma_{\Delta z} = 0.17(1+z_{\rm FIR})$, respectively, for these real counterparts. This suggests that the FIR photometric redshifts presented here slightly under-estimate the optical/NIR photometric redshifts by $\mu_{\Delta z} = 0.16$ at $z = 3$, although this correction is intrinsically uncertain to $\sigma_{\Delta z} = 0.68$.

Thus, before I evaluated the association probabilities of NIR galaxies around ultra-red galaxies using Equation 4.6, I shifted the FIR photometric redshift distribution of the ultra-red galaxies by $+0.04(1+z_{\rm FIR})$, where $z_{\rm FIR}$ was taken from the peak of a given FIR photometric redshift distribution.

4.5.2 Stellar Masses and Absolute Colours

With knowledge of how the FIR photometric redshifts correlate with the optical/NIR photometric redshifts, I examined the stellar masses ($M_{\rm stars}$) and absolute ($M_B - M_I$) colours of the NIR galaxies surrounding the ultra-red galaxies presented in this chapter. To recap, there are 42 ultra-red galaxies with optical/NIR coverage, 30 within the COSMOS field and 12 within the UDS field.

At the positions of each of these ultra-red galaxies, I extracted all of NIR galaxies that lie within a radius of $R_{\rm e} \approx 5'$ and recorded their stellar masses, absolute M_B and M_I magnitudes, probability of being associated (to the 'adjusted' FIR photometric redshift) using Equation 4.6 and radial distances to these positions. I also generated a control sample for each ultra-red galaxy by extracting the same properties but at 100 random positions, purposefully selected to avoid any overlap with the ultra-red galaxies.

Key Point 4.10
On average, there are $\approx$ 28 NIR galaxies that are 'associated' to given ultra-red galaxy but this varies considerably from $\approx$ 3–53. Although this only accounts for

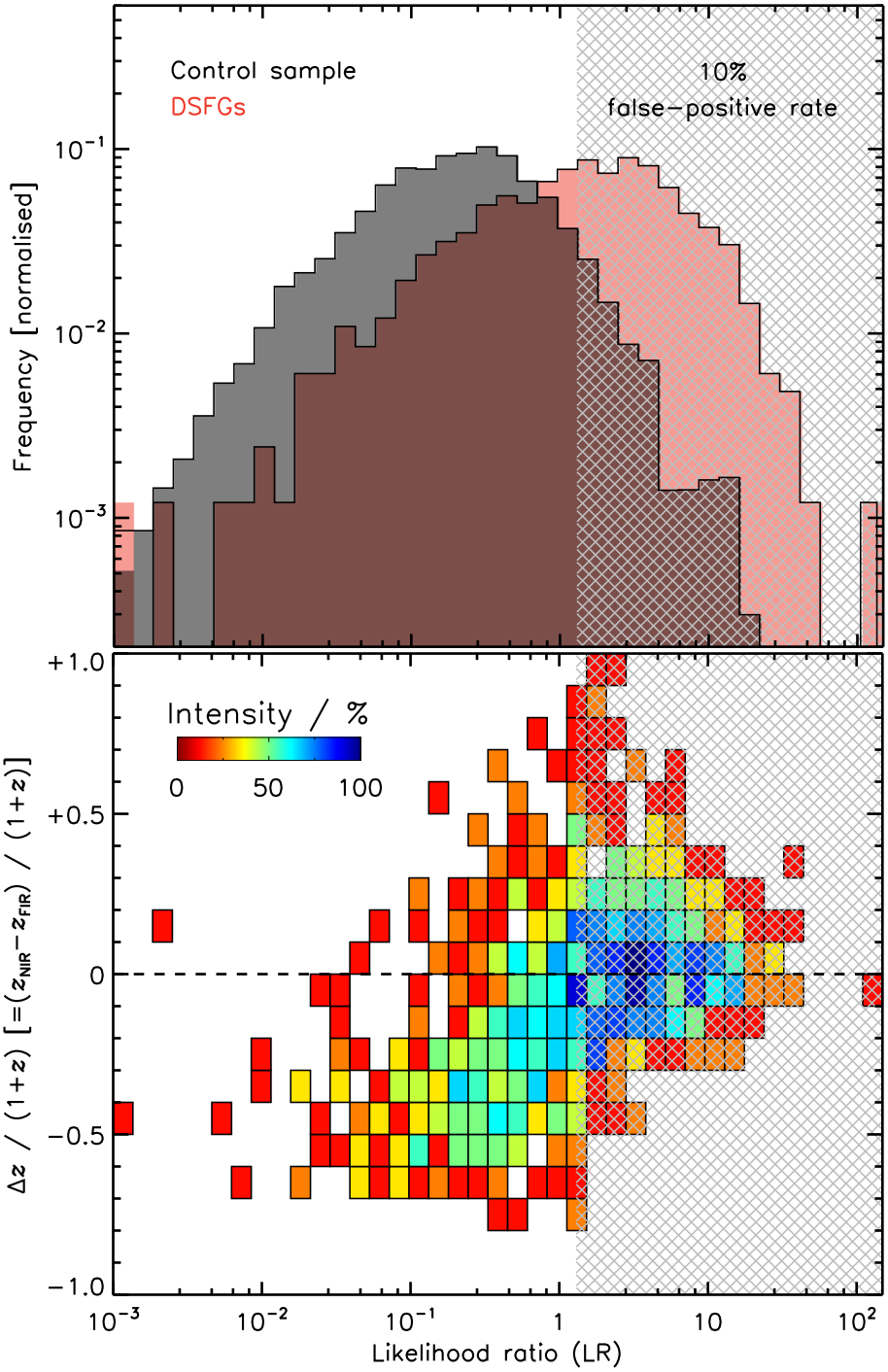

Figure 4.9: Top: histogram of the LRs for potential optical/NIR counterparts to DSFGs catalogued in the COSMOS field (black), which I compared to random positions (red). This comparison results in a false-positive rate of 10% above a LR of LR $\gtrsim$ 1.3 (chequered light grey region). Only 50% of DSFGs in the COSMOS field have a potential counter above this LR. **Bottom:** normalised difference, $(z_{\rm NIR} - z_{\rm FIR})/(1 + z_{\rm FIR})$, as a function of LR, between photometric redshifts determined using optical/NIR and FIR photometry. I obtain a LR-weighted mean and LR-weighted standard deviation of $\mu_{\Delta z} = +0.04(1 + z_{\rm FIR})$ and $\sigma_{\Delta z} = 0.17(1 + z_{\rm FIR})$, respectively, for potential counterparts above LR $\gtrsim$ 1.3. Therefore, the FIR photometric redshifts presented here slightly under-estimate the optical/NIR photometric redshifts by $\mu_{\Delta z} = 0.16$ at $z = 3$, although this correction is uncertain to $\sigma_{\Delta z} = 0.68$. Potential counterparts with LRs less than LR < 1, have FIR photometric redshifts that are significantly higher than the optical/NIR ones – suggesting that they are likely foreground galaxies.

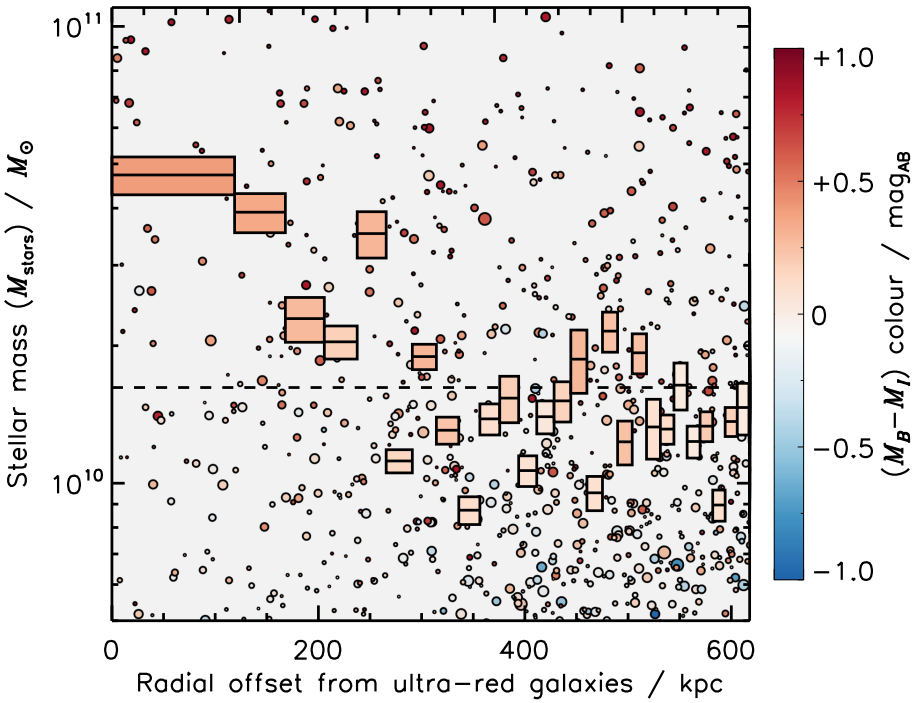

Figure 4.10: Stellar mass and absolute colour variations of NIR galaxies within $\lesssim$ 500 kpc of their respective central ultra-red galaxies. Individual stellar mass measurements of the surrounding NIR galaxies are represented as circles, colour-coded to represent their absolute $(M_B - M_I)$ colour and scaled to represent their association probability to their respective ultra-red galaxies. I show the average and standard error of the stellar mass within annuli of equal area. This figure illustrates that as the radial distance from an ultra-red galaxy increases out to $\sim$ 400 kpc, the average stellar mass decreases by a factor of $\sim 4\times$ to $M_{\rm stars} = (1.1 \pm 0.1) \times 10^{10}\,M_\odot$. This increasing average stellar mass with radius suggests that ultra-red galaxies reside in over-dense environments. The black dashed line shows the typical annuli average stellar mass from the control sample $M_{\rm stars} = (1.62 \pm 0.05) \times 10^{10}\,M_\odot$. **Note.** This figure assumes that all ultra-red galaxies are lying at $z \sim 3$, where $1'$ corresponds to $\approx$ 470 kpc.

$\sim$ 1% of the optical/NIR galaxies that are typically within $R_{\rm e} \approx 5'$ of an ultra-red galaxy, this is still a factor of $\sim$ 20$\times$ the number of DSFGs that I was able to associate.

Thus, the contribution from surrounding NIR galaxies is definitely not insignificant and, like for the associated DSFGs, is probably under-estimated here, too.

Stellar Masses

In Figure 4.10, I show the stellar masses of the surrounding NIR galaxies weighted by their association probability as a function of proper radial distance to their respective central ultra-red galaxies (assuming that they reside at $z \sim 3$). The average stellar mass in annuli of equal area shows a slight decrease from $(4.7 \pm 0.4) \times 10^{10}\,M_\odot$ at $\approx$ 60 kpc to $(1.1 \pm 0.1) \times 10^{10}\,M_\odot$ at $\approx$ 400 kpc.

Key Point 4.11
Furthermore, the average $(M_B - M_I)$-colour decreases from 0.57 ± 0.02 at ≈ 60 kpc to 0.28 ± 0.02 at ≈ 400 kpc, too. Although modest in size, these trends suggest that the ultra-red galaxies are residing near the centres of potential wells extending over $\lesssim 500$ kpc scales, and that these environmental factors are causing a factor of $\sim 4\times$ and $\sim 2\times$ increase in the stellar masses and colours of the surrounding NIR galaxies, respectively.

At larger distances from the ultra-red galaxies, the average stellar masses of the NIR galaxies fluctuates around the control average of $M_{\rm stars} = (1.62 \pm 0.05) \times 10^{10}\,M_{\odot}$, which itself shows no significant change in each annuli (as might be expected for a control sample).

Although some of the contribution to the central annulus will be influenced by the presence of the ultra-red galaxies themselves, which on occasions will have multiple possible counterparts (due to the multiplicity of DSFGs), it is very unlikely that the ≈ 140 kpc (or $\sim 20''$) annulus will contain the real LBG counterparts to any of these ultra-red galaxies. The average stellar mass and colour in this annulus are $(3.8\pm0.4)\times10^{10}\,M_{\odot}$ and 0.52 ± 0.03, respectively, which is still a factor of $\sim 3.5\times$ and $\sim 2\times$ increase in the stellar masses and colours of the surrounding NIR galaxies, respectively.

Finally, the average total stellar mass from $K \lesssim 24$-mag$_{\rm AB}$ NIR galaxies within the vicinity of ultra-red galaxies is $\sum M_{\rm stars} = 4.7 \times 10^{11}\,M_{\odot}$, though this ranges by an order of magnitude from 7.8×10^{10}–$1.1 \times 10^{12}\,M_{\odot}$ (in-line with the range of the associated number of NIR galaxies).

Key Point 4.12
Thus, the potential total $z \sim 0$ stellar mass of these candidate proto-clusters is $\sim 8 \times 10^{11}\,M_{\odot}$ – assuming that the DSFGs convert all of their molecular gas into stars and their 850-μm flux densities have not been severely boosted by chance gravitational lensing. Although very much a lower limit, these total stellar masses correspond to DM halos with masses of $M_{\rm halo} \sim 10^{14}$–$10^{15} M_{\odot}$ (Behroozi et al., 2013) – similar to those observed for Fornax-/Virgo-type galaxy clusters.

Absolute $(M_B - M_I)$ Colours

The absolute M_B and M_I magnitudes allow a quantitative measure on whether the red sequence has emerged around ultra-red galaxies as they are suitably positioned at either ends of the optical spectrum, which additionally allows any future comparisons with local galaxy clusters to be made. Furthermore, at $z \sim 3$ these colours are derived from the $\approx J$-/K-band apparent magnitudes, which I have placed sufficient constraints on to ensure that these measurements are both reliable and complete. Thus, for each ultra-red galaxy, I evaluated the CDF for the $(M_B - M_I)$ colours of the surrounding NIR galaxies, again

weighted by their association probability. In the bottom-panel of Figure 4.11, I show the average of these CDFs for all of 42 ultra-red galaxies and their respective control samples. A K-S test using Equation 4.4 yielded a value of $D_{\text{K-S}} = 0.21$ – equating to a probability of $P_{\text{K-S}} \sim 2\%$ that the control and ultra-red galaxy samples are drawn from the same distribution.

As an aid, in the top-panel of Figure 4.11, I show the approximate locations of the red/blue sequences and the so-called 'green valley' at $z < 1$ and $2 < z < 5$, each modelled as a Gaussian distribution. The peak of the blue sequence and green valley galaxies appears to have been shifted towards bluer colours at earlier epochs – suggestive of a younger stellar population.

Key Point 4.13
This aid highlights that there is a $\gtrsim$ 1-σ deficit in blue-sequence galaxies around ultra-red galaxies. Furthermore, this deficit is continued far into the colour space occupied by the green-valley galaxies, which suggests that the emergence of the red sequence is happening at a faster rate around ultra-red galaxies than in the (control) field.

Could the Surrounding NIR/Optical Galaxies Just be Dusty?

Although tentative evidence of the accelerated emergence of a red sequence around ultra-red galaxies has been presented in the previous section, I now analyse whether this same result could be achieved if the surrounding NIR/optical galaxies were simply dustier in composition, rather than 'dead' in nature.

As the process of star formation increases the dust content in the ISM of star-bursting galaxies experiencing enhanced star formation, it is very plausible that the excess of red galaxies seen residing around ultra-red galaxies is due to a dustier population. Again, similar to the findings in Chapter 3, such a scenario could hint at the presence of some large-scale mechanism capable of simultaneously enhancing the star formation across multiple galaxies within a dense environment (e.g. Oteo et al., 2017a).

The variation of extinction with passband is usually defined using the R_V parameter that takes into account the ratio of V- and B-band extinction, or A_V and A_B, respectively, as follows:

$$R_V \equiv \frac{A_V}{A_B} - 1, \tag{4.10}$$

For the Milky Way or a starburst-like galaxy, R_V typically ranges from 3.1–3.2. The magnitudes of extinction experienced by the B- and I-bands assuming a value of $R_V = 3.1$ are listed in Table 4.3. Hence, the $(M_B - M_I)$-colour extinction (or $A_B - A_I$) can be defined as a function of V-band extinction as follows:

$$A_B - A_I = (1.321 - 0.594)A_V \approx 0.7A_V, \tag{4.11}$$

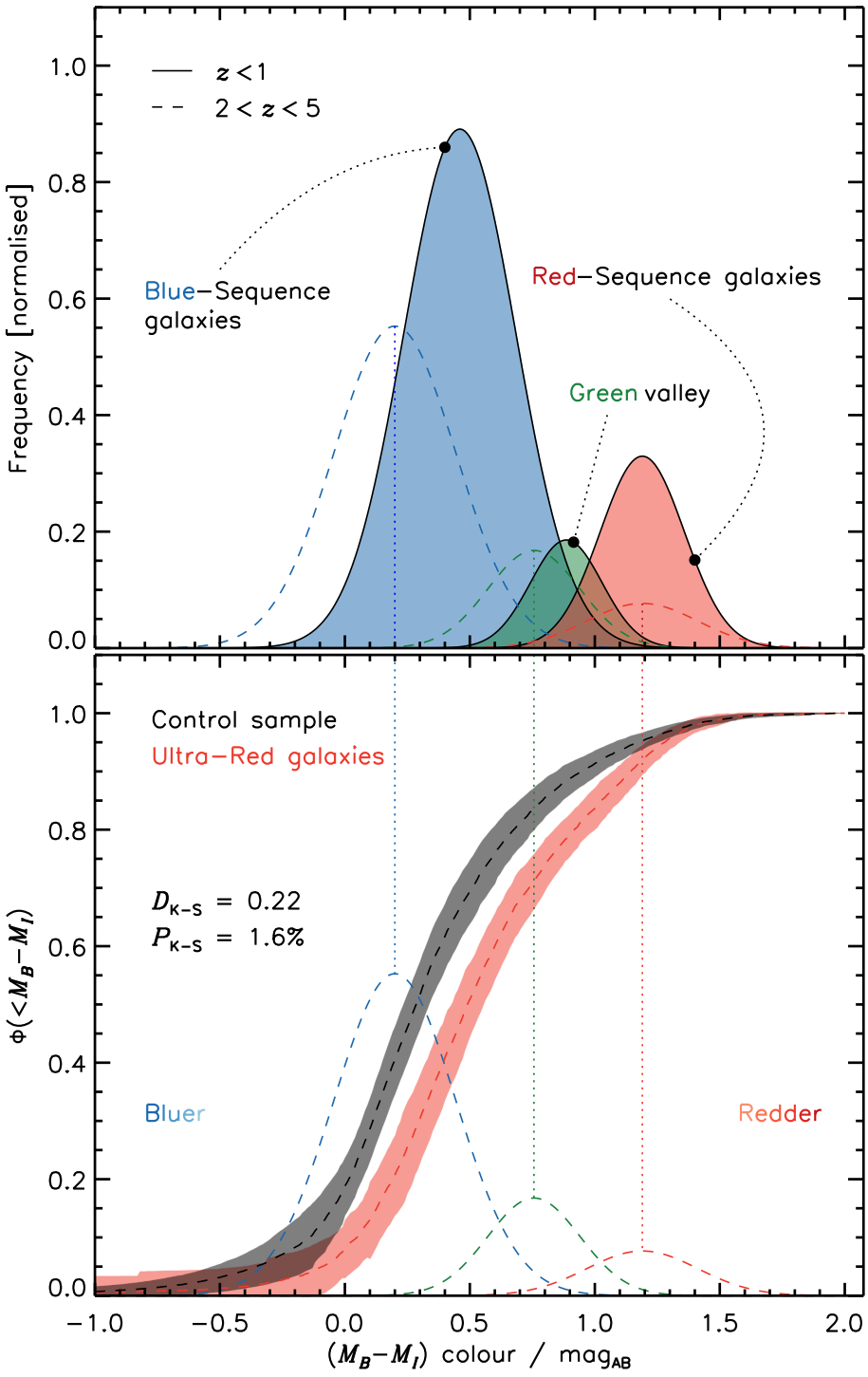

Figure 4.11: Top: empirically derived Gaussian distributions representing the red/blue sequences and so-called 'green valley' at $z < 1$ (solid lines) and $z \approx 2$–5 (dashed lines). The distributions for the blue sequence and green valley are shifted to relatively bluer colours at $z \approx 2$–5 compared to $z < 1$ – reflecting the prevalence of a younger stellar at these distant epochs. The peaks of these distributions at $z \approx 2$–5 are indicated by dotted lines as an aid to the bottom panel of this figure. **Bottom:** CDF of the $(M_B - M_I)$ colour for NIR galaxies detected within $R_e \approx 5'$ of an ultra-red galaxy (red) or a random control position (black). NIR galaxies from both samples have been weighted by their respective association probabilities using Equation 4.6. The CDFs for ultra-red galaxies and the control sample diverge around $(M_B - M_I) = 0.0$–1.0, which suggests that there is a larger number of red-sequence NIR galaxies in the vicinity of ultra-red galaxies than compared ...

Figure 4.11 (continued from previous page): ... to the field. Furthermore, given the excess of green-valley NIR galaxies around ultra-red galaxies, it would appear that environmental effects are resulting in red-sequence galaxies appearing at a faster rate around ultra-red galaxies than in the field, too. **Note**. NIR galaxies with smaller/larger values of $(M_B - M_I)$ appear bluer/redder, as shown by the annotations in the bottom left/right of this figure.

Table 4.3: Magnitudes of extinction for the B- and I-band photometry assuming the $R_V = 3.1$ extinction laws of Cardelli et al. (1989) and O'Donnell (1994). **Note.** These data were obtained from Table 6 in Schlegel et al. (1998).

Facility	Filter	$1/\lambda_{\rm eff}$ $\mu{\rm m}^{-1}$	$A_{\lambda_{\rm eff}}/A_V$
Subaru Suprime-Cam	B	2.3	1.3
Subaru Suprime-Cam	I	1.2	0.6
			$\rightarrow \boldsymbol{A_B - A_I = 0.7 A_V}$

or equivalently, the $(M_B - M_I)$ colour is reddened by $\approx 70\%$ of the V-band obscuration experienced by a given galaxy.

In Figure 4.12, I show the effect of increasing the A_V extinction on the $(M_B - M_I)$ colour for the control sample by $A_V = (0\text{–}1)\,{\rm mag_{AB}}$. Clearly evident is that $A_V = 1\,{\rm mag_{AB}}$ of extinction shifts the control sample to a redder $(M_B - M_I)$ colour (by $\approx 0.5\,{\rm mag_{AB}}$) than compared to the ultra-red galaxies.

Key Point 4.14
Performing a least-squares fit to the A_V-corrected, $(M_B - M_I)$ colour of the control sample against the $(M_B - M_I)$ colour of the ultra-red galaxies yields a value of $A_V \sim (0.26 \pm 0.05)\,{\rm mag_{AB}}$. Thus, the control sample *could* be mapped onto the ultra-red galaxy sample if it was to experience a very moderate dust reddening of $A_V \sim 0.3\,{\rm mag_{AB}}$.

Thus, it is very plausible that the optical/NIR galaxies surrounding ultra-red galaxies are experiencing enhanced star formation that is slightly increasing the amount of dust within their ISM.

4.5.3 Unable to Accurately Measure *K*-Band Morphologies

Using ground-based, K-band images for the UDS, Lani et al. (2013) investigated how the sizes of galaxies varied as a function of their environment density up to $z \sim 2$. These authors compared their ground-based results to those derived from space-based observations and found that although they correlated well, the scatter in this correlation increased sharply below $K \leq 22\,{\rm mag_{AB}}$. The over-densities examined here are typically located at $z \gtrsim 3$ and applying such an aggressive magnitude cut of $K \leq 22\,{\rm mag_{AB}}$ in order to reduce this scatter

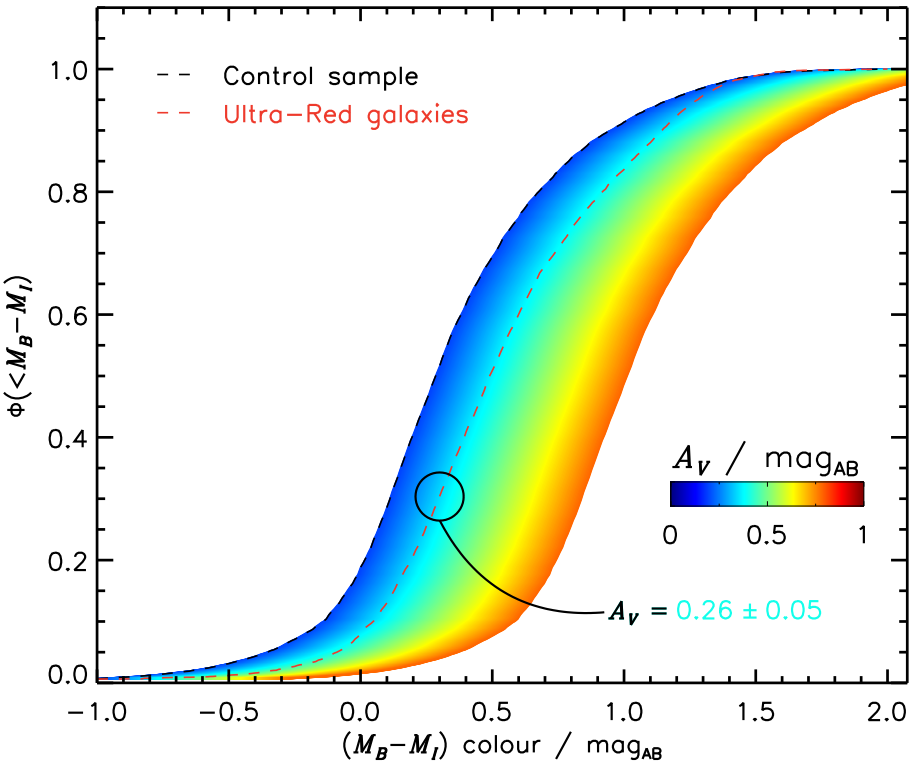

Figure 4.12: CDFs of the $(M_B - M_I)$ colour for the control sample and the ultra-red galaxies as shown in Figure 4.11. I adjust the $(M_B - M_I)$ colours of the control sample to account for varying amounts of V-band extinction up to $A_V = 1\,\mathrm{mag_{AB}}$ shown by the shaded region. Indicated by a black circle is the best-fit value of the extinction corrected CDF of the $(M_B - M_I)$ colour for the control sample to that of the ultra-red galaxies. This best-fit, least-squares value suggests that the control sample could be mapped onto the ultra-red galaxy sample if they were to experience a very moderate dust reddening of $A_V \sim 0.3\,\mathrm{mag_{AB}}$.

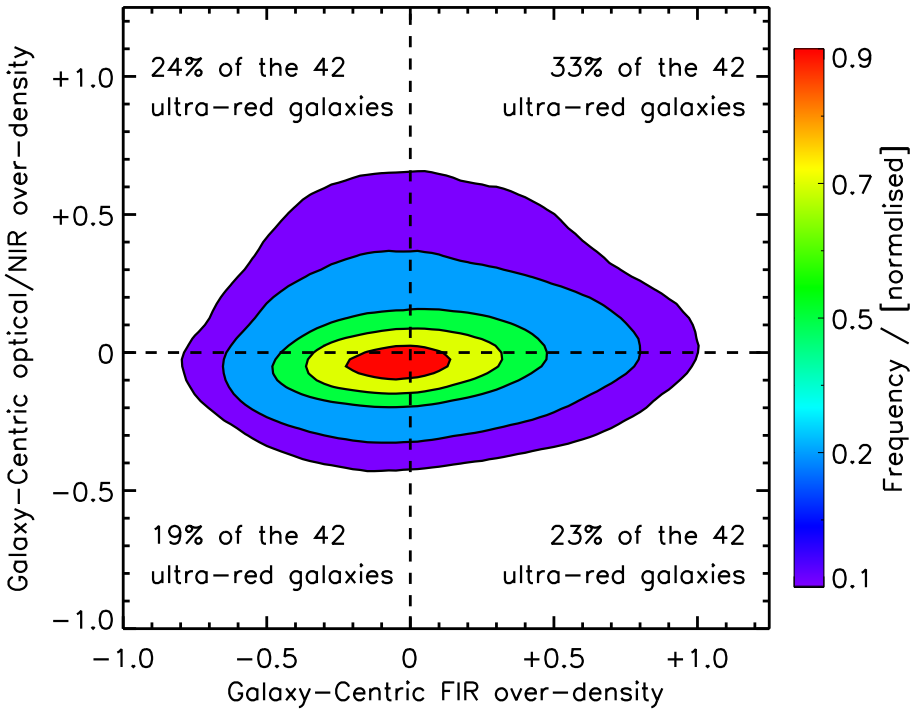

Figure 4.13: Optical/NIR versus FIR over-densities for the 42 ultra-red galaxies with optical/NIR data. **Note**. The comparatively low over-density parameter values reported here are due to the large apertures over which they are measured that effectively dilutes the signal from all but the largest over-densities.

results in *no* K-band galaxies above $z > 3$ (reflective of the increasing average K-band magnitude with increasing redshift).

However, I still attempted to eyeball these K-band images in order to see if there was any dependence on morphology of associated NIR galaxies with their distance to the ultra-red galaxies. Similar to the slight increase in both the stellar masses and absolute colours with distance to the ultra-red galaxies, I expected to see more elliptical/disturbed morphologies as the distance decreases. However, deciphering any trend was largely unsuccessfully as the eyeballing typically relied on only a handful of pixels – making any consistent morphological classification difficult.

Thus, in this chapter I have not been able to discern whether there is any morphological density relation established around ultra-red galaxies at $z \sim 3$.

4.5.4 Over-Densities of NIR/Optical Galaxies

I computed the optical/NIR over-density parameters around the ultra-red galaxies by comparing the number of massive $M_{\rm stars} > 10^{10}$-$M_{\odot}$ galaxies residing in their 5-arcmin environments to that expected from the field. Throughout this calculation, I took into account the varying instrumental noise and edge effects by 'conserving' the number of pixels within each 5-arcmin aperture around the positions of ultra-red galaxies and their respective control samples.

In Figure 4.13, I show how these optical/NIR over-densities vary as a function of the FIR over-densities computed previously in Section 4.3.1.

Key Point 4.15
Thus, it would appear that not all over-densities of DSFGs equate to over-densities of NIR galaxies, at least not *strongly* since there does appear to be a *slight* tilt in the contours, which may suggest that they correlate weakly.

However, only $\sim 60\%$ of the 32 ultra-red galaxies with available optical/NIR data reside in over-dense regions of the Universe, and of these, only $\sim 60\%$ are over-dense in NIR galaxies. Or put another way, only a third of ultra-red galaxies appear to be over-dense in both DSFGs *and* NIR galaxies. Overall though, $\sim 80\%$ of ultra-red galaxies signpost regions that are either over-dense in DSFGs, or NIR galaxies or both.

4.6 Conclusion

In this chapter, I have presented a multi-wavelength analysis of 64 ultra-red galaxies – selected via their ultra-red probabilities – within the S2CLS and S2COSMOS imaging surveys.

I found that just over half of these ultra-red galaxies reside in over-dense regions of DSFGs. In terms of global FIR over-density peaks, it appears that ultra-red galaxies play a central ($<$ a few megaparsec) role in medium-value global over-density peaks. By weighting each DSFG by its probability of being associated to the central DSFG, I found that the average total dust masses surrounding these ultra-red galaxies was $\sim 2 \times 10^9\,M_\odot$ (having been corrected for the 'missing' DSFGs within their vicinities). These values are consistent with those reported in the previous chapter. However, I was still only able to associate ≈ 1 surrounding DSFG to its central ultra-red galaxy using this new association method, which perhaps suggests that this is the limit achievable with FIR-based photometric redshifts.

Using optical/NIR ground-based data (down to 5-σ_K depths of $\lesssim 24\,\mathrm{mag_{AB}}$) for 42 ultra-red galaxies within the COSMOS and UDS fields, I was able to associate an average of ≈ 28 NIR galaxies to within $\lesssim 5'$ of a given ultra-red galaxy – a factor of $\sim 30\times$ the number of DSFGs. These associated NIR galaxies showed a factor of $\approx 5\times$ increase in stellar mass and a factor of $3\times$ increase in absolute $(M_B - M_I)$ colour as their distance to the ultra-red galaxies decreased over $\approx 500\,\mathrm{kpc}$ (or $\approx 2'$) scales. This suggests that the red sequence has already emerged, or is beginning to emerge, around these ultra-red galaxies at $z \sim 3$. In particular, there appears to be a higher fraction of green-valley galaxies around ultra-red galaxies than compared to the field, supporting the concept that, on average, the red sequence is emerging at a faster rate around ultra-red galaxies. With an average total stellar mass contribution from the NIR galaxies of $4.7 \times 10^{11}\,M_\odot$, and assuming that the ultra-red galaxies convert all of their molecular gas into stars, these candidate,

high-redshift proto-clusters have the potential to form systems with stellar masses of at least $M_{\rm stars} \sim 10^{12}\,M_{\odot}$ by $z \sim 0$.

Thus, I have shown that there is a sizeable contribution from NIR galaxies to these high-redshift systems that are signposted by ultra-red galaxies. Although these systems have average optical/NIR/FIR properties that are consistent with their evolution into present-day galaxy clusters with DM halos of mass $M_{\rm halo} \sim 10^{14}$–$10^{15}\,M_{\odot}$, I am still likely missing a sizeable contribution from NIR galaxies that my association probability has failed to associate. Therefore, the results presented here should be regarded as firm lower limits on the optical/NIR/FIR properties of the environments around ultra-red galaxies, which can now only be improved upon when spectroscopic data increases the accuracy of the redshift estimates.

Finally, I tabulate the FIR and optical/NIR data for these ultra-red galaxies and provide a continuation of Figure 4.5 in Appendix C.

Thesis Summary and Future Prospects

'HAMM: [Angrily.] To hell with the universe!' – excerpt from 'Endgame'

S. B. Beckett (1906–1989)

I now provide a brief summary of the three science objectives covered in this thesis and discuss a handful of directions that future prospects could take.

5.1 Summary

In Chapter 2, I presented work from Ivison et al. (2016) that analysed a sample of 109 so-called 'ultra-red galaxies'. These distant DSFGs were selected from the *H*-ATLAS imaging survey (covering $\approx 600\,\mathrm{deg}^2$) based on their *Herschel*-SPIRE flux densities ($S_{500} \geq 3.5\sigma_{500}$ and $S_{500} < 100\,\mathrm{mJy}$) and flux-density ratios ($S_{500}/S_{250} \geq 1.5$ and $S_{500}/S_{350} \geq 0.85$) and imaged with SCUBA-2 and/or LABOCA in order to better constrain their photometric redshifts. The photometric redshifts were derived using three template SEDs (shown to have an intrinsic uncertainty of $\sigma_{\Delta z} = 0.14(1+z)$) with the observed 250–850-μm photometry. The ultra-red galaxies were determined to lie at a median redshift of $z_{\mathrm{phot}} = 3.66$ with an IQR of $z_{\mathrm{phot}} = 3.30$–4.27 and peak at a considerably higher ($\Delta z \approx +1.5$) redshift than that inferred from 870-μm-selected galaxies. Furthermore, comparison with a phenomenological model of galaxy evolution designed to mimic the ultra-red-selection technique significantly under-predicted the redshift peak by $\Delta z \approx -1$ – suggesting that our current understanding of how massive, distant DSFGs evolve is currently incomplete.

Roughly a third ($33 \pm 6\%$) of these ultra-red galaxies have photometric redshifts that are consistent with lying at $z > 4$, which translates into a $z > 4$ space density of $\rho \approx 6 \times 10^{-7}\,\mathrm{Mpc}^{-3}$ (assuming a star-formation burst of $t_{\mathrm{burst}} = 100\,\mathrm{Myr}$). This space density is $\approx 30\times$ lower than that derived for $M_{\mathrm{stars}} \gtrsim 10^{10}$-$M_{\odot}$, NIR-selected galaxies at $z = 3$–4 (Straatman et al., 2014). This suggests that ultra-red galaxies – at least above the $S_{500} \gtrsim 30$-mJy flux-density limit analysed here – cannot fully account for these galaxies. However, the $M_{\mathrm{stars}} > 10^{11}$-$M_{\odot}$, NIR-selected galaxies at the $z = 3$–4 are only $\approx 7\times$ more numerous, which suggests that ultra-red galaxies may well evolve into the most massive,

quiescent galaxies seen today – typically observed to be residing in the centres of rich galaxy clusters.

In Chapter 3, I presented work from Lewis et al. (2017) that analysed the 870-μm environments around 22 ultra-red galaxies at $z \gtrsim 3$ (12 selected from *H*-ATLAS and 10 selected from *Her*MES). The aim of this chapter was to test whether the environments around ultra-red galaxies showed evidence of being 'over-dense' compared to the field. This would be expected if their constituents were to evolve into the most massive ETGs that reside in the centres of present-day galaxy clusters, as the previous chapter suggested is possible. To determine this, I detected (and extracted) 86 DSFGs surrounding these 22 ultra-red galaxies above a SNR of $S/N > 3.5$ and compared their flux-density distributions to those expected from LESS (a suitablely chosen blank-field survey imaged at 870 μm — Weiß et al., 2009).

The number counts of these surrounding galaxies implied that the environments around ultra-red galaxies *are* over-dense at all flux densities greater than $S_{870} \gtrsim 5\,\mathrm{mJy}$, but especially so at $S_{870} > 8.5\,\mathrm{mJy}$ (a flux-density limit that surveys an area of $\mathcal{A} \approx 0.2\,\mathrm{deg}^2$). This suggested that ultra-red galaxies reside in environments rich with bright DSFGs, modulo chance gravitational lensing of course. I 'associated' the surrounding galaxies likely responsible for the $S_{870} > 8.5$-mJy over-density by analysing their FIR photometric redshifts and found that, on average, each ultra-red galaxy has ≈ 1 associated DSFG. The majority of these associated galaxies are distributed within $\sim 2\,\mathrm{Mpc}$ of their ultra-red galaxy signposts and have median SFRs of $\psi \approx 1{,}000 \pm 200\,M_\odot\,\mathrm{yr}^{-1}$. Thus, I estimated that the eventual stellar mass of these candidate proto-clusters (as probed by their FIR photometry) is at least $M_\mathrm{stars} \sim 10^{11}\,M_\odot$ (assuming that their constituent DSFGs convert all of their molecular gas into stars from $z \sim 3$ until the present).

Furthermore, I derived a space density of $\sim 9 \times 10^{-7}\,\mathrm{Mpc}^{-3}$ between $2 \lesssim z \lesssim 6$ for the ultra-red galaxies with over-dense environments. This is similar to that of the most massive ($M_\mathrm{halo} \sim 10^{15}\,M_\odot$) galaxy clusters at $z < 0.2$ (Bahcall & Cen, 1993; Overzier, 2016) – making it plausible that each galaxy within these environments will evolve into a massive ETG, which populates the centre of a rich, present-day galaxy cluster. However, until deep optical imaging *and* spectroscopy of these environments has been taken, I am potentially missing a significant contribution to the overall stellar mass budget from associated LBGs, and thus their eventual fate is still fairly uncertain.

Lastly, in Chapter 4, I extracted PACS and SPIRE photometry at the catalogued positions of DSFGs within the S2CLS (Geach et al., 2017) and S2COSMOS (Simpson et al., in preparation) imaging surveys, in order to generate a sample of 64 ultra-red galaxies with both deep *and* wide 850-μm data. I selected this sample based on their 'ultra-red probability', which I introduced for the first time in Chapter 3. I found that these ultra-red galaxies are also preferentially located in 'over-dense' regions extending $\sim 5'$ (or $\sim 2\,\mathrm{Mpc}$ at $z \sim 3$) compared to galaxies that are not ultra-red. Furthermore, I derived total dust masses and total star-formation rates of $M_\mathrm{dust} \sim 2 \times 10^9\,M_\odot$ and $\Phi \sim 2 \times 10^3\,M_\odot\,\mathrm{yr}^{-1}$,

respectively, which is in agreement with the previous chapter and thus supports the concept that these DSFGs have the potential to evolve into $M_{\rm stars} \sim 10^{11}$-$M_{\odot}$ ETGs.

Using ground-based optical/NIR imaging around a subset of 42 ultra-red galaxies, I was able to 'associate', on average, 28 LBGs to each ultra-red galaxy – a factor of $\sim 30\times$ more numerous than the number of associated DSFGs. These associated LBGs showed a factor of $\sim 5\times$ increase in their stellar mass as their distance to the central ultra-red galaxy decreased from $\sim 500\,$kpc. Additionally, over this range, the absolute $(M_B - M_I)$ colour increased by a factor of $\sim 3\times$ – supporting the concept that ultra-red galaxies (typically) reside in deep potential wells, whose ICM is stripping galaxies of their fuel for further star formation. This concept was supported by a 1-σ increase in the fraction of 'green-valley' galaxies found within $\sim 5'$ compared to the field, which suggests that red-sequence galaxies are appearing at a faster rate around ultra-red galaxies than in the field. With an average total stellar mass contribution from the LBGs of $4.7\times10^{11}\,M_{\odot}$, and assuming that the ultra-red galaxies convert all of their molecular gas into stars, these candidate, high-redshift proto-clusters have the potential to form systems with stellar masses of at least $M_{\rm stars} \sim 10^{12}\,M_{\odot}$ (or DM halos with masses of $M_{\rm halo} \sim 10^{14}$–$10^{15}\,M_{\odot}$) by $z \sim 0$.

5.2 Future Prospects

The first and foremost work that I would embark on would be to compare the results obtained in Chapters 3–4 with that expected from N-body simulations. In particular, I would use simulations to identify Fornax-, Virgo- and Coma-type galaxy clusters at $z = 0$ (thus covering a broad range of potential present-day halo masses) and trace their merger trees out to $z \sim 6$, i.e. the maximum redshift occupied by ultra-red galaxies. Then by computing, comparing and contrasting the projected 850-/870-μm number counts in different redshift slices to those presented in this thesis, I will be able to test whether observations agree with theory.

The next work worthy of embarking on is to use this ultra-red-probability technique to select the most robust ultra-red galaxies with the *H*-ATLAS and examine their 250-μm environments to check for preliminary signs of over-densities. Any promising candidates (which cursory tinkering suggests that there are), along with a robust sub-sample selected from Chapter 3 should be followed up with deep, LABOCA (or soon to be replaced by the APEX Microwave Kinetic Inductance Detector, A-MKID — Heyminck et al., 2010) imaging in order to improve the fidelity of any associated galaxies. Following this, it is then vital to use ALMA (or NOEMA) in order to search for CO (3–2) and CO (4–3) lines in the 80–100 GHz range (expected at $z \sim 3$ and $z \sim 4$, respectively) - to constrain the redshifts of these robust ultra-red galaxies and their less luminous and/or colder associated galaxies. This will facilitate *robust* associations for the surrounding LBG population, too, and will thus allow a more rigorous analysis on their eventual fate, which has this far relied solely on optical/NIR/FIR photometry.

Bibliography

Aravena, M., Decarli, R., Walter, F., Da Cunha, E., Bauer, F. E. et al. 2016, ApJ, 833, 68 [arXiv:1607.06769]; go back to page 59

Arnouts, S., Cristiani, S., Moscardini, L., Matarrese, S., Lucchin, F. et al. 1999, MNRAS, 310, 540 [arXiv:astro-ph/9902290]; go back to page 112

Asboth, V., Conley, A., Sayers, J., Bethermin, M., Chapman, S. C. et al. 2016, ArXiv e-prints [arXiv:1601.02665]; go back to page 41, 51, 56

Aversa, R., Lapi, A., de Zotti, G., Shankar, F., and Danese, L. 2015, ApJ, 810, 74 [arXiv:1507.07318]; go back to page 5, 51

Bahcall, N. A. and Cen, R. 1993, ApJ, 407, L49 ; go back to page 88, 128

Baldry, I. K., Glazebrook, K., Brinkmann, J., Ivezić, Ž., Lupton, R. H. et al. 2004, ApJ, 600, 681 [arXiv:astro-ph/0309710]; go back to page 14

Balogh, M. L., Navarro, J. F., and Morris, S. L. 2000, ApJ, 540, 113 [arXiv:astro-ph/0004078]; go back to page 16

Barger, A. J., Cowie, L. L., Sanders, D. B., Fulton, E., Taniguchi, Y. et al. 1998, Nature, 394, 248 [arXiv:astro-ph/9806317]; go back to page 9, 19

Barger, A. J., Cowie, L. L., Smail, I., Ivison, R. J., Blain, A. W. et al. 1999, AJ, 117, 2656 [arXiv:astro-ph/9903142]; go back to page 9

Barlow, R. 2004, ArXiv Physics e-prints [arXiv:physics/0406120]; go back to page 109

Barnes, J. E. and Hernquist, L. 1992, ARA&A, 30, 705 ; go back to page 6

Baugh, C. M., Lacey, C. G., Frenk, C. S., Granato, G. L., Silva, L. et al. 2005, MNRAS, 356, 1191 [arXiv:astro-ph/0406069]; go back to page 5, 87

Beelen, A., Omont, A., Bavouzet, N., Kovács, A., Lagache, G. et al. 2008, A&A, 485, 645 [arXiv:0803.1615]; go back to page 69, 70

Behroozi, P. S., Wechsler, R. H., and Conroy, C. 2013, ApJ, 770, 57 [arXiv:1207.6105]; go back to page 14, 119

Belloche, A., Schuller, F., Parise, B., André, P., Hatchell, J. et al. 2011, A&A, 527, A145 [arXiv:1101.0718]; go back to page 30

Bernardi, M., Nichol, R. C., Sheth, R. K., Miller, C. J., and Brinkmann, J. 2006, AJ, 131, 1288 [arXiv:astro-ph/0509360]; go back to page 14

Béthermin, M., Daddi, E., Magdis, G., Sargent, M. T., Hezaveh, Y. et al. 2012, ApJ, 757, L23 [arXiv:1208.6512]; go back to page 14, 47, 48

Béthermin, M., De Breuck, C., Sargent, M., and Daddi, E. 2015, A&A, 576, L9 [arXiv:1502.04710]; go back to page 14, 47, 48

Blain, A. W. 1999, MNRAS, 304, 669 [arXiv:astro-ph/9903221]; go back to page 9, 19

Blain, A. W., Chapman, S. C., Smail, I., and Ivison, R. 2004, ApJ, 611, 725 [arXiv:astro-ph/0405035]; go back to page 107

Blain, A. W., Ivison, R. J., and Smail, I. 1998, MNRAS, 296, L29 [arXiv:astro-ph/9710003]; go back to page 7

Blain, A. W. and Longair, M. S. 1993, MNRAS, 264, 509 ; go back to page 11

—. 1996, MNRAS, 279, 847 ; go back to page 8

Blain, A. W., Smail, I., Ivison, R. J., Kneib, J., and Frayer, D. T. 2002, Phys. Rep., 369, 111 [arXiv:arXiv:astro-ph/0202228]; go back to page 8

Bothwell, M. S., Smail, I., Chapman, S. C., Genzel, R., Ivison, R. J. et al. 2013, MNRAS, 429, 3047 [arXiv:1205.1511]; go back to page 51

Bourne, N., Dunne, L., Maddox, S. J., Dye, S., Furlanetto, C. et al. 2016, MNRAS, 462, 1714 [arXiv:1606.09254]; go back to page 20

Bower, R. G., Kodama, T., and Terlevich, A. 1998, MNRAS, 299, 1193 [arXiv:astro-ph/9805290]; go back to page 14

Bussmann, R. S., Pérez-Fournon, I., Amber, S., Calanog, J., Gurwell, M. A. et al. 2013, ApJ, 779, 25 [arXiv:1309.0836]; go back to page 41

Bussmann, R. S., Riechers, D., Fialkov, A., Scudder, J., Hayward, C. C. et al. 2015, ApJ, 812, 43 [arXiv:1504.05256]; go back to page 71

Capak, P. L., Riechers, D., Scoville, N. Z., Carilli, C., Cox, P. et al. 2011, Nature, 470, 233 [arXiv:1101.3586]; go back to page 16, 107

Cardelli, J. A., Clayton, G. C., and Mathis, J. S. 1989, ApJ, 345, 245 ; go back to page 122

Carilli, C. L. and Yun, M. S. 1999, ApJ, 513, L13 [arXiv:astro-ph/9812251]; go back to page 11

Casali, M., Adamson, A., Alves de Oliveira, C., Almaini, O., Burch, K. et al. 2007, A&A, 467, 777 ; go back to page 94

Casey, C. M. 2016, ApJ, 824, 36 [arXiv:1603.04437]; go back to page 16, 17, 88, 106

Casey, C. M., Chen, C.-C., Cowie, L. L., Barger, A. J., Capak, P. et al. 2013, MNRAS, 436, 1919 [arXiv:1302.2619]; go back to page 61

Casey, C. M., Cooray, A., Capak, P., Fu, H., Kovac, K. et al. 2015, ApJ, 808, L33 [arXiv:1506.01715]; go back to page 88, 106, 107

Casey, C. M., Narayanan, D., and Cooray, A. 2014, Phys. Rep., 541, 45 [arXiv:1402.1456]; go back to page 8

Chabrier, G. 2003, ApJ, 586, L133 [arXiv:astro-ph/0302511]; go back to page 5

Chapin, E. L., Berry, D. S., Gibb, A. G., Jenness, T., Scott, D. et al. 2013, MNRAS, 430, 2545 [arXiv:1301.3652]; go back to page 32, 33

Chapin, E. L., Chapman, S. C., Coppin, K. E., Devlin, M. J., Dunlop, J. S. et al. 2011, MNRAS, 411, 505 [arXiv:1003.2647]; go back to page 20, 113

Chapman, S. C., Blain, A., Ibata, R., Ivison, R. J., Smail, I. et al. 2009, ApJ, 691, 560 [arXiv:0809.1159]; go back to page 107

Chapman, S. C., Blain, A. W., Ivison, R. J., and Smail, I. R. 2003, Nature, 422, 695 [arXiv:astro-ph/0304235]; go back to page 11

Chapman, S. C., Blain, A. W., Smail, I., and Ivison, R. J. 2005, ApJ, 622, 772 [arXiv:astro-ph/0412573]; go back to page 11, 85

Chiang, Y.-K., Overzier, R., and Gebhardt, K. 2013, ApJ, 779, 127 [arXiv:1310.2938]; go back to page 16, 17, 88, 99

Chiang, Y.-K., Overzier, R. A., Gebhardt, K., and Henriques, B. 2017, ApJ, 844, L23 [arXiv:1705.01634]; go back to page 16

Clements, D. L., Braglia, F., Petitpas, G., Greenslade, J., Cooray, A. et al. 2016, MNRAS, 461, 1719 [arXiv:1605.06433]; go back to page 16

Cole, S., Aragon-Salamanca, A., Frenk, C. S., Navarro, J. F., and Zepf, S. E. 1994, MNRAS, 271, 781 [arXiv:astro-ph/9402001]; go back to page 77

Cole, S., Lacey, C. G., Baugh, C. M., and Frenk, C. S. 2000, MNRAS, 319, 168 [arXiv:astro-ph/0007281]; go back to page 77

Condon, J. J. 1974, ApJ, 188, 279 ; go back to page 6

Condon, J. J. Deepest Astronomical Surveys, ed. , J. AfonsoH. C. FergusonB. Mobasher & R. Norris, 189 Astronomical Society of the Pacific Conference Series, Vol. 380, 71, 79

Conley, A., Cooray, A., Vieira, J. D., González Solares, E. A., Kim, S. et al. 2011, ApJ, 732, L35 [arXiv:1104.4113]; go back to page 18, 20

Coppin, K., Chapin, E. L., Mortier, A. M. J., Scott, S. E., Borys, C. et al. 2006, MNRAS, 372, 1621 [arXiv:astro-ph/0609039]; go back to page 69

Cowie, L. L., Songaila, A., Hu, E. M., and Cohen, J. G. 1996, AJ, 112, 839 [arXiv:astro-ph/9606079]; go back to page 12

Cowley, W. I., Lacey, C. G., Baugh, C. M., and Cole, S. 2015, MNRAS, 446, 1784 [arXiv:1406.0855]; go back to page 71, 77

Cox, P., Krips, M., Neri, R., Omont, A., Güsten, R. et al. 2011, ApJ, 740, 63 [arXiv:1107.2924]; go back to page 13

da Cunha, E., Groves, B., Walter, F., Decarli, R., Weiss, A. et al. 2013, ApJ, 766, 13 [arXiv:1302.0844]; go back to page 46

Daddi, E., Dannerbauer, H., Stern, D., Dickinson, M., Morrison, G. et al. 2009, ApJ, 694, 1517 [arXiv:0810.3108]; go back to page 107

Dannerbauer, H., Kurk, J. D., De Breuck, C., Wylezalek, D., Santos, J. S. et al. 2014, A&A, 570, A55 [arXiv:1410.3730]; go back to page 69, 70, 79

de Jong, T., Klein, U., Wielebinski, R., and Wunderlich, E. 1985, A&A, 147, L6 ; go back to page 11

Dempsey, J. T., Friberg, P., Jenness, T., Tilanus, R. P. J., Thomas, H. S. et al. 2013, MNRAS, 430, 2534 [arXiv:1301.3773]; go back to page 32, 35, 97

Dey, A., Lee, K.-S., Reddy, N., Cooper, M., Inami, H. et al. 2016, ApJ, 823, 11 [arXiv:1604.08627]; go back to page 108

Dickey, J. M. and Lockman, F. J. 1990, ARA&A, 28, 215 ; go back to page 94

Dowell, C. D., Conley, A., Glenn, J., Arumugam, V., Asboth, V. et al. 2014, ApJ, 780, 75 [arXiv:1310.7583]; go back to page 13

Downes, A. J. B., Peacock, J. A., Savage, A., and Carrie, D. R. 1986, MNRAS, 218, 31 ; go back to page 113

Draine, B. T. and Li, A. 2007, ApJ, 657, 810 [arXiv:astro-ph/0608003]; go back to page 3

Dressler, A., Oemler, A., Jr., Couch, W. J., Smail, I., Ellis, R. S. et al. 1997, ApJ, 490, 577 [arXiv:astro-ph/9707232]; go back to page 14

Dunlop, J. S., McLure, R. J., Yamada, T., Kajisawa, M., Peacock, J. A. et al. 2004, MNRAS, 350, 769 [arXiv:astro-ph/0205480]; go back to page 9

Dwek, E., Arendt, R. G., Hauser, M. G., Fixsen, D., Kelsall, T. et al. 1998, ApJ, 508, 106 [arXiv:astro-ph/9806129]; go back to page 1

Eales, S., Dunne, L., Clements, D., Cooray, A., de Zotti, G. et al. 2010, PASP, 122, 499 [arXiv:0910.4279]; go back to page 13

Eales, S., Lilly, S., Gear, W., Dunne, L., Bond, J. R. et al. 1999, ApJ, 515, 518 [arXiv:astro-ph/9808040]; go back to page 9

Eales, S., Smith, M. W. L., Auld, R., Baes, M., Bendo, G. J. et al. 2012, ApJ, 761, 168 [arXiv:1202.0547]; go back to page 6

Eddington, A. S. 1913, MNRAS, 73, 359 ; go back to page 26

Edge, A., Sutherland, W., Kuijken, K., Driver, S., McMahon, R. et al. 2013, The Messenger, 154, 32 ; go back to page 92

Elbaz, D., Daddi, E., Le Borgne, D., Dickinson, M., Alexander, D. M. et al. 2007, A&A, 468, 33 [arXiv:astro-ph/0703653]; go back to page 16

Engel, H., Tacconi, L. J., Davies, R. I., Neri, R., Smail, I. et al. 2010, ApJ, 724, 233 ; go back to page 8, 19

Fassbender, R., Nastasi, A., Böhringer, H., Šuhada, R., Santos, J. S. et al. 2011, A&A, 527, L10 [arXiv:1101.3313]; go back to page 88

Fixsen, D. J., Dwek, E., Mather, J. C., Bennett, C. L., and Shafer, R. A. 1998, ApJ, 508, 123 [arXiv:astro-ph/9803021]; go back to page 1

Fleuren, S., Sutherland, W., Dunne, L., Smith, D. J. B., Maddox, S. J. et al. 2012, MNRAS, 423, 2407 [arXiv:1202.3891]; go back to page 113

Fudamoto, Y., Ivison, R. J., Oteo, I., Krips, M., Zhang, Z.-Y. et al. 2017, MNRAS, 472, 2028 [arXiv:1707.08967]; go back to page 13, 42, 43, 44, 48, 88, 89

Geach, J. E., Chapin, E. L., Coppin, K. E. K., Dunlop, J. S., Halpern, M. et al. 2013, MNRAS, 432, 53 [arXiv:1211.6668]; go back to page 62

Geach, J. E., Dunlop, J. S., Halpern, M., Smail, I., van der Werf, P. et al. 2017, MNRAS, 465, 1789 [arXiv:1607.03904]; go back to page 62, 69, 94, 95, 97, 128

Gehrels, N. 1986, ApJ, 303, 336 ; go back to page 48, 68, 70

Gerke, B. F., Newman, J. A., Faber, S. M., Cooper, M. C., Croton, D. J. et al. 2007, MNRAS, 376, 1425 [arXiv:astro-ph/0608569]; go back to page 14

Giavalisco, M. 2002, ARA&A, 40, 579 ; go back to page 1

Gomez, H. L., Vlahakis, C., Stretch, C. M., Dunne, L., Eales, S. A. et al. 2010, MNRAS, 401, L48 [arXiv:0911.0176]; go back to page 30

Greve, T. R., Bertoldi, F., Smail, I., Neri, R., Chapman, S. C. et al. 2005, MNRAS, 359, 1165 [arXiv:astro-ph/0503055]; go back to page 6, 11

Greve, T. R., Ivison, R. J., Bertoldi, F., Stevens, J. A., Dunlop, J. S. et al. 2004, MNRAS, 354, 779 [arXiv:astro-ph/0405361]; go back to page 75

Griffin, M. J., Abergel, A., Abreu, A., Ade, P. A. R., André, P. et al. 2010, A&A, 518, L3 [arXiv:1005.5123]; go back to page 11

Groth, E. J., Kristian, J. A., Lynds, R., O'Neil, E. J., Jr., Balsano, R. et al. 1994, in Bulletin of the American Astronomical Society, Vol. 26, American Astronomical Society Meeting Abstracts, 1403 94

Gunn, J. E. and Gott, J. R., III. 1972, ApJ, 176, 1 ; go back to page 14

Hartley, W. G., Almaini, O., Mortlock, A., Conselice, C. J., Grützbauch, R. et al. 2013, MNRAS, 431, 3045 [arXiv:1303.0816]; go back to page 111

Hauser, M. G., Arendt, R. G., Kelsall, T., Dwek, E., Odegard, N. et al. 1998, ApJ, 508, 25 [arXiv:astro-ph/9806167]; go back to page 1

Hayward, C. C., Narayanan, D., Kereš, D., Jonsson, P., Hopkins, P. F. et al. 2013, MNRAS, 428, 2529 [arXiv:1209.2413]; go back to page 5

Helou, G., Soifer, B. T., and Rowan-Robinson, M. 1985, ApJ, 298, L7 ; go back to page 11

Heyminck, S., Klein, B., Güsten, R., Kasemann, C., Baryshev, A. et al. 2010, in Twenty-First International Symposium on Space Terahertz Technology, 262 129

Hickox, R. C., Wardlow, J. L., Smail, I., Myers, A. D., Alexander, D. M. et al. 2012, MNRAS, 421, 284 [arXiv:1112.0321]; go back to page 51

Hildebrand, R. H. 1983, QJRAS, 24, 267 ; go back to page 2

Hinshaw, G., Weiland, J. L., Hill, R. S., Odegard, N., Larson, D. et al. 2009, ApJS, 180, 225 [arXiv:0803.0732]; go back to page 18

Hodge, J. A., Carilli, C. L., Walter, F., Daddi, E., and Riechers, D. 2013, ApJ, 776, 22 [arXiv:1307.4763]; go back to page 107

Hogg, D. W. 1999, ArXiv Astrophysics e-prints [arXiv:astro-ph/9905116]; go back to page 51

Holland, W. S., Bintley, D., Chapin, E. L., Chrysostomou, A., Davis, G. R. et al. 2013, MNRAS, 430, 2513 [arXiv:1301.3650]; go back to page 24

Holland, W. S., Robson, E. I., Gear, W. K., Cunningham, C. R., Lightfoot, J. F. et al. 1999, MNRAS, 303, 659 [arXiv:astro-ph/9809122]; go back to page 8

Houck, J. R., Schneider, D. P., Danielson, G. E., Neugebauer, G., Soifer, B. T. et al. 1985, ApJ, 290, L5 ; go back to page 2

Huchra, J. P., Macri, L. M., Masters, K. L., Jarrett, T. H., Berlind, P. et al. 2012, ApJS, 199, 26 [arXiv:1108.0669]; go back to page 15

Hughes, D. H., Serjeant, S., Dunlop, J., Rowan-Robinson, M., Blain, A. et al. 1998, Nature, 394, 241 [arXiv:arXiv:astro-ph/9806297]; go back to page 9, 19

Hung, C.-L., Casey, C. M., Chiang, Y.-K., Capak, P. L., Cowley, M. J. et al. 2016, ApJ, 826, 130 [arXiv:1605.07176]; go back to page 107

Ibar, E., Ivison, R. J., Cava, A., Rodighiero, G., Buttiglione, S. et al. 2010, MNRAS, 409, 38 [arXiv:1009.0262]; go back to page 94

Ikarashi, S., Ivison, R. J., Caputi, K. I., Aretxaga, I., Dunlop, J. S. et al. 2015, ApJ, 810, 133 [arXiv:1411.5038]; go back to page 12, 51

Ikarashi, S., Kohno, K., Aguirre, J. E., Aretxaga, I., Arumugam, V. et al. 2011, MNRAS, 415, 3081 [arXiv:1009.1455]; go back to page 98

Ivison, R. J., Dunlop, J. S., Smail, I., Dey, A., Liu, M. C. et al. 2000, ApJ, 542, 27 [arXiv:astro-ph/0005234]; go back to page 16

Ivison, R. J., Greve, T. R., Dunlop, J. S., Peacock, J. A., Egami, E. et al. 2007, MNRAS, 380, 199 [arXiv:astro-ph/0702544]; go back to page 9, 64, 71, 95, 113

Ivison, R. J., Greve, T. R., Smail, I., Dunlop, J. S., Roche, N. D. et al. 2002, MNRAS, 337, 1 [arXiv:astro-ph/0206432]; go back to page 9, 11

Ivison, R. J., Lewis, A. J. R., Weiss, A., Arumugam, V., Simpson, J. M. et al. 2016, ApJ, 832, 78 [arXiv:1611.00762]; go back to page xi, 13, 19, 53, 127

Ivison, R. J., Magnelli, B., Ibar, E., Andreani, P., Elbaz, D. et al. 2010a, A&A, 518, L31 [arXiv:1005.1072]; go back to page 11

Ivison, R. J., Papadopoulos, P. P., Smail, I., Greve, T. R., Thomson, A. P. et al. 2011, MNRAS, 412, 1913 [arXiv:1009.0749]; go back to page 51

Ivison, R. J., Smail, I., Le Borgne, J., Blain, A. W., Kneib, J. et al. 1998, MNRAS, 298, 583 [arXiv:arXiv:astro-ph/9712161]; go back to page 9

Ivison, R. J., Swinbank, A. M., Swinyard, B., Smail, I., Pearson, C. P. et al. 2010b, A&A, 518, L35 [arXiv:1005.1071]; go back to page 22, 46

James, A., Dunne, L., Eales, S., and Edmunds, M. G. 2002, MNRAS, 335, 753 [arXiv:astro-ph/0204519]; go back to page 3

Karim, A., Swinbank, A. M., Hodge, J. A., Smail, I. R., Walter, F. et al. 2013, MNRAS, 432, 2 [arXiv:1210.0249]; go back to page 35

Kelvin, L. S., Driver, S. P., Robotham, A. S. G., Taylor, E. N., Graham, A. W. et al. 2014, MNRAS, 444, 1647 [arXiv:1407.7555]; go back to page 88

Kennicutt, R. C., Jr. 1998, ARA&A, 36, 189 [arXiv:astro-ph/9807187]; go back to page 3, 5, 48, 87

Klaas, U., Haas, M., Heinrichsen, I., and Schulz, B. 1997, A&A, 325, L21 ; go back to page 4

Knudsen, K. K., van der Werf, P. P., and Jaffe, W. 2003, A&A, 411, 343 [arXiv:astro-ph/0308438]; go back to page 8

Knudsen, K. K., van der Werf, P. P., and Kneib, J.-P. 2008, MNRAS, 384, 1611 [arXiv:0712.1904]; go back to page 8

Lacey, C. G., Baugh, C. M., Frenk, C. S., Benson, A. J., Bower, R. G. et al. 2016, MNRAS, 462, 3854 [arXiv:1509.08473]; go back to page 77

Laigle, C., McCracken, H. J., Ilbert, O., Hsieh, B. C., Davidzon, I. et al. 2016, ApJS, 224, 24 [arXiv:1604.02350]; go back to page 111

Landsman, W. B. Astronomical Society of the Pacific Conference Series, Vol. 52, , Astronomical Data Analysis Software and Systems II, ed. R. J. HanischR. J. V. Brissenden & J. Barnes, 246 in 35

Landy, S. D. and Szalay, A. S. 1993, ApJ, 412, 64 ; go back to page 77, 78

Lani, C., Almaini, O., Hartley, W. G., Mortlock, A., Häußler, B. et al. 2013, MNRAS, 435, 207 [arXiv:1307.3247]; go back to page 122

Lapi, A., González-Nuevo, J., Fan, L., Bressan, A., De Zotti, G. et al. 2011, ApJ, 742, 24 [arXiv:1108.3911]; go back to page 39

Lapi, A., Raimundo, S., Aversa, R., Cai, Z.-Y., Negrello, M. et al. 2014, ApJ, 782, 69 [arXiv:1312.3751]; go back to page 5, 51

Larson, R. B. 1981, MNRAS, 194, 809 ; go back to page 3

Larson, R. B., Tinsley, B. M., and Caldwell, C. N. 1980, ApJ, 237, 692 ; go back to page 16

Lawrence, A., Walker, D., Rowan-Robinson, M., Leech, K. J., and Penston, M. V. 1986, MNRAS, 219, 687 ; go back to page 2

Lawrence, A., Warren, S. J., Almaini, O., Edge, A. C., Hambly, N. C. et al. 2007, MNRAS, 379, 1599 [arXiv:astro-ph/0604426]; go back to page 94, 111

Le Floc'h, E., Aussel, H., Ilbert, O., Riguccini, L., Frayer, D. T. et al. 2009, ApJ, 703, 222 [arXiv:0909.4303]; go back to page 8

Leitherer, C. and Heckman, T. M. 1995, ApJS, 96, 9 ; go back to page 5

Lewis, A. J. R., Ivison, R. J., Best, P. N., Simpson, J. M., Weiss, A. et al. 2017, ArXiv e-prints [arXiv:1711.08803]; go back to page xi, 55, 128

Lilly, S. J., Cowie, L. L., and Gardner, J. P. 1991, ApJ, 369, 79 ; go back to page 94

Lilly, S. J., Eales, S. A., Gear, W. K. P., Hammer, F., Le Fèvre, O. et al. 1999, ApJ, 518, 641 [arXiv:astro-ph/9901047]; go back to page 9

Lonsdale, C. J., Farrah, D., and Smith, H. E. 2006, Ultraluminous Infrared Galaxies, ed. J. W. Mason, 285 1

Lutz, D., Poglitsch, A., Altieri, B., Andreani, P., Aussel, H. et al. 2011, A&A, 532, A90 [arXiv:1106.3285]; go back to page 94

Lynds, R. 1971, ApJ, 164, L73 ; go back to page 1

Madau, P., Ferguson, H. C., Dickinson, M. E., Giavalisco, M., Steidel, C. C. et al. 1996, MNRAS, 283, 1388 [arXiv:astro-ph/9607172]; go back to page 8

Maddox, S. J., Dunne, L., Rigby, E., Eales, S., Cooray, A. et al. 2010, A&A, 518, L11 [arXiv:1005.2406]; go back to page 20

Maddox, S. J., Valiante, E., Cigan, P., Dunne, L., Eales, S. et al. 2018, ApJS, 236, 30 [arXiv:1712.07241]; go back to page 20

Markwardt, C. B. Astronomical Society of the Pacific Conference Series, Vol. 411, , Astronomical Data Analysis Software and Systems XVIII, ed. D. A. BohlenderD. Durand & P. Dowler, 251 [arXiv:0902.2850] 95

Martin, C. L. 1999, ApJ, 513, 156 [arXiv:astro-ph/9810233]; go back to page 6

Matsuura, M., Barlow, M. J., Zijlstra, A. A., Whitelock, P. A., Cioni, M.-R. L. et al. 2009, MNRAS, 396, 918 [arXiv:0903.1123]; go back to page 2

McAlpine, K., Jarvis, M. J., and Bonfield, D. G. 2013, MNRAS, 436, 1084 [arXiv:1309.0358]; go back to page 113

McCracken, H. J., Milvang-Jensen, B., Dunlop, J., Franx, M., Fynbo, J. P. U. et al. 2012, A&A, 544, A156 [arXiv:1204.6586]; go back to page 111

Michałowski, M. J., Dunlop, J. S., Koprowski, M. P., Cirasuolo, M., Geach, J. E. et al. 2017, MNRAS, 469, 492 [arXiv:1610.02409]; go back to page 108

Miley, G. K., Overzier, R. A., Zirm, A. W., Ford, H. C., Kurk, J. et al. 2006, ApJ, 650, L29 [arXiv:astro-ph/0610909]; go back to page 69

Miller, T. B., Chapman, S. C., Hayward, C. C., Behroozi, P. S., Bradford, C. M. et al. 2016, ArXiv e-prints [arXiv:1611.08552]; go back to page 16

Miller, T. B., Hayward, C. C., Chapman, S. C., and Behroozi, P. S. 2015, MNRAS, 452, 878 [arXiv:1501.04105]; go back to page 16

Morselli, L., Mignoli, M., Gilli, R., Vignali, C., Comastri, A. et al. 2014, A&A, 568, A1 [arXiv:1406.3961]; go back to page 71

Mortlock, A., Conselice, C. J., Hartley, W. G., Duncan, K., Lani, C. et al. 2015, MNRAS, 447, 2 [arXiv:1411.3339]; go back to page 112

Mortlock, A., Conselice, C. J., Hartley, W. G., Ownsworth, J. R., Lani, C. et al. 2013, MNRAS, 433, 1185 [arXiv:1305.2204]; go back to page 112

Narayanan, D., Turk, M., Feldmann, R., Robitaille, T., Hopkins, P. et al. 2015, Nature, 525, 496 [arXiv:1509.06377]; go back to page 73

Negrello, M., Amber, S., Amvrosiadis, A., Cai, Z.-Y., Lapi, A. et al. 2017, MNRAS, 465, 3558 [arXiv:1611.03922]; go back to page 18

Negrello, M., González-Nuevo, J., Magliocchetti, M., Moscardini, L., De Zotti, G. et al. 2005, MNRAS, 358, 869 [arXiv:astro-ph/0406388]; go back to page 16

Negrello, M., Hopwood, R., De Zotti, G., Cooray, A., Verma, A. et al. 2010, Science, 330, 800 [arXiv:1011.1255]; go back to page 18, 20

Nelan, J. E., Smith, R. J., Hudson, M. J., Wegner, G. A., Lucey, J. R. et al. 2005, ApJ, 632, 137 [arXiv:astro-ph/0505301]; go back to page 12

Neri, R., Genzel, R., Ivison, R. J., Bertoldi, F., Blain, A. W. et al. 2003, ApJ, 597, L113 [arXiv:astro-ph/0307310]; go back to page 11

Neugebauer, G., Habing, H. J., van Duinen, R., Aumann, H. H., Baud, B. et al. 1984, ApJ, 278, L1 ; go back to page 2

Newman, A. B., Ellis, R. S., Bundy, K., and Treu, T. 2012, ApJ, 746, 162 [arXiv:1110.1637]; go back to page 12, 51

Nguyen, H. T., Schulz, B., Levenson, L., Amblard, A., Arumugam, V. et al. 2010, A&A, 518, L5 [arXiv:1005.2207]; go back to page 94, 95

O'Donnell, J. E. 1994, ApJ, 422, 158 ; go back to page 122

Oke, J. B. and Gunn, J. E. 1983, ApJ, 266, 713 ; go back to page 18

Oteo, I., Ivison, R. J., Dunne, L., Manilla-Robles, A., Maddox, S. et al. 2017a, ArXiv e-prints [arXiv:1709.02809]; go back to page 16, 39, 85, 89, 120

Oteo, I., Ivison, R. J., Negrello, M., Smail, I., Pérez-Fournon, I. et al. 2017b, ArXiv e-prints [arXiv:1709.04191]; go back to page 90

Overzier, R. A. 2016, A&ARv, 24, 14 [arXiv:1610.05201]; go back to page 16, 17, 128

Overzier, R. A., Guo, Q., Kauffmann, G., De Lucia, G., Bouwens, R. et al. 2009a, MNRAS, 394, 577 [arXiv:0810.2566]; go back to page 14

Overzier, R. A., Shu, X., Zheng, W., Rettura, A., Zirm, A. et al. 2009b, ApJ, 704, 548 [arXiv:0909.1082]; go back to page 88

Pardo, J. R., Cernicharo, J., and Serabyn, E. 2001, ITAP, 49, 1683 ; go back to page 7

Partridge, R. B. and Peebles, P. J. E. 1967, ApJ, 148, 377 ; go back to page 1

Pearson, E. A., Eales, S., Dunne, L., Gonzalez-Nuevo, J., Maddox, S. et al. 2013, MNRAS, 435, 2753 [arXiv:1308.5681]; go back to page 39, 41

Peebles, P. J. E. 1993, Principles of Physical Cosmology 51

Peebles, P. J. E. and Yu, J. T. 1970, ApJ, 162, 815 ; go back to page 14

Pilbratt, G. L., Riedinger, J. R., Passvogel, T., Crone, G., Doyle, D. et al. 2010, A&A, 518, L1+ [arXiv:1005.5331]; go back to page 11

Pope, A., Chary, R., Alexander, D. M., Armus, L., Dickinson, M. et al. 2008, ApJ, 675, 1171 [arXiv:0711.1553]; go back to page 26, 39, 41, 67, 97, 107

Puget, J.-L., Abergel, A., Bernard, J.-P., Boulanger, F., Burton, W. B. et al. 1996, A&A, 308, L5 ; go back to page 1

Reichertz, L. A., Weferling, B., Esch, W., and Kreysa, E. 2001, A&A, 379, 735 ; go back to page 29

Riechers, D. A., Bradford, C. M., Clements, D. L., Dowell, C. D., Pérez-Fournon, I. et al. 2013, Nature, 496, 329 [arXiv:1304.4256]; go back to page 13, 41

Riechers, D. A., Capak, P. L., Carilli, C. L., Cox, P., Neri, R. et al. 2010, ApJ, 720, L131 [arXiv:1008.0389]; go back to page 107

Riechers, D. A., Leung, T. K. D., Ivison, R. J., Perez-Fournon, I., Lewis, A. J. R. et al. 2017, ArXiv e-prints [arXiv:1705.09660]; go back to page 89, 90

Rigby, E. E., Hatch, N. A., Röttgering, H. J. A., Sibthorpe, B., Chiang, Y. K. et al. 2014, MNRAS, 437, 1882 [arXiv:1310.5710]; go back to page 16

Robertson, B., Li, Y., Cox, T. J., Hernquist, L., and Hopkins, P. F. 2007, ApJ, 667, 60 [arXiv:astro-ph/0703456]; go back to page 14

Robson, E. I., Ivison, R. J., Smail, I., Holland, W. S., Geach, J. E. et al. 2014, ApJ, 793, 11 [arXiv:1403.0247]; go back to page 16

Rodriguez-Gomez, V., Genel, S., Vogelsberger, M., Sijacki, D., Pillepich, A. et al. 2015, MNRAS, 449, 49 [arXiv:1502.01339]; go back to page 8

Roehlly, Y., Buat, V., Heinis, S., Moreau, C., and Gimenez, S. Astronomical Data Analysis Software and Systems XX, ed. , I. N. EvansA. AccomazziD. J. Mink & A. H. Rots, 25 Astronomical Society of the Pacific Conference Series, Vol. 442, 56

Romano, D., Matteucci, F., Zhang, Z.-Y., Papadopoulos, P. P., and Ivison, R. J. 2017, MNRAS, 470, 401 [arXiv:1704.06701]; go back to page 5, 87

Roseboom, I. G., Ivison, R. J., Greve, T. R., Amblard, A., Arumugam, V. et al. 2012, MNRAS, 419, 2758 [arXiv:1109.2887]; go back to page 56

Roseboom, I. G., Oliver, S. J., Kunz, M., Altieri, B., Amblard, A. et al. 2010, MNRAS, 409, 48 [arXiv:1009.1658]; go back to page 56

Safarzadeh, M., Lu, Y., and Hayward, C. C. 2017, ArXiv e-prints [arXiv:1705.05377]; go back to page 5

Salpeter, E. E. 1955, ApJ, 121, 161 ; go back to page 5

Sanders, D. B. and Mirabel, I. F. 1996, ARA&A, 34, 749 ; go back to page 2

Sanders, D. B., Soifer, B. T., Elias, J. H., Madore, B. F., Matthews, K. et al. 1988, ApJ, 325, 74 ; go back to page 2

Santini, P., Maiolino, R., Magnelli, B., Silva, L., Grazian, A. et al. 2010, A&A, 518, L154 [arXiv:1005.5678]; go back to page 6

Schlegel, D. J., Finkbeiner, D. P., and Davis, M. 1998, ApJ, 500, 525 [arXiv:astro-ph/9710327]; go back to page 122

Schuller, F. 2012, in Society of Photo-Optical Instrumentation Engineers (SPIE) Conference Series, Vol. 8452, Society of Photo-Optical Instrumentation Engineers (SPIE) Conference Series [arXiv:1211.6485] 29

Schuller, F., Menten, K. M., Contreras, Y., Wyrowski, F., Schilke, P. et al. 2009, A&A, 504, 415 [arXiv:0903.1369]; go back to page 29, 30

Scott, S. E., Dunlop, J. S., and Serjeant, S. 2006, MNRAS, 370, 1057 [arXiv:astro-ph/0608482]; go back to page 77

Scott, S. E., Fox, M. J., Dunlop, J. S., Serjeant, S., Peacock, J. A. et al. 2002, MNRAS, 331, 817 [arXiv:astro-ph/0107446]; go back to page 9

Scoville, N., Aussel, H., Brusa, M., Capak, P., Carollo, C. M. et al. 2007, ApJS, 172, 1 [arXiv:astro-ph/0612305]; go back to page 94

Scoville, N., Aussel, H., Sheth, K., Scott, K. S., Sanders, D. et al. 2014, ApJ, 783, 84 [arXiv:1401.2987]; go back to page 6, 87

Scoville, N., Murchikova, L., Walter, F., Vlahakis, C., Koda, J. et al. 2017, ApJ, 836, 66 [arXiv:1605.09381]; go back to page 6

Scoville, N., Sheth, K., Walter, F., Manohar, S., Zschaechner, L. et al. 2015, ApJ, 800, 70 [arXiv:1412.5183]; go back to page 6

Scoville, N. Z. Evolution of star formation and gas, ed. , J. Falcón-BarrosoJ. H. Knapen, 491 2013 87

Serjeant, S. 2012, MNRAS, 424, 2429 [arXiv:1203.2647]; go back to page 9, 19

Serjeant, S., Dunlop, J. S., Mann, R. G., Rowan-Robinson, M., Hughes, D. et al. 2003, MNRAS, 344, 887 [arXiv:astro-ph/0201502]; go back to page 20

Simpson, J. M., Smail, I., Swinbank, A. M., Almaini, O., Blain, A. W. et al. 2015, ApJ, 799, 81 [arXiv:1411.5025]; go back to page 12, 71, 114

Simpson, J. M., Swinbank, A. M., Smail, I., Alexander, D. M., Brandt, W. N. et al. 2014, ApJ, 788, 125 [arXiv:1310.6363]; go back to page 12, 47, 48, 51, 85, 115

Siringo, G., Kreysa, E., Kovács, A., Schuller, F., Weiß, A. et al. 2009, A&A, 497, 945 [arXiv:0903.1354]; go back to page 24, 29

Skrutskie, M. F., Cutri, R. M., Stiening, R., Weinberg, M. D., Schneider, S. et al. 2006, AJ, 131, 1163 ; go back to page 15

Smail, I., Ivison, R. J., and Blain, A. W. 1997, ApJ, 490, L5+ [arXiv:arXiv:astro-ph/9708135]; go back to page 8, 19

Smail, I., Ivison, R. J., Blain, A. W., and Kneib, J. 2002, MNRAS, 331, 495 [arXiv:arXiv:astro-ph/0112100]; go back to page 9

Smail, I., Ivison, R. J., Blain, A. W., and Kneib, J.-P. 1998, ApJ, 507, L21 [arXiv:astro-ph/9806061]; go back to page 8

Smail, I., Ivison, R. J., Owen, F. N., Blain, A. W., and Kneib, J.-P. 2000, ApJ, 528, 612 [arXiv:astro-ph/9907083]; go back to page 9

Snyder, G. F., Brodwin, M., Mancone, C. M., Zeimann, G. R., Stanford, S. A. et al. 2012, ApJ, 756, 114 [arXiv:1207.4790]; go back to page 12, 88

Soifer, B. T., Neugebauer, G., Helou, G., Lonsdale, C. J., Hacking, P. et al. 1984, ApJ, 283, L1 ; go back to page 2

Spergel, D. N., Verde, L., Peiris, H. V., Komatsu, E., Nolta, M. R. et al. 2003, ApJS, 148, 175 [arXiv:astro-ph/0302209]; go back to page 14

Springel, V., White, S. D. M., Jenkins, A., Frenk, C. S., Yoshida, N. et al. 2005, Nature, 435, 629 [arXiv:astro-ph/0504097]; go back to page 14, 17, 99

Steidel, C. C., Giavalisco, M., Pettini, M., Dickinson, M., and Adelberger, K. L. 1996, ApJ, 462, L17 [arXiv:astro-ph/9602024]; go back to page 1

Stevens, J. A., Ivison, R. J., Dunlop, J. S., Smail, I. R., Percival, W. J. et al. 2003, Nature, 425, 264 [arXiv:astro-ph/0309495]; go back to page 16

Stevens, J. A., Page, M. J., Ivison, R. J., Smail, I., and Carrera, F. J. 2004, ApJ, 604, L17 [arXiv:astro-ph/0402098]; go back to page 16

Straatman, C. M. S., Labbé, I., Spitler, L. R., Allen, R., Altieri, B. et al. 2014, ApJ, 783, L14 [arXiv:1312.4952]; go back to page 12, 20, 52, 55, 127

Strandet, M. L., Weiss, A., De Breuck, C., Marrone, D. P., Vieira, J. D. et al. 2017, ApJ, 842, L15 [arXiv:1705.07912]; go back to page 14

Strandet, M. L., Weiss, A., Vieira, J. D., de Breuck, C., Aguirre, J. E. et al. 2016, ApJ, 822, 80 [arXiv:1603.05094]; go back to page 14, 41

Sutherland, W., Emerson, J., Dalton, G., Atad-Ettedgui, E., Beard, S. et al. 2015, A&A, 575, A25 [arXiv:1409.4780]; go back to page 92

Swinbank, A. M., Chapman, S. C., Smail, I., Lindner, C., Borys, C. et al. 2006, MNRAS, 371, 465 ; go back to page 48

Swinbank, A. M., Simpson, J. M., Smail, I., Harrison, C. M., Hodge, J. A. et al. 2014, MNRAS, 438, 1267 ; go back to page 39, 44, 48, 79

Swinbank, A. M., Smail, I., Longmore, S., Harris, A. I., Baker, A. J. et al. 2010, Nature, 464, 733 [arXiv:1003.3674]; go back to page 22

Symeonidis, M., Page, M. J., and Seymour, N. 2011, MNRAS, 411, 983 [arXiv:1009.3778]; go back to page 14

Symeonidis, M., Vaccari, M., Berta, S., Page, M. J., Lutz, D. et al. 2013, MNRAS, 431, 2317 [arXiv:1302.4895]; go back to page 46

Tacconi, L. J., Genzel, R., Neri, R., Cox, P., Cooper, M. C. et al. 2010, Nature, 463, 781 [arXiv:1002.2149]; go back to page 8, 12

Takagi, T., Matsuhara, H., Wada, T., Oyabu, S., Ohyama, Y. et al. AKARI, a Light to Illuminate the Misty Universe, ed. , T. OnakaG. J. WhiteT. Nakagawa & I. Yamamura, 275 Astronomical Society of the Pacific Conference Series, Vol. 418, 94

Tamura, Y., Kohno, K., Nakanishi, K., Hatsukade, B., Iono, D. et al. 2009, Nature, 459, 61 [arXiv:0905.0890]; go back to page 16

Tanaka, M., Finoguenov, A., Mirkazemi, M., Wilman, D. J., Mulchaey, J. S. et al. 2013, PASJ, 65, 17 [arXiv:1210.0302]; go back to page 16

Thomas, D., Maraston, C., Bender, R., and Mendes de Oliveira, C. 2005, ApJ, 621, 673 [arXiv:astro-ph/0410209]; go back to page 12, 88

Thomas, D., Maraston, C., Schawinski, K., Sarzi, M., and Silk, J. 2010, MNRAS, 404, 1775 [arXiv:0912.0259]; go back to page 12, 88

Toft, S., Smolčić, V., Magnelli, B., Karim, A., Zirm, A. et al. 2014, ApJ, 782, 68 [arXiv:1401.1510]; go back to page 12, 51

Uchiyama, H., Toshikawa, J., Kashikawa, N., Overzier, R., Chiang, Y.-K. et al. 2017, ArXiv e-prints [arXiv:1704.06050]; go back to page 16

Valiante, E., Smith, M. W. L., Eales, S., Maddox, S. J., Ibar, E. et al. 2016, MNRAS, 462, 3146 [arXiv:1606.09615]; go back to page 20, 26

van Dokkum, P. G. 2005, AJ, 130, 2647 [arXiv:astro-ph/0506661]; go back to page 12

van Dokkum, P. G., Franx, M., Kriek, M., Holden, B., Illingworth, G. D. et al. 2008, ApJ, 677, L5 [arXiv:0802.4094]; go back to page 12

Venemans, B. P., Röttgering, H. J. A., Miley, G. K., van Breugel, W. J. M., de Breuck, C. et al. 2007, A&A, 461, 823 [arXiv:astro-ph/0610567]; go back to page 108

Vieira, J. D., Crawford, T. M., Switzer, E. R., Ade, P. A. R., Aird, K. A. et al. 2010, ApJ, 719, 763 [arXiv:0912.2338]; go back to page 14

Walter, F., Decarli, R., Carilli, C., Bertoldi, F., Cox, P. et al. 2012, Nature, 486, 233 [arXiv:1206.2641]; go back to page 107

Wang, W.-H., Cowie, L. L., and Barger, A. J. 2004, ApJ, 613, 655 [arXiv:astro-ph/0406261]; go back to page 94

Weiß, A., De Breuck, C., Marrone, D. P., Vieira, J. D., Aguirre, J. E. et al. 2013, ApJ, 767, 88 [arXiv:1303.2726]; go back to page 14, 41

Weiß, A., Kovács, A., Coppin, K., Greve, T. R., Walter, F. et al. 2009, ApJ, 707, 1201 [arXiv:0910.2821]; go back to page 30, 69, 73, 75, 76, 79, 128

Zavala, J. A., Montaña, A., Hughes, D. H., Yun, M. S., Ivison, R. J. et al. 2018, Nature Astronomy, 2, 56 [arXiv:1707.09022]; go back to page 13, 88, 90

Zepf, S. E., Moustakas, L. A., and Davis, M. 1997, ApJ, 474, L1 [arXiv:astro-ph/9606153]; go back to page 9

Zhang, Z.-Y., Papadopoulos, P. P., Ivison, R. J., Galametz, M., Smith, M. W. L. et al. 2016, R. Soc. open sci., 3, 160025 [arXiv:1605.03885]; go back to page 46

Zhang, Z.-Y., Romano, D., Ivison, R. J., Papadopoulos, P. P., and Matteucci, F. 2018, ArXiv e-prints [arXiv:1806.01280]; go back to page 5

Appendix

In this Appendix, I present *Herschel*-SPIRE, JCMT-SCUBA-2 and APEX-LABOCA $3' \times 3'$ cut-outs of the sample of 109 ultra-red galaxies presented in Chapter 2. These cut-outs cover the five fields of the *H*-ATLAS imaging survey; GAMA 09, GAMA 12, GAMA 15, NGP and SGP and are ordered, from left to right, by increasing passband wavelength. The SPIRE 250-μm and SCUBA-2/LABOCA 850-μm/870-μm cut-outs have been convolved with $7''$ and $13''/19''$ gaussians, respectively. I linearly stretch the SPIRE and SCUBA-2/LABOCA cut-outs relative to their local median between $-6{:}{+}60\,\mathrm{mJy\,beam^{-1}}$ and $-3{:}{+}30\,\mathrm{mJy\,beam^{-1}}$, respectively. The aperture used to measure the 45-arcsec flux density is shown on the SCUBA-2/LABOCA cut-outs as a purple circle centred on the ultra-red galaxy. The annulus used to measure the sky background is shown in the upper-most panel for each page of cut-outs as purple dashed lines. Finally, the stamps are orientated such that North is up and East is left.

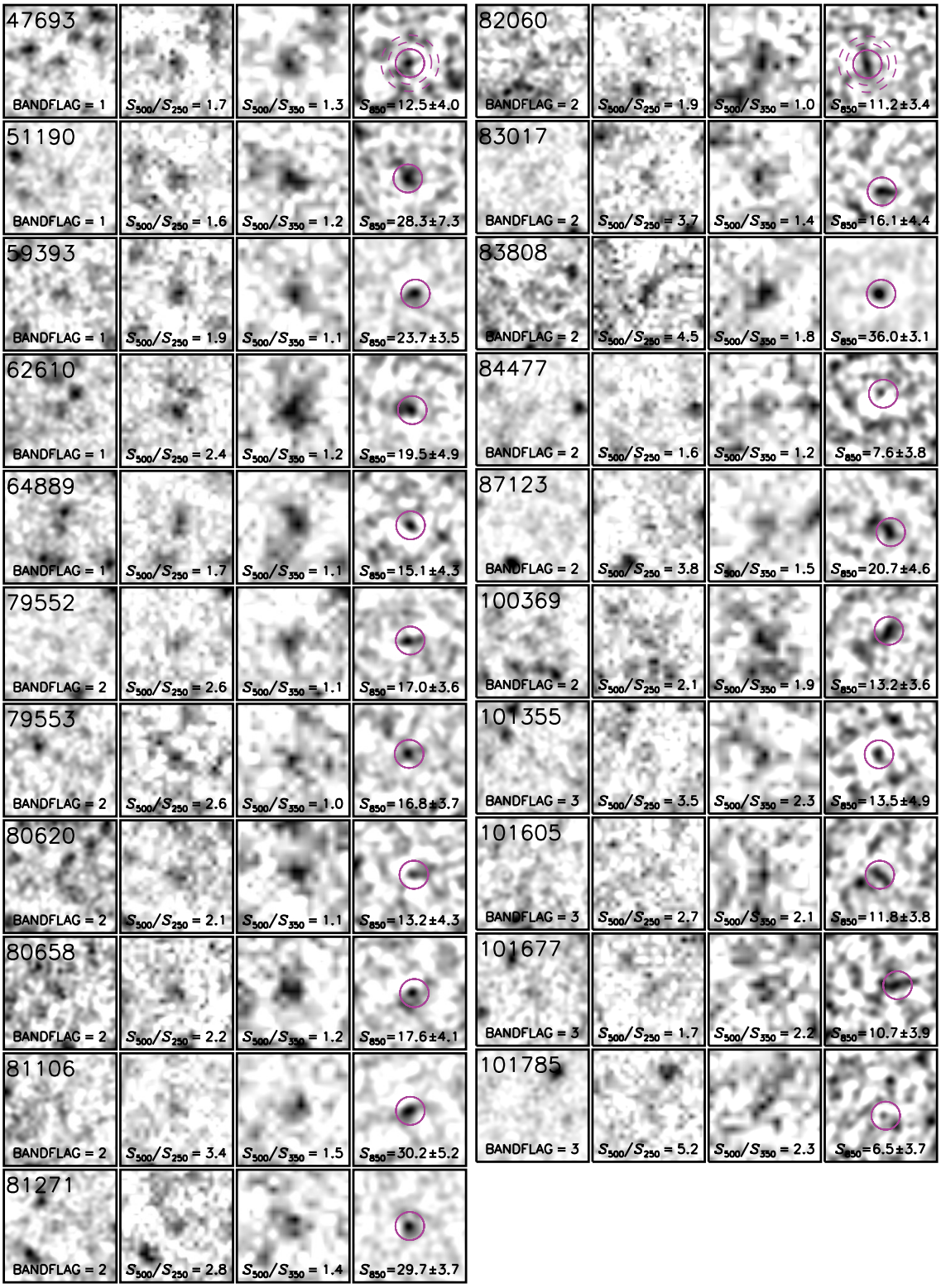

Figure A.1: Ultra-Red galaxies observed by SCUBA-2 in the GAMA 09 field.

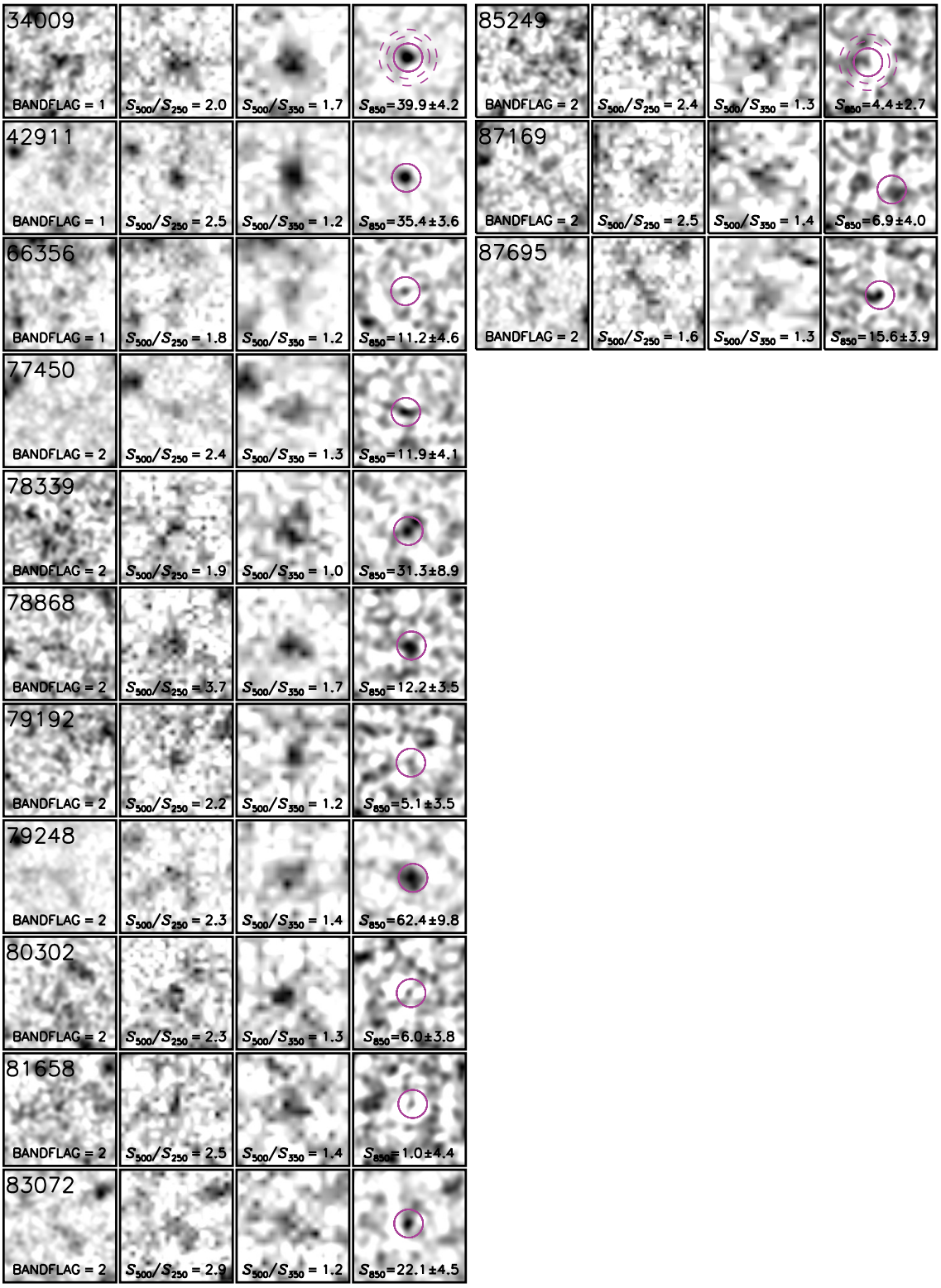

Figure A.2: Ultra-Red galaxies observed by SCUBA-2 in the GAMA 12 field.

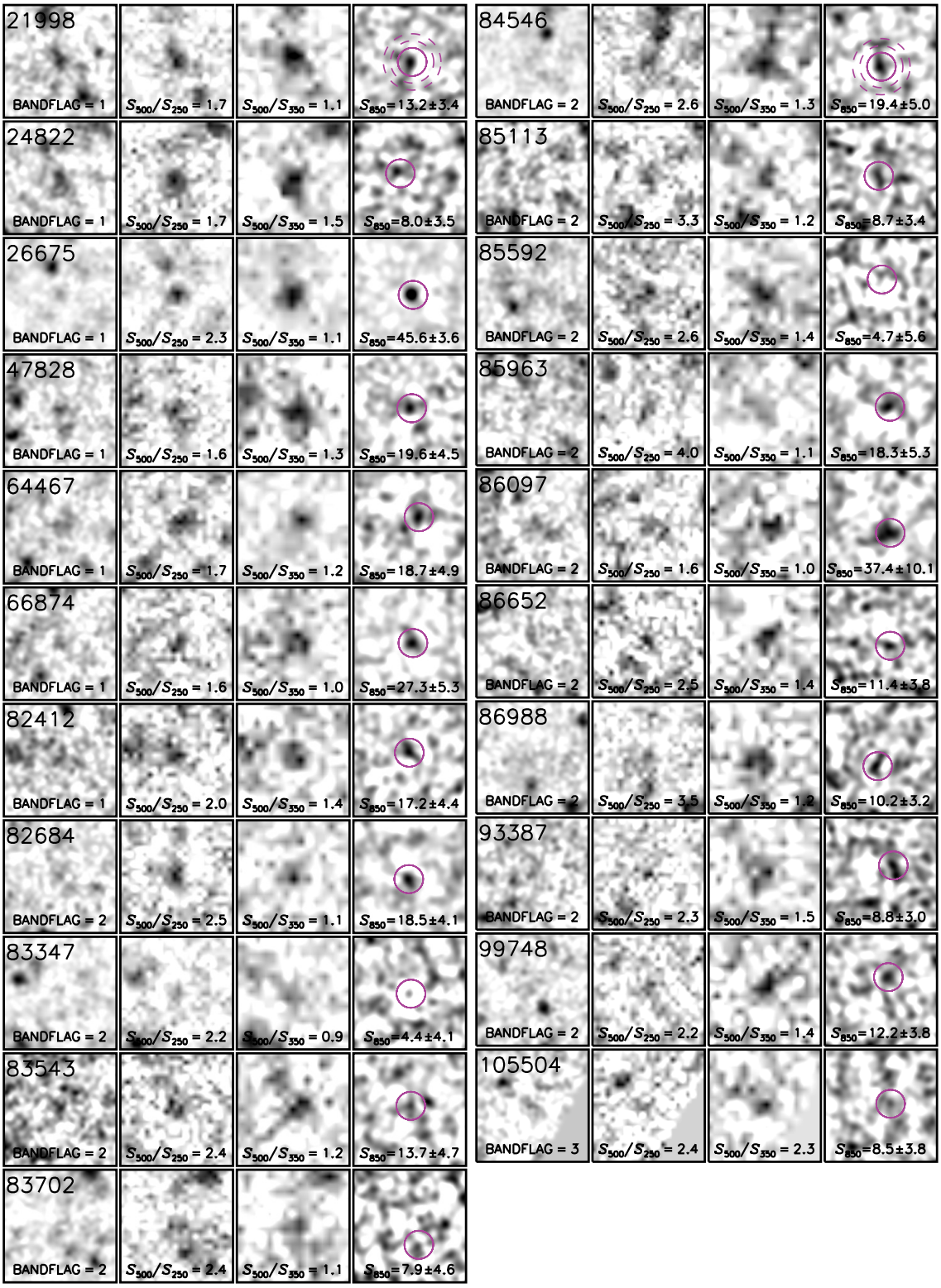

Figure A.3: Ultra-Red galaxies observed by SCUBA-2 in the GAMA 15 field.

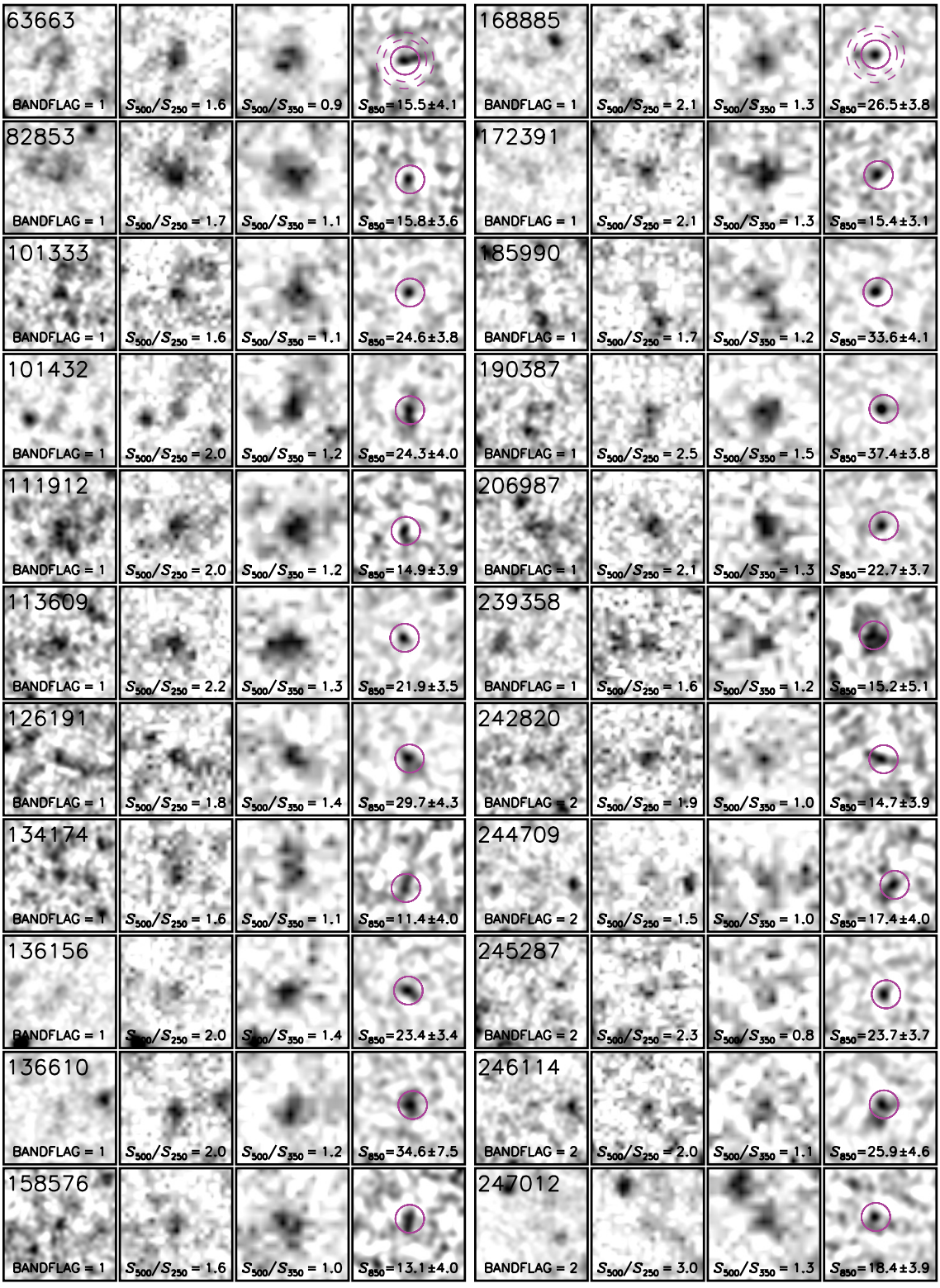

Figure A.4: Ultra-Red galaxies observed by SCUBA-2 in the NGP field.

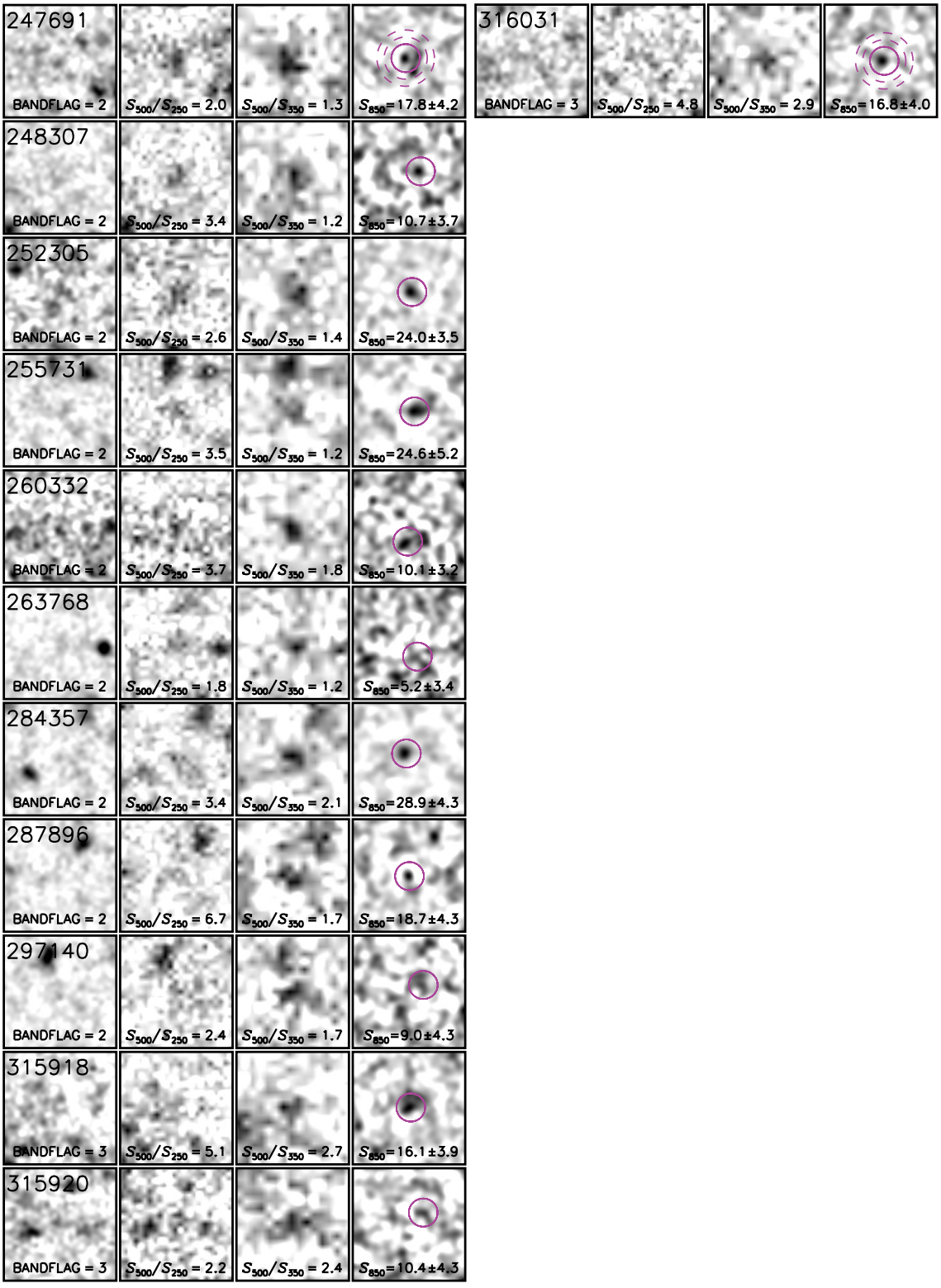

Figure A.4 (continued from previous page)

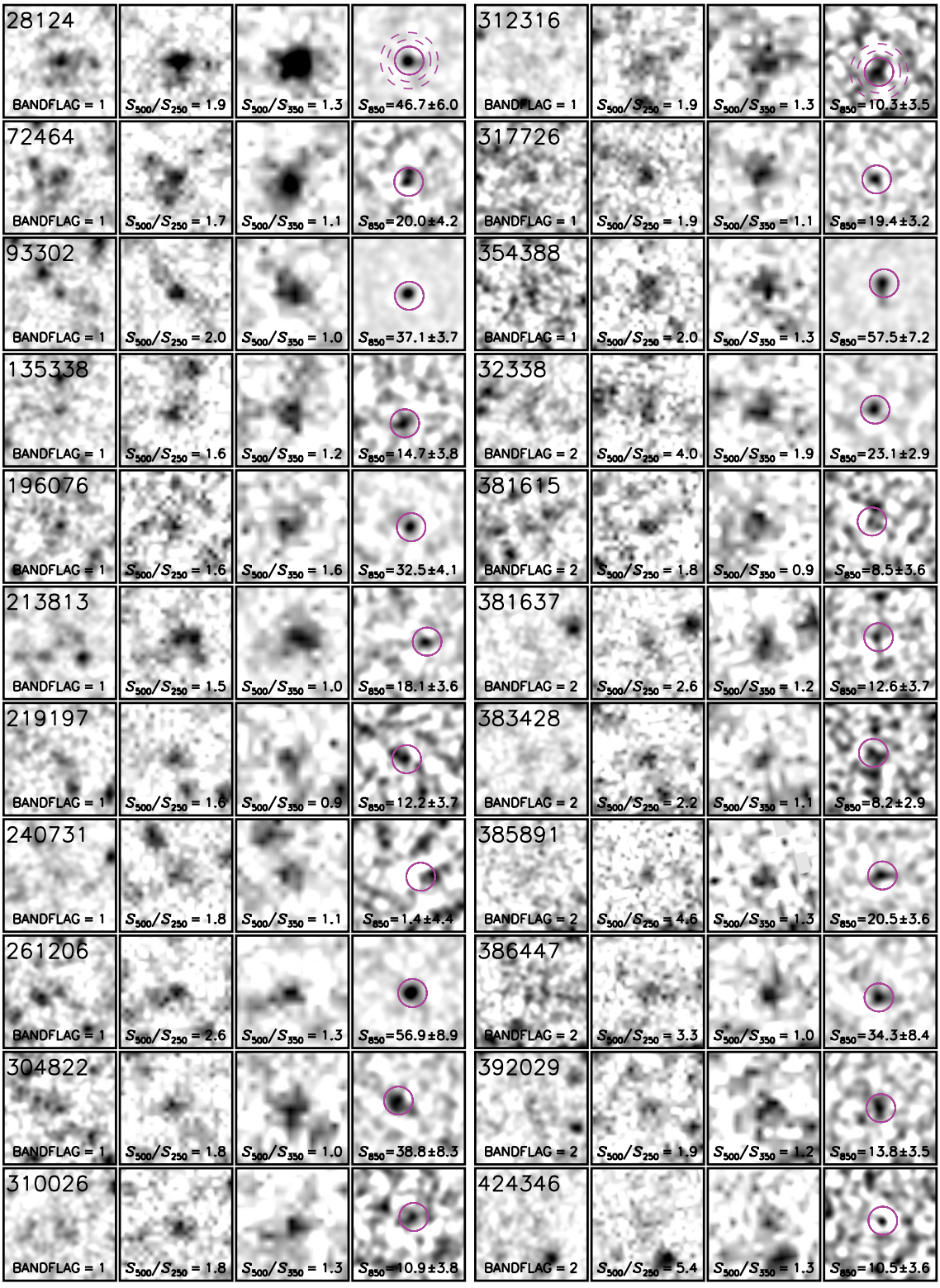

Figure A.5: Ultra-Red galaxies observed by SCUBA-2 in the SGP field.

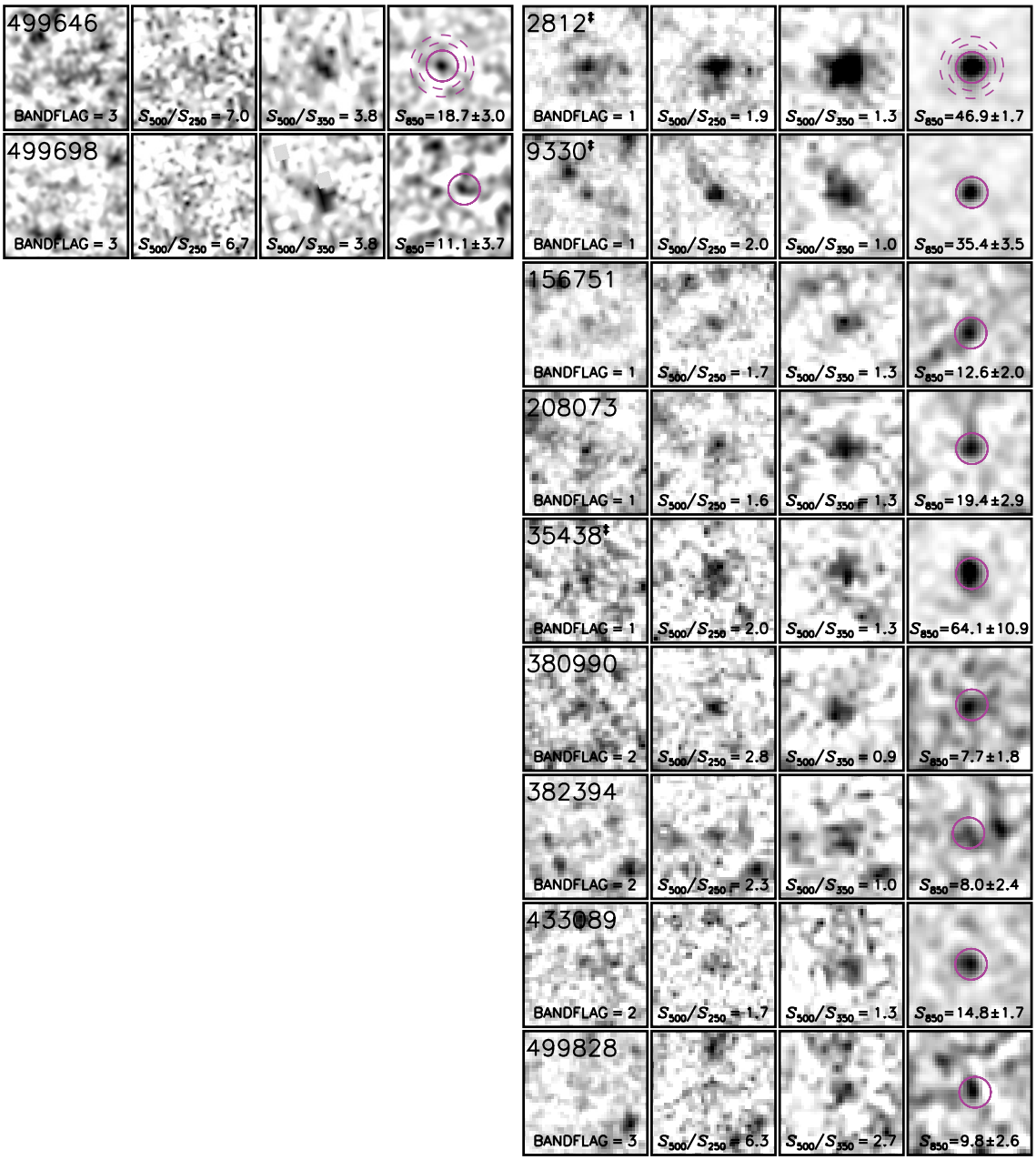

Figure A.5 (continued from previous page): Note. The right-hand column shows the ultra-red galaxies that were observed with LABOCA. Ultra-Red galaxies observed with both LABOCA and SCUBA-2 are marked with a '‡' symbol.

Appendix

B

In this Appendix, I present the *Herschel*-SPIRE and LABOCA imaging as well as the photometry and photometric redshift catalogues for the sample of signpost ultra-red galaxies and their surrounding DSFGs that feature in Chapter 3.

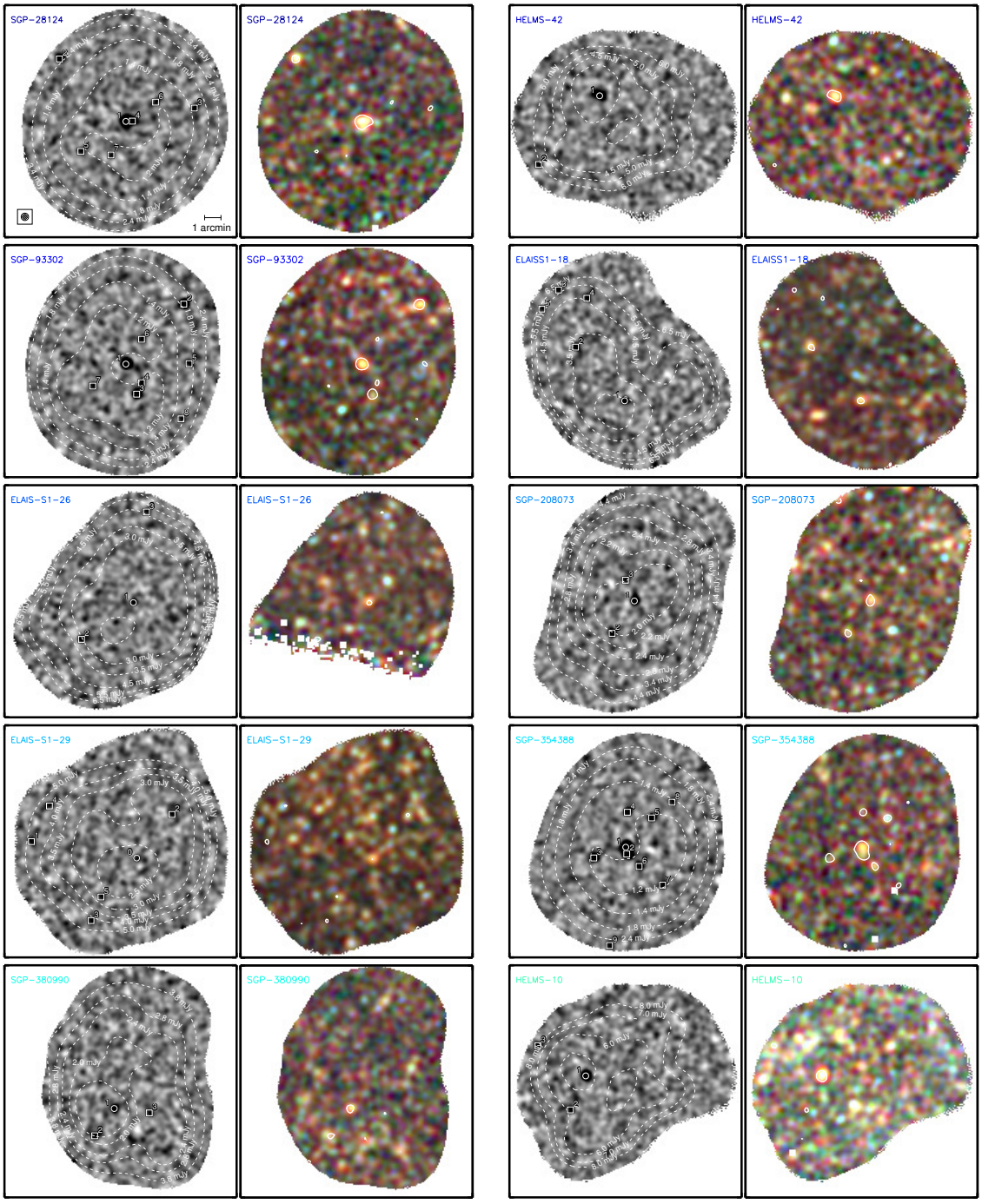

Figure B.1: *Left*: $14' \times 14'$ cut-outs of the LABOCA SNR images at a spatial resolution of $\approx 27''$, linearly stretched between $\pm 3.5\sigma$ (see beam inset and scale on top-left panel). The cut-outs are orientated such that North is up and East is left. Detections above $S/N > 3.5$ are numbered in decreasing order of S/N with hollow circles and squares representing the ultra-red galaxy signposts and their surrounding DSFGs, respectively. Ultra-Red galaxy signposts numbered '0' are sources that I have been unable to detect above $> 3.5\sigma$. I have placed dashed white contours at varying values of instrumental noise and I show a distance scale and the LABOCA PSF on the top row. *Right*: false-colour, PSF-filtered *Herschel*-SPIRE, $14' \times 14'$ cut-outs of the same region. White dashed contours are placed at > 3.5-σ_{850} values. **Note**. Cut-Outs are presented in increasing order of right ascension, (i.e. in the same order as they appear in Table B.1) and their labels have been colour-coded from blue to red.

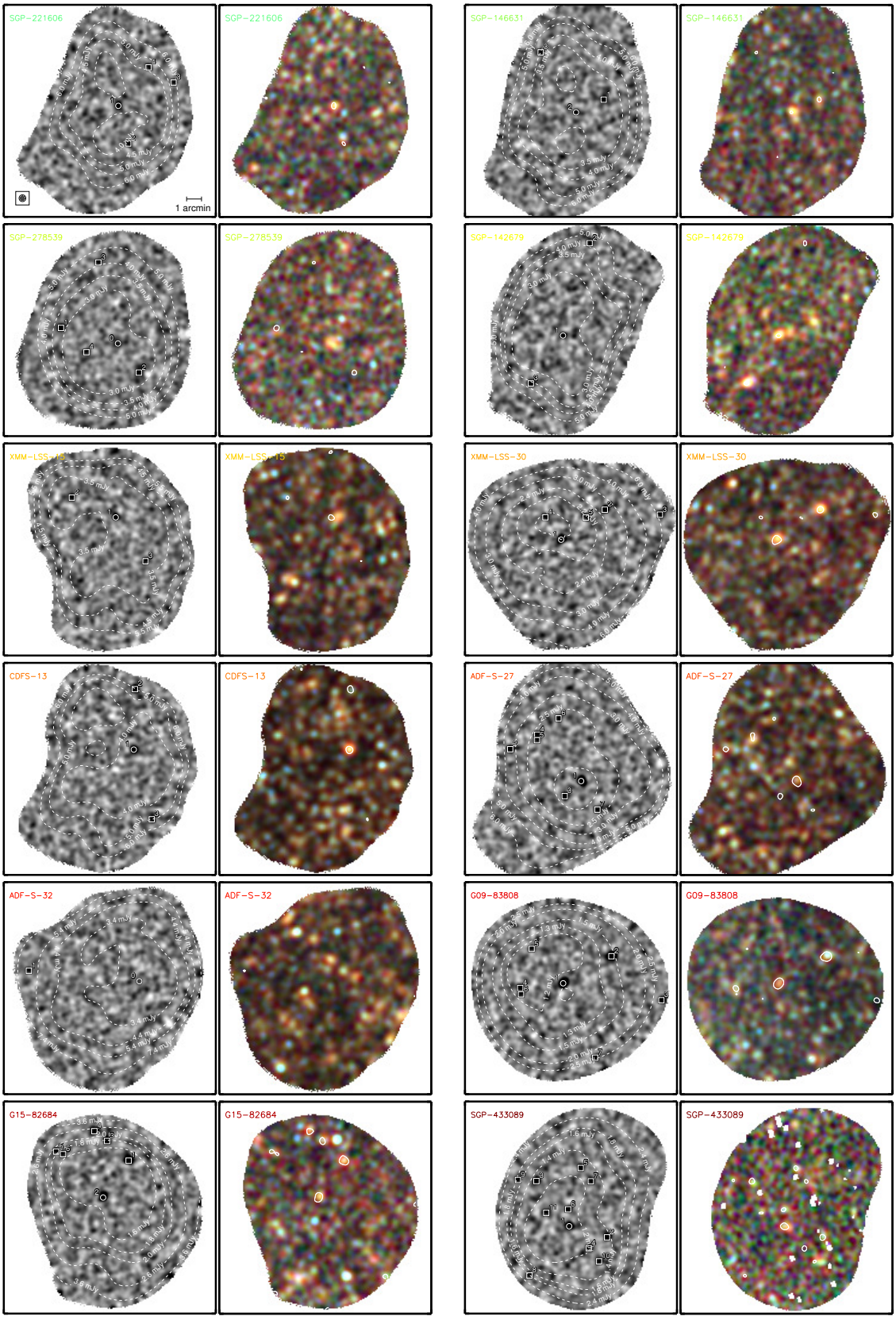

Figure B.1 (continued from previous page)

Table B.1: Photometric properties around ultra-red galaxy signposts.

IAU name	α (J2000) h m s	δ ° ′ ″	$S^{\dagger}_{250}$ mJy beam^{-1}	$S^{\dagger}_{350}$ mJy beam^{-1}	$S^{\dagger}_{500}$ mJy beam^{-1}	$S^{\dagger}_{870}$ mJy	$\mathcal{B}$	$\mathcal{F}$
			SGP-28124					
LURGS J000124.9−354212	**00:01:24.88**	**−35:42:12.2**	**62.2 ± 9.1**	**89.8 ± 8.8**	**119.9 ± 9.3**	**44.3 ± 1.4**	**1.04**	**1.00**
LURGS J000145.0−353822	00:01:44.95	−35:38:22.1	55.9 ± 7.9	67.4 ± 8.6	52.4 ± 9.4	15.9 ± 2.6	1.15	1.00
LURGS J00014.2−354123	00:01:04.20	−35:41:23.0	5.9 ± 7.5	11.7 ± 8.8	4.7 ± 9.7	6.4 ± 1.5	1.35	0.97
LURGS J000122.9−354211	00:01:22.91	−35:42:11.2	31.9 ± 9.0	47.9 ± 8.7	87.8 ± 9.4	10.2 ± 1.4	1.11	0.92
LURGS J000138.5−35442	00:01:38.50	−35:44:02.3	4.0 ± 9.2	9.2 ± 9.2	−3.6 ± 10.3	4.7 ± 1.2	1.55	0.85
LURGS J000115.9−35411	00:01:15.90	−35:41:01.3	28.4 ± 8.1	27.4 ± 8.6	6.2 ± 9.3	4.4 ± 1.2	1.59	0.85
LURGS J000129.4−354416	00:01:29.39	−35:44:15.7	30.0 ± 9.6	23.6 ± 9.0	26.7 ± 10.2	3.5 ± 1.2	1.65	0.57
			HeLMS-42					
LURGS J00034.2+024114	**00:03:04.17**	**+02:41:13.7**	**39.8 ± 9.2**	**60.3 ± 9.9**	**81.0 ± 11.3**	**42.6 ± 3.6**	**1.89**	**1.00**
LURGS J000319.2+02371	00:03:19.16	+02:37:00.7	1.3 ± 8.6	3.6 ± 8.9	−1.1 ± 11.0	24.5 ± 6.5	5.06	0.87
			SGP-93302					
LURGS J000624.4−323018	**00:06:24.44**	**−32:30:17.7**	**32.1 ± 7.1**	**59.6 ± 8.3**	**59.6 ± 8.9**	**32.0 ± 1.3**	**1.03**	**1.00**
LURGS J00067.7−322638	00:06:07.68	−32:26:38.0	24.0 ± 7.7	49.7 ± 9.3	60.9 ± 9.1	32.4 ± 1.9	1.03	1.00
LURGS J000621.3−32328	00:06:21.31	−32:32:07.9	15.8 ± 7.5	27.3 ± 7.8	22.9 ± 8.5	13.3 ± 1.1	1.05	1.00
LURGS J000619.9−323126	00:06:19.92	−32:31:26.2	23.2 ± 7.6	21.6 ± 8.0	21.2 ± 8.4	5.3 ± 1.2	1.43	0.99
LURGS J00066.1−323016	00:06:06.14	−32:30:16.1	40.1 ± 7.2	23.2 ± 8.8	13.9 ± 8.7	7.3 ± 1.7	1.48	0.96
LURGS J000619.9−322847	00:06:19.91	−32:28:46.8	23.7 ± 7.8	23.3 ± 8.5	18.6 ± 8.8	4.7 ± 1.2	1.57	0.85
LURGS J000634.0−323138	00:06:34.00	−32:31:38.1	11.8 ± 7.2	10.7 ± 7.7	10.8 ± 8.1	4.0 ± 1.0	1.67	0.75
LURGS J00068.5−323338	00:06:08.47	−32:33:38.2	6.7 ± 7.4	6.3 ± 8.1	5.3 ± 8.0	5.7 ± 1.7	1.79	0.61
			ELAIS-S1-18					
LURGS J002851.3−431353	**00:28:51.31**	**−43:13:52.8**	**33.4 ± 5.7**	**48.8 ± 7.0**	**46.5 ± 7.3**	**17.8 ± 2.9**	**1.44**	**1.00**
LURGS J00297.7−431036	00:29:07.74	−43:10:36.2	35.7 ± 5.6	43.5 ± 6.6	42.4 ± 7.4	18.9 ± 3.4	1.66	1.00
LURGS J002913.4−43077	00:29:13.39	−43:07:07.0	6.7 ± 5.1	−0.2 ± 6.2	6.5 ± 7.1	25.1 ± 5.9	3.20	0.99
LURGS J00294.0−430737	00:29:03.95	−43:07:37.2	17.7 ± 5.8	11.1 ± 6.6	4.2 ± 7.2	18.0 ± 4.6	4.60	0.87
LURGS J002919.0−430817	00:29:19.01	−43:08:16.8	−1.6 ± 5.3	−1.8 ± 6.2	7.7 ± 7.5	17.5 ± 5.9	5.29	0.69
			ELAIS-S1-26					
LURGS J003352.4−452015	**00:33:52.39**	**−45:20:14.6**	**24.5 ± 6.6**	**37.0 ± 8.3**	**43.1 ± 9.6**	**12.6 ± 2.6**	**1.57**	**1.00**
LURGS J003410.4−452230	00:34:10.40	−45:22:29.7	45.7 ± 9.2	37.6 ± 9.1	18.6 ± 10.2	14.8 ± 3.1	1.55	1.00
LURGS J003347.9−451441	00:33:47.86	−45:14:40.8	11.6 ± 6.1	20.6 ± 6.9	13.8 ± 7.3	15.9 ± 4.6	3.11	0.78
			SGP-208073					
LURGS J003533.9−280260	**00:35:33.90**	**−28:02:59.5**	**27.7 ± 7.7**	**37.4 ± 8.8**	**47.6 ± 9.7**	**19.2 ± 1.8**	**1.16**	**1.00**
LURGS J003540.1−280459	00:35:40.07	−28:04:58.7	32.3 ± 7.6	31.2 ± 8.5	28.1 ± 9.8	12.4 ± 2.0	1.22	1.00
LURGS J003536.4−280143	00:35:36.37	−28:01:43.3	14.7 ± 7.9	16.8 ± 9.0	23.4 ± 9.7	7.1 ± 2.0	2.23	0.72
			ELAIS-S1-29					
LURGS J003756.6−421519†	**00:37:56.62**	**−42:15:19.0**	**24.9 ± 6.2**	**35.1 ± 7.5**	**43.5 ± 8.0**	**7.7 ± 2.3**	—	—
LURGS J003831.5−421418	00:38:31.49	−42:14:18.4	−2.3 ± 5.7	1.8 ± 6.6	−1.4 ± 7.3	20.0 ± 4.8	2.02	0.95
LURGS J003744.9−421240	00:37:44.90	−42:12:39.6	41.7 ± 6.7	45.8 ± 7.7	27.8 ± 8.3	10.3 ± 2.7	2.59	0.90
LURGS J003811.7−42198	00:38:11.74	−42:19:08.0	0.5 ± 5.5	−0.5 ± 6.1	0.2 ± 7.2	16.4 ± 4.3	2.73	0.87
LURGS J003825.5−42128	00:38:25.48	−42:12:08.1	59.5 ± 6.0	29.6 ± 6.9	15.3 ± 8.0	15.7 ± 4.5	3.14	0.78

Table B.1 (continued from previous page)

IAU name	α (J2000) h m s	δ ° ′ ″	$S^{\dagger}_{250}$ mJy beam^{-1}	$S^{\dagger}_{350}$ mJy beam^{-1}	$S^{\dagger}_{500}$ mJy beam^{-1}	$S^{\dagger}_{870}$ mJy	$\mathcal{B}$	$\mathcal{F}$
ine LURGS J00388.4−421742	00:38:08.44	−42:17:41.7	23.8 ± 5.7	33.7 ± 6.4	22.8 ± 7.7	9.3 ± 2.7	3.22	0.72
			SGP-354388					
LURGS J004223.7−334325	**00:42:23.73**	**−33:43:25.0**	$\mathbf{15.4 \pm 8.6}$	$\mathbf{47.6 \pm 8.8}$	$\mathbf{59.7 \pm 9.8}$	$\mathbf{34.3 \pm 1.2}$	**1.04**	**1.00**
LURGS J004223.5−334350	00:42:23.46	−33:43:49.6	23.4 ± 8.5	35.3 ± 8.9	33.8 ± 9.9	17.5 ± 1.2	1.05	1.00
LURGS J004233.2−33444	00:42:33.16	−33:44:04.2	12.8 ± 8.1	14.3 ± 8.9	14.8 ± 9.5	9.4 ± 1.2	1.09	1.00
LURGS J004223.2−334117	00:42:23.25	−33:41:16.9	18.8 ± 8.0	13.8 ± 9.0	17.6 ± 9.6	8.7 ± 1.2	1.11	1.00
LURGS J004216.1−334138	00:42:16.11	−33:41:37.8	63.5 ± 8.2	56.3 ± 9.2	28.9 ± 9.7	7.9 ± 1.2	1.13	1.00
LURGS J004219.8−334435	00:42:19.79	−33:44:35.2	16.8 ± 8.7	34.0 ± 8.9	34.1 ± 10.0	7.2 ± 1.2	1.16	1.00
LURGS J004212.9−334544	00:42:12.86	−33:45:43.5	5.5 ± 8.6	8.7 ± 9.0	3.8 ± 10.3	5.5 ± 1.2	1.30	0.99
LURGS J004210.1−334040	00:42:10.09	−33:40:40.0	1.8 ± 8.6	-1.1 ± 8.6	-9.0 ± 9.6	4.9 ± 1.4	1.57	0.75
LURGS J004228.5−334925	00:42:28.53	−33:49:24.6	-4.0 ± 8.6	-1.1 ± 9.2	-15.2 ± 10.3	10.9 ± 2.8	1.49	0.72
			SGP-380990					
LURGS J004614.6−321828	**00:46:14.55**	**−32:18:28.1**	$\mathbf{20.4 \pm 8.2}$	$\mathbf{43.1 \pm 8.9}$	$\mathbf{46.6 \pm 9.3}$	$\mathbf{10.4 \pm 1.6}$	**1.18**	**1.00**
LURGS J004620.2−32209	00:46:20.19	−32:20:08.5	24.3 ± 8.5	29.2 ± 9.0	34.3 ± 9.3	9.2 ± 1.8	1.31	1.00
LURGS J00464.4−321844	00:46:04.41	−32:18:44.2	23.2 ± 8.0	17.4 ± 8.6	8.3 ± 9.3	7.6 ± 2.2	2.18	0.69
			HeLMS-10					
LURGS J005258.6+061318	**00:52:58.61**	**+06:13:18.2**	$\mathbf{68.9 \pm 11.5}$	$\mathbf{105.4 \pm 11.2}$	$\mathbf{124.3 \pm 11.7}$	$\mathbf{81.7 \pm 4.7}$	**2.19**	**1.00**
LURGS J00532.4+061113	00:53:02.41	+06:11:12.9	7.3 ± 9.8	-3.7 ± 10.7	6.7 ± 12.3	23.8 ± 5.8	7.62	0.98
LURGS J005310.4+061510	00:53:10.40	+06:15:09.5	45.3 ± 11.4	51.6 ± 11.8	29.5 ± 12.5	38.3 ± 8.4	3.59	0.98
			SGP-221606					
LURGS J011918.9−294516	**01:19:18.93**	**−29:45:15.7**	$\mathbf{34.9 \pm 7.7}$	$\mathbf{53.6 \pm 8.8}$	$\mathbf{52.1 \pm 9.9}$	$\mathbf{20.3 \pm 3.9}$	**1.82**	**1.00**
LURGS J011915.9−294748	01:19:15.86	−29:47:47.6	1.2 ± 8.0	0.0 ± 9.0	22.6 ± 9.1	16.2 ± 4.1	3.80	0.94
LURGS J01191.8−294342	01:19:01.83	−29:43:42.0	7.9 ± 7.6	7.2 ± 9.1	-3.1 ± 9.9	17.9 ± 5.5	5.92	0.69
LURGS J01199.6−294241	01:19:09.59	−29:42:40.6	-0.1 ± 7.7	-0.9 ± 9.6	0.5 ± 9.8	15.5 ± 4.6	5.87	0.61
			SGP-146631					
LURGS J013155.8−311147	01:31:55.82	−31:11:47.0	26.1 ± 7.4	32.7 ± 7.5	39.9 ± 8.0	15.0 ± 3.3	1.87	0.98
LURGS J01324.5−311239	**01:32:04.46**	**−31:12:38.5**	$\mathbf{47.2 \pm 7.9}$	$\mathbf{78.7 \pm 7.6}$	$\mathbf{67.9 \pm 8.5}$	$\mathbf{11.5 \pm 3.2}$	**3.92**	**0.94**
LURGS J013215.5−310837	01:32:15.51	−31:08:36.6	5.7 ± 8.5	8.6 ± 8.8	6.4 ± 9.4	14.9 ± 4.0	3.73	0.85
			SGP-278539					
LURGS J01428.2−323426†	**01:42:08.20**	**−32:34:26.3**	$\mathbf{22.7 \pm 8.3}$	$\mathbf{39.0 \pm 9.2}$	$\mathbf{50.7 \pm 9.5}$	$\mathbf{8.7 \pm 2.8}$	—	—
LURGS J014226.2−323324	01:42:26.25	−32:33:23.8	7.0 ± 8.4	2.6 ± 8.5	8.2 ± 9.2	17.2 ± 3.2	1.40	1.00
LURGS J01421.6−323624	01:42:01.58	−32:36:23.8	6.7 ± 8.7	7.4 ± 9.0	9.3 ± 9.0	14.1 ± 2.9	1.49	0.99
LURGS J014214.4−32290	01:42:14.41	−32:29:00.2	6.1 ± 8.1	9.5 ± 8.6	8.6 ± 9.6	15.7 ± 4.2	2.83	0.92
LURGS J014218.2−32352	01:42:18.19	−32:35:01.5	-0.1 ± 8.3	-7.2 ± 8.7	-2.8 ± 9.2	9.6 ± 2.8	3.26	0.65
			SGP-142679					
LURGS J014456.9−284146	**01:44:56.88**	**−28:41:46.0**	$\mathbf{29.9 \pm 8.1}$	$\mathbf{65.0 \pm 9.8}$	$\mathbf{71.7 \pm 9.9}$	$\mathbf{12.9 \pm 2.8}$	**1.59**	**1.00**
LURGS J014448.8−283535	01:44:48.78	−28:35:35.4	7.5 ± 7.7	-9.0 ± 8.5	10.5 ± 8.9	18.3 ± 4.2	1.88	0.97
LURGS J01456.7−284457	01:45:06.66	−28:44:57.3	97.2 ± 8.5	101.8 ± 9.8	82.2 ± 9.8	15.6 ± 3.5	1.70	0.96
			XMM-LSS-15					
LURGS J021745.3−030912	**02:17:45.30**	**−03:09:12.3**	$\mathbf{12.6 \pm 6.2}$	$\mathbf{22.2 \pm 7.2}$	$\mathbf{24.0 \pm 7.8}$	$\mathbf{17.6 \pm 3.0}$	**1.47**	**1.00**

Table B.1 (continued from previous page)

IAU name	α (J2000) h m s	δ ° ′ ″	S_{250} mJy beam^{-1}	S_{350} mJy beam^{-1}	S_{500} mJy beam^{-1}	S_{870} mJy	$\mathcal{B}$	$\mathcal{F}$
LURGS J021757.1−030753	02:17:57.12	−03:07:53.0	56.8 ± 6.5	34.5 ± 7.4	14.6 ± 7.6	11.5 ± 2.9	2.67	0.90
LURGS J021737.3−03128	02:17:37.29	−03:12:08.0	0.5 ± 6.7	-0.3 ± 7.5	4.6 ± 8.2	10.8 ± 3.2	3.55	0.69
..... **XMM-LSS-30**								
LURGS J022656.6−032711	**02:26:56.60**	**−03:27:11.1**	$\mathbf{25.6 \pm 6.3}$	$\mathbf{44.8 \pm 7.0}$	$\mathbf{61.6 \pm 7.1}$	$\mathbf{23.3 \pm 2.0}$	**1.16**	**1.00**
LURGS J022644.9−032510	02:26:44.90	−03:25:10.1	44.2 ± 6.3	65.6 ± 6.8	63.9 ± 7.5	18.8 ± 2.6	1.23	1.00
LURGS J022630.2−032530	02:26:30.16	−03:25:30.0	20.7 ± 5.7	24.3 ± 7.0	18.4 ± 7.7	29.8 ± 6.4	2.04	0.97
LURGS J02270.8−032541	02:27:00.81	−03:25:41.0	10.3 ± 6.5	10.3 ± 7.1	13.9 ± 7.8	7.6 ± 2.0	3.38	0.93
LURGS J022650.0−032542	02:26:50.00	−03:25:41.9	28.9 ± 6.5	28.6 ± 6.7	18.0 ± 7.3	7.6 ± 2.1	3.53	0.61
..... **CDFS-13**								
LURGS J03370.7−292148	**03:37:00.72**	**−29:21:48.0**	$\mathbf{41.1 \pm 5.9}$	$\mathbf{51.0 \pm 7.1}$	$\mathbf{55.4 \pm 7.2}$	$\mathbf{26.2 \pm 3.5}$	**1.45**	**1.00**
LURGS J03370.3−291746	03:37:00.35	−29:17:45.8	23.3 ± 5.8	20.6 ± 6.8	10.5 ± 6.8	37.6 ± 5.9	1.45	1.00
LURGS J033655.2−292627	03:36:55.23	−29:26:26.9	11.6 ± 7.3	15.7 ± 7.3	7.6 ± 7.0	17.8 ± 5.0	5.46	0.75
..... **ADF-S-27**								
LURGS J043657.0−543813	**04:36:57.01**	**−54:38:13.2**	$\mathbf{16.5 \pm 6.0}$	$\mathbf{24.0 \pm 7.1}$	$\mathbf{28.2 \pm 7.8}$	$\mathbf{25.3 \pm 1.8}$	**1.24**	**1.00**
LURGS J043729.9−54365	04:37:29.90	−54:36:04.5	14.9 ± 6.8	17.9 ± 7.9	19.9 ± 7.7	18.0 ± 3.3	1.34	1.00
LURGS J04374.7−543914	04:37:04.65	−54:39:13.7	3.7 ± 6.0	2.4 ± 8.0	0.4 ± 7.8	10.2 ± 1.9	1.35	1.00
LURGS J043717.4−54356	04:37:17.35	−54:35:06.2	13.5 ± 7.1	21.7 ± 7.9	25.5 ± 7.6	8.8 ± 2.4	2.35	0.98
LURGS J043717.5−543528	04:37:17.49	−54:35:28.3	48.7 ± 7.1	54.5 ± 7.8	49.0 ± 7.6	6.2 ± 2.3	2.59	0.93
LURGS J04377.5−54341	04:37:07.51	−54:34:00.6	34.2 ± 6.6	27.3 ± 7.9	13.6 ± 7.9	8.9 ± 2.3	2.18	0.93
LURGS J043649.4−54408	04:36:49.44	−54:40:08.4	7.9 ± 5.4	13.9 ± 6.9	5.2 ± 8.2	9.0 ± 2.2	2.00	0.78
..... **ADF-S-32**								
LURGS J044410.1−534949†	**04:44:10.13**	**−53:49:49.1**	$\mathbf{13.1 \pm 6.0}$	$\mathbf{16.6 \pm 6.8}$	$\mathbf{20.8 \pm 8.0}$	$\mathbf{5.5 \pm 2.8}$	—	—
LURGS J04450.4−53496	04:45:00.43	−53:49:06.2	9.3 ± 5.6	0.9 ± 6.8	-0.6 ± 8.0	20.0 ± 6.0	3.81	0.78
..... **G09-83808**								
LURGS J090045.7+004124	**09:00:45.74**	**+00:41:24.1**	$\mathbf{10.9 \pm 7.5}$	$\mathbf{24.1 \pm 8.3}$	$\mathbf{42.4 \pm 8.7}$	$\mathbf{26.3 \pm 1.3}$	**1.06**	**1.00**
LURGS J090032.8+004313	09:00:32.77	+00:43:13.0	79.5 ± 6.6	69.2 ± 7.7	40.9 ± 8.1	18.5 ± 1.4	1.06	1.00
LURGS J090019.4+004016	09:00:19.37	+00:40:15.7	5.6 ± 6.4	-2.3 ± 7.4	-8.1 ± 7.3	18.3 ± 3.3	1.18	1.00
LURGS J090057.3+00415	09:00:57.28	+00:41:04.8	30.1 ± 7.3	32.5 ± 8.2	28.1 ± 9.0	5.5 ± 1.1	1.25	1.00
LURGS J090054.2+004343	09:00:54.21	+00:43:43.1	19.2 ± 7.5	18.8 ± 8.2	19.9 ± 8.9	3.7 ± 1.1	1.66	0.75
LURGS J090057.1+004039	09:00:57.08	+00:40:39.4	26.9 ± 7.4	33.6 ± 8.4	32.7 ± 9.0	3.2 ± 1.2	1.66	0.61
LURGS J090037.1+003624	09:00:37.14	+00:36:24.3	72.9 ± 6.6	65.4 ± 7.4	43.8 ± 8.3	8.6 ± 2.4	1.60	0.61
..... **G15-82684**								
LURGS J14506.3+015038	14:50:06.29	+01:50:38.4	31.5 ± 7.1	37.9 ± 7.4	45.4 ± 8.9	17.4 ± 1.5	1.07	1.00
LURGS J145013.1+014810	**14:50:13.10**	**+01:48:09.8**	$\mathbf{17.7 \pm 7.5}$	$\mathbf{36.4 \pm 8.1}$	$\mathbf{39.0 \pm 9.2}$	$\mathbf{17.2 \pm 1.5}$	**1.08**	**1.00**
LURGS J145012.1+015158	14:50:12.06	+01:51:57.5	30.5 ± 7.3	34.0 ± 7.2	34.4 ± 8.7	11.2 ± 1.8	1.17	1.00
LURGS J145015.4+015237	14:50:15.43	+01:52:37.1	18.5 ± 7.3	33.9 ± 7.6	37.9 ± 8.5	13.2 ± 2.3	1.21	1.00
LURGS J145025.7+015115	14:50:25.66	+01:51:14.8	21.9 ± 7.8	31.7 ± 7.7	22.8 ± 9.1	7.1 ± 1.9	1.68	1.00
LURGS J145023.8+01514	14:50:23.82	+01:51:04.4	13.7 ± 7.6	9.8 ± 7.7	23.9 ± 8.9	5.4 ± 1.7	1.92	0.92
..... **SGP-433089**								
LURGS J222737.4−333835	**22:27:37.37**	**−33:38:34.7**	$\mathbf{28.3 \pm 9.2}$	$\mathbf{36.8 \pm 10.0}$	$\mathbf{35.1 \pm 10.8}$	$\mathbf{8.1 \pm 1.1}$	**1.12**	**1.00**

Table B.1 (continued from previous page)

IAU name	α (J2000) h m s	δ ° ′ ″	S_{250} mJy beam^{-1}	S_{350} mJy beam^{-1}	S_{500} mJy beam^{-1}	S_{870} mJy	$\mathcal{B}$	$\mathcal{F}$
LURGS J222725.2−333920	22:27:25.22	−33:39:19.5	35.3 ± 9.4	38.8 ± 10.4	20.2 ± 11.3	8.1 ± 1.4	1.16	1.00
LURGS J222747.9−333533	22:27:47.89	−33:35:32.7	21.7 ± 9.4	32.0 ± 9.8	25.1 ± 10.9	7.5 ± 1.3	1.17	1.00
LURGS J222731.1−33404	22:27:31.09	−33:40:03.7	5.0 ± 9.1	-8.0 ± 10.4	-1.1 ± 11.1	6.3 ± 1.2	1.21	1.00
LURGS J222733.7−333440	22:27:33.67	−33:34:40.2	40.2 ± 9.7	43.8 ± 10.0	28.8 ± 10.7	6.4 ± 1.3	1.24	1.00
LURGS J222737.7−333727	22:27:37.70	−33:37:26.8	49.7 ± 9.5	47.2 ± 9.9	23.2 ± 10.5	5.1 ± 1.1	1.31	0.99
LURGS J222730.4−333534	22:27:30.44	−33:35:33.6	18.5 ± 9.5	18.8 ± 9.9	18.2 ± 11.0	5.5 ± 1.3	1.35	0.96
LURGS J222750.1−334153	22:27:50.14	−33:41:53.2	10.3 ± 9.9	11.5 ± 10.3	19.9 ± 10.8	7.0 ± 1.8	1.50	0.93
LURGS J222753.8−333529	22:27:53.81	−33:35:28.5	4.3 ± 9.7	38.1 ± 10.2	16.2 ± 10.9	6.4 ± 1.7	1.55	0.90
LURGS J222727.8−334056	22:27:27.79	−33:40:56.3	17.5 ± 9.6	27.9 ± 10.5	25.9 ± 11.1	5.2 ± 1.3	1.44	0.85
LURGS J222744.7−333741	22:27:44.74	−33:37:40.8	5.5 ± 9.4	37.0 ± 9.9	27.6 ± 10.8	4.5 ± 1.1	1.46	0.75

‡ SPIRE and LABOCA flux densities have been corrected to reflect the radial offset and de-boosted, respectively.
† Ultra-Red galaxies that are undetected in any SPIRE image.
Note. Ultra-Red galaxies are listed in order of increasing right ascension and are highlighted in **bold**.

Table B.2: Photometric redshift properties around ultra-red galaxy signposts.

IAU Name	$z_{\rm phot}$ †	χ^2	$\log_{10}(L_{\rm FIR})$ $[L_\odot]$	IAU Name	$z_{\rm phot}$ †	χ^2	$\log_{10}(L_{\rm FIR})$ $[L_\odot]$
			SGP-28124				
LURGS J000124.9−354212	$\mathbf{3.4^{+0.1}_{-0.1}}$	**5.99**	$\mathbf{13.50^{+0.02}_{-0.02}}$	LURGS J000145.0−353822	$2.5^{+0.2}_{-0.2}$	0.19	$13.05^{+0.05}_{-0.06}$
LURGS J00014.2−354123	$3.6^{+2.0}_{-0.8}$	0.36	$12.59^{+0.30}_{-0.19}$	LURGS J000122.9−354211	$2.5^{+0.2}_{-0.2}$	32.37	$12.95^{+0.05}_{-0.05}$
LURGS J000138.5−35442	$3.7^{+6.3}_{-1.4}$	1.02	$12.38^{+0.64}_{-0.35}$	LURGS J000115.9−35411	$1.6^{+0.4}_{-0.4}$	0.69	$12.36^{+0.17}_{-0.26}$
LURGS J000129.4−354416	$1.6^{+0.4}_{-0.5}$	2.20	$12.35^{+0.18}_{-0.28}$				
			HeLMS-42				
LURGS J00034.2+024114	$\mathbf{3.2^{+0.2}_{-0.2}}$	**3.30**	$\mathbf{13.26^{+0.04}_{-0.05}}$	LURGS J000319.2+02371‡	—	—	—
			SGP-93302				
LURGS J000624.4−323018	$\mathbf{3.7^{+0.2}_{-0.2}}$	**0.14**	$\mathbf{13.41^{+0.03}_{-0.03}}$	LURGS J00067.7−322638	$4.4^{+0.2}_{-0.2}$	0.02	$13.45^{+0.04}_{-0.03}$
LURGS J000621.3−32328	$3.6^{+0.4}_{-0.3}$	0.26	$13.02^{+0.08}_{-0.06}$	LURGS J000619.9−323126	$2.2^{+0.4}_{-0.4}$	0.64	$12.50^{+0.12}_{-0.15}$
LURGS J00066.1−323016	$1.8^{+0.4}_{-0.5}$	1.05	$12.58^{+0.17}_{-0.29}$	LURGS J000619.9−322847	$1.9^{+0.4}_{-0.4}$	0.42	$12.43^{+0.14}_{-0.18}$
LURGS J000634.0−323138	$2.3^{+0.8}_{-0.7}$	0.13	$12.33^{+0.23875}_{-0.28}$	LURGS J00068.5−323338‡	—	—	—
			ELAISS1-18				
LURGS J002851.3−431353	$\mathbf{2.9^{+0.2}_{-0.2}}$	**0.87**	$\mathbf{13.03^{+0.05}_{-0.06}}$	LURGS J00297.7−431036	$2.8^{+0.2}_{-0.2}$	0.81	$13.05^{+0.06}_{-0.07}$
LURGS J002913.4−43077	$6.3^{+3.7}_{-4.1}$	1.38	$12.87^{+0.28}_{-0.71}$	LURGS J00294.0−430737	$1.4^{+1.1}_{-1.4}$	0.37	$12.08^{+0.44}_{-0.44}$
LURGS J002919.0−430817	$6.3^{+3.7}_{-4.1}$	0.75	$12.52^{+0.29}_{-0.76}$				
			ELAISS1-26				
LURGS J003352.4−452015	$\mathbf{2.8^{+0.3}_{-0.3}}$	**2.47**	$\mathbf{12.88^{+0.07}_{-0.08}}$	LURGS J003410.4−452230	$2.2^{+0.4}_{-0.5}$	1.44	$12.83^{+0.13}_{-0.18}$
LURGS J003347.9−451441	$2.9^{+0.7}_{-0.7}$	0.16	$12.60^{+0.15}_{-0.20}$				
			SGP-208073				
LURGS J003533.9−280260	$\mathbf{3.6^{+0.3}_{-0.2}}$	**0.96**	$\mathbf{13.19^{+0.05}_{-0.05}}$	LURGS J003540.1−280459	$2.7^{+0.3}_{-0.3}$	0.64	$12.92^{+0.08}_{-0.09}$
LURGS J003536.4−280143	$2.5^{+0.6}_{-0.6}$	1.25	$12.50^{+0.16}_{-0.20}$				
			ELAISS1-29				
LURGS J003756.6−421519	$\mathbf{2.8^{+0.2}_{-0.3}}$	**3.89**	$\mathbf{12.87^{+0.06}_{-0.07}}$	LURGS J003831.5−421418‡	—	—	—
LURGS J003744.9−421240	$2.0^{+0.3}_{-0.3}$	1.15	$12.70^{+0.10}_{-0.12}$	LURGS J003811.7−42198‡	—	—	—
LURGS J003825.5−42128	$0.9^{+0.5}_{-0.7}$	0.34	$12.34^{+0.35}_{-1.29}$	LURGS J00388.4−421742	$2.3^{+0.3}_{-0.3}$	1.66	$12.64^{+0.10}_{-0.13}$
			SGP-354388				
LURGS J004223.7−334325	$\mathbf{4.2^{+0.2}_{-0.2}}$	**0.19**	$\mathbf{13.37^{+0.04}_{-0.03}}$	LURGS J004223.5−334350	$3.5^{+0.3}_{-0.3}$	0.18	$13.15^{+0.06}_{-0.06}$
LURGS J004233.2−33444	$3.7^{+0.9}_{-0.5}$	0.36	$12.85^{+0.15}_{-0.11}$	LURGS J004223.2−334117	$3.2^{+0.6}_{-0.5}$	1.09	$12.81^{+0.12}_{-0.11}$
LURGS J004216.1−334138	$1.8^{+0.2}_{-0.2}$	0.06	$12.77^{+0.07}_{-0.09}$	LURGS J004219.8−334435	$2.6^{+0.3}_{-0.3}$	2.39	$12.72^{+0.08}_{-0.09}$
LURGS J004212.9−334544‡	—	—	—	LURGS J004210.1−334040‡	—	—	—
LURGS J004228.5−334925‡	—	—	—				
			SGP-380990				
LURGS J004614.6−321828	$\mathbf{2.8^{+0.2}_{-0.2}}$	**4.55**	$\mathbf{12.88^{+0.06}_{-0.06}}$	LURGS J004620.2−32209	$2.7^{+0.3}_{-0.3}$	1.34	$12.77^{+0.09}_{-0.10}$
LURGS J00464.4−321844	$2.0^{+0.7}_{-1.0}$	0.23	$12.43^{+0.24}_{-0.55}$				
			HeLMS-10				

Table B.2 (continued from previous page)

IAU Name	$z_{\rm phot}$ †	χ^2	$\log_{10}(L_{\rm FIR})$ $[L_\odot]$	IAU Name	$z_{\rm phot}$ †	χ^2	$\log_{10}(L_{\rm FIR})$ $[L_\odot]$
LURGS J005258.6+061318	$\mathbf{3.2^{+0.1}_{-0.2}}$	**3.56**	$\mathbf{13.48^{+0.03}_{-0.04}}$	LURGS J00532.4+061113‡	—	—	—
LURGS J005310.4+061510	$2.5^{+0.5}_{-0.5}$	0.12	$12.97^{+0.13}_{-0.18}$				
SGP-221606							
LURGS J011918.9−294516	$\mathbf{2.8^{+0.2}_{-0.2}}$	**1.59**	$\mathbf{13.04^{+0.06}_{-0.07}}$	LURGS J011915.9−294748	$4.4^{+1.7}_{-1.2}$	2.72	$12.65^{+0.23875}_{-0.23875}$
LURGS J01191.8−294342	$1.3^{+3.7}_{-1.3}$	0.56	$11.71^{+0.99}_{-0.99}$	LURGS J01199.6−294241‡	—	—	—
SGP-146631							
LURGS J013155.8−311147	$2.9^{+0.3}_{-0.3}$	2.26	$12.89^{+0.08}_{-0.09}$	**LURGS J01324.5−311239**	$\mathbf{2.4^{+0.2}_{-0.2}}$	**20.97**	$\mathbf{13.03^{+0.05}_{-0.06}}$
LURGS J013215.5−310837‡	—	—	—				
SGP-278539							
LURGS J01428.2−323426	$\mathbf{2.9^{+0.3}_{-0.3}}$	**4.62**	$\mathbf{12.94^{+0.07}_{-0.08}}$	LURGS J014226.2−323324‡	—	—	—
LURGS J01421.6−323624	$5.2^{+4.1}_{-1.4}$	0.23	$12.91^{+0.37}_{-0.21}$	LURGS J014214.4−32290	$3.8^{+2.5}_{-1.6}$	0.06	$12.63^{+0.34}_{-0.41}$
LURGS J014218.2−32352‡	—	—	—				
SGP-142679							
LURGS J014456.9−284146	$\mathbf{2.7^{+0.2}_{-0.2}}$	**15.33**	$\mathbf{13.03^{+0.05}_{-0.06}}$	LURGS J014448.8−283535	$7.3^{+2.7}_{-2.2}$	2.69	$12.96^{+0.19}_{-0.23}$
LURGS J01456.7−284457	$2.1^{+0.1}_{-0.1}$	8.07	$13.12^{+0.05}_{-0.06}$				
XMM-15							
LURGS J021745.3−030912	$\mathbf{3.7^{+0.5}_{-0.5}}$	**0.01**	$\mathbf{13.00^{+0.09}_{-0.09}}$	LURGS J021757.1−030753	$1.2^{+0.4}_{-0.5}$	0.09	$12.51^{+0.23}_{-0.43}$
LURGS J021737.3−03128‡	—	—	—				
XMM-30							
LURGS J022656.6−032711	$\mathbf{3.5^{+0.2}_{-0.2}}$	**3.23**	$\mathbf{13.19^{+0.03}_{-0.03}}$	LURGS J022644.9−032510	$2.8^{+0.2}_{-0.1}$	3.05	$13.13^{+0.04}_{-0.04}$
LURGS J022630.2−032530	$2.9^{+0.7}_{-0.6}$	1.45	$12.84^{+0.15}_{-0.18}$	LURGS J02270.8−032541	$2.5^{+0.8}_{-0.9}$	0.53	$12.32^{+0.20}_{-0.32}$
LURGS J022650.0−032542	$1.8^{+0.4}_{-0.4}$	0.70	$12.47^{+0.14}_{-0.21}$				
CDFS-13							
LURGS J03370.7−292148	$\mathbf{3.0^{+0.2}_{-0.2}}$	**1.51**	$\mathbf{13.21^{+0.05}_{-0.05}}$	LURGS J03370.3−291746	$3.0^{+2.3}_{-0.8}$	13.23	$12.83^{+0.40}_{-0.25}$
LURGS J033655.2−292627	$2.6^{+1.1}_{-1.1}$	0.15	$12.44^{+0.26}_{-0.47}$				
ADFS-27							
LURGS J043657.0−543813	$\mathbf{4.4^{+0.4}_{-0.3}}$	**0.92**	$\mathbf{13.23^{+0.06}_{-0.06}}$	LURGS J043729.9−54365	$4.0^{+0.7}_{-0.6}$	0.80	$13.02^{+0.12}_{-0.12}$
LURGS J04374.7−543914‡	—	—	—	LURGS J043717.4−54356	$2.7^{+0.5}_{-0.5}$	1.90	$12.63^{+0.11}_{-0.14}$
LURGS J043717.5−543528	$2.0^{+0.2}_{-0.2}$	11.45	$12.80^{+0.07}_{-0.09}$	LURGS J04377.5−54341	$1.9^{+0.4}_{-0.5}$	0.05	$12.57^{+0.17}_{-0.28}$
LURGS J043649.4−54408	$3.1^{+0.9}_{-0.8}$	0.54	$12.54^{+0.18}_{-0.23}$				
ADFS-32							
LURGS J044410.1−534949	$\mathbf{3.0^{+0.6}_{-0.6}}$	**0.45**	$\mathbf{12.65^{+0.12}_{-0.15}}$	LURGS J04450.4−53496‡	—	—	—
G09-83808							
LURGS J090045.7+004124	$\mathbf{4.5^{+0.4}_{-0.3}}$	**0.23**	$\mathbf{13.25^{+0.05}_{-0.05}}$	LURGS J090032.8+004313	$2.3^{+0.1}_{-0.1}$	6.55	$13.15^{+0.04}_{-0.05}$
LURGS J090019.4+004016‡	—	—	—	LURGS J090057.3+00415	$2.1^{+0.3}_{-0.3}$	1.20	$12.60^{+0.09}_{-0.11}$
LURGS J090054.2+004343	$1.9^{+0.5}_{-0.5}$	1.16	$12.34^{+0.16}_{-0.23}$	LURGS J090057.1+004039	$1.8^{+0.3}_{-0.3}$	6.49	$12.45^{+0.12}_{-0.17}$

Table B.2 (continued from previous page)

IAU Name	$z_{\rm phot}$ †	χ^2	$\log_{10}(L_{\rm FIR})$ $[L_\odot]$	IAU Name	$z_{\rm phot}$ †	χ^2	$\log_{10}(L_{\rm FIR})$ $[L_\odot]$
LURGS J090037.1+003624	$1.8^{+0.2}_{-0.2}$	2.45	$12.83^{+0.07}_{-0.09}$				
..... **G15-82684**							
LURGS J14506.3+015038	$3.2^{+0.2}_{-0.2}$	1.24	$13.14^{+0.04}_{-0.05}$	**LURGS J145013.1+014810**	$\mathbf{3.5^{+0.3}_{-0.2}}$	**0.05**	$\mathbf{13.07^{+0.05}_{-0.05}}$
LURGS J145012.1+015158	$2.7^{+0.3}_{-0.3}$	0.58	$12.93^{+0.07}_{-0.08}$	LURGS J145015.4+015237	$3.2^{+0.3}_{-0.3}$	0.83	$12.94^{+0.07}_{-0.07}$
LURGS J145025.7+015115	$2.3^{+0.4}_{-0.4}$	0.83	$12.62^{+0.11}_{-0.14}$	LURGS J145023.8+01514	$2.5^{+0.7}_{-0.7}$	2.67	$12.48^{+0.18}_{-0.25}$
..... **SGP-433089**							
LURGS J222737.4−333835	$\mathbf{2.5^{+0.3}_{-0.2}}$	**0.87**	$\mathbf{12.77^{+0.08}_{-0.08}}$	LURGS J222725.2−333920	$2.4^{+0.3}_{-0.3}$	0.14	$12.83^{+0.09}_{-0.10}$
LURGS J222747.9−333533	$2.5^{+0.4}_{-0.3}$	0.21	$12.71^{+0.10}_{-0.10}$	LURGS J222731.1−33404‡	—	—	—
LURGS J222733.7−333440	$1.9^{+0.3}_{-0.3}$	0.66	$12.66^{+0.10}_{-0.12}$	LURGS J222737.7−333727	$1.5^{+0.2}_{-0.3}$	0.81	$12.57^{+0.12}_{-0.15}$
LURGS J222730.4−333534	$2.3^{+0.6}_{-0.5}$	0.16	$12.57^{+0.16}_{-0.19}$	LURGS J222750.1−334153	$3.1^{+1.0}_{-0.7}$	0.51	$12.56^{+0.19}_{-0.18}$
LURGS J222753.8−333529	$2.6^{+0.5}_{-0.4}$	4.51	$12.58^{+0.13}_{-0.14}$	LURGS J222727.8−334056	$2.2^{+0.4}_{-0.4}$	1.43	$12.52^{+0.13}_{-0.15}$
LURGS J222744.7−333741	$2.3^{+0.4}_{-0.4}$	6.69	$12.49^{+0.13}_{-0.13}$				

† Photometric redshift errors are based on the $\chi^2{}_{\rm min}+1$ values, without the adding the intrinsic template SED scatter in quadrature.
‡ SPIRE non-detections, for which I do not provide any photometric redshifts; I do not include these in my analysis.

Appendix

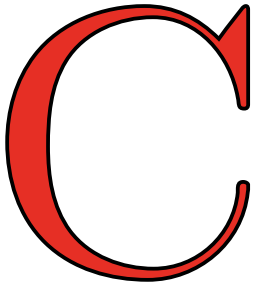

In this Appendix, I present the over-density and *Herschel*-SPIRE cut-outs and the optical/NIR/FIR environmental properties for the sample of 64 ultra-red galaxies within the S2CLS and S2COSMOS imaging surveys that feature in Chapter 4.

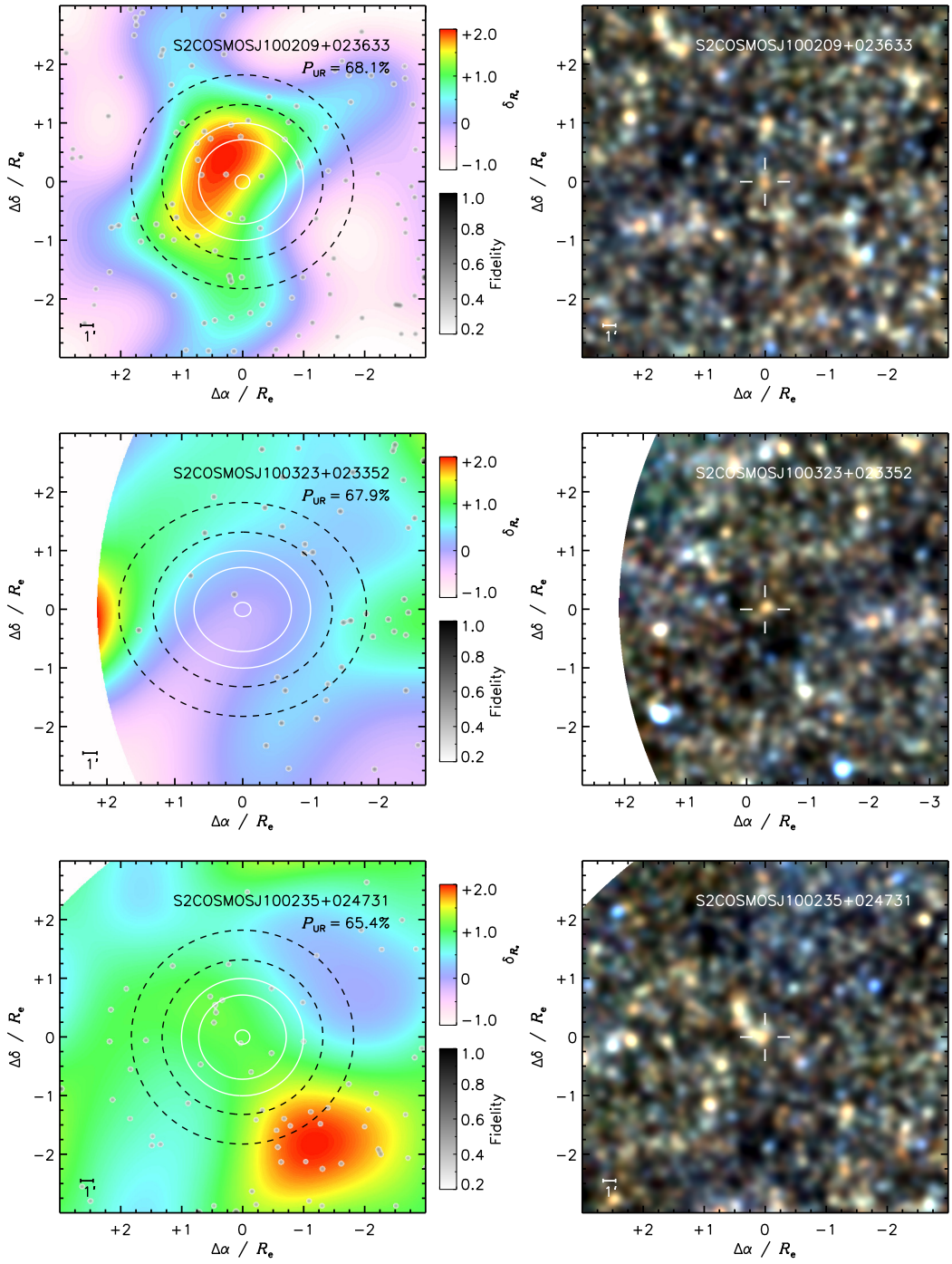

Figure C.1 (continued from Figure 4.5)

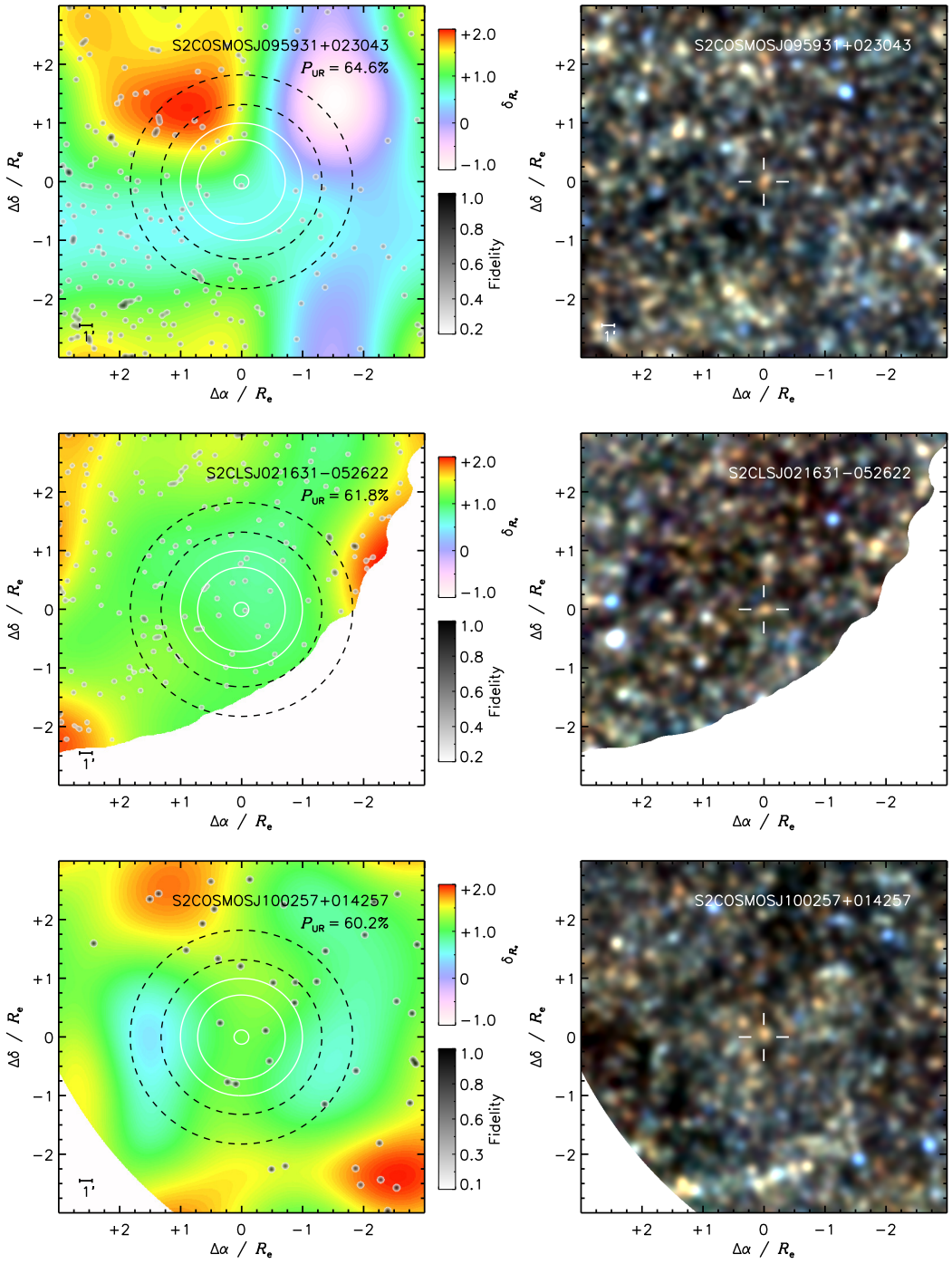

Figure C.1 (continued from previous page)

Table C.1: Ultra-Red galaxies and their environmental properties.

IAU	Field	z	$P_{\rm UR}$ %	$\sum \mathcal{F}$	$\delta^{\dagger}_{R_{\rm e}}$	$\sum \mathcal{P}^{\dagger}_{\rm assoc}$	$\log_{10}(M_{\rm dust})^{\dagger}$ $[M_{\odot}]$	$\log_{10}(\Psi)^{\dagger}$ $[M_{\odot}\,{\rm yr}^{-1}]$	$\sum \mathcal{P}_{\rm assoc}$	$\delta_{R_{\rm e}}$	$\log_{10}(M_{\rm stars})$ $[M_{\odot}]$
				FIR					**Optical/NIR**		
S2COSMOSJ100249+023255	COSMOS	$3.72^{+0.35}_{-0.33}$	$91.1^{+0.3}_{-0.3}$	$8.7^{+4.0}_{-2.8}$	$+0.3^{+0.6}_{-0.4}$	$0.2^{+0.1}_{-0.1}$	$9.5^{+0.1}_{-0.1}$	$3.4^{+0.1}_{-0.1}$	$10.5^{+1.0}_{-1.3}$	$-0.1^{+0.3}_{-0.2}$	11.2
S2COSMOSJ095748+015843	COSMOS	$3.25^{+0.40}_{-0.34}$	$70.9^{+0.3}_{-0.3}$	$4.8^{+3.3}_{-2.1}$	$-0.2^{+0.6}_{-0.4}$	$0.3^{+0.2}_{-0.1}$	$9.3^{+0.1}_{-0.1}$	$3.1^{+0.1}_{-0.1}$	$22.3^{+2.2}_{-2.6}$	$+0.1^{+0.3}_{-0.2}$	11.5
S2CLSJ021620-045054	UDS	$2.85^{+0.32}_{-0.28}$	$70.7^{+0.3}_{-0.3}$	$16.7^{+4.9}_{-3.9}$	$-0.4^{+0.2}_{-0.1}$	$0.6^{+0.2}_{-0.2}$	$9.2^{+0.2}_{-0.2}$	$3.1^{+0.2}_{-0.2}$	$15.3^{+2.7}_{-1.4}$	$-0.1^{+0.1}_{-0.1}$	11.5
S2COSMOSJ100209+023633	COSMOS	$3.22^{+0.36}_{-0.32}$	$68.1^{+0.3}_{-0.3}$	$13.5^{+4.7}_{-3.6}$	$+0.9^{+0.7}_{-0.5}$	$0.4^{+0.1}_{-0.1}$	$9.3^{+0.1}_{-0.1}$	$3.2^{+0.1}_{-0.1}$	$29.0^{+2.0}_{-3.6}$	$+0.3^{+0.5}_{-0.3}$	11.6
S2COSMOSJ100323+023352	COSMOS	$2.73^{+0.27}_{-0.26}$	$67.9^{+0.3}_{-0.3}$	$1.0^{+2.3}_{-0.8}$	$-0.8^{+0.4}_{-0.1}$	$0.3^{+0.8}_{-0.3}$	$9.3^{+0.1}_{-0.1}$	$3.2^{+0.1}_{-0.1}$	—	—	—
S2COSMOSJ100235+024731	COSMOS	$2.88^{+0.35}_{-0.29}$	$65.4^{+0.3}_{-0.3}$	$9.9^{+4.2}_{-3.1}$	$+0.6^{+0.7}_{-0.5}$	$0.6^{+0.2}_{-0.2}$	$9.2^{+0.2}_{-0.2}$	$3.1^{+0.2}_{-0.2}$	$34.1^{+3.1}_{-3.9}$	$+0.2^{+0.4}_{-0.3}$	11.7
S2COSMOSJ095931+023043	COSMOS	$2.87^{+0.28}_{-0.26}$	$64.6^{+0.3}_{-0.3}$	$9.6^{+4.1}_{-3.0}$	$+0.1^{+0.5}_{-0.3}$	$0.4^{+0.2}_{-0.1}$	$9.3^{+0.1}_{-0.1}$	$3.1^{+0.1}_{-0.1}$	$28.6^{+2.4}_{-3.9}$	$+0.2^{+0.5}_{-0.3}$	11.6
S2CLSJ021631-052622	UDS	$2.79^{+0.27}_{-0.25}$	$61.8^{+0.2}_{-0.2}$	$16.5^{+5.1}_{-4.0}$	$-0.1^{+0.3}_{-0.2}$	$0.6^{+0.2}_{-0.1}$	$9.3^{+0.1}_{-0.1}$	$3.2^{+0.1}_{-0.1}$	—	—	—
S2COSMOSJ100257+014257	COSMOS	$2.58^{+0.30}_{-0.27}$	$60.2^{+0.2}_{-0.2}$	$5.0^{+3.4}_{-2.1}$	$-0.1^{+0.6}_{-0.4}$	$0.6^{+0.4}_{-0.2}$	$9.2^{+0.1}_{-0.2}$	$3.1^{+0.1}_{-0.2}$	—	—	—
S2COSMOSJ100115+024257	COSMOS	$2.44^{+0.23}_{-0.23}$	$56.5^{+0.2}_{-0.2}$	$6.9^{+3.7}_{-2.5}$	$-0.2^{+0.4}_{-0.3}$	$0.6^{+0.3}_{-0.2}$	$9.3^{+0.1}_{-0.1}$	$3.2^{+0.1}_{-0.1}$	$52.8^{+3.6}_{-4.3}$	$+0.2^{+0.4}_{-0.3}$	12.0
S2COSMOSJ095738+015813	COSMOS	$3.02^{+0.35}_{-0.32}$	$56.4^{+0.2}_{-0.2}$	$4.9^{+3.3}_{-2.1}$	$+1.4^{+1.6}_{-1.0}$	$0.5^{+0.3}_{-0.2}$	$9.3^{+0.1}_{-0.1}$	$3.1^{+0.1}_{-0.1}$	$19.8^{+2.6}_{-3.5}$	$-0.2^{+0.3}_{-0.2}$	11.5
S2COSMOSJ100140+023011	COSMOS	$2.76^{+0.44}_{-0.38}$	$55.2^{+0.2}_{-0.2}$	$4.9^{+3.3}_{-2.1}$	$-0.4^{+0.4}_{-0.3}$	$0.4^{+0.3}_{-0.2}$	$9.2^{+0.2}_{-0.2}$	$3.0^{+0.2}_{-0.2}$	$46.9^{+2.5}_{-4.3}$	$+0.3^{+0.5}_{-0.3}$	11.9
S2COSMOSJ100142+014033	COSMOS	$2.87^{+0.30}_{-0.27}$	$52.5^{+0.2}_{-0.2}$	$6.9^{+3.7}_{-2.5}$	$+0.1^{+0.6}_{-0.4}$	$0.6^{+0.3}_{-0.2}$	$9.4^{+0.1}_{-0.1}$	$3.2^{+0.1}_{-0.1}$	$26.4^{+2.6}_{-4.8}$	$-0.2^{+0.4}_{-0.2}$	11.6
S2CLSJ141715+523630	EGS	$2.70^{+0.30}_{-0.27}$	$51.5^{+0.2}_{-0.2}$	$10.5^{+4.2}_{-3.1}$	$+0.3^{+0.5}_{-0.4}$	$0.6^{+0.3}_{-0.2}$	$9.3^{+0.1}_{-0.2}$	$3.1^{+0.1}_{-0.2}$	—	—	—
S2CLSJ021730-045936	UDS	$2.82^{+0.25}_{-0.24}$	$51.4^{+0.2}_{-0.2}$	$18.9^{+5.3}_{-4.2}$	$-0.0^{+0.3}_{-0.2}$	$0.5^{+0.1}_{-0.1}$	$9.3^{+0.1}_{-0.1}$	$3.2^{+0.1}_{-0.1}$	$21.8^{+2.0}_{-2.4}$	$-0.1^{+0.1}_{-0.1}$	11.5
S2CLSJ104456+584959	Lockman Hole North	$2.82^{+0.31}_{-0.29}$	$51.3^{+0.2}_{-0.2}$	$9.0^{+3.8}_{-2.8}$	$-0.2^{+0.4}_{-0.3}$	$0.3^{+0.1}_{-0.1}$	$9.4^{+0.1}_{-0.1}$	$3.1^{+0.1}_{-0.1}$	—	—	—
S2CLSJ021940-045618	UDS	$2.09^{+0.21}_{-0.23}$	$51.0^{+0.2}_{-0.2}$	$20.2^{+5.4}_{-4.4}$	$+0.2^{+0.3}_{-0.3}$	$1.0^{+0.3}_{-0.2}$	$9.2^{+0.1}_{-0.2}$	$3.1^{+0.1}_{-0.2}$	—	—	—
S2COSMOSJ100207+024137	COSMOS	$2.55^{+0.30}_{-0.28}$	$50.6^{+0.2}_{-0.2}$	$10.6^{+4.3}_{-3.2}$	$+0.6^{+0.7}_{-0.5}$	$0.7^{+0.3}_{-0.2}$	$9.3^{+0.1}_{-0.2}$	$3.1^{+0.1}_{-0.2}$	$45.5^{+4.3}_{-3.8}$	$+0.2^{+0.5}_{-0.3}$	11.9
S2CLSJ021744-052008	UDS	$3.20^{+0.36}_{-0.28}$	$50.4^{+0.2}_{-0.2}$	$20.8^{+5.5}_{-4.4}$	$+0.0^{+0.3}_{-0.2}$	$0.6^{+0.2}_{-0.1}$	$9.4^{+0.2}_{-0.2}$	$3.2^{+0.2}_{-0.1}$	$12.6^{+1.1}_{-1.4}$	$-0.0^{+0.1}_{-0.1}$	11.3
S2COSMOSJ095821+015937	COSMOS	$3.01^{+0.38}_{-0.30}$	$50.2^{+0.2}_{-0.2}$	$7.7^{+3.8}_{-2.7}$	$+0.1^{+0.5}_{-0.4}$	$0.5^{+0.2}_{-0.2}$	$9.2^{+0.2}_{-0.2}$	$3.1^{+0.2}_{-0.2}$	$33.7^{+2.6}_{-3.9}$	$+0.2^{+0.4}_{-0.2}$	11.8
S2COSMOSJ100136+021109	COSMOS	$2.79^{+0.27}_{-0.24}$	$49.0^{+0.2}_{-0.2}$	$17.5^{+5.2}_{-4.1}$	$+0.2^{+0.3}_{-0.3}$	$0.9^{+0.3}_{-0.2}$	$9.3^{+0.2}_{-0.2}$	$3.2^{+0.2}_{-0.1}$	$38.1^{+3.2}_{-4.9}$	$+0.3^{+0.5}_{-0.3}$	11.8
S2COSMOSJ100153+021941	COSMOS	$2.47^{+0.26}_{-0.25}$	$48.1^{+0.2}_{-0.2}$	$18.4^{+5.3}_{-4.2}$	$+0.5^{+0.4}_{-0.3}$	$0.9^{+0.3}_{-0.2}$	$9.2^{+0.2}_{-0.2}$	$3.1^{+0.2}_{-0.2}$	$33.0^{+2.7}_{-5.8}$	$+0.1^{+0.4}_{-0.2}$	11.8
S2COSMOSJ100059+013307	COSMOS	$4.93^{+0.76}_{-0.45}$	$48.0^{+0.2}_{-0.2}$	$4.9^{+3.3}_{-2.1}$	$+0.7^{+1.1}_{-0.8}$	$0.1^{+0.1}_{-0.0}$	$9.7^{+0.1}_{-0.1}$	$3.4^{+0.1}_{-0.1}$	—	—	—
S2COSMOSJ100317+024944	COSMOS	$2.75^{+0.26}_{-0.25}$	$47.1^{+0.2}_{-0.2}$	$3.0^{+2.9}_{-1.6}$	$+0.4^{+1.3}_{-0.8}$	$0.8^{+0.7}_{-0.4}$	$9.4^{+0.1}_{-0.1}$	$3.3^{+0.1}_{-0.1}$	—	—	—
S2COSMOSJ100025+022605	COSMOS	$2.95^{+0.36}_{-0.30}$	$47.1^{+0.2}_{-0.2}$	$35.3^{+6.9}_{-5.9}$	$-0.1^{+0.2}_{-0.2}$	$1.0^{+0.2}_{-0.2}$	$9.3^{+0.2}_{-0.2}$	$3.2^{+0.2}_{-0.2}$	$27.8^{+2.3}_{-3.7}$	$+0.0^{+0.4}_{-0.2}$	11.7
S2CLSJ021556-052106	UDS	$2.46^{+0.21}_{-0.20}$	$46.6^{+0.2}_{-0.2}$	$17.4^{+5.0}_{-4.0}$	$+0.3^{+0.4}_{-0.3}$	$0.8^{+0.2}_{-0.2}$	$9.4^{+0.2}_{-0.1}$	$3.3^{+0.1}_{-0.1}$	—	—	—
S2CLSJ021702-052718	UDS	$2.22^{+0.31}_{-0.33}$	$46.3^{+0.2}_{-0.2}$	$21.0^{+5.4}_{-4.3}$	$+0.1^{+0.3}_{-0.2}$	$0.9^{+0.2}_{-0.2}$	$9.1^{+0.2}_{-0.2}$	$3.0^{+0.2}_{-0.2}$	$38.0^{+3.2}_{-3.1}$	$-0.1^{+0.1}_{-0.1}$	11.9
S2COSMOSJ095946+015715	COSMOS	$3.08^{+0.34}_{-0.29}$	$46.2^{+0.2}_{-0.2}$	$12.7^{+4.6}_{-3.5}$	$+0.3^{+0.5}_{-0.4}$	$0.6^{+0.2}_{-0.2}$	$9.3^{+0.2}_{-0.1}$	$3.2^{+0.1}_{-0.1}$	$29.5^{+2.3}_{-2.7}$	$-0.0^{+0.3}_{-0.2}$	11.6
S2CLSJ021724-044030	UDS	$2.65^{+0.31}_{-0.28}$	$46.1^{+0.2}_{-0.2}$	$13.9^{+4.6}_{-3.5}$	$-0.2^{+0.3}_{-0.2}$	$0.7^{+0.2}_{-0.2}$	$9.2^{+0.2}_{-0.2}$	$3.1^{+0.2}_{-0.2}$	$17.5^{+2.8}_{-2.3}$	$-0.1^{+0.1}_{-0.1}$	11.5
S2CLSJ123633+621408	GOODS-N	$2.97^{+0.25}_{-0.23}$	$45.6^{+0.2}_{-0.2}$	$23.6^{+5.7}_{-4.7}$	$+0.4^{+0.3}_{-0.3}$	$0.9^{+0.2}_{-0.2}$	$9.4^{+0.1}_{-0.1}$	$3.2^{+0.1}_{-0.1}$	—	—	—
S2CLSJ021753-051100	UDS	$2.61^{+0.27}_{-0.25}$	$45.2^{+0.2}_{-0.2}$	$28.4^{+6.2}_{-5.2}$	$+0.4^{+0.3}_{-0.3}$	$1.3^{+0.3}_{-0.2}$	$9.3^{+0.2}_{-0.2}$	$3.1^{+0.2}_{-0.2}$	$33.5^{+3.3}_{-2.3}$	$+0.0^{+0.1}_{-0.1}$	11.9
S2COSMOSJ095715+022008	COSMOS	$2.96^{+0.43}_{-0.44}$	$45.2^{+0.2}_{-0.2}$	$1.9^{+2.6}_{-1.3}$	$+0.5^{+1.9}_{-1.0}$	$0.4^{+0.6}_{-0.3}$	$9.3^{+0.1}_{-0.2}$	$3.2^{+0.1}_{-0.2}$	$3.3^{+2.4}_{-3.6}$	$-0.9^{+0.0}_{-0.0}$	10.9
S2CLSJ021915-044408	UDS	$2.38^{+0.24}_{-0.22}$	$44.4^{+0.2}_{-0.2}$	$16.2^{+5.0}_{-3.9}$	$-0.2^{+0.3}_{-0.2}$	$0.8^{+0.2}_{-0.2}$	$9.3^{+0.1}_{-0.1}$	$3.2^{+0.1}_{-0.1}$	—	—	—
S2CLSJ021644-050222	UDS	$2.57^{+0.22}_{-0.21}$	$44.3^{+0.2}_{-0.2}$	$21.8^{+5.6}_{-4.5}$	$+0.1^{+0.3}_{-0.2}$	$1.1^{+0.3}_{-0.2}$	$9.4^{+0.1}_{-0.1}$	$3.2^{+0.1}_{-0.1}$	—	—	—

Table C.1 (continued from previous page)

IAU	Field	z	$P_{\rm UR}$ %	$\sum \mathcal{F}$	$\delta^{\dagger}_{R_{\rm e}}$	$\sum \mathcal{P}^{\dagger}_{\rm assoc}$	$\log_{10}(M_{\rm dust})^{\dagger}$ $[M_{\odot}]$	$\log_{10}(\Psi)^{\dagger}$ $[M_{\odot}\,{\rm yr}^{-1}]$	$\sum \mathcal{P}_{\rm assoc}$	$\delta_{R_{\rm e}}$	$\log_{10}(M_{\rm stars})$ $[M_{\odot}]$
				FIR					**Optical/NIR**		
S2COSMOSJ095835+025327	COSMOS	$2.63^{+0.28}_{-0.26}$	$43.8^{+0.2}_{-0.2}$	$2.9^{+2.8}_{-1.6}$	$-0.6^{+0.4}_{-0.2}$	$0.4^{+0.4}_{-0.2}$	$9.3^{+0.1}_{-0.1}$	$3.1^{+0.1}_{-0.1}$	—	—	—
S2COSMOSJ095947+013659	COSMOS	$2.70^{+0.31}_{-0.28}$	$43.1^{+0.2}_{-0.2}$	$5.9^{+3.5}_{-2.3}$	$-0.1^{+0.5}_{-0.4}$	$0.5^{+0.3}_{-0.2}$	$9.2^{+0.2}_{-0.2}$	$3.1^{+0.1}_{-0.2}$	$22.3^{+2.8}_{-4.2}$	$-0.1^{+0.4}_{-0.2}$	11.5
S2COSMOSJ100013+023429	COSMOS	$2.77^{+0.33}_{-0.29}$	$42.6^{+0.2}_{-0.2}$	$25.6^{+6.1}_{-5.0}$	$+0.4^{+0.3}_{-0.3}$	$1.1^{+0.3}_{-0.2}$	$9.4^{+0.2}_{-0.1}$	$3.2^{+0.2}_{-0.1}$	$28.5^{+3.3}_{-3.7}$	$+0.3^{+0.4}_{-0.3}$	11.6
S2CLSJ021543-050050	UDS	$2.42^{+0.32}_{-0.31}$	$41.9^{+0.2}_{-0.2}$	$11.2^{+4.3}_{-3.2}$	$-0.1^{+0.3}_{-0.3}$	$0.6^{+0.2}_{-0.2}$	$9.2^{+0.2}_{-0.2}$	$3.0^{+0.2}_{-0.2}$	—	—	—
S2CLSJ021931-045826	UDS	$2.83^{+0.36}_{-0.28}$	$41.1^{+0.2}_{-0.2}$	$23.1^{+5.8}_{-4.7}$	$+0.3^{+0.3}_{-0.3}$	$0.7^{+0.2}_{-0.1}$	$9.2^{+0.2}_{-0.2}$	$3.1^{+0.2}_{-0.2}$	$18.6^{+2.1}_{-2.1}$	$+0.0^{+0.1}_{-0.1}$	11.5
S2CLSJ021756-045244	UDS	$2.36^{+0.26}_{-0.24}$	$41.0^{+0.2}_{-0.2}$	$15.2^{+4.8}_{-3.8}$	$-0.2^{+0.2}_{-0.2}$	$0.6^{+0.2}_{-0.2}$	$9.2^{+0.2}_{-0.2}$	$3.0^{+0.1}_{-0.2}$	$29.8^{+3.4}_{-3.2}$	$+0.0^{+0.1}_{-0.1}$	11.7
S2COSMOSJ100202+014453	COSMOS	$3.19^{+0.36}_{-0.31}$	$40.9^{+0.2}_{-0.2}$	$6.7^{+3.6}_{-2.5}$	$+0.0^{+0.5}_{-0.4}$	$0.4^{+0.2}_{-0.1}$	$9.3^{+0.1}_{-0.1}$	$3.2^{+0.1}_{-0.1}$	$10.2^{+2.0}_{-3.3}$	$-0.3^{+0.3}_{-0.2}$	11.2
S2CLSJ021833-052042	UDS	$2.46^{+0.28}_{-0.27}$	$40.7^{+0.2}_{-0.2}$	$26.3^{+6.0}_{-4.9}$	$+0.3^{+0.3}_{-0.3}$	$1.2^{+0.3}_{-0.2}$	$9.3^{+0.2}_{-0.2}$	$3.1^{+0.2}_{-0.2}$	$42.7^{+3.6}_{-2.7}$	$+0.0^{+0.1}_{-0.1}$	11.9
S2COSMOSJ100039+023843	COSMOS	$2.63^{+0.35}_{-0.31}$	$40.5^{+0.2}_{-0.2}$	$15.7^{+5.0}_{-3.9}$	$+0.2^{+0.4}_{-0.3}$	$0.7^{+0.2}_{-0.2}$	$9.2^{+0.2}_{-0.2}$	$3.1^{+0.2}_{-0.2}$	$25.6^{+3.1}_{-4.1}$	$+0.0^{+0.4}_{-0.2}$	11.7
S2COSMOSJ095829+025227	COSMOS	$2.66^{+0.38}_{-0.33}$	$40.3^{+0.2}_{-0.2}$	$5.8^{+3.5}_{-2.3}$	$-0.2^{+0.5}_{-0.3}$	$0.5^{+0.3}_{-0.2}$	$9.1^{+0.2}_{-0.2}$	$3.0^{+0.1}_{-0.2}$	—	—	—
S2COSMOSJ100340+023638	COSMOS	$2.65^{+0.34}_{-0.37}$	$39.6^{+0.2}_{-0.2}$	$2.0^{+2.6}_{-1.3}$	$+0.9^{+2.5}_{-1.2}$	$0.9^{+1.1}_{-0.6}$	$9.4^{+0.1}_{-0.2}$	$3.2^{+0.1}_{-0.2}$	—	—	—
S2COSMOSJ100242+021407	COSMOS	$2.61^{+0.30}_{-0.26}$	$39.5^{+0.2}_{-0.2}$	$7.8^{+3.9}_{-2.7}$	$-0.2^{+0.4}_{-0.3}$	$0.5^{+0.3}_{-0.2}$	$9.2^{+0.1}_{-0.2}$	$3.1^{+0.1}_{-0.2}$	$37.3^{+3.3}_{-4.4}$	$+0.0^{+0.5}_{-0.2}$	11.8
S2CLSJ021803-045526	UDS	$2.87^{+0.27}_{-0.24}$	$39.0^{+0.2}_{-0.2}$	$20.7^{+5.4}_{-4.4}$	$+0.0^{+0.3}_{-0.2}$	$0.6^{+0.2}_{-0.1}$	$9.5^{+0.1}_{-0.1}$	$3.2^{+0.1}_{-0.1}$	$18.8^{+1.7}_{-2.7}$	$-0.0^{+0.1}_{-0.1}$	11.4
S2CLSJ021921-052716	UDS	$2.52^{+0.25}_{-0.23}$	$38.8^{+0.2}_{-0.2}$	$11.5^{+4.4}_{-3.3}$	$+0.2^{+0.5}_{-0.3}$	$0.6^{+0.2}_{-0.2}$	$9.2^{+0.1}_{-0.1}$	$3.1^{+0.1}_{-0.2}$	—	—	—
S2COSMOSJ100252+024159	COSMOS	$2.57^{+0.18}_{-0.18}$	$38.7^{+0.2}_{-0.2}$	$4.9^{+3.3}_{-2.1}$	$-0.3^{+0.5}_{-0.3}$	$0.6^{+0.4}_{-0.3}$	$9.5^{+0.1}_{-0.1}$	$3.4^{+0.1}_{-0.1}$	$40.7^{+3.7}_{-4.4}$	$-0.0^{+0.4}_{-0.2}$	11.8
S2COSMOSJ100117+014247	COSMOS	$2.90^{+0.26}_{-0.25}$	$38.1^{+0.2}_{-0.2}$	$8.7^{+4.0}_{-2.9}$	$+0.2^{+0.5}_{-0.4}$	$0.5^{+0.2}_{-0.2}$	$9.4^{+0.1}_{-0.1}$	$3.2^{+0.1}_{-0.1}$	$38.8^{+3.7}_{-2.9}$	$+0.1^{+0.4}_{-0.2}$	11.7
S2CLSJ141557+520711	EGS	$3.21^{+0.41}_{-0.31}$	$37.9^{+0.2}_{-0.2}$	$4.7^{+3.2}_{-2.0}$	$-0.4^{+0.4}_{-0.2}$	$0.1^{+0.1}_{-0.1}$	$9.3^{+0.1}_{-0.1}$	$3.2^{+0.1}_{-0.1}$	—	—	—
S2COSMOSJ100252+022903	COSMOS	$2.59^{+0.29}_{-0.27}$	$37.7^{+0.2}_{-0.2}$	$6.7^{+3.6}_{-2.5}$	$-0.1^{+0.5}_{-0.3}$	$0.6^{+0.3}_{-0.2}$	$9.3^{+0.1}_{-0.1}$	$3.1^{+0.1}_{-0.1}$	$33.7^{+2.9}_{-4.1}$	$-0.2^{+0.3}_{-0.2}$	11.8
S2CLSJ021600-045938	UDS	$2.34^{+0.28}_{-0.25}$	$37.3^{+0.2}_{-0.2}$	$19.8^{+5.3}_{-4.3}$	$+0.1^{+0.3}_{-0.2}$	$1.1^{+0.3}_{-0.2}$	$9.3^{+0.2}_{-0.2}$	$3.1^{+0.2}_{-0.2}$	—	—	—
S2CLSJ021931-052156	UDS	$2.44^{+0.32}_{-0.28}$	$36.6^{+0.2}_{-0.2}$	$11.3^{+4.3}_{-3.2}$	$+0.4^{+0.5}_{-0.4}$	$0.5^{+0.2}_{-0.1}$	$9.1^{+0.2}_{-0.2}$	$3.0^{+0.2}_{-0.2}$	—	—	—
S2COSMOSJ095921+014737	COSMOS	$2.78^{+0.30}_{-0.27}$	$36.5^{+0.2}_{-0.2}$	$4.7^{+3.2}_{-2.0}$	$-0.3^{+0.5}_{-0.3}$	$0.4^{+0.3}_{-0.2}$	$9.2^{+0.1}_{-0.1}$	$3.1^{+0.1}_{-0.1}$	$35.0^{+2.3}_{-4.4}$	$+0.0^{+0.4}_{-0.2}$	11.8
S2COSMOSJ095759+014111	COSMOS	$3.00^{+0.46}_{-0.36}$	$36.4^{+0.2}_{-0.2}$	$1.9^{+2.5}_{-1.2}$	$-0.7^{+0.4}_{-0.2}$	$0.3^{+0.4}_{-0.2}$	$9.1^{+0.2}_{-0.2}$	$3.0^{+0.2}_{-0.2}$	$32.5^{+1.8}_{-3.8}$	$+0.1^{+0.4}_{-0.2}$	11.7
S2COSMOSJ095942+022937	COSMOS	$3.27^{+0.34}_{-0.29}$	$36.4^{+0.2}_{-0.2}$	$12.5^{+4.5}_{-3.4}$	$-0.1^{+0.3}_{-0.3}$	$0.4^{+0.1}_{-0.1}$	$9.4^{+0.1}_{-0.1}$	$3.3^{+0.1}_{-0.1}$	$20.3^{+1.8}_{-3.0}$	$+0.3^{+0.5}_{-0.3}$	11.4
S2CLSJ141826+524154	EGS	$2.96^{+0.41}_{-0.31}$	$36.0^{+0.2}_{-0.2}$	$20.2^{+5.4}_{-4.4}$	$+0.2^{+0.3}_{-0.3}$	$0.6^{+0.2}_{-0.1}$	$9.2^{+0.2}_{-0.2}$	$3.1^{+0.2}_{-0.2}$	—	—	—
S2COSMOSJ100141+022713	COSMOS	$3.39^{+0.36}_{-0.32}$	$36.0^{+0.2}_{-0.2}$	$7.8^{+3.9}_{-2.7}$	$-0.1^{+0.5}_{-0.3}$	$0.3^{+0.1}_{-0.1}$	$9.6^{+0.1}_{-0.1}$	$3.4^{+0.1}_{-0.1}$	$27.4^{+1.7}_{-2.5}$	$+0.2^{+0.4}_{-0.2}$	11.7
S2COSMOSJ095958+023459	COSMOS	$2.98^{+0.37}_{-0.29}$	$35.9^{+0.2}_{-0.2}$	$20.5^{+5.5}_{-4.4}$	$+0.5^{+0.4}_{-0.3}$	$0.7^{+0.2}_{-0.1}$	$9.2^{+0.2}_{-0.2}$	$3.1^{+0.2}_{-0.2}$	$22.7^{+2.7}_{-3.1}$	$+0.2^{+0.5}_{-0.3}$	11.6
S2COSMOSJ095922+025137	COSMOS	$3.41^{+0.43}_{-0.35}$	$35.9^{+0.2}_{-0.2}$	$6.8^{+3.7}_{-2.5}$	$+0.1^{+0.6}_{-0.4}$	$0.3^{+0.2}_{-0.1}$	$9.6^{+0.1}_{-0.1}$	$3.3^{+0.1}_{-0.1}$	—	—	—
S2CLSJ021805-051050	UDS	$3.63^{+0.41}_{-0.32}$	$35.5^{+0.2}_{-0.2}$	$24.2^{+5.7}_{-4.7}$	$+0.2^{+0.3}_{-0.2}$	$0.4^{+0.1}_{-0.1}$	$9.5^{+0.1}_{-0.1}$	$3.3^{+0.2}_{-0.1}$	$7.3^{+0.8}_{-0.6}$	$+0.0^{+0.1}_{-0.1}$	11.1
S2COSMOSJ095936+020419	COSMOS	$2.44^{+0.26}_{-0.25}$	$35.4^{+0.2}_{-0.2}$	$7.8^{+3.8}_{-2.7}$	$-0.2^{+0.4}_{-0.3}$	$0.5^{+0.3}_{-0.2}$	$9.2^{+0.2}_{-0.2}$	$3.0^{+0.1}_{-0.2}$	$37.2^{+2.5}_{-5.8}$	$+0.1^{+0.4}_{-0.2}$	11.8
S2CLSJ021822-050738	UDS	$2.98^{+0.43}_{-0.32}$	$35.2^{+0.2}_{-0.2}$	$16.4^{+4.9}_{-3.8}$	$-0.1^{+0.3}_{-0.2}$	$0.5^{+0.2}_{-0.1}$	$9.2^{+0.2}_{-0.2}$	$3.0^{+0.2}_{-0.2}$	$25.5^{+1.2}_{-2.3}$	$-0.0^{+0.1}_{-0.1}$	11.6

† These parameters have been adjusted to account for 'missing' DSFGs.

Note. Ultra-Red galaxies are listed in decreasing order of ultra-red probability ($P_{\rm UR}$).

— The End —